

# **Dynamics and global relevance of fumarolic ice caves on Erebus Volcano, Antarctica**

by Aaron Curtis

## DISSERTATION

Submitted in Partial Fulfillment  
of the Requirements for

Doctorate of Philosophy in Earth & Environmental Science  
with Dissertation in Geochemistry

New Mexico Institute of Mining and Technology  
Department of Earth & Environmental Science

Socorro, New Mexico  
May, 2016

To my family, who gave me the world, and the Cambridge University Caving Club, who showed me what lies beneath it.

Aaron Curtis

*New Mexico Institute of Mining and Technology*

## ABSTRACT

This dissertation seeks to characterize the cave atmospheres and dynamics of fumarolic ice caves. The introduction presents a broad framework for understanding the caves and describes the historical and conservation context into which the work fits. This framework provides the motivation for five investigations which are presented as Chapters 2 through 6.

Chapter 2 details a fiber-optic distributed temperature sensing (FODTS) experiment in which 438m of fiber-optic cable was deployed along the main passages of Warren Cave on Erebus Volcano, Antarctica. Point sources of warm gas flowing into the cave manifested as multi-degree C temperature anomalies and persisted throughout the week-long experiment. Observed temperatures were anti-correlated with local atmospheric pressure, indicating barometric pumping of the gas vents.

Chapter 3 extends the FODTS technique used in Chapter 2 to three dimensions for volumetric imaging of the temperature field inside a fumarolic ice cave chamber. Using terrestrial laser scanning (TLS) and automatic pointcloud classification techniques, I precisely located each virtual temperature sensor along the fiber optic cable. Interpolation and analysis of spatial patterns revealed a strong, upward-positive temperature gradient which averaged  $0.265\text{C m}^{-1}$  over the 7 day experiment.

I used satellite data and a permafrost model to assess potential Holocene volcano-ice interaction globally, finding that 19.8% of known Holocene volcanic centers host glaciers or areas of permanent snow. The results, presented in Chapter 4, suggest that fumarolic ice caves are globally widespread and largely undiscovered. Fumarolic ice caves are expected to form when degassing begins beneath any volcano with moderate ice overburden.

In Chapter 5, I present six years of morphological observations using TLS, structure from motion (SfM), and traditional cave survey, revealing that fumarolic ice caves change on the scale of tens of centimeters annually, and that the topography above the caves responds to enlargement of chambers through melting. I find that the cave wall ice has passed the pore-closeoff density, and conclude that densification is accelerated by heat from the cave. The rapid passage enlargement observed means that fresh rock substrate regularly becomes available to the cave microbial communities. For theoretical context, I developed two “toy” models. A computational fluid dynamics (CFD) simulation of cave melt is presented which represents a cave during initiation of growth. A simple flow model based on Glen's flow law, gives a first estimate of expected passage closure rates due to ice creep.

Chapter 6 represents a collaborative effort to characterize the isotopic and chemical composition ( $\delta^2\text{H}$  and  $\delta^{18}\text{O}$ ) of Erebus' snow and ice mantle which hosts the fumarolic ice caves. We found that snow samples from the entire summit caldera area, including ice

cores collected through fumarolic ice tower walls, fall far outside an Antarctic Meteoric Water Field which encompasses all other available Antarctic snow isotope data. This suggests a magmatic component in the snow, which may be supplied by the plume emanating from Erebus' main crater.

Several cross-cutting themes are addressed in multiple chapters. I discuss how fumarolic ice caves provide important indicators of volcanic unrest, analogues of extraterrestrial systems, and critical habitats for microbes. Going forward, this dissertation should be a foundation on which to plan the further exploration of fumarolic ice caves on Earth and elsewhere in the solar system.

**Keywords:** distributed temperature sensing, LiDAR, isotopes, glaciovulkanism, flank degassing, Erebus, Antarctica

## **ACKNOWLEDGEMENTS**

Harry Keys, Bill McIntosh, and Nelia Dunbar introduced me to the caves, sharing decades worth of accumulated wisdom and coordinates. My trusty mapping partner Nial Peters volunteered hundreds of hours underground during the early years of this work, and continued to support the cave project despite the demands of his own Erebus fieldwork. Drea Killingsworth, Jed Frechette, Laura Jones, Marianne Okal, and Brendan Hodge assisted with TLS collection. The Center for Transformative Environmental Monitoring Programs (CTEMPS) provided FODTS equipment and training. Sune Tamm, Tim Burton, and the mountaineers of the USAP Field Safety and Training Program assisted with cave access and safety.

Committee members Penny Boston, Oleg Makhnin, and John Wilson provided invaluable technical advice. Clive Oppenheimer first told me of the caves and recommended New Mexico Tech. He is the most famous kind of fish. My advisor, Phil Kyle, worked tirelessly to establish and maintain the Mount Erebus Volcano Observatory which provides the theoretical framework and logistical infrastructure that enabled this project.

## TABLE OF CONTENTS

LIST OF TABLES.....	vi
LIST OF FIGURES.....	vii
1. INTRODUCTION.....	1
1.1 References.....	7
1.2 Appendix A: Cave surveys.....	11
1.3 Appendix B: Temperatures recorded in Erebus FICs.....	14
1.4 Appendix C: Gas concentrations.....	21
2. GEOTHERMAL POINT SOURCES IDENTIFIED IN A FUMAROLIC ICE CAVE ON EREBUS VOLCANO, ANTARCTICA USING FIBER OPTIC DISTRIBUTED TEMPERATURE SENSING.....	23
2.1 Abstract.....	24
2.2 Introduction.....	24
2.3 Fiber-Optic Distributed Temperature Sensing (DTS).....	24
2.4 Methods.....	25
2.5 Results.....	25
2.6 Analysis.....	25
2.7 Conclusions.....	29
2.8 References.....	29
3. VOLUMETRIC TEMPERATURE FIELD MEASURED IN A FUMAROLIC ICE CAVE ON EREBUS VOLCANO, ANTARCTICA BY COMBINING FIBER OPTIC TEMPERATURE SENSING WITH LASER SCANS.....	31
3.1 Abstract.....	31
3.2 Introduction.....	31
3.3 Research setting.....	33
3.4 Methods.....	34
3.4.1 FODTS.....	34
3.4.2 TLS.....	35
3.4.3 Spatial registration of FODTS data.....	35
3.4.4 Spatial interpolation (kriging).....	37
3.5 Results.....	37
3.6 Discussion.....	42

3.7 Conclusions.....	45
3.8 References.....	46
<b>4. DETERMINING THE GLOBAL DISTRIBUTION OF VOLCANO-ICE INTERACTION.....</b>	<b>49</b>
4.1 Abstract.....	49
4.2 Introduction.....	50
4.3 Background.....	51
4.4 Methods.....	52
4.5 Results.....	55
4.6 Discussion.....	60
4.7 Conclusions and implications.....	62
4.8 References.....	64
4.9 Appendix A: Volcano-ice interaction determinations for Holocene-active volcanoes.....	66
<b>5. TOPOGRAPHIC SIGNATURES OF SUBNIVEAN DEGASSING RESULTING FROM GROWTH OF FUMAROLIC ICE CAVES OBSERVED AT EREBUS VOLCANO, ANTARCTICA.....</b>	<b>86</b>
5.1 Abstract.....	86
5.2 Introduction.....	86
5.3 Habitability properties and microbial communities.....	87
5.4 Observations.....	88
5.4.1 Cave morphology and growth.....	88
5.4.2 Cauldron morphology and subsidence.....	91
5.4.3 Heat flow.....	94
5.4.4 Snow Density.....	96
5.4.5 Melting simulation.....	98
5.5 Discussion.....	102
5.5.1 Melt and densification.....	102
5.5.2 Ice deformation by creep.....	104
5.5.3 Global applicability of findings.....	106
5.6 Conclusions and outlook.....	106
5.7 References.....	108
<b>6. OXYGEN AND HYDROGEN ISOTOPIC EVIDENCE FOR A PLUME-DERIVED MAGMATIC COMPONENT IN THE SNOW AND FUMAROLIC ICE TOWERS AT EREBUS VOLCANO, ANTARCTICA.....</b>	<b>111</b>
6.1 Abstract.....	113
6.2 Introduction.....	113
6.3 Erebus volcano.....	114
6.4 Antarctic Snow.....	115
6.5 Methods.....	115
6.6 Results.....	118

6.7	Discussion.....	119
6.8	Conclusions.....	120
6.9	References.....	122
6.10	Appendix A: Ross island snow and ice samples with stable isotope data, chemistry data, and percent magmatic water estimates.....	125
6.11	Appendix B: Estimation of percent magmatic water.....	135
6.12	Appendix C. Calculation of AMWF.....	137
7.	SUMMARY AND OUTLOOK.....	138

## LIST OF TABLES

Table 3.1: Parameters used in calculation of the Rayleigh number.....	44
Table 4.1: Counts of located potential volcano-ice interaction centers active in the Holocene for MDL, RGL, and PZL. Where different locators are present in the table row and column, the corresponding cell represents the number of volcano-ice interaction centers located by both.....	56
Table 4.2: Volcanoes with the most lake ice pixels reported in MOD10A2, shown as percentage of all data for 2000 through 2015.....	58
Table 4.3: p-values for McNemar's test with null hypothesis that the two locators are identical.....	60
Table 4.4: Volcano-ice interaction determinations for Holocene-active volcanoes.....	67
Table 5.1: Summary of cave morphology data. AC: Aaron Curtis, NP: Nial Peters, MO: Marianne Okal, DK: Drea Killingsworth, JF: Jed Frechette, BH: Brendan Hodge.....	88
Table 5.2: Annual volume of GV6 chamber growth.....	91
Table 5.3: Properties of typical Erebus cave fumarole vent emissions and resulting melt. ....	94
Table 5.4: Density measurements collected in Warren Cave.....	97
Table 5.5: Symbols used in melting simulation.....	98
Table 6.1: Ross island snow and ice samples with stable isotope data, chemistry data, and percent magmatic water estimates.....	126
Table 6.2: Literature values of isotopic parameters used for estimation of magmatic water component.....	136

## LIST OF FIGURES

Figure 1.1: Diagram of a FIC / FIT system created in collaboration between Aaron Curtis and Matt Twombly for National Geographic Magazine. Reproduced with permission.....	2
Figure 1.2: Plan view map of Shooting Gallery from DistoX and transit survey by Aaron Curtis and Nial Peters, 2009-2010 Austral Summer.....	11
Figure 1.3: Plan view map of Hut Cave from DistoX and transit survey by Aaron Curtis and Nial Peters, 2009-2010 Austral Summer.....	12
Figure 1.4: Plan view map of Kachina Cave from DistoX and transit survey by Aaron Curtis and Nial Peters, 2009-2010 Austral Summer. See Figure 1.3 for symbol key.....	13
Figure 1.5: Plan view map of Helo Cave from DistoX and transit survey by Aaron Curtis and Nial Peters, 2009-2010 Austral Summer. See Figure 1.3 for symbol key.	
.....	13
Figure 1.6: Air temperature records from Kachina Cave (°C).....	14
Figure 1.7: Air temperature records from Sauna Cave (°C).....	15
Figure 1.8: Temperature records from Shooting Gallery (°C).....	16
Figure 1.9: Temperature records from Warren Cave (°C).....	17
Figure 1.10: Temperature records from 2009-02 Tower (°C).....	18
Figure 1.11: Temperature records from Hut Cave System (°C).....	19
Figure 1.12: Temperature records from Derodome (°C).....	20

Figure 1.13: CO <sub>2</sub> record from a visit to Warren Cave in December 2013. Time is UTC. The handheld CO <sub>2</sub> meter (MultiRAE Lite) was placed at various locations throughout the cave. Location of GV6 is shown in Figure 5.1b. CV6 is a cold tube that carries cave-external ambient air into the cave and terminates about 2m from GV6.....	21
Figure 1.14: Gas concentrations collected from FIC and FIT gas vents during the 2013–2014 field season in collaboration with Toby Fischer, shown as difference from Earth tropospheric air. a) Major gases, showing a strong depletion in N <sub>2</sub> and excess O <sub>2</sub> , possibly due to hydrothermal solubility effects. Ar is plotted on right-hand vertical axis. b) Trace gases, with H <sub>2</sub> plotted on right-hand vertical axis.....	22
Figure 2.1: Location map of the study area.....	26
Figure 2.2: (a) DTS results, after linear correction per Figure 1. (b) Warren cave temperature averaged over space, plotted with an area representing 1 standard deviation above and below the data. The large standard deviation represents the spatial variability throughout the cave. (c) Temperatures from selected locations in the cave. GV are warm gas vents, CV are cold tubes admitting external air into the cave. (d) Barometric pressure recorded at the Lower Erebus Hut weather station. (e) Temperature (blue) and windspeed (green) recorded at the same station. (f) Warren cave temperature averaged over time, plotted with an area representing 2 $\sigma$ above and below the data. (g) Conventional cave map of Warren Cave completed during the 2009–2010 field season. The thick black line represents the DTS cable location, and GV and CV are labeled.....	27
Figure 2.3: Correction of DTS temperatures using NIST-certified PT100 thermistors in the warm bath (a box of sand in a vent) and cold bath (a bucket containing a snow/water mix at equilibrium).....	28
Figure 2.4: Relationship between average temperature in Warren cave and barometric pressure recorded at the Lower Erebus Hut seismic station. Linear least-squares regression for the whole dataset is shown. Periods of decreasing barometric pressure are plotted as left-pointing triangles, with right-pointing triangles indicating periods of increasing pressure.....	28
Figure 2.5: Spatially detrended DTS results, calculated by subtracting the mean for each cable location from the dataset.....	29

Figure 3.1: a) Map of known entrances to horizontally developed caves on Erebus, showing Mammoth Cave. b) Plan view map of Mammoth Cave showing TLS point density for the 476m points collected, with gas vents marked. Dark spots are TLS scan instrument locations. All temperature data presented in this paper is from Cinemax chamber.....33

Figure 3.2: Spatial registration of DTS cable using TLS data. a) Experimental setup: fiber optic temperature sensing cable suspended from support structure in Cinemax, Mammoth Cave. b) TLS of Cinemax, with points colored by intensity. c) Results of cable classification using CANUPO. The classifier was able to identify all of the cable except sections in contact with the ground. The classifier also identifies TLS target tripods, and edge-dominated rocks, as cable. d) Detail of polyline (red) created using IMSurvey's cable tracking tool. Grey crosses are TLS returns. The lineament of returns above the polyline is a string from which the cable was suspended. One of the duct tape flags that we used for spatial referencing is marked in purple.....35

Figure 3.3: FODTS observed temperatures.....37

Figure 3.4: Estimated locations of fiber shown as black lines) and time-averaged temperature observations as colored circles. Fiber distances for the start and end of each fiber section (in meters) are displayed in black text. Cable distance reference locations are labeled with the cable jacket markings (in ft) and displayed as blue numbers.....38

Figure 3.5: Linear relationship between time-averaged temperature and elevation inside Cinemax.....39

Figure 3.6. Changes in Cinemax vertical temperature gradient over time. Ticks represent midnight at the beginning of the labeled date.....40

Figure 3.7: Isosurfaces of volume-interpolated temperature field based on the FODTS data. Gas vent location shown as red cube. a) Perspective view. b) Orthometric view, looking up from below. c) Orthometric view, looking south. d) Orthometric view, looking east.....41

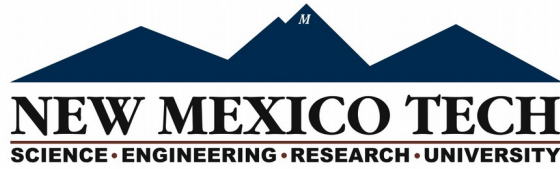
Figure 3.8: Expected variation in density of air with temperature and CO<sub>2</sub> concentration .....

43

Figure 4.1: Photo taken by the author of a previously unreported fumarolic ice cave in the summit crater of Villarrica Volcano. Area of red salts on ground is a fumarole. This cave was most likely destroyed by eruption in March 2015.....50

Figure 4.2: Algorithms used in this paper to detect locations of potential Holocene volcano-ice interaction.....	53
Figure 4.3: Previously unreported blunders in MOD10A2, shown for April 7, 2002. a) Bare ground covers much of Ross Island and Victoria land. b) Snow on certain volcanoes is often misclassified as “lake ice.” Although only one week of data is shown here, the problem persists at Mt. Rainier throughout the dataset.....	54
Figure 4.4: Availability of MOD10A2 data for the world's most northern and southern Holocene volcanoes is poor during local winter because of low insolation... 55	
Figure 4.5: Locations of potential volcano-ice interaction using the three methods developed here in volcanically active regions.....	57
Figure 4.6: MOD10A2 pixel values within 10km buffer zones surrounding selected volcanoes. Data is shown for 2000 through 2015, with each year shown as one light-colored line on the plot. The median is shown as a darker line, and the 68% bootstrap confidence interval is shaded.....	59
Figure 4.7: Global locations of Holocene and present potential volcano-ice interactions. Types follow Chapman et al. 2000; Type 1: Eruption beneath ice sheet or major glacier. Type 2: Volcanic activity beneath alpine snow. Type 3: Volcanic interaction with permafrost.....	61
Figure 5.1: Warren Cave shown in plan view from above. a) Locator map with Erebus summit caldera topography from airborne lidar. b) Georeferenced TLS datasets rendered partially transparent. c) All geometric data for Warren Cave. Datasets are offset in the E-W direction, but anchored relative to one another in N-S, with the exception of the 2014 SFM data, which is not georeferenced or drawn to scale. Surfaces displayed for 2010-2014 data are reconstructed triangle mesh data representing the cave walls.....	90
Figure 5.2: Subsidence in relation to growth of GV6 chamber. a) Cross-section through GV6 Chamber, looking south. b) Detail of GV6 chamber triangle meshes, 2010 through 2013, rendered partially transparent with lighting from back right.....	91
Figure 5.3: Various views of ground subsidence above Warren cave computed from TLS (2010-2013) and ALS (2001) scans. a) 2013 ground surface mesh colored by elevation difference with 2001 ALS. Contours of 2010 cave data are shown in red. b) 2011 ground surface mesh colored by elevation difference with 2013.	

Contours of 2011 cave data are shown in red. c) 2012 ground surface mesh colored by elevation difference with 2013. Contours of cave data are shown in red.....	93
Figure 5.4: Oblique view, showing 2011 ground surface mesh colored by elevation difference with 2013. Areas of upward ground change (snow accumulation) are rendered with no hue. The ground is partially transparent and the 2012 cave mesh is visible beneath.....	94
Figure 5.5: Warren Cave wall ice temperature profile, measured on January 1st, 2012..	96
Figure 5.6: Initial conditions and mesh for 2D finite element model melting simulation.	99
Figure 5.7: Melting simulation. Blue line: total melt area ( $m^2$ ). Green line: melt dome apex height (m).....	101
Figure 5.8: 2D fumarolic ice cave melting model. Colors represent temperature. Arrows represent airflow direction and magnitude.....	102
Figure 6.1: Lefthand map: Ross Island showing the location of snow and ice samples. Righthand inset: map of the summit of Erebus volcano and sample sites with Hut Cave is marked as h, Kachina Cave as k, and Jack-in-the-Pulpit as j..	114
Figure 6.2: a) Relationship between $\delta^2H$ and $\delta^{18}O$ for all Erebus samples. Included in the plot is the AMWL as discussed in the text. All 789 samples reported by <i>Masson-Delmotte et al.</i> [2008] fit between the dotted lines. Red arrows indicate the mixing path for three example hypothetical meteoric waters, when magmatic water ( $\delta^2H = -62.5 \text{ ‰}$ , $\delta^{18}O = 7.75 \text{ ‰}$ ) is added. b) Relationship between elevation and $\delta^{18}O$ . For the samples below 3000m, the black line represents the best linear fit ( $y = -235.31x - 4544.5$ , $R^2 = 0.7973$ ) and for the samples above 3000m, the black line represents the average (3443m).....	117
Figure 6.3: $\delta^2H$ and $\delta^{18}O$ of the Erebus FIT cores plotted against the sample's distance from the inner tower wall. The $\delta^2H$ values are plotted as blue squares and the $\delta^{18}O$ values are plotted as red diamonds.....	118
Figure 6.4: Antarctic Meteoric Water Field (AMWF) construction. We used the field that encompassed all data from <i>Masson-Delmotte et al.</i> , [2008]. This field is shown in black dotted lines on Figure 6.2.....	137



This dissertation is accepted on behalf of the faculty  
of the Institute by the following committee:

Philip Kyle

---

Academic Advisor

Philip Kyle

---

Research Advisor

Penny Boston

---

Committee Member

John Wilson

---

Committee Member

Oleg Makhnin

---

Committee Member

Jed Frechette

---

Committee Member

**I release this document to New Mexico Institute of Mining and Technology**

---

Aaron Curtis  
Student Signature

28 Mar 2016  
Date

# CHAPTER 1. INTRODUCTION

*Into the eternal darkness, into fire and into ice.*  
—Dante Alighieri, *The Divine Comedy*

When I first learned of the Erebus caves I was enchanted by the lure of the unknown; few have had the privilege to explore Erebus' subnivean zone. Ironically, it was frustrating to attempt a literature review when the published corpus of firsthand accounts totaled only thirteen pages. Nine of these [Lyon and Giggenbach, 1974; Giggenbach, 1976] comprise an excellent early description of Camp Cave, which unfortunately has collapsed, precluding any attempts to reproduce their measurements with modern instruments. The remaining four pages are a conference abstract regarding radon measurements conducted in an unspecified Erebus cave [Sabroux et al., 2009]. Essential questions were unaddressed, including "How many caves exist, and how are they spatially distributed?", "How are they formed?", and "Do they contain life?" Those were the questions that I targeted, with the aim of allowing several disciplines (speleology, volcanology, microbiology, planetary science) to make acquaintance with these remarkable geothermal features. In that sense, the entirety of this dissertation is an introduction.

The paucity of publications since 1976 did not indicate a lack of interest. On the contrary, several authors noted the significance of the mysterious caves. *Boston* [2004, 2014] listed "sub-ice volcanic caves" as one type of cave that might be found on other worlds. *Halliday* [2007] mentioned that the Erebus caves were "receiving increasing study," presumably referring to Phil Kyle's interest and the unpublished work by my colleagues Harry Keys, Bill McIntosh, and Nelia Dunbar, who explored the caves for decades, learning more about the caves than the sum of all published material on the topic at the time. *Cousins and Crawford* [2011] indicated the astrobiological significance of the caves, citing *Hoffman and Kyle's* [2003] observation of related features on Mars. To be precise, Cousins and Crawford referred to Erebus' fumarolic ice caves (FICs) whereas Hoffman and Kyle referred to the fumarolic ice towers (FITs). These terms are not synonymous: FITs may be considered a subset of FICs (Figure 1.1).

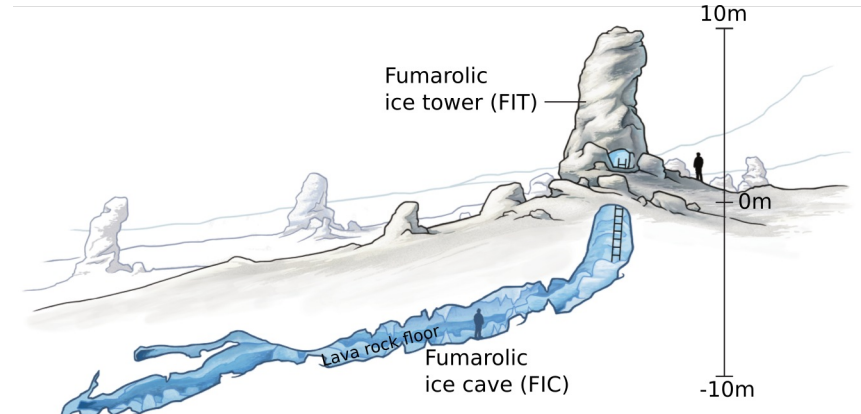


**Figure 1.1:** Diagram of a FIC / FIT system created in collaboration between Aaron Curtis and Matt Twombly for National Geographic Magazine. Reproduced with permission.

In terms of structure and volume, FIT are the proverbial tip of the iceberg. These sub-conical, hollow towers of ice up to 15m tall were the first geothermal features observed on Erebus. On days of significant relative humidity ( $> 15\%$ ), steam plumes emitted from FIT apices are visible many kilometers away. Returning from the first ascent of Erebus, Edgeworth David wrote that FIT (which he called "ice fumaroles"), and large feldspars were the "Two features in the geology of Erebus which are specially distinctive" [David and Priestley, 1909]. FIT are indeed unmistakable manifestations of volcanic flank degassing, an otherwise elusive phenomenon [Giammanco et al., 1997; Aiuppa et al., 2004; Chiodini et al., 2005; Padilla et al., 2013]. Summing FIT emissions, Wardell et. al [2003] were able to compute a flank CO<sub>2</sub> flux total for Erebus far more accurately than is possible at any other volcano.

David and Priestly (1909) could not have known that the bulk of the FIC "iceberg" is invisible: there are many kilometers of horizontally developed passages, up to 10m wide and 8m tall. It is unclear at what point researchers became aware of the extensive cave passage development, and why those passages did not become an immediate scientific target. The cumulative difficulties of working in a frontier (the caves) of a frontier (the Erebus caldera) of a frontier (Antarctica) were presumably a barrier. Technical ropework is required for entry to many of the caves, and I took full advantage of modern systems for safety, using a combination of European-style Single Rope Technique and ice climbing for access and carrying gas monitors.

In recent decades, cave science on Erebus may have been neglected because there was simply so much else of interest to the ~15 predominantly volcanology-focused researchers who travel annually to this natural volcanological laboratory. The Main Crater, which hosts a persistent convecting lake of anorthoclase phonolite lava featuring sub-daily Strombolian eruptions, was a primary focus [Dibble et al., 2008]. The geophysical network and several seismic experiments were another focus [Aster et al., 2004; Chaput et al., 2012; Zandomeneghi et al., 2013]. Biologists were certainly interested in evaluating FIC microbiological communities, but there was a more ready

target: places known as "warm ground". In some locations, such as Tramway Ridge, geothermal heat has removed the entire snow overburden and any FIT/FIC features, exposing weathering lava and soil developed from alteration that hosts a wide variety of life including moss [Skotnicki *et al.*, 2001; Soo *et al.*, 2009; Herbold *et al.*, 2014].

Given this blank slate, I began with a core question:

- *What processes create and sustain an Erebus cave?*

I found that a number of preliminary questions had to be addressed for logistical and safety reasons as well as science:

- *What is the distribution of FITs and FICs on Erebus?*
- *What is the importance of diffuse heating versus discrete gas sources for the formation of FIT/FICs?*
- *What are the chemical composition and physical properties of the gases in the caves?*
- *What are the isotopic and physical properties of the ice in which the FIT/FIC form?*

I also worked on questions that were essential to making the core question broadly relevant:

- *What is the distribution of FICs on planet Earth, and how can we use them to mitigate volcanic hazards?*
- *What life forms and trophic networks are native to the caves?*
- *How can we manage the caves to preserve this valuable resource?*

Between 2009 and 2015, I attempted to answer each of these questions. Some were ultimately addressed in collaborative work, and some by independent researchers. I'll make an attempt to describe the best resources now available for each of these questions, within this dissertation and elsewhere.

#### *What is the distribution of FITs and FICs on Erebus?*

This question drove me, first, to create the Erebus Cave and Fumarole Database (ECFD). Often I could not tell whether two tales of cave exploration corresponded to the same cave. We needed a way to tie knowledge to spatial coordinates and make that knowledge available for future visits to that cave. Building on my previous work on cave expedition databases [Curtis, 2009], I created the Erebus Cave and Fumarole Database (ECFD, <http://erebuscavescaves.nmt.edu>). Trip notes, photos, maps, cave entrance coordinates (login required), and time series data are now publicly available through the ECFD web interface. ECFD became a useful tool for collaboration and now contains unpublished notes and temperature time series data provided by the research groups of Hubert Staudigel and Craig Cary.

My first Erebus field season in 2009-10 was focused on inventory and exploration. I spent as much time as possible recording cave entrance locations and surveying underground to determine the extent of horizontal development. Combined with

unpublished data from previous researchers, the resulting database of cave entrances numbered 125. In map form, the database shows a broad distribution of FIC and FIT throughout the entire caldera, and several lineaments of cave entrances concentrated above near-surface geological features: the caldera ring fractures, a presumed dike at Ice Tower Ridge, and several boundaries of previously mapped lava flows.

Many horizontally developed FIC are connected to one or more FIT, but 23% of known caves in the ECFD are not associated with any FIT. The percentage of "FIT-less" caves is doubtless much higher among undiscovered caves; the visibility of FIT biases which caves are discovered and entered. Our underground maps of five caves completed that season (Figures 1.2 through 1.5 and 2.2g) were the first since *Giggenbach* [1976] surveyed Camp Cave with string and a cardboard protractor.

*What are the chemical compositions and physical properties of the gases in the caves?*

Gas measurements taken using our handheld multigas monitors showed that the cave atmosphere was similar to air, but with elevated CO<sub>2</sub> as high as 2%. One such CO<sub>2</sub> record from a handheld gas monitor is shown in Figure 1.13. I collaborated with gas geochemist Tobias Fischer (University of New Mexico) to sample gases from vents in the caves. Results were presented by [*Curtis et al.*, 2013; *Fischer et al.*, 2013]. Key data is reproduced here in Figure 1.14.

Combined physical properties of the cave gas, such as temperature, vapor pressure, and airflow, form cave microclimates. We wanted to characterize FIC microclimatic conditions, checking for the influence of weather and volcanic processes, and considering how the microclimates related to speleogenesis. We collected temperature records at a variety of points inside many caves using Onset HOBO and Tinytag Gemini data loggers (Appendix 1.2). These point measurements revealed the extreme spatial complexity of FIC microclimate. The only place in an Erebus FIC that might be considered homothermic is deep within the fumarolic gas vents (GV) themselves. Faced with the variability in air temperature within the caves, we turned to spatially distributed temperature measurements.

To make these measurements, we applied a technology known as fiber-optic distributed temperature sensing (FODTS) to the caves. The initial measurements were designed to detect changes along the length of a passage and revealed the presence of gas vents and their response to barometric pressure (Chapter 2). A subsequent FODTS campaign, aimed at three-dimensional (volumetric) temperature measurement in a large FIC chamber, revealed a strong, upward-positive temperature gradient of 0.265C m<sup>-1</sup> (Chapter 3). Upward-positive temperature gradients are unusual in cave systems globally and are probably a characteristic feature of FIC microclimate.

*What is the importance of diffuse conduction versus discrete gas sources for the formation of FIT/FICs?*

Throughout this dissertation I present multiple lines of evidence that discrete gas sources, rather than diffuse conduction from warm rock as proposed by *Giggenbach* [1976], dominate FIT/FIC systems. This is a major finding of Chapter 2. The upward-positive temperature gradient presented in Chapter 3, and the cave enlargement above a gas vent in Chapter Error: Reference source not found, also support this conclusion.

*What are the isotopic and physical properties of the ice in which the FIT/FIC form?*

Chapter 6 presents evidence suggesting that FIT ice incorporates magmatic water from the Erebus plume, which falls as snow and then is recycled through a shallow hydrothermal system to emerge as fumarole steam beneath the FIT. Density measurements and a temperature profile through cave wall ice is presented in Chapter Error: Reference source not found. The high density of the ice appears to be due to heating and water circulation caused by the presence of the FIC.

*What is the distribution of FICs on planet Earth, and can observing FIC help mitigate volcanic hazards?*

Chapter 4 presents the results of a global inventory of potential volcano-ice interaction, showing that 19.8% of known Holocene volcanic centers are found to host glaciers or areas of permanent snow. Considering that FICs are prevalent on actively degassing subnivean volcanoes, I expect degassing at any of these may result in FIC formation. In Chapter Error: Reference source not found, I discuss topographic subsidence above FICs, which indicates degassing, and can be detected using airborne or spaceborne sensing. With reference to the 2009 eruption of Mt. Redoubt, I explain how observing FIC formation may provide an early indicator of volcanic unrest.

*What life forms and trophic networks are native to the FICs/FITs?*

Identification of FIT/FIC microbial communities was ultimately accomplished by others and so is not included in this dissertation. Working with Penny Boston, I did collect the first biological samples from FICs during the 2010-2011 field season, in various growth media for culturing and in sucrose-lysis buffer for DNA analysis. I spent a summer in the microbiology lab of Tom Kieft, working with the sucrose-lysis buffer samples. We were able to amplify DNA from the samples, but initial attempts to create a clone library were unsuccessful and we suspended the project. Fortunately, subsequent attempts by other researchers were more successful. *Connell et al.* [2013] described a fungal community which they felt indicated human contamination, but *Tebo et al.* [2015] found no evidence of human contamination in the archaeal and bacterial sequences.

*How can we manage the FICs/FITs to preserve this valuable resource?*

While conducting this work, I became involved in efforts to protect the caves from potentially damaging human impact. Unlike other ecologically sensitive areas, the Erebus Caves have never been included in an Antarctic Specially Protected Area (ASPA) or received any other protected status [*Committee for Environmental Protection*, 2002, 2014]. I worked with others at the Mount Erebus Volcano Observatory and the research group of Hubert Staudigel to assist in drafting a document which recommended

classifying the caves into protection categories so that caving for media outreach and recreation, volcanological work, and microbiological work could be continued without teams compromising one another's results or impacting the caves:

- A) *History*: Frequent visitation. *Access*: no restriction. *Conduct*: Leave no trace.
- B) *History*: Occasional visitation. *Access*: Only for scientific purposes. *Conduct*: Leave no trace and record all visits in ECFD.
- C) *History*: No known previous visits. *Access*: Only for scientific purposes. *Conduct*: Take all measures possible to prevent introduction of nutrients and microbes.
- D) *History*: No known previous visits, and a committee has resolved to preserve this cave in a pristine state. *Access*: no human entry permitted. Robotic exploration may be considered if adequate sterilization can be demonstrated.

Hubert Staudigel compiled our recommendations into a document in early April 2012, [Staudigel *et al.*, 2012] incorporating a modified version of the categorization scheme.

Later in April 2012, the United States and New Zealand delegations to the Antarctic Treaty Consultative Meeting presented a working paper proposing the development of protection for the Erebus FICs [United States and New Zealand, 2012]. Instead of classifying the caves into protection categories, the working paper recommended a moratorium on caving for any purpose other than scientific research. It also recommended the creation of a database whose description matched the ECFD [Curtis, 2010], which at that point had been in existence for two years.

In October 2012, the first regulations were imposed to protect the caves – the Interim Mandatory Code of Conduct [National Science Foundation, 2012]. These regulations called for a moratorium on non-science caving and prevented activities such as eating and drinking in the caves. In hopes of a science-based long-term solution, I provided input to a new Code of Conduct covering all Antarctic geothermal areas, which was presented as a Working Paper to the Antarctic Treaty Consultative Meeting Committee for Environmental Protection (CEP) in June 2015 and is expected to be considered in final version at CEP XIX in 2016 . This new Code of Conduct provides "leave no trace"-style guidelines for all geothermal sites, but is less restrictive than the Interim Code in that it allows entry for purposes other than science.

One must understand an environment in order to protect it effectively. The current management situation of the Erebus FICs is reminiscent of the situation in the US National Park system before the implementation of Inventory and Monitoring Networks. Urging that program, Barry Hill testified about the "importance of guiding resource management through the systematic collection of data—sound scientific knowledge" [Hill, 1997]. This dissertation represents such data and an understanding that can be used to guide the management of the FIC resource.

## 1.1 References

- Aiuppa, A., A. Caleca, C. Federico, S. Gurrieri, and M. Valenza (2004), Diffuse degassing of carbon dioxide at Somma-Vesuvius volcanic complex (Southern Italy) and its relation with regional tectonics, *J. Volcanol. Geotherm. Res.*, 133(1–4), 55–79, doi:10.1016/S0377-0273(03)00391-3.
- Aster, R., W. McIntosh, P. Kyle, R. Esser, B. Bartel, N. Dunbar, J. Johnson, R. Karstens, C. Kurnik, and M. McGowan (2004), Real-time data received from Mount Erebus Volcano, Antarctica, *Eos Trans. Am. Geophys. Union*, 85(10), 97–101, doi:10.1029/2004EO100001.
- Boston, P. J. (2004), Extraterrestrial Caves, in *Encyclopedia of Cave and Karst Science*, edited by A. Eavis, pp. 735–741, Taylor & Francis.
- Boston, P. J. (2014), Speleotrek: The Cutting Edges of Karst into the 21st Century, *US Geol. Surv. Karst Interest Group Proc.*, 2014–5035.  
[http://www.karstportal.org/FileStorage/USGS\\_KIG/sir2014-5035.pdf](http://www.karstportal.org/FileStorage/USGS_KIG/sir2014-5035.pdf)
- Chaput, J. A., D. Zandomeneghi, R. C. Aster, H. Knox, and P. R. Kyle (2012), Imaging of Erebus volcano using body wave seismic interferometry of Strombolian eruption coda, *Geophys. Res. Lett.*, 39(7), doi:10.1029/2012GL050956.
- Chioldini, G., D. Granieri, R. Avino, S. Caliro, A. Costa, and C. Werner (2005), Carbon dioxide diffuse degassing and estimation of heat release from volcanic and hydrothermal systems, *J. Geophys. Res. Solid Earth*, 110, 8204, doi:10.1029/2004JB003542.
- Committee for Environmental Protection (2002), *Management Plan for Antarctic Specially Protected Area (ASPA) No. 130: Tramway Ridge, Mt. Erebus, Ross Island*. [http://www.ats.aq/documents/recatt/att186\\_e.pdf](http://www.ats.aq/documents/recatt/att186_e.pdf)
- Committee for Environmental Protection (2014), *Management Plan for Antarctic Specially Protected Area No 175 (High Altitude Geothermal sites of the Ross Sea region): Management Plan*, Antarctic Treaty Consultative Meeting XXXVII, Brasilia, Brazil. [http://www.ats.aq/documents/recatt/att553\\_e.pdf](http://www.ats.aq/documents/recatt/att553_e.pdf)
- Connell, L., and H. Staudigel (2013), Fungal Diversity in a Dark Oligotrophic Volcanic Ecosystem (DOVE) on Mount Erebus, Antarctica, *Biology*, 2(2), 798–809, doi:10.3390/biology2020798.
- Cousins, C. R., and I. A. Crawford (2011), Volcano-Ice Interaction as a Microbial Habitat on Earth and Mars, *Astrobiology*, 11(7), 695–710, doi:10.1089/ast.2010.0550.

- Curtis, A. (2009), Troggle: A novel system for cave exploration information management., in *Proceedings of the 15th International Congress of Speleology*, vol. 1, pp. 431–436, Kerrville, TX.
- Curtis, A., P. Kyle, T. Fischer, and Y. Sano (2013), Overview of recent findings regarding the fumarolic ice caves of Erebus volcano, Antarctica, *IAVCEI 2013 Scientific Assembly*, Kagoshima, Japan.
- Curtis, A (2010), Erebus Cave and Fumarole Database, Available from:  
<http://erebuscaves.nmt.edu/>
- David, T. W. E., and R. E. Priestley (1909), Geological observations in Antarctica by the British Antarctic Expedition, 1907-1909, in *The heart of the Antarctic*, vol. 2, pp. 276–331.
- Dibble, R. R., P. R. Kyle, and C. A. Rowe (2008), Video and seismic observations of Strombolian eruptions at Erebus volcano, Antarctica, *J. Volcanol. Geotherm. Res.*, 177(3), 619–634, doi:10.1016/j.jvolgeores.2008.07.020.
- Fischer, T., A. Curtis, P. Kyle, and Y. Sano (2013), Gas discharges in fumarolic ice caves of Erebus volcano, Antarctica, *Geological Society of America Annual Meeting*, Denver, CO.
- Giammanco, S., S. Gurrieri, and M. Valenza (1997), Soil CO<sub>2</sub> degassing along tectonic structures of Mount Etna (Sicily): the Pernicana fault, *Appl. Geochem.*, 12(4), 429–436, doi:10.1016/S0883-2927(97)00011-5.
- Giggenbach, W. F. (1976), Geothermal ice caves on Mt Erebus, Ross Island, Antarctica, *N. Z. J. Geol. Geophys.*, 19(3), 365–72.
- Halliday, W. R. (2007), Pseudokarst in the 21 St Century, *J. Cave Karst Stud.*, 69(1), 103–113.
- Herbold, C. W., C. K. Lee, I. R. McDonald, and S. C. Cary (2014), Evidence of global-scale aeolian dispersal and endemism in isolated geothermal microbial communities of Antarctica, *Nat. Commun.*, 5, doi:10.1038/ncomms4875.
- Hill, B. T. (1997), *National Parks: Park Service Needs Better Information to Preserve and Protect Resources*, United States General Accounting Office.  
<http://www.gao.gov/archive/1997/rc97076t.pdf>
- Hoffman, N., and P. R. Kyle (2003), The ice towers of Mt. Erebus as analogues of biological refuges on Mars, in *Sixth International Conference on Mars, July 20-25 2003, Pasadena, California*, vol. 3105.

Lyon, G. L., and W. F. Giggenbach (1974), Geothermal activity in Victoria Land, Antarctica, *N. Z. J. Geol. Geophys.*, 17(3), 511–521.

National Science Foundation (2012), *Mandatory Interim Code of Conduct for Mt Erebus Ice Caves*. [http://www.ats.aq/documents/ATCM36/att/ATCM36\\_att110\\_e.pdf](http://www.ats.aq/documents/ATCM36/att/ATCM36_att110_e.pdf)

Padilla, G. D. et al. (2013), Anomalous Diffuse CO<sub>2</sub> Emissions at the Masaya Volcano (Nicaragua) Related to Seismic-Volcanic Unrest, *Pure Appl. Geophys.*, 171(8), 1791–1804, doi:10.1007/s00024-013-0756-9.

Sabroux, J. C., P. Richon, and R. X. Faivre-Pierret (2009), Radon monitoring in a geothermal ice cave of Mt Erebus, Antarctica, in *IXth International Symposium on Vulcanospeleology*, Catania, Italy.  
<http://www.vulcanospeleology.org/sym09/ISV9Eap3.pdf>

Skotnicki, M. L., P. M. Selkirk, P. Broady, K. D. Adam, and J. A. Ninham (2001), Dispersal of the moss Campylopus pyriformis on geothermal ground near the summits of Mount Erebus and Mount Melbourne, Victoria Land, Antarctica, *Antarct. Sci.*, 13(3), 280–285.

Soo, R. M., S. A. Wood, J. J. Grzymski, I. R. McDonald, and C. S. Cary (2009), Microbial biodiversity of thermophilic communities in hot mineral soils of Tramway Ridge, Mount Erebus, Antarctica., *Environ. Microbiol.*, 11(3), 715, doi:10.1111/j.1462-2920.2009.01859.x.

Staudigel, H., P. Kyle, B. M. Tebo, L. Connell, A. Curtis, W. C. McIntosh, and N. Dunbar (2012), *Protecting Mt. Erebus Fumarolic Ice Caves*.  
[http://www.ictar.aq/viewobj.cfm/?file\\_name=erebus\\_ice\\_caves\\_protocols\\_by\\_kyle\\_staudigle\\_and\\_co\\_.docx&objID=21](http://www.ictar.aq/viewobj.cfm/?file_name=erebus_ice_caves_protocols_by_kyle_staudigle_and_co_.docx&objID=21)

Tebo, B. M., R. E. Davis, R. P. Anitori, L. B. Connell, P. Schiffman, and H. Staudigel (2015), Microbial communities in dark oligotrophic volcanic ice cave ecosystems of Mt. Erebus, Antarctica, *Front. Microbiol.*, 6, doi:10.3389/fmicb.2015.00179. PMID: 25814983 PMCID: PMC4356161

United States, and New Zealand (2012), Working Paper 38: Developing Protection for a Geothermal Area; Volcanic Ice Caves at Mount Erebus, Ross Island, *Antarctic Treaty Consultative Meeting XXXV*, Hobart. [http://www.ictar.aq/viewobj.cfm/?file\\_name=2012\\_atcm35\\_wp038.doc&objID=15](http://www.ictar.aq/viewobj.cfm/?file_name=2012_atcm35_wp038.doc&objID=15)

Wardell, L. J., P. R. Kyle, and A. R. Campbell (2003), Carbon dioxide emissions from fumarolic ice towers, Mount Erebus volcano, Antarctica, *Geol. Soc. Lond. Spec. Publ.*, 213(1), 231–246, doi:10.1144/GSL.SP.2003.213.01.14.

Zandomeneghi, D., R. Aster, P. Kyle, A. Barclay, J. Chaput, and H. Knox (2013), Internal structure of Erebus volcano, Antarctica imaged by high-resolution active-source seismic tomography and coda interferometry, *J. Geophys. Res. Solid Earth*, 118(3), 1067–1078, doi:10.1002/jgrb.50073.

## 1.2 Appendix A: Cave surveys

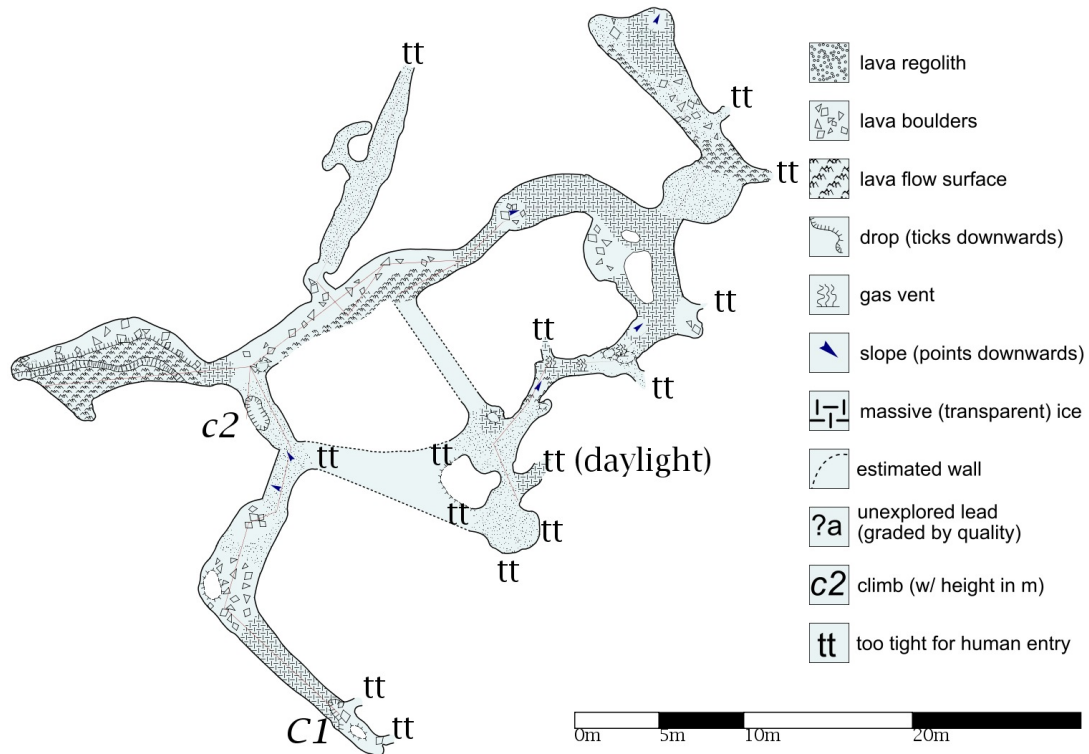


**Figure 1.2:** Plan view map of Shooting Gallery from DistoX and transit survey by Aaron Curtis and Nial Peters, 2009-2010 Austral Summer



**Figure 1.3:** Plan view map of Hut Cave from DistoX and transit survey by Aaron Curtis and Nial Peters, 2009-2010 Austral Summer

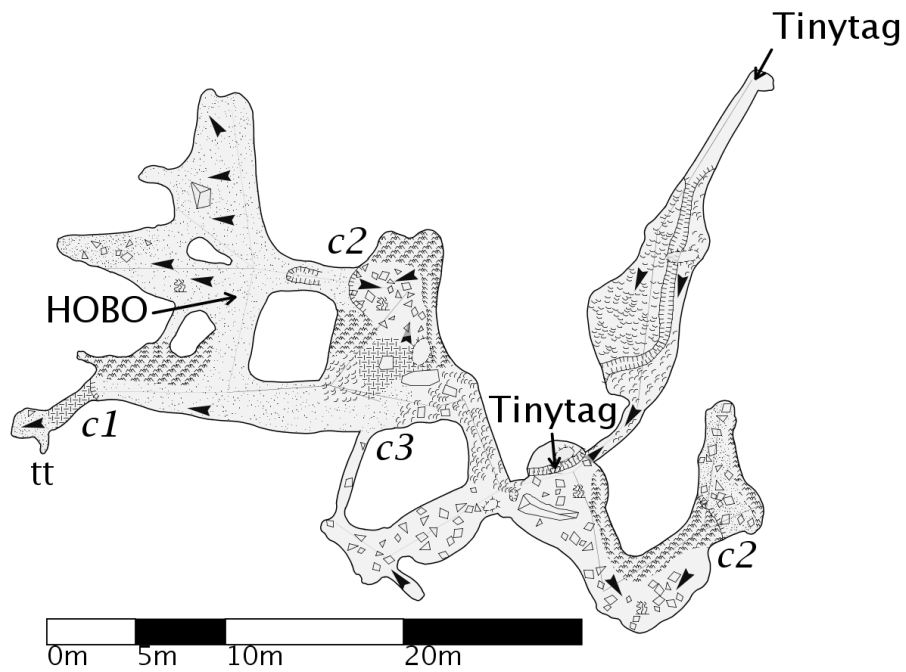


**Figure 1.4:** Plan view map of Kachina Cave from DistoX and transit survey by Aaron Curtis and Nial Peters, 2009-2010 Austral Summer. See Figure 1.3 for symbol key.

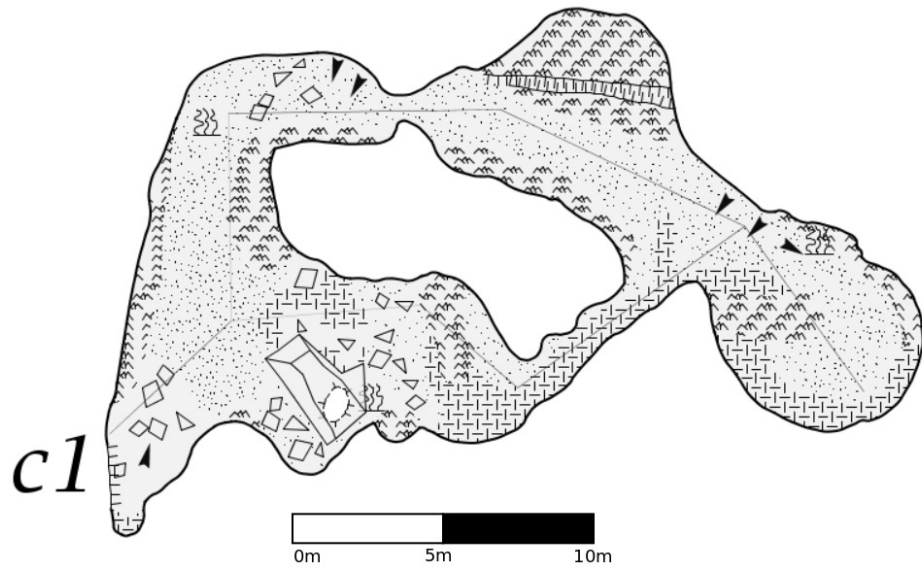


**Figure 1.5:** Plan view map of Helo Cave from DistoX and transit survey by Aaron Curtis and Nial Peters, 2009-2010 Austral Summer. See Figure 1.3 for symbol key.

### 1.3 Appendix B: Temperatures recorded in Erebus FICs

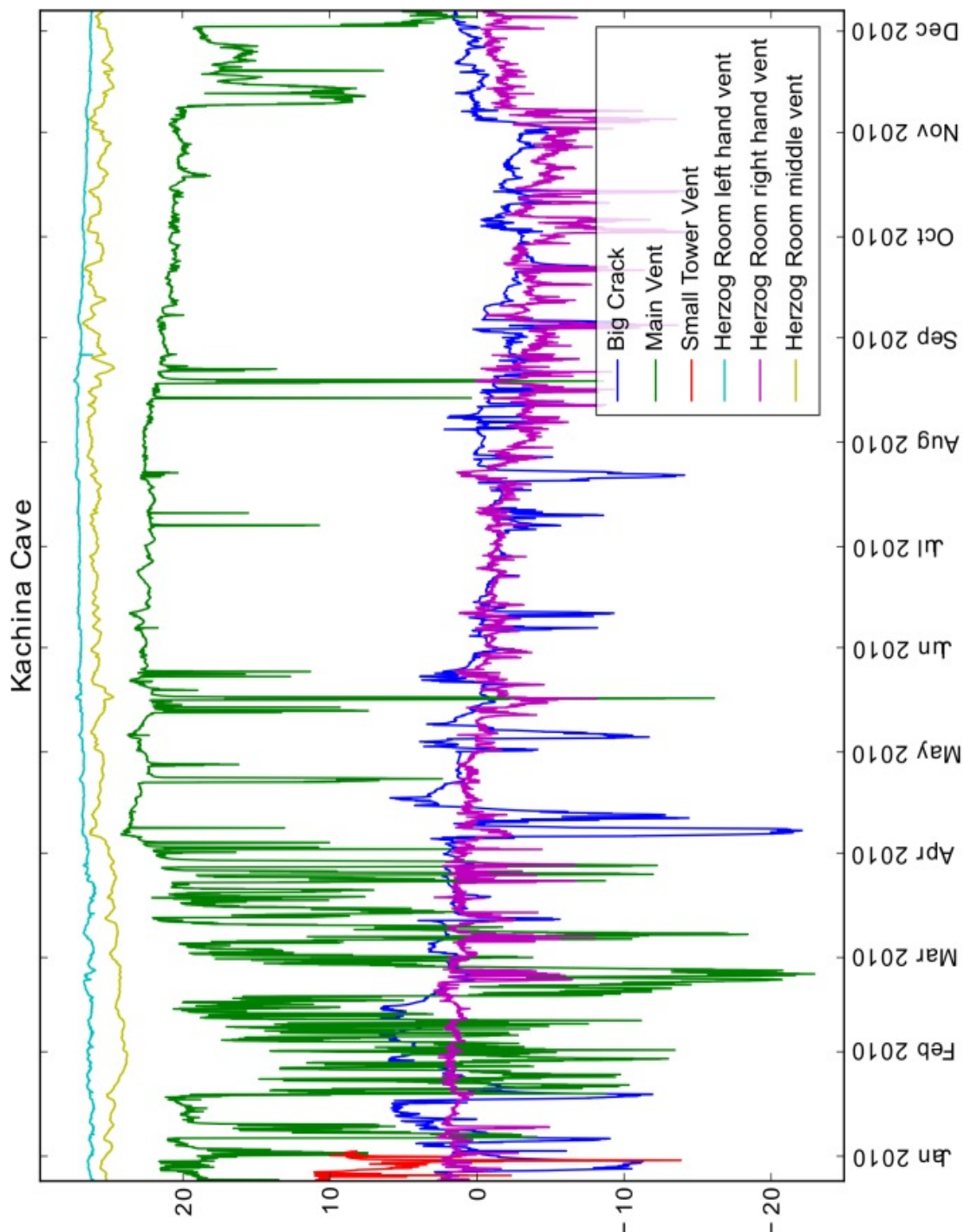


**Figure 1.6:** Air temperature records from Kachina Cave ( $^{\circ}\text{C}$ )

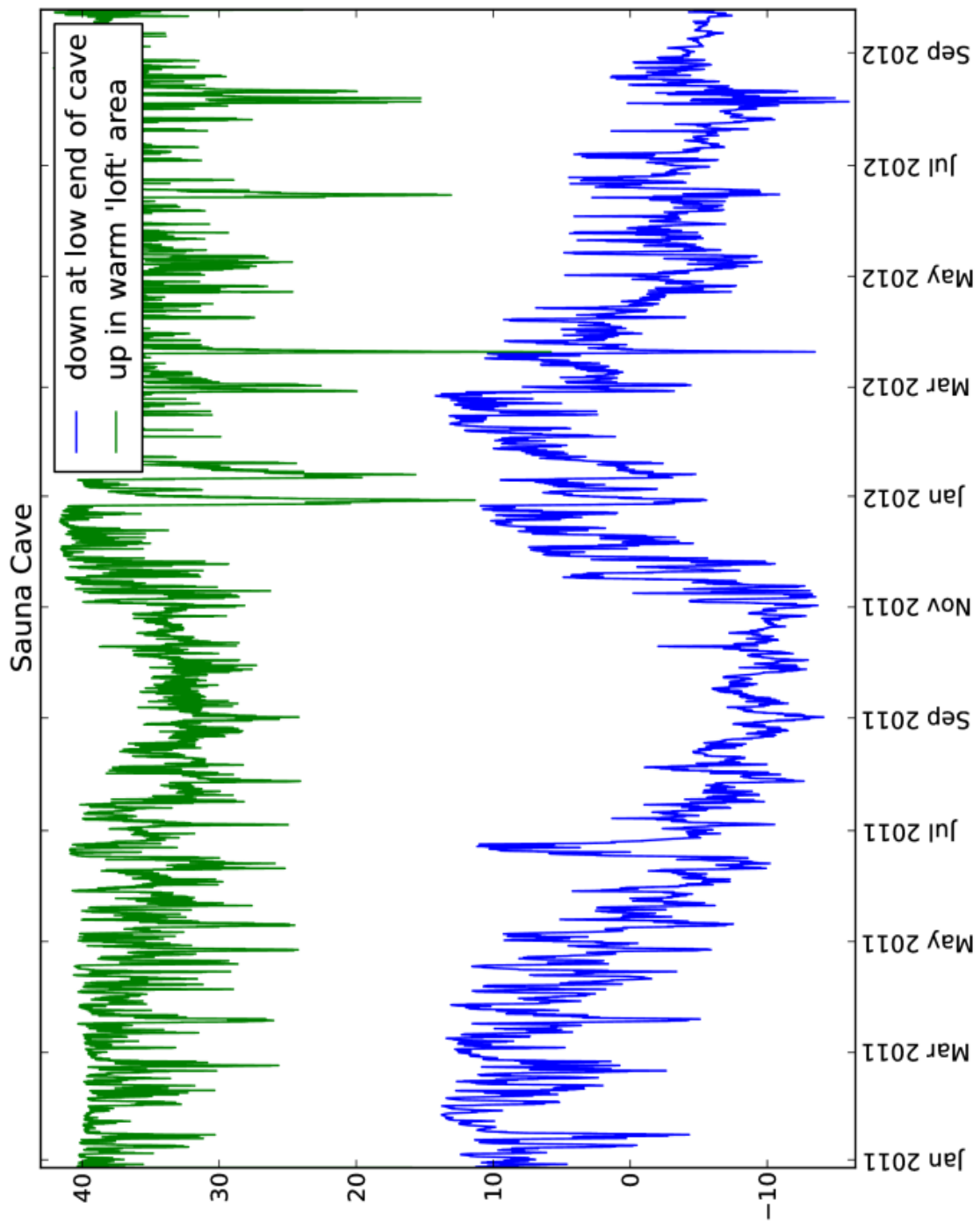


**Figure 1.7:** Air temperature records from Sauna Cave ( $^{\circ}\text{C}$ )

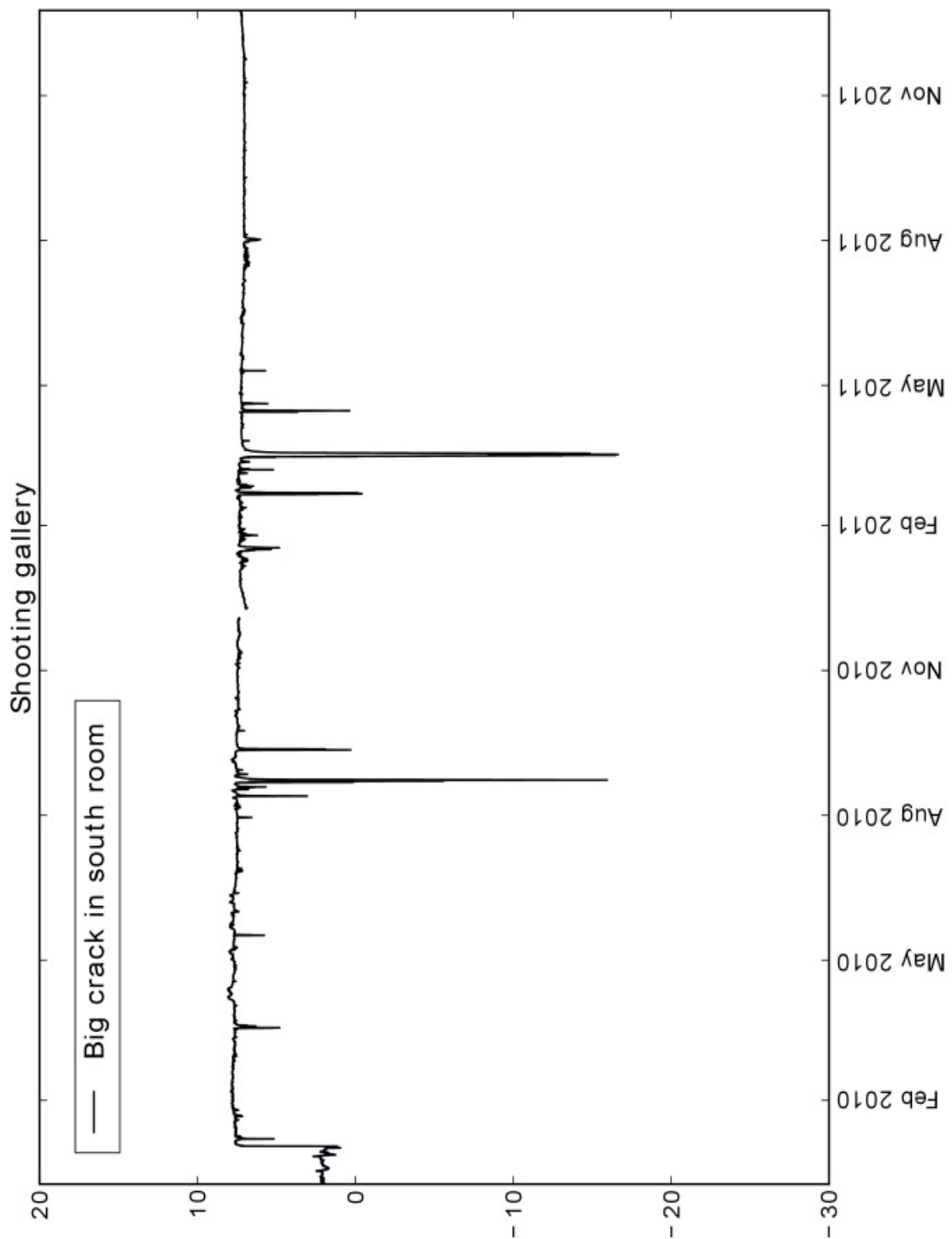


**Figure 1.8:** Temperature records from Shooting Gallery ( $^{\circ}\text{C}$ )

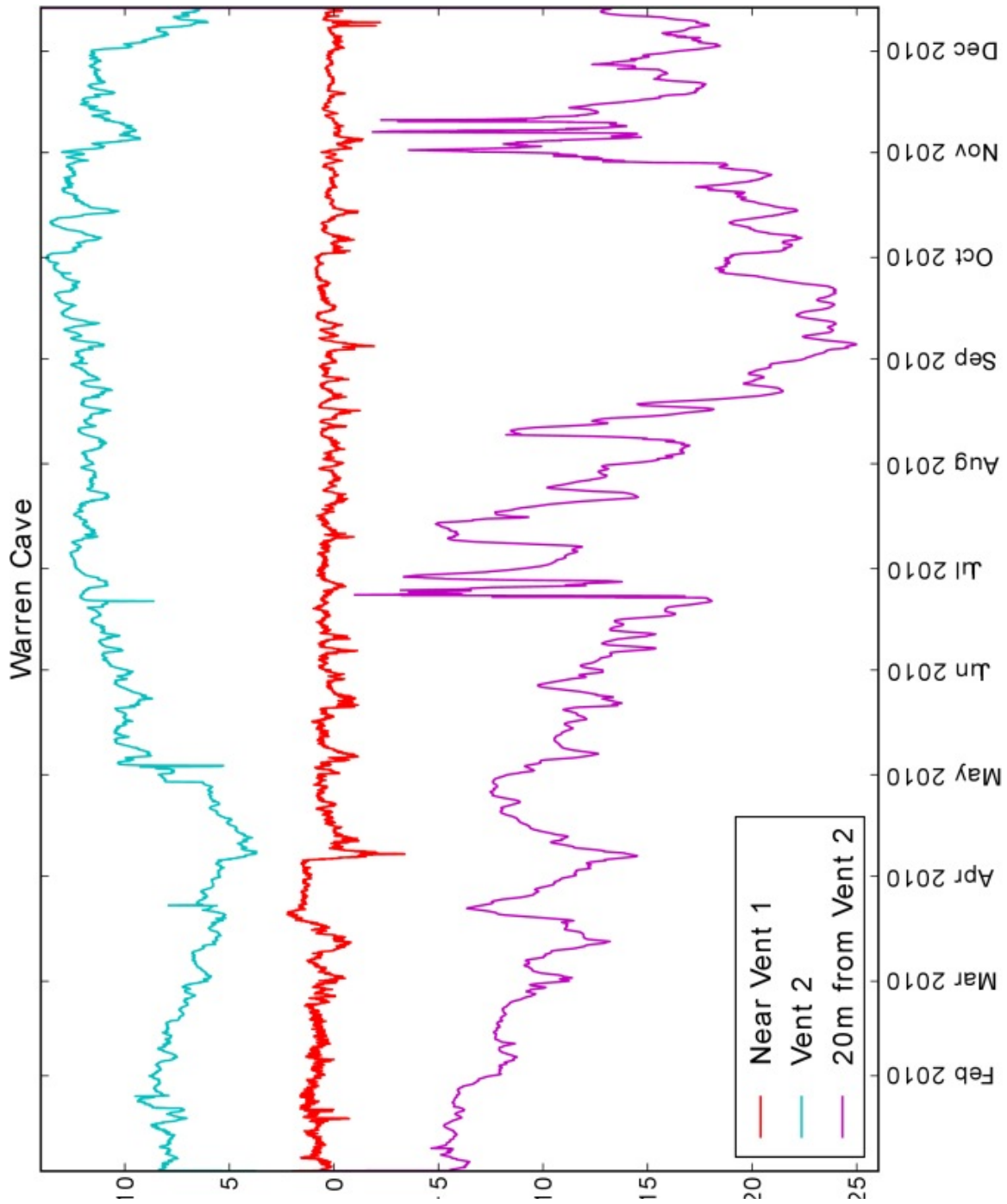


**Figure 1.9:** Temperature records from Warren Cave ( $^{\circ}\text{C}$ )

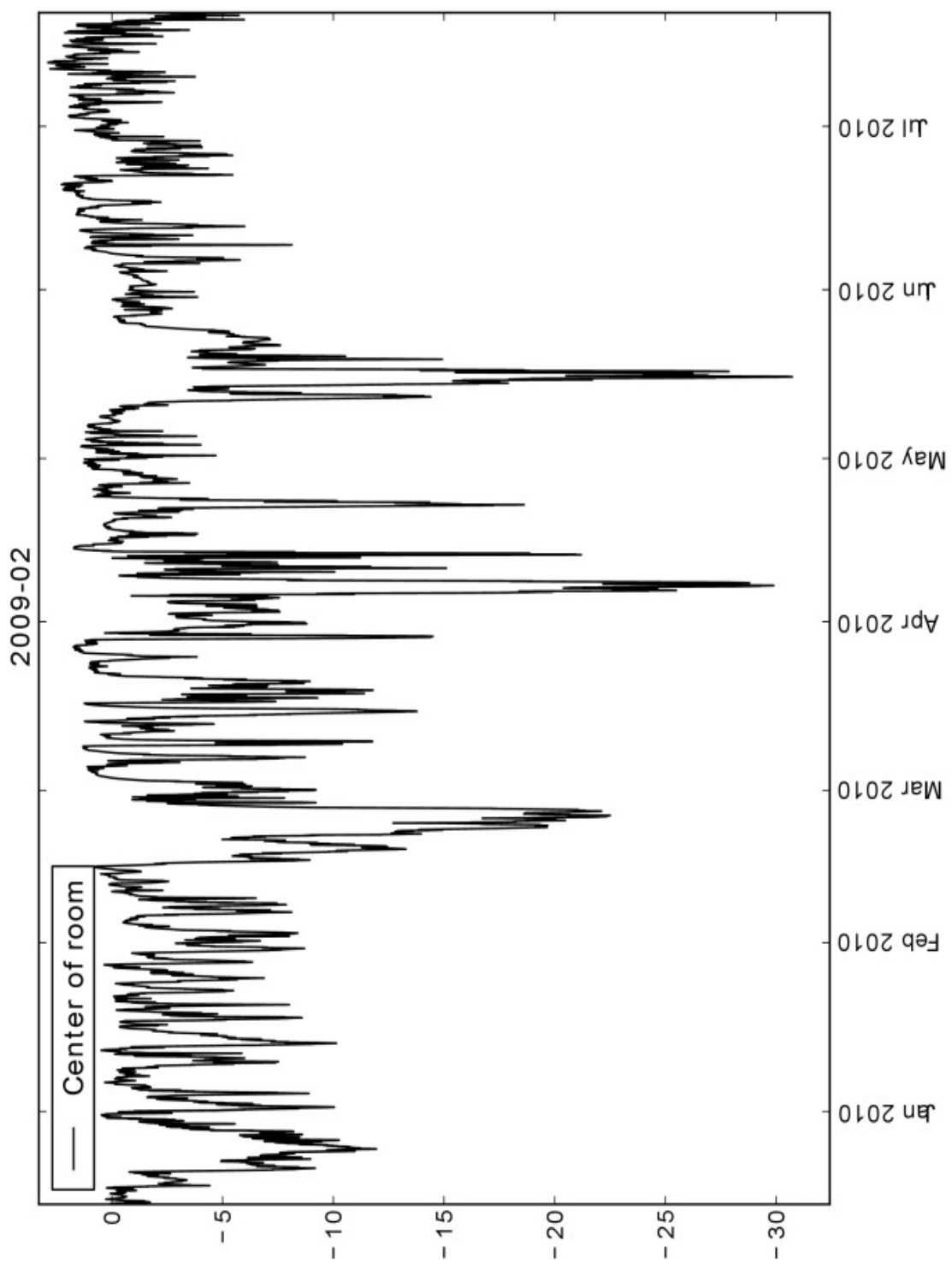


**Figure 1.10:** Temperature records from 2009-02 Tower ( $^{\circ}\text{C}$ )

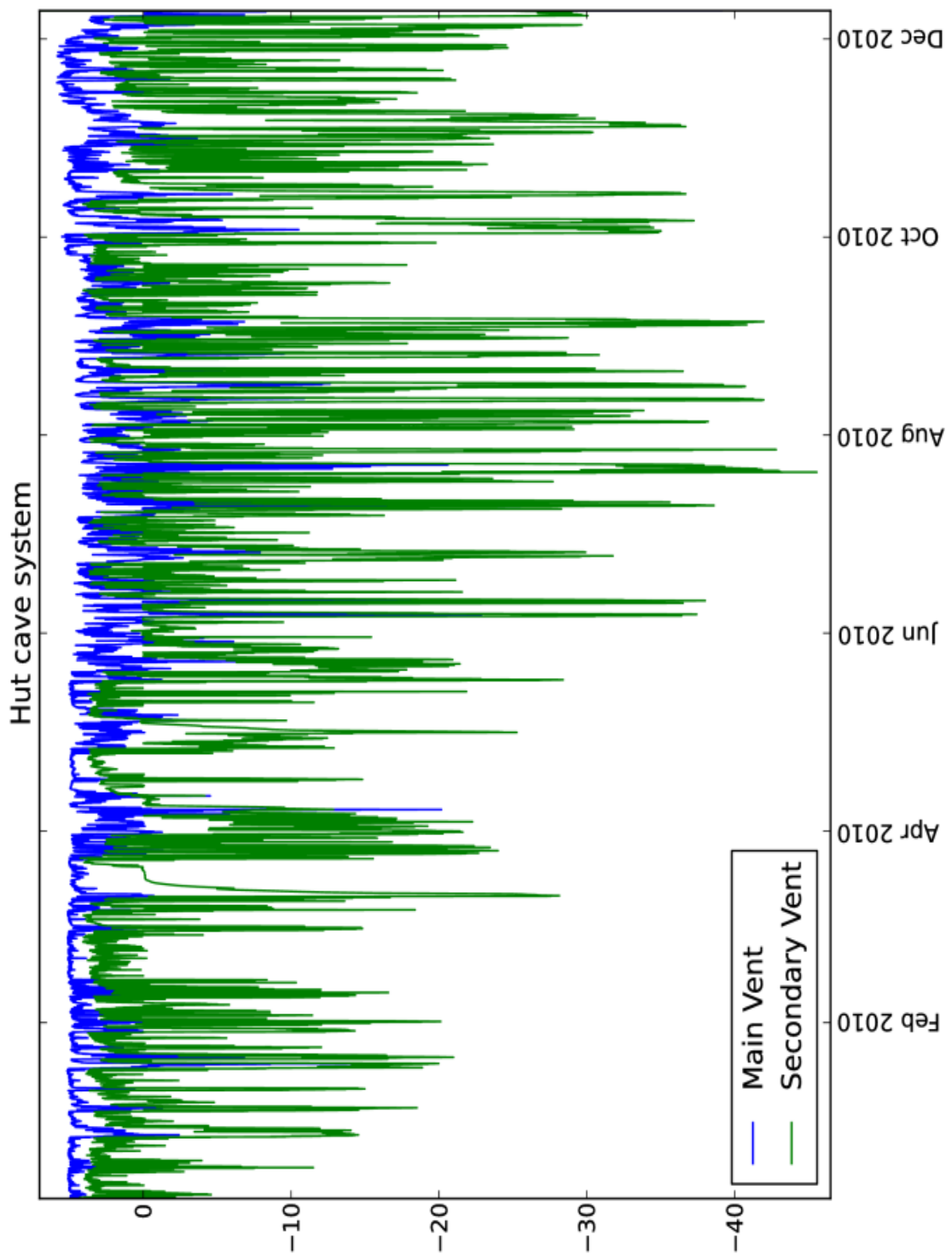


**Figure 1.11:** Temperature records from Hut Cave System ( $^{\circ}\text{C}$ )

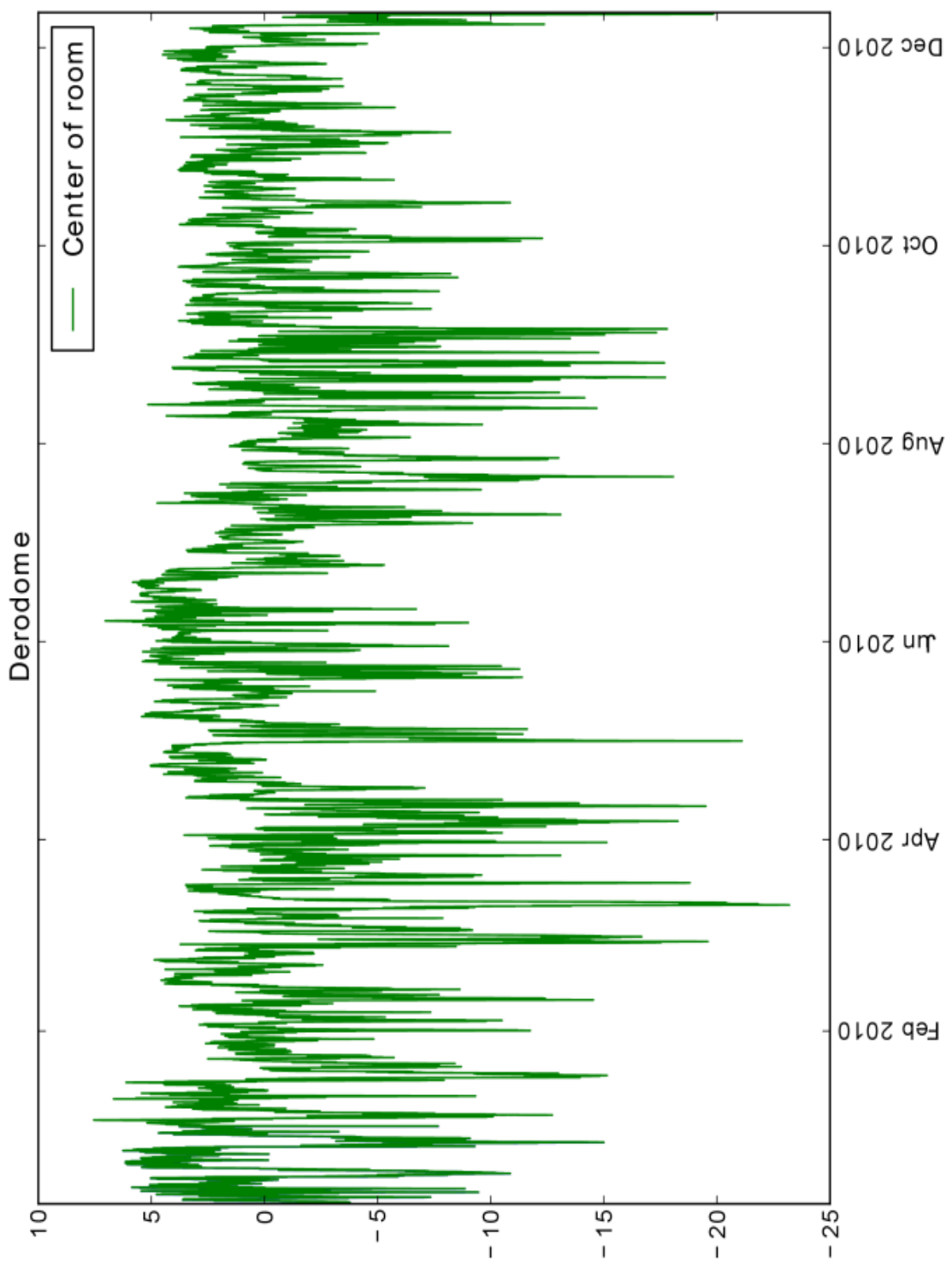


**Figure 1.12:** Temperature records from Derodome ( $^{\circ}\text{C}$ )

## 1.4 Appendix C: Gas concentrations

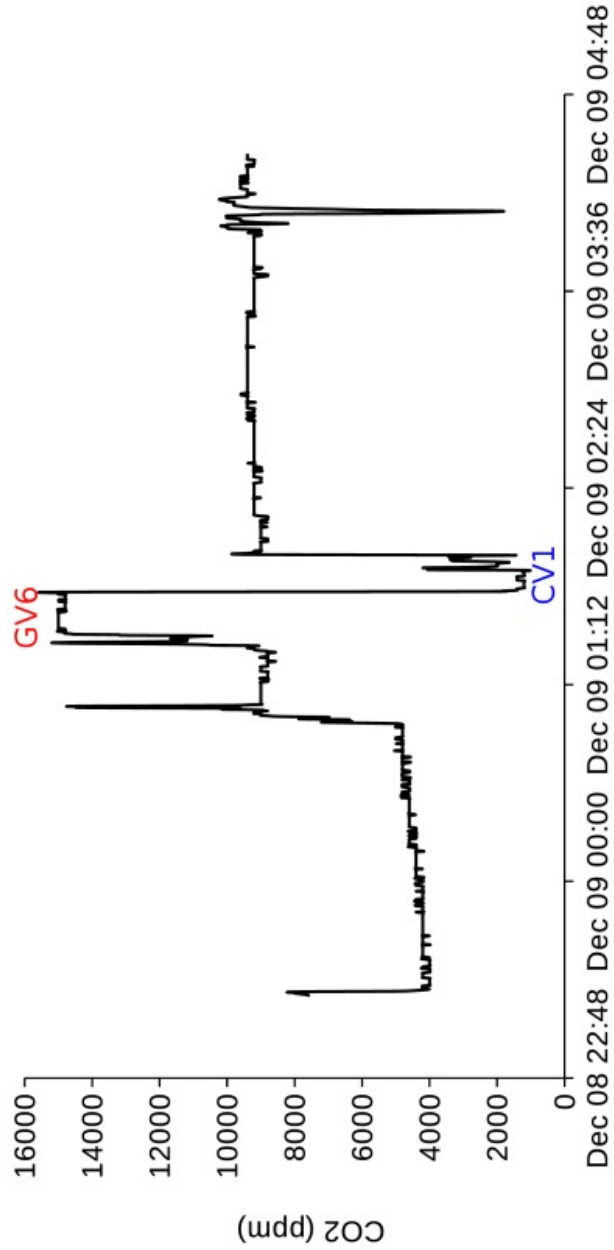


**Figure 1.13:** CO<sub>2</sub> record from a visit to Warren Cave in December 2013. Time is UTC. The handheld CO<sub>2</sub> meter (MultiRAE Lite) was placed at various locations throughout the cave. Location of GV6 is shown in Figure 5.1b. CV1 is a cold tube that carries cave-external ambient air into the cave and terminates about 2m from GV6.

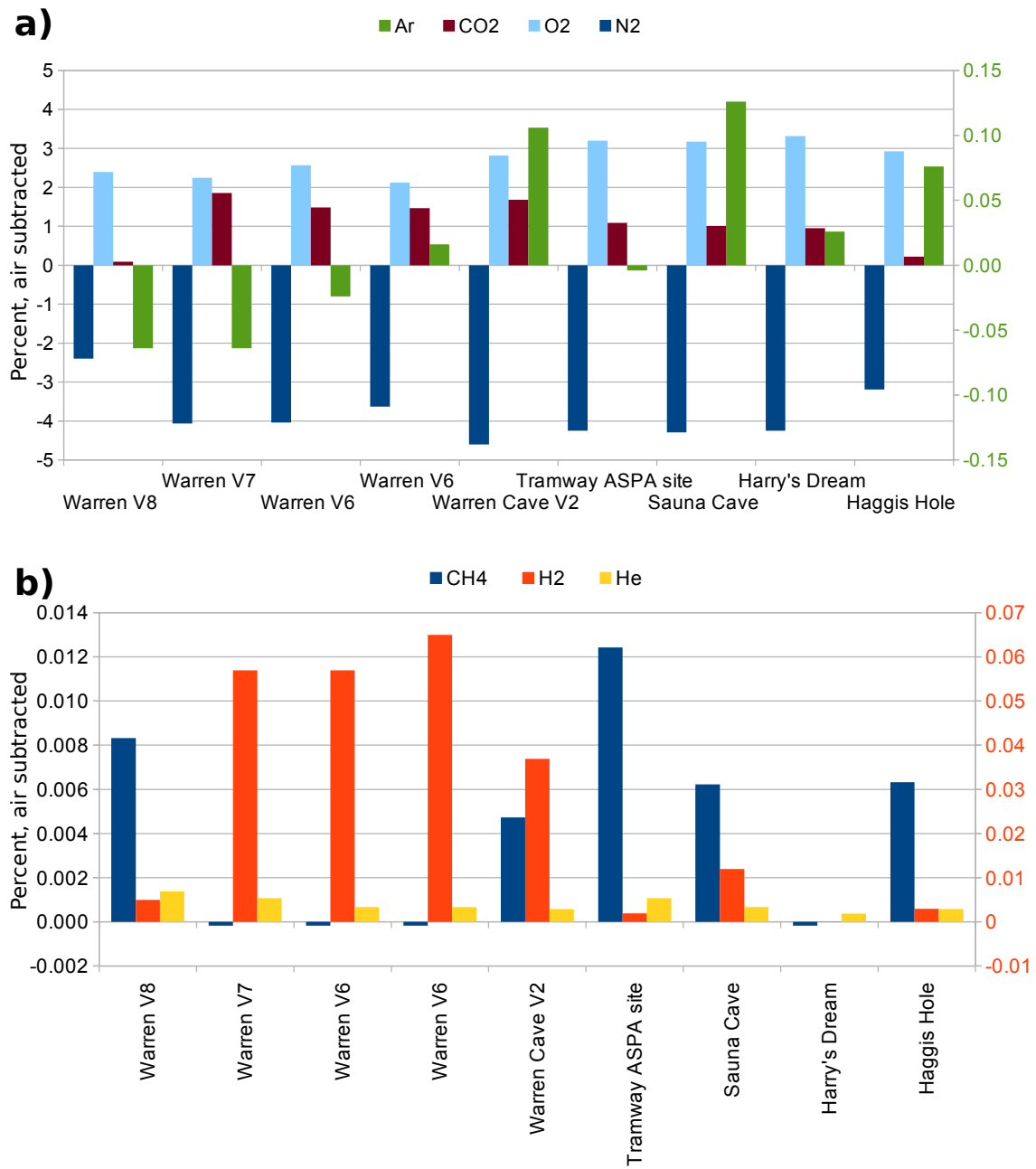


**Figure 1.14:** Gas concentrations collected from FIC and FIT gas vents during the 2013-2014 field season in collaboration with Toby Fischer, shown as difference from Earth tropospheric air. **a)** Major gases, showing a strong depletion in N<sub>2</sub> and excess O<sub>2</sub>, possibly due to hydrothermal solubility effects. Ar is plotted on right-hand vertical axis. **b)** Trace gases, with H<sub>2</sub> plotted on right-hand vertical axis.

## **CHAPTER 2. GEOTHERMAL POINT SOURCES IDENTIFIED IN A FUMAROLIC ICE CAVE ON EREBUS VOLCANO, ANTARCTICA USING FIBER OPTIC DISTRIBUTED TEMPERATURE SENSING**

*This chapter is a reprint of Curtis and Kyle (2011), published in Geophysical Research Letters.*

## Geothermal point sources identified in a fumarolic ice cave on Erebus volcano, Antarctica using fiber optic distributed temperature sensing

Aaron Curtis<sup>1</sup> and Philip Kyle<sup>1</sup>

Received 27 May 2011; revised 11 July 2011; accepted 12 July 2011; published 17 August 2011.

[1] Degassing of CO<sub>2</sub> on the flanks of the active Erebus volcano is thought to occur mainly through fumarolic ice caves (FIC) and associated fumarolic ice towers. There is also minor CO<sub>2</sub> degassing from isolated areas of warm ground. The mechanism supplying heat and CO<sub>2</sub> gas into the FIC is poorly understood. To investigate this system, a fiber optic distributed temperature sensing (DTS) system was deployed in a FIC to obtain temperature measurements every meter. The DTS data reveal that localized gas vents (GV) supply heat to the FIC air mass and are an important component of the FIC microclimate. FIC temperature is anti-correlated with local atmospheric pressure, indicating barometric pumping of the GV. These results enable the use of FIC temperature as a proxy for flank degassing rate on Erebus, and represent the first application of DTS for monitoring an active volcano.

**Citation:** Curtis, A., and P. Kyle (2011), Geothermal point sources identified in a fumarolic ice cave on Erebus volcano, Antarctica using fiber optic distributed temperature sensing, *Geophys. Res. Lett.*, 38, L16802, doi:10.1029/2011GL048272.

### 1. Introduction

[2] Fumarolic ice caves (FIC) in the summit caldera of the active Erebus volcano are geothermal features which permit a unique opportunity to quantify and understand volcanic flank degassing, and may also serve as important analogues for extraterrestrial phenomena. FIC are networks of passages melted into the base of the snowpack, where geothermal heat and warm gases are supplied to the ice-rock interface. Permafrost and ice cover typically seals the bedrock surface of Erebus to gas release except at the entrances of FIC. Conical towers of ice up to 10m tall, known as fumarolic ice towers, form over many of the FIC entrances. There are over a 100 FIC in the summit plateau of Erebus volcano (Figure 1). Some additional heat and gas escapes directly through isolated areas of warm ground. Wardell *et al.* [2003] measured CO<sub>2</sub> emissions at 43 entrances and estimated that Erebus releases 0.46 kg s<sup>-1</sup> of CO<sub>2</sub> from its flanks. Erebus is thus an excellent laboratory for the study of diffuse flank degassing. A better understanding of the dynamics at work in the Erebus FIC can improve management and mitigation at the many volcanic areas around the world where flank degassing is a poorly understood hazard [D'Alessandro, 2006]. As structures where warm, vapor-rich gas is channeled through a frozen barrier into a dry, low-pressure (about 600 hPa)

environment well below freezing, the FIC systems may share dynamics with the “misty ice caverns” [Spencer, 2009] theorized to exist beneath geysers observed emitting H<sub>2</sub>O and salts near the south pole of Saturn’s moon Enceladus [Matson *et al.*, 2007]. A typical FIC consists of several hundred meters of passage and contains over 1 km<sup>3</sup> of air and volcanic gas.

[3] FIC microclimates are strongly out of equilibrium with the average Erebus surface conditions of -32.9°C and low relative humidity. Air temperatures observed in the FIC are typically around 0°C, relative humidity is 80 to 100%, and CO<sub>2</sub> levels are usually elevated and can be over 2% [Wardell *et al.*, 2003]. Giggenbach [1976] attributed the thermal disequilibrium in Camp Cave at Erebus to conductive heat flux through the lava floor. Based on isotherms from 50 temperature points taken at 15 cm depth into the lava regolith he estimated a heat flux of  $11.3 \times 10^{-4}$  J cm<sup>-2</sup> s<sup>-1</sup>. We observed that nearly all FIC had discrete gas vents (GV) on their rock floors which emit warm gas (5°C to 25°C). Where GV occur the ceiling of the cave chamber above the vent is often domed due to localized melting. We also observed cold vents (CV) where ambient surface air leaked into the cave.

### 2. Fiber-Optic Distributed Temperature Sensing (DTS)

[4] To determine the relative importance of the diffuse, conductive heat flux versus the advective flux localized at GV, cave air temperature data with high spatial and temporal resolution was required. Fiber optic distributed temperature sensing (DTS) allows measurement of temperature along a fiber optic cable with spatial resolution as fine as 0.25 m and temporal resolution of 1 Hz. Pioneered by the energy industry, DTS is now an emerging tool in the environmental sciences [Tyler *et al.*, 2009], particularly hydrology [Selker *et al.*, 2006]. A recent investigation in Carlsbad Caverns pioneered the use of DTS in a limestone cave [Dwivedi, 2010], but the technology has yet to be applied to ice caves, glacier caves, or lava tubes. Thus far geothermal applications of DTS had been limited to well monitoring [e.g., Ouyang and Belanger, 2006], and it had not yet been deployed on an active volcano.

[5] DTS entails sending a laser pulse down a fiber-optic cable and comparing the transmitted spectrum against light returning to the laser source [Smolen and Van der Speck, 2003]. Returning light is sourced from scattering at the fiber’s core-cladding boundary, which occurs along the entire length of the cable. The return spectrum contains useful wavelength peaks in addition to the primary peak (which is the incident wavelength). Raman-spectrum DTS studies such as ours obtain a temperature value by comparing the

<sup>1</sup>Department of Earth and Environmental Science, New Mexico Institute of Mining and Technology, Socorro, New Mexico, USA.

two wavelength peaks resulting from inelastic scattering: the Stokes and anti-Stokes bands. The prevalence of anti-Stokes scattering events is highly dependent on temperature, compared to the Stokes scattering events which are only slightly affected by temperature. As a result, the ratio between the Stokes and anti-Stokes band peak intensities is proportional to temperature.

### 3. Methods

[6] In this study we examine the temperature distribution in Warren cave, a passage system with one simple entrance (no ice tower). We deployed 438 m of double stranded Infinicor SXi 50/125 micrometer optical fiber in a tight buffer cable with an Aramid strength member in a loop extending to the back of the cave (Figure 2g). The cable was suspended from poles so that it was not affected directly by conduction from the rock but instead measured the adjacent cave air temperature. The cable was over 50 cm from rock and ice except in two passages <1 m in diameter.

[7] A conventional survey was made of Warren cave in the 2009–2010 Austral summer field seasons and a LiDAR survey in 2010–2011. These combined with a survey of the cable location gave a 3-dimensional location for each temperature point in the cave. Fiber length was verified using an air-activated chemical hand warmer pack tied to the cable at 397 m. Both ends of the cable terminated near the cave entrance. The cable's two fiber strands were spliced together at the “far end” in a plastic turnaround box. At the “near end,” the two fibers were each connected to one channel of a Sensornet Oryx DTS system using E2000 connectors. In this configuration, the laser pulse is sent along the entire length of the fiber in alternating directions. This double-ended method allows correction for differential loss of the Stokes and anti-Stokes signals which occurs with distance along the fiber optic cable.

[8] Temperatures were calibrated using warm and cold calibration baths. Absolute temperatures of each were continuously recorded with a NIST-certified platinum resistance thermistor. The cold bath was a bucket filled with a slush of snow with a small amount of water to maintain near-freezing temperatures. The warm bath was a box of sand placed in a GV to maintain a temperature near the upper limit encountered in Warren Cave. Both baths contained 15m of coiled fiber-optic cable.

[9] The DTS was programmed to collect a temperature trace every 10 minutes. Each measurement cycle consisted of firing laser pulses for 15 seconds from the forward channel, followed by 15 seconds of pulses from the reverse channel, and a standby period. Average Stokes and anti-Stokes intensities from the 15 second periods were recorded into onboard memory and processed into temperature using Sensornet software. Using the time of flight based on the constant speed of light in the fiber, the DTS split the return signal into segments corresponding to 1.01m intervals along the fiber.

### 4. Results

[10] About 0.5 million temperature points were recorded in Warren cave between 6:10 (UTC) on 16 December 2010 and 15:30 on 26 December 2010. The DTS temperatures were converted to absolute temperatures using a linear least-

squares regression between the PT100 and DTS calibration bath measurements (Figure 3). The resulting dataset is shown in Figure 2a. The temperature values have a resolution better than  $\pm 0.13^\circ\text{C}$  calculated using the standard deviation of temperatures from the calibration baths [Smolen and Van der Speck, 2003]. This value assumes the calibration baths to be precisely the same temperature throughout. In reality there is some degree of thermal heterogeneity and stratification in the sand and ice/water slush and therefore the actual resolution is probably closer to the manufacturer's estimated value of  $0.05^\circ\text{C}$ .

[11] Location of the DTS cable is shown in Figure 2g. Before and during cable installation, GV and CV locations were recorded. Three gas vents, GV2 (at 630 m along the fiber cable), GV4 (670 m), and GV5 (705 m), are marked by time-averaged temperature anomalies of greater than  $1^\circ\text{C}$  (Figure 2c). GV1, at 299m, is marked by a less conspicuous temperature anomaly of  $0.3^\circ\text{C}$ . The two CV are each associated with a  $-3^\circ\text{C}$  temperature anomaly. The CV2 anomaly appears at 260m, and CV1 is at both 137m and 377m because the cable passes through that area (Ostrich hall) twice. Our distance verification hand warmer caused a temperature spike from  $1.2$  to  $2.4^\circ\text{C}$ , which relaxed to background after about 24 hours.

[12] Spatially averaged cave temperature ( $T_c$ ) varied from  $0.1$  to  $1.3^\circ\text{C}$  during the DTS campaign. Two periods of low temperatures can be identified: Dec 17 to 19 and Dec 21 to 24. These cold excursions are also present in the GV and CV temperatures, but with a range of amplitudes below and above the amplitude of the cave average. The relative amplitude of temporal variation is reflected in the width of the confidence intervals. Figure 2b shows temperatures averaged over time for each virtual thermometer, with confidence intervals based on 26 of all data from that virtual thermometer. Temperature, windspeed and pressure records from the Lower Erebus Hut weather station, located 1.0 km northwest of the Warren cave entrance, are shown in Figures 2d and 2e for comparison with the cave data.

### 5. Analysis

[13] There is a strong negative correlation between spatially averaged cave temperature ( $T_c$ ) in Warren cave and barometric pressure at the Lower Erebus Hut (Figures 2b and 2d). A linear least-squares regression of  $T_c$  versus air pressure has an adjusted  $r^2$  of 0.66 (Figure 4). There is no correlation between  $T_c$  and air temperature or windspeed, so storms can be ruled out as a driver of cave temperature change and the relationship between barometric pressure and  $T_c$  must be direct. A similar effect was observed at Mammoth Mountain, California by Rogie *et al.* [2001], in which changes in barometric pressure affected the flux of diffuse soil  $\text{CO}_2$  emissions. At Mammoth Mountain, soil  $\text{CO}_2$  concentration was effectively a proxy for soil gas flux. The temperatures measured at Warren cave are likewise a proxy for gas flux into the FIC. A time series of  $\text{CO}_2$  concentration data from GV in Warren Cave are currently being collected to confirm the assumption that temperature can be used as a proxy for FIC gas flux. Both systems probably share a physical mechanism: a pressure head is set up in response to pressure imbalance between the atmosphere and the gas volume in the volcanic edifice, and gas flux occurs in proportion to that head. At Mammoth Mountain, spatially distributed soil

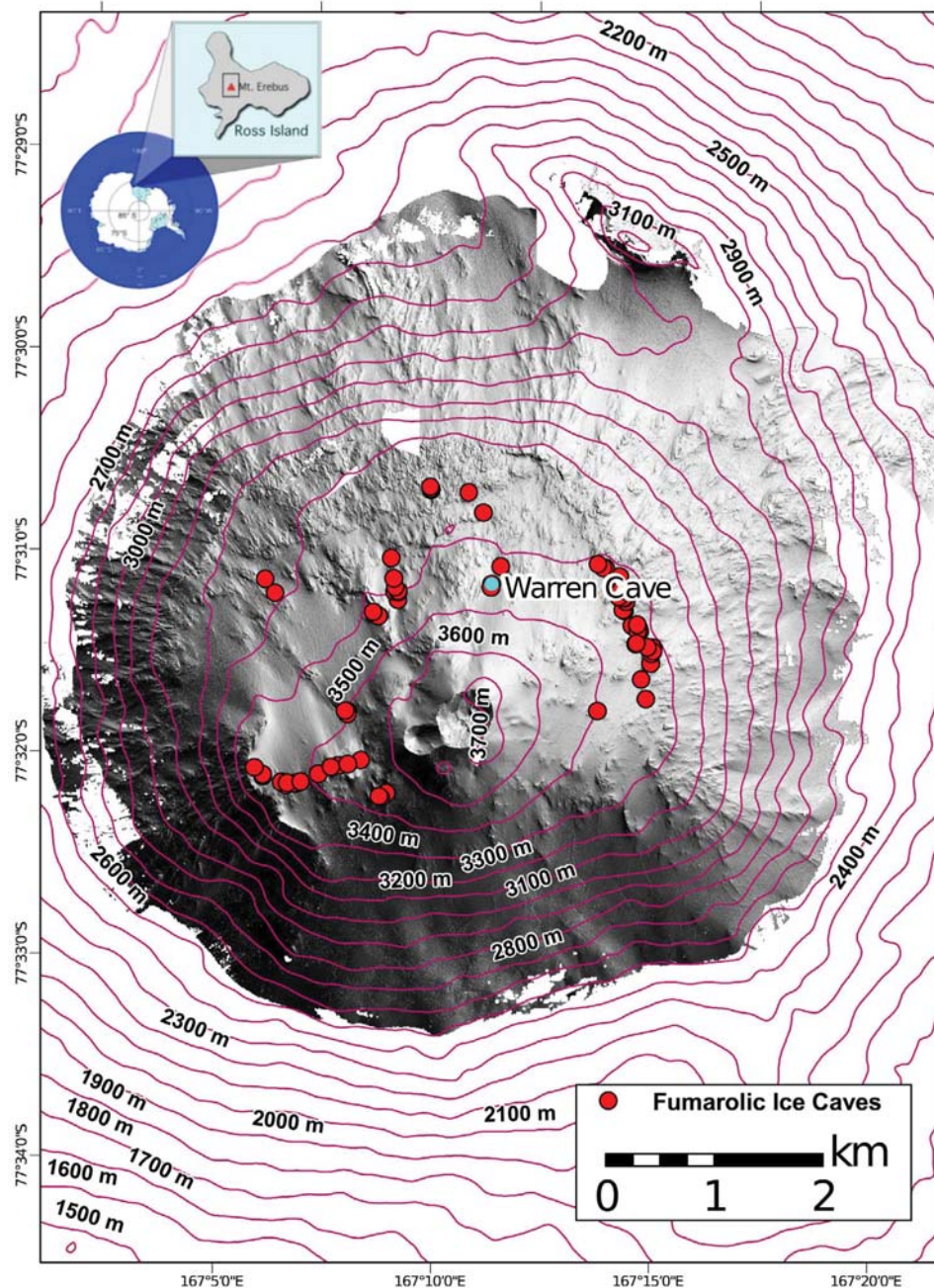
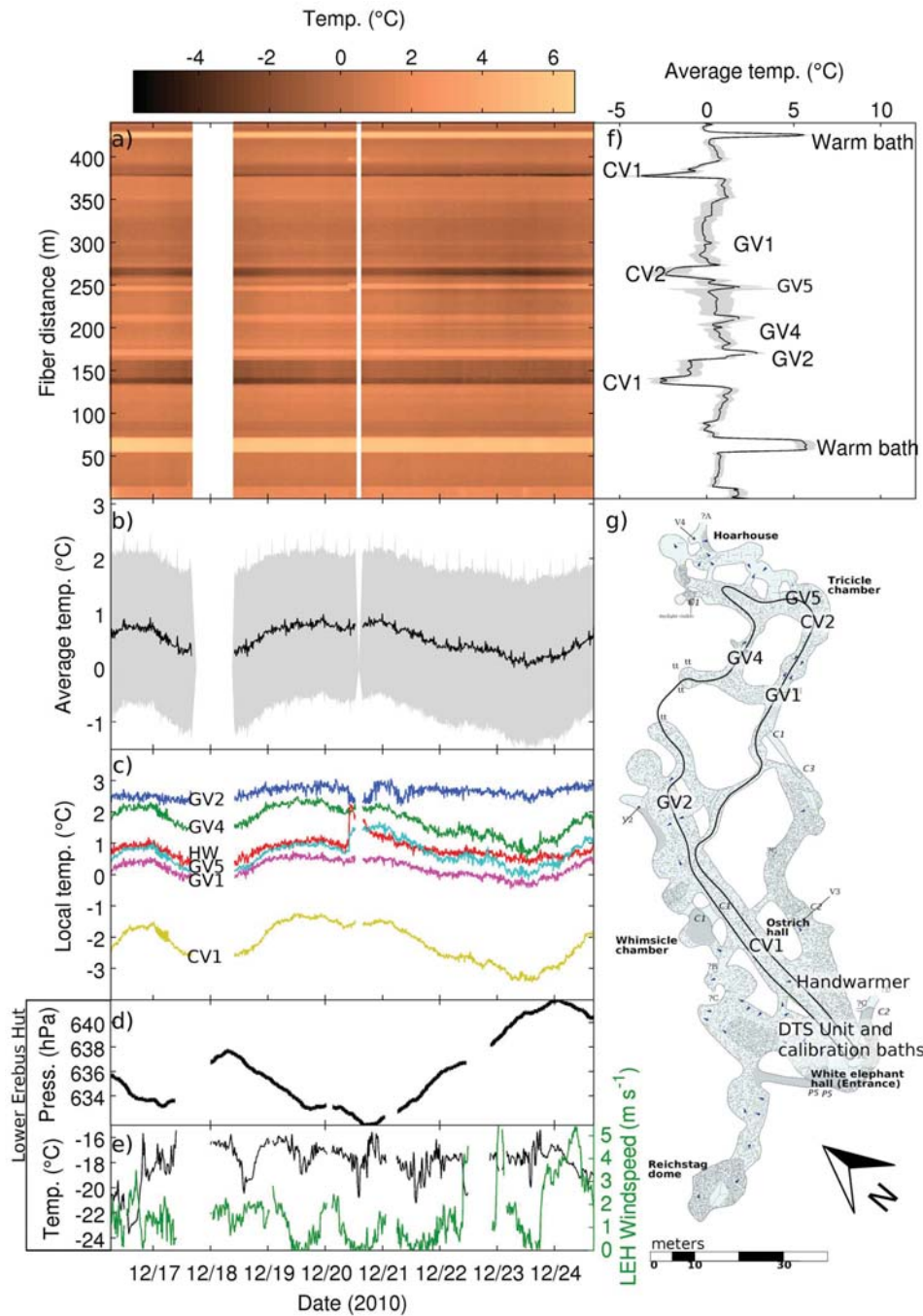


Figure 1. Location map of the study area.

$\text{CO}_2$  measurements revealed diffuse gas release over  $2 \text{ km}^2$ , but within that area there were at least five point sources where gas flux was more than 40 times greater than the average gas flux. Those areas are comparable to the GV in Warren Cave.

[14] The relationship between barometric pressure and  $T_c$  exhibits hysteresis (Figure 4). During periods of decreasing pressure (green circles), the temperature/pressure relationship has a steeper slope than during periods of increasing pressure (blue circles). Physically, this indicates that the



**Figure 2.** (a) DTS results, after linear correction per Figure 1. (b) Warren cave temperature averaged over space, plotted with an area representing  $1\sigma$  above and below the data. The large standard deviation represents the spatial variability throughout the cave. (c) Temperatures from selected locations in the cave. GV are warm gas vents, CV are cold tubes admitting external air into the cave. (d) Barometric pressure recorded at the Lower Erebus Hut weather station. (e) Temperature (blue) and windspeed (green) recorded at the same station. (f) Warren cave temperature averaged over time, plotted with an area representing  $2\sigma$  above and below the data. (g) Conventional cave map of Warren Cave completed during the 2009–2010 field season. The thick black line represents the DTS cable location, and GV and CV are labeled.

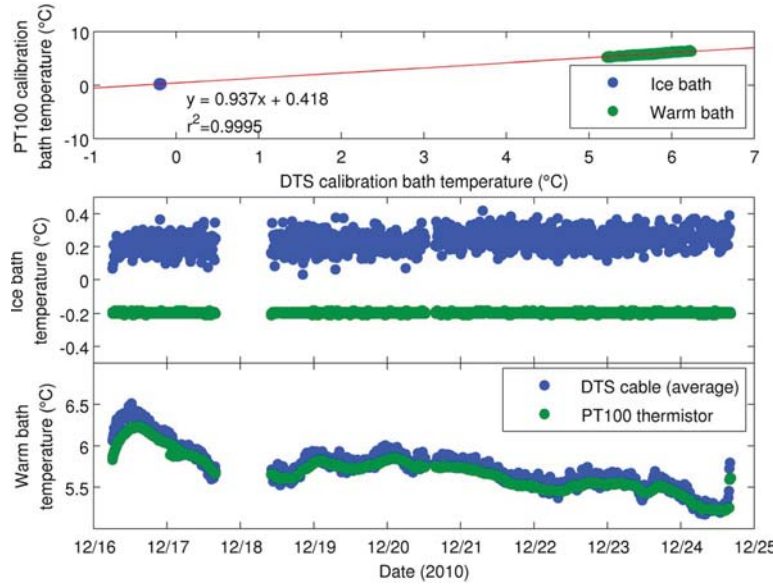


**Figure 3.** Correction of DTS temperatures using NIST-certified PT100 thermistors in the warm bath (a box of sand in a vent) and cold bath (a bucket containing a snow/water mix at equilibrium).

“drawing out” of volcanic gas by a pressure drop is a more effective process than the inhibition of gas flow by “pushing in.” If the GV and CV are primary sites for gas “draw out,” amplitudes of temperature change should be larger at those locations than the amplitude of change in spatially averaged data from the whole cave. GV4, GV5, CV2 all exhibited roughly twice the average cave temperature amplitude, whereas GV1 and GV2 were roughly equal to the average cave amplitude.

[15] Time series of cave temperature at all locations are within 10 minutes (the sampling rate) of being in phase with the cave average. This most likely reflects a well-mixed system due to the strong air flow in the cave. We observed air flow of between  $0.5 \text{ m s}^{-1}$  and  $15 \text{ m s}^{-1}$  in passages, consistently flowing towards the entrance from the Tricicle chamber area, which has the lowest elevation is furthest from the entrance. This regime would allow a heat pulse from GV5 in Tricicle chamber to reach the entire cave within a single

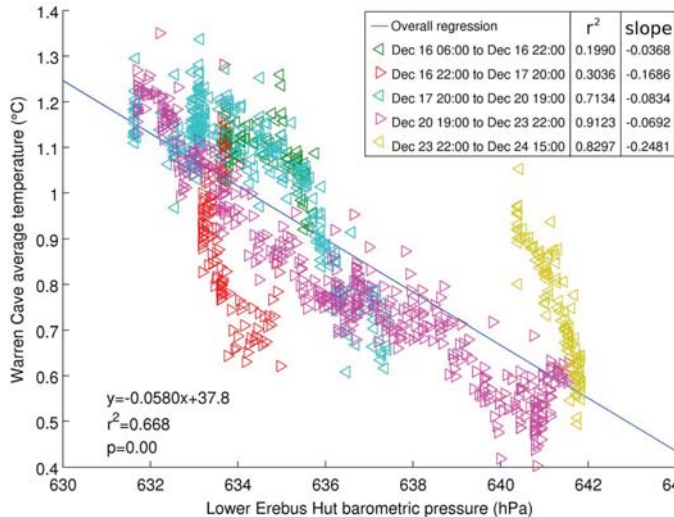


**Figure 4.** Relationship between average temperature in Warren cave and barometric pressure recorded at the Lower Erebus Hut seismic station. Linear least-squares regression for the whole dataset is shown. Periods of decreasing barometric pressure are plotted as left-pointing triangles, with right-pointing triangles indicating periods of increasing pressure.

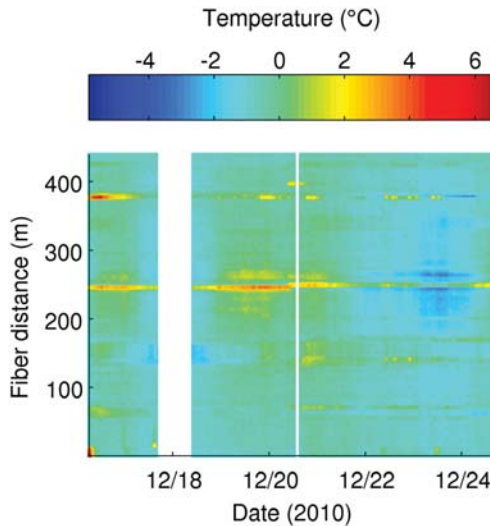


**Figure 5.** Spatially detrended DTS results, calculated by subtracting the mean for each cable location from the dataset.

sampling period. Synchronization of temperature throughout the cave can be imaged by spatially detrending the data. In Figure 5, the mean of the data obtained at each location has been subtracted from all data for that location. Anomalies visible at 248 m and 375 m are the result of movement in the cable due to redeployment of a section of cable to cover a larger section of the Tricicle chamber area around 10am on 20 Dec and should be ignored. The most significant pattern in the detrended data is that the cold period from 19 to 21 Dec and the warm period from 21 to 24 Dec are stronger at the lower elevations of the cave, furthest from Warren's entrance (center of the plot).

[16] In addition to GV and CV proximity, one explanation for a reduction in temperature variability as the air flows up through the cave towards the entrance involves latent heat associated with sublimation and deposition of ice crystals on the cave walls. Many of the passage walls in Warren cave are covered in large frost crystals which form by direct deposition of water vapor [Knight, 1985]. Conversely, liquid water has been observed flowing down melting ice near GV2. Buffering by latent heat has been identified as an important influence on cave air temperatures in European ice caves [Luetscher, 2005] and would explain why the majority of air temperature observations in Erebus' FIC are within five degrees of freezing.

## 6. Conclusions

[17] DTS enabled the identification of thermal point sources, determination of spatially averaged temperatures, and investigation of the spatial synchronicity of temperature change in Warren cave. The instrument and our particular cable configuration performed well despite the challenges inherent in powering and operating such a system in a FIC on an Antarctic volcano. In comparison to transportation, installation, and data management of the over 400 sensors that would constitute an equivalent electronic temperature

sensing system, the DTS had a far lower cost, both in terms of money and man-hours. This system is recommended as a component of monitoring campaigns on other active volcanoes around the world. Particularly of interest are volcanoes representing significant hazards and hosting FIC systems including Mt Rainier [Zimbelman *et al.*, 2000] and Mt Baker [Kiver, 1978].

[18] Although heat flow to the cave floor surface is primarily conductive [Giggenbach, 1976], the high temperature amplitudes and airflows observed at GV demonstrate that localized advection is likely to be a major component of heat transfer from the cave floor to the cave airmass. Advective flux at GV and CV is in turn modulated by barometric pressure. A pressure drop causes a temperature increase throughout the cave, and a pressure increase is associated with temperature drop. These findings lend support to the concept of diffuse degassing in response to barometric pumping and suggest that meteorological observation and prediction could be used to prevent injuries and fatalities such as those that occurred on Etna in 1993 [D'Alessandro, 2006] and Mammoth Mountain in 2006 [Rogie *et al.*, 2001].

[19] Over longer timescales, other controls on FIC temperature may be present such as variations in the volcanic geothermal system supplying the GV or changes in the snowpack permeability such as the depth hoar described by Sokratov and Golubev [2009]. Further investigation, including a longer DTS time series and installation in a variety of FIC, is required to examine these processes.

[20] **Acknowledgments.** Funding for this project was provided by the NSFC Office of Polar Programs through Grant ANT-0838817 and a NASA Space Grant. DTS hardware and configuration support was supplied by Scott Tyler and Francisco Suarez at the Center for Transformative Environmental Monitoring Programs (CTEMPs). Thanks to Nial Peters, Bill Mcintosh, Nelia Dunbar, Matt Zimmerer, Nels Iverson, and Yves Moussallam for assistance in the field, Jevon Harding for fiber splicing lessons, Julian Todd for his open-source cave sketching program Tunnel, and Laura Jones for lidar measurements. Field work was supported by Raytheon Polar Services Company, PHI and Helicopters New Zealand. The manuscript was revised with input from Giovanni Chiodini, Clive Oppenheimer, and an anonymous reviewer.

[21] The Editor thanks Giovanni Chiodini and an anonymous reviewer for their assistance in evaluating this paper.

## References

- D'Alessandro, W. (2006), Gas hazard: An often neglected natural risk in volcanic areas, in *Geo-environment and Landscape Evolution II*, edited by J. F. Martin-Duque *et al.*, *WIT Trans. Ecol. Environ.*, 89, 369–378.
- Dwivedi, R. (2010), Modeling and field study of cave micrometeorology: Role of natural convection, M.S. thesis, Dep. of Earth and Environ. Sci., N. M. Inst. of Min. and Technol., Socorro.
- Giggenbach, W. F. (1976), Geothermal ice caves on Mt Erebus, Ross Island, Antarctica, *N. Z. J. Geol. Geophys.*, 19(3), 365–372.
- Kiver, E. P. (1978), Mount Baker's changing fumaroles, *Ore Bin*, 40, 133–145.
- Knight, C. A. (1985), Growth forms of large frost crystals in the Antarctic, *J. Glaciol.*, 31(108), 127–135.
- Luetscher, M. (2005), Processes in ice caves and their significance for paleoenvironmental reconstructions, Ph.D. thesis, Swiss Inst. for Speleol. and Karst Res., La Chaux-de-Fonds, Switzerland.
- Matson, D. L., J. C. Castillo, J. Lunine, and T. V. Johnson (2007), Enceladus' plume: Compositional evidence for a hot interior, *Icarus*, 187(2), 569–573, doi:10.1016/j.icarus.2006.10.016.
- Ouyang, L.-B., and D. Belanger (2006), Flow profiling by Distributed Temperature Sensor (DTS) system—Expectation and reality, *SPE Prod. Oper.*, 21(2), 269–281.
- Rogie, J. D., D. M. Kerrick, M. L. Sorey, G. Chiodini, and D. L. Galloway (2001), Dynamics of carbon dioxide emission at Mammoth Mountain, California, *Earth Planet. Sci. Lett.*, 188(3–4), 535–541, doi:10.1016/S0012-821X(01)00344-2.

**L16802**

CURTIS AND KYLE: DTS IN EREBUS FUMAROLIC ICE CAVE

**L16802**

- Selker, J. S., L. Thévenaz, H. Huwald, A. Mallet, W. Luxemburg, N. Van De Giesen, M. Stejskal, J. Zeman, M. Westhoff, and M. B. Parlange (2006), Distributed fiber-optic temperature sensing for hydrologic systems, *Water Resour. Res.*, 42, W12202, doi:10.1029/2006WR005326.
- Smolen, J. J., and A. Van der Speck (2003), Distributed temperature sensing—A DTS primer for oil & gas production [online]. *Unclassif. Shell Rep. EP2003*, Shell Int., Rijswijk, Netherlands. [Available at [http://ctemps.org/pdfs/Shell\\_DTS\\_Primer.pdf](http://ctemps.org/pdfs/Shell_DTS_Primer.pdf)]
- Sokratov, S., and V. Golubev (2009), Snow isotopic content change by sublimation, *J. Glaciol.*, 55(193), 823–828, doi:10.3189/002214309790152456.
- Spencer, J. (2009), Planetary science: Enceladus with a grain of salt, *Nature*, 459(7250), 1067–1068, doi:10.1038/4591067a.
- Tyler, S. W., J. S. Selker, M. B. Hausner, C. E. Hatch, T. Torgersen, C. E. Thodal, and S. G. Schladow (2009), Environmental temperature sensing using Raman spectra DTS fiber-optic methods, *Water Resour. Res.*, 45, W00D23, doi:10.1029/2008WR007052.
- Wardell, L. J., P. R. Kyle, and A. R. Campbell (2003), Carbon dioxide emissions from fumarolic ice towers, Mount Erebus volcano, Antarctica, in *Volcanic Degassing*, edited by C. Oppenheimer, D. M. Pyle, and J. Barclay, *Spec. Publ. Geol. Soc.*, 213, 231–246.
- Zimbelman, D. R., R. O. Rye, and G. P. Landis (2000), Fumaroles in ice caves on the summit of Mount Rainier—Preliminary stable isotope, gas, and geochemical studies, *J. Volcanol. Geotherm. Res.*, 97(1–4), 457–473, doi:10.1016/S0377-0273(99)00180-8.

---

A. Curtis and P. Kyle, Department of Earth and Environmental Science, New Mexico Institute of Mining and Technology, 801 Leroy Pl., Socorro, NM 87801, USA. (aarongc@nmt.edu)

# **CHAPTER 3. VOLUMETRIC TEMPERATURE FIELD MEASURED IN A FUMAROLIC ICE CAVE ON EREBUS VOLCANO, ANTARCTICA BY COMBINING FIBER OPTIC TEMPERATURE SENSING WITH LASER SCANS**

*This chapter is a manuscript for submission to Earth and Planetary Science Letters. It represents the original work of the author.*

## **3.1 Abstract**

I describe a method which combines fiber-optic distributed temperature sensing (FODTS) and laser scanning (TLS) to measure a three-dimensional air temperature field. The method allows observation of cave microclimate patterns such as thermal gradients and convection cells. By extracting the cable from the TLS scene using a dimensional classifier (CANUPO), I was able to spatially reference the temperature measurements in the cave chamber, and then interpolated these data points using kriging to obtain the temperature field. I applied the method to investigate the three-dimensional air temperature field of a 15x20x12m cave chamber in a fumarolic ice cave on Erebus volcano, Antarctica, at ten-minute intervals for seven days. A strong, upward-positive temperature gradient persisted throughout the experiment with a mean gradient of 0.265°C per meter of elevation. Convection cells are not apparent; either the chamber is stably stratified, or cells are not apparent at meter-scale spatial resolution.

## **3.2 Introduction**

The three-dimensional temperature field inside a cave is of great interest, but it is difficult to measure. Observations of cave air temperature are essential for understanding microclimates [Palmer, 2007]. The temperature regime controls many other variables including airflow, humidity, and pressure fluctuations. Cave air temperature patterns constrain habitability for life and are of interest for paleoclimate studies [Luetscher, 2005]. Tourism in caves that contain permanent ice masses is a significant economic

activity in countries including Austria, Switzerland and France, and in these caves the cave air temperatures are studied intensely because they impact the ice mass and thus the value of the cave as an attraction [Silvestru, 1999; Zelinka, 2002].

Cave temperatures are primarily monitored by collecting point temperature data (zero spatial dimensions). Usually, this involves deploying temperature data loggers. Temporal trends from point data do reveal interesting cave dynamics such as transfer functions between surface and subsurface meteorology [Luetscher *et al.*, 2008]. However, without the context of the spatial temperature patterns that surround the point, interpretation of the point data is problematic due to equifinality. For example, an observed seasonal temperature increase at a point could be the result of overall warming within a chamber, but it could also result from a change in vertical temperature gradient if the chamber exhibits temperature stratification.

Recently, microclimate investigators have conducted one-dimensional investigations using multiple sensors in vertical and/or longitudinal transects, which can be interpreted to provide measurements of temperature gradients and turbulent eddy processes. A vertical temperature transect can be measured by mounting sensors at a range of heights on a tower. Transects spanning hundreds of meters along the length of a cave passage have recently become possible using fiber-optic distributed temperature sensing (FODTS) technology. This one-dimensional temperature data is sufficient for detection of point sources of hot and cold air [Curtis and Kyle, 2011]. Dwivedi [2010] conducted both tower measurements and FODTS measurements in Carlsbad Caverns, but did not attempt to observe the temperature field volumetrically.

Higher-dimensional temperature data, recorded in 2 or preferably 3 spatial dimensions, is required to observe some temperature patterns, including radial temperature gradients and convection cells. The methods employed by Curtis and Kyle (2011) were sufficient to detect the *presence* of point source heat inputs, but not to determine the volumes in which they have a warming impact on the surrounding cave air. Two-dimensional temperature and CO<sub>2</sub> observations in caves have been fruitful (see e.g. Fernandez-Cortez *et al.* [2006]), but collection of a dense three-dimensional dataset has not been possible until the present work.

Here I report on measurements of the three-dimensional temperature field made by combining terrestrial laser scan (TLS) techniques with FODTS. The data provides the first measurements near the roof of a large fumarolic ice cave (FIC) chamber, and evidence of vertical and horizontal thermal gradients. We found a strong, upward-positive vertical gradient: the reverse of the gradient in the ice and rock surrounding the cave. Upward-positive temperature gradients are extremely unusual in other cave systems, and may be a unique feature of FICs. The gradient appears to result from turbulent natural convection driven by heat input from a gas vent in the cave floor. This convection is an important aspect of FIC speleogenesis, and could provide trophic connections between microbial communities.

### 3.3 Research setting

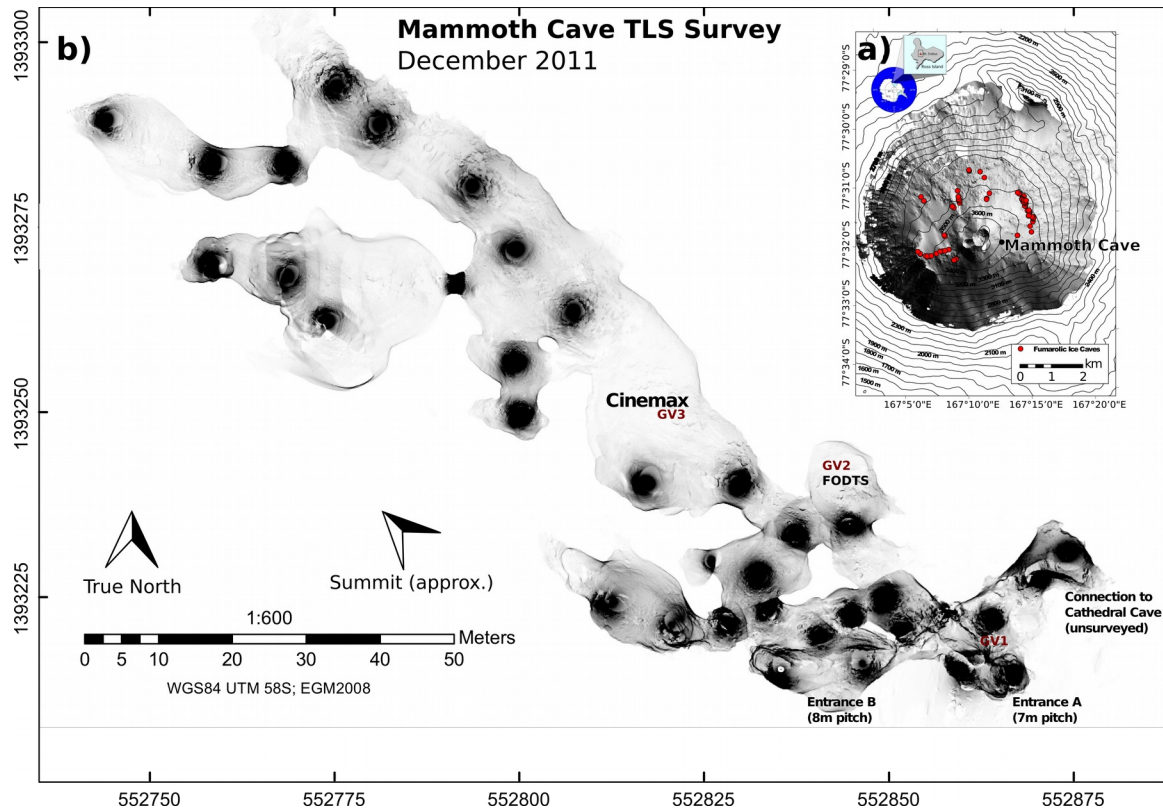


**Figure 3.1:** a) Map of known entrances to horizontally developed caves on Erebus, showing Mammoth Cave. b) Plan view map of Mammoth Cave showing TLS point density for the 476m points collected, with gas vents marked. Dark spots are TLS scan instrument locations. All temperature data presented in this paper is from Cinemax chamber.

We deployed the system in Cinemax, a large chamber inside an FIC on Erebus. Erebus hosts between 100 and 200 FICs that are melted into the snowpack (Figure 3.1a). Most of the cave chambers and passages are located at the rock / ice interface, with vertical entrances that provide access to the solidified phonolite edifice of the volcano.

On Erebus, cave air temperature is of special significance: temperature patterns in the airmass are the result of volcanic heat input, and the cause of speleogenesis. The warm air mass that fills the cave is the accumulation of gas output from point sources: fumarolic gas vents (GV), and cold vents which carry the ambient atmosphere above the cave into the subsurface. Just as the cave air mass is a time-integrated signal representing the vents, the geometry of the cave itself is a time-integrated representation of the melting which results from heat transfer between the cave air mass and the cave walls.

The Erebus caves are of great interest because they are known to host microbial communities, and represent the best available analogues for some processes and structures that may occur on other planets and moons [Cousins and Crawford, 2011]. The environment is extremely oligotrophic (low nutrient availability), and yet a flourishing native microbial community of extremophiles has recently been identified [Connell and Staudigel, 2013; Tebo *et al.*, 2015]. Detailed knowledge of the cave microclimate provides important context to the microbiological discoveries – we must understand the temperatures at which these microbes live in order to determine where else in the universe such communities might be expected.

Entrances to the Mammoth – Cathedral cave system are located to the east of the summit crater at about 3600m elevation. This is slightly above the break in slope between the caldera floor and the summit cone. A large, roughly triangular subsidence cauldron extends uphill from the cave entrance, reaching the crater rim. Mammoth Cave contains the largest explored passages on Erebus. A tight passage often links Mammoth to another extensive cave known as Cathedral Cave, but this is often not passable. Cathedral Cave has not been surveyed. Cinemax is the largest chamber in Mammoth Cave, with about 9m vertical extent and a volume of about 3400m<sup>3</sup> (modeled as half of a 9x15x12m ellipsoid).

## 3.4 Methods

### 3.4.1 FODTS

We deployed 869m of DTS fiber in Cinemax. We suspended the fiber from a temporary support structure constructed from bamboo rods and string anchored to the cave walls using ice screws (Figure 3.2a). The fiber optic cable was double stranded Infinicor SXi 50/125 µm in a tight buffer with an Aramid strength member. The cable was marked with distance by the manufacturer every 20ft (6.1m). To make these distance markings visible in the TLS scan and facilitate spatial registration of the temperature data, we attached 20cm long duct tape tags at some of the cable distance markings. For most of its length, the fiber ran upwards and downwards in 19 vertical transects spread out so as to fill the volume of the chamber as completely as possible (Figure 3.2).

We connected the fiber to a SensorNet Oryx FODTS unit programmed to fire a laser and collect Raman spectrum reflection data integrated over 15 seconds every 10 minutes, with a spatial averaging distance of 1.014m. A turnaround box (Tyco Gator 12F Splice Closure) at the far end of the fiber allowed us to connect the cable in a duplexed configuration.

For calibration control, we kept two reference sections of cable submerged in buckets intended to stay at a uniform temperature. One bucket was filled with a slush bath whose temperature remained at the freezing point of water, and the second bucket was filled with sand and placed near a vent. Using Algorithm 2 from Hausner *et al.* [2011], we converted the observed Stokes and anti-Stokes spectral power to temperature based on these calibration baths.

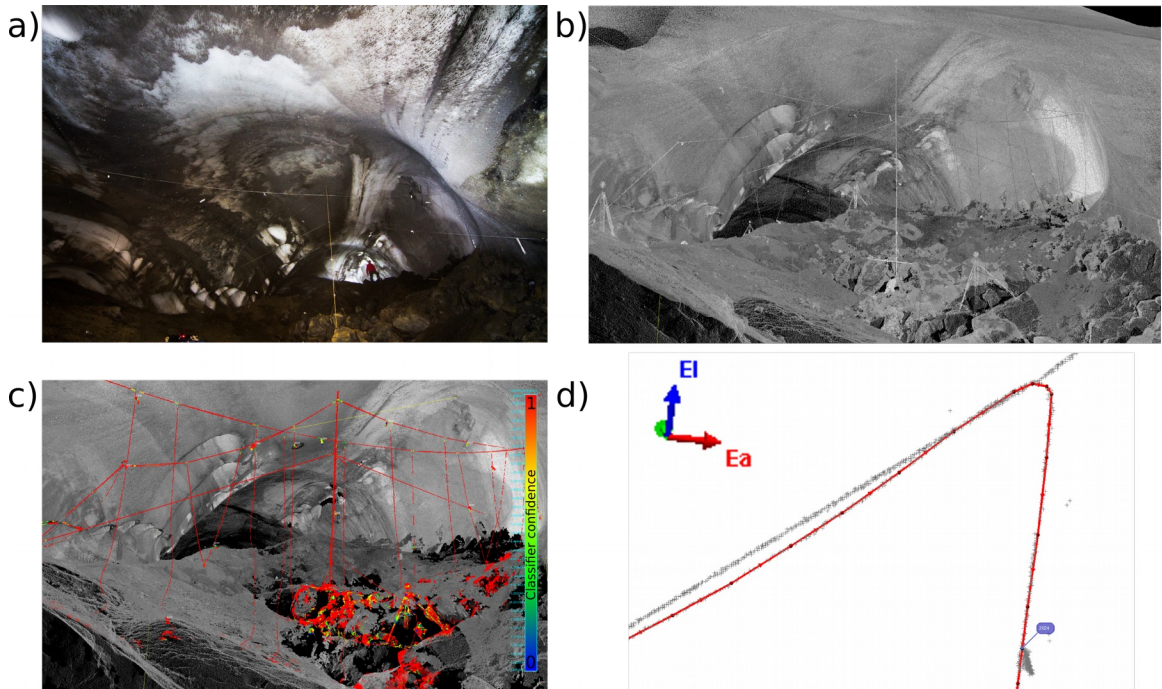


**Figure 3.2:** Spatial registration of DTS cable using TLS data. **a)** Experimental setup: fiber optic temperature sensing cable suspended from support structure in Cinemax, Mammoth Cave. **b)** TLS of Cinemax, with points colored by intensity. **c)** Results of cable classification using CANUPO. The classifier was able to identify all of the cable except sections in contact with the ground. The classifier also identifies TLS target tripods, and edge-dominated rocks, as cable. **d)** Detail of polyline (red) created using IMSurvey's cable tracking tool. Grey crosses are TLS returns. The lineament of returns above the polyline is a string from which the cable was suspended. One of the duct tape flags that we used for spatial referencing is marked in purple.

### 3.4.2 TLS

During the 2012-2013 field season, we scanned Mammoth Cave in its entirety using a Leica ScanStation C10 with a transit-style workflow. The cave was assembled from 45 scans, but for the purposes of this report, I worked with the four scans covering the area of interest. Scans were collected at  $0.06^\circ$  angular resolution in both directions and each scan consisted of about 14m points. We conducted all scans while the FODTS installation was in place.

### 3.4.3 Spatial registration of FODTS data

The first step towards determining the location of the observed temperature points is to isolate the points which represent the DTS cable from the rest of the TLS point cloud (the cave floor and walls). This would be difficult and labor-intensive to accomplish manually. Instead, I used the automatic point cloud classification algorithm CANUPO [Brodu and Lague, 2012]. CANUPO classifies point clouds based on local dimensionality.

The DTS cable is a reliably one-dimensional object when sampled on the scale of centimeters. The walls of Cinemax curve gradually and therefore are approximately two-dimensional at that scale. The cave floor is composed of lava flows and lava bomb material that has weathered to gravel and finer material; this is a challenge to classify because has has a mixture of 2D and 3D structure at various scales. Preparation for CANUPO requires the calculation of a “.msc” file which contains dimensionality data for the scene at the requested length scales of interest; 0.2, 0.4, 0.6, and 0.8m length scales were chosen for this study. Using a temporary virtual server (Amazon Web Services “m4.4xlarge” instance), the .msc file generation was completed in roughly 30 hours, running on 16 cores. I then manually separated small point cloud sections of cable, cave wall, and cave floor and used these to train two classifiers: one to distinguish cable from wall, and one to distinguish cable from floor. We combined these using CANUPO’s `combine_classifiers.exe` to produce a three-way classifier. The resulting classifier positively identified 100% of the cable, with some false positives where edges were apparent in the cave floor (Figure 3.2c).

To facilitate mathematical treatment of the cable pointcloud, I approximated it as a series of straight lines between points. I completed this process using the “Create polylines” tool in Innovmetrics IMSurvey. Using “From tracking” with subtype “Cable,” IMSurvey was able to follow the cable through all gentle bends as well as some of the sharp bends, producing polylines with a few points per meter. It was then a straightforward manual operation to merge and clean the polylines. Using IMSurvey, we also identified the location of points corresponding to the duct tape tags at known cable distances, which became the cable distance reference points.

To add spatial data to each FODTS temperature datum, it was necessary to combine three datasets: the cable distance reference points (coordinates: X, Y, Z, cable distance), the cable polylines (X, Y, Z), and the FODTS data (coordinates: fiber distance). To automate this work, I created an open-source software package called dtspy [Curtis, 2015].

In pseudocode, the algorithm for combining the data is:

```
for each polyline representing a cable segment:
    for each distance reference point:
        — Determine which two cable polyline points are
           closest to this distance reference point
        — Insert the distance reference point into the
           polyline data table between those two points
        — Calculate the euclidean distance from each point
           to the next point and store it
        — Calculate the cumulative euclidean distance from
           each point to the beginning of the cable section
        — Using univariate spline interpolation, estimate
           the cable distance at each polyline point based on
           the distance reference points
        — Calculate fiber distances from cable distances
```

- Using univariate spline interpolation, estimate the location of each FODTS observation based on the polyline distance points

### 3.4.4 Spatial interpolation (kriging)

We extended the spatially referenced temperature data from the 111 observed points to a grid of points filling the chamber using an interpolation method known as Gaussian process regression or kriging. To best account for the expected vertical temperature gradient, I selected the “regression kriging” method available in the pyKriging library [Paulson and Ragkousis, 2015]. Regression kriging is also known as “universal kriging” or “Kriging With External Drift.” pyKriging uses an evolutionary algorithm to minimize error and find the optimal kriging weights.

## 3.5 Results

Over the period of investigation, FODTS temperatures clearly reflected their relative position in 3D space. Viewing the time-averaged temperatures in 3D space (Figure 3.3), it is clear that the 10 strong warm streaks correspond to the raised sections of FODTS cable (Figure 3.4). These streaks represent spatial temperature variability in the chamber on the order of 3°C which persists throughout the experiment.

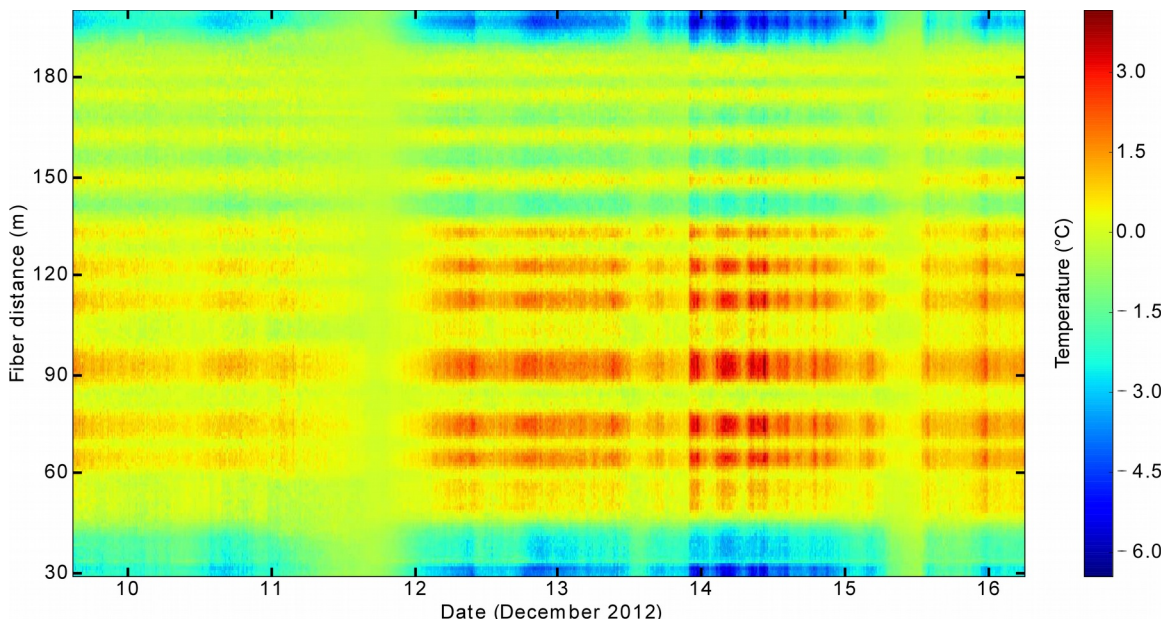


**Figure 3.3:** FODTS observed temperatures.

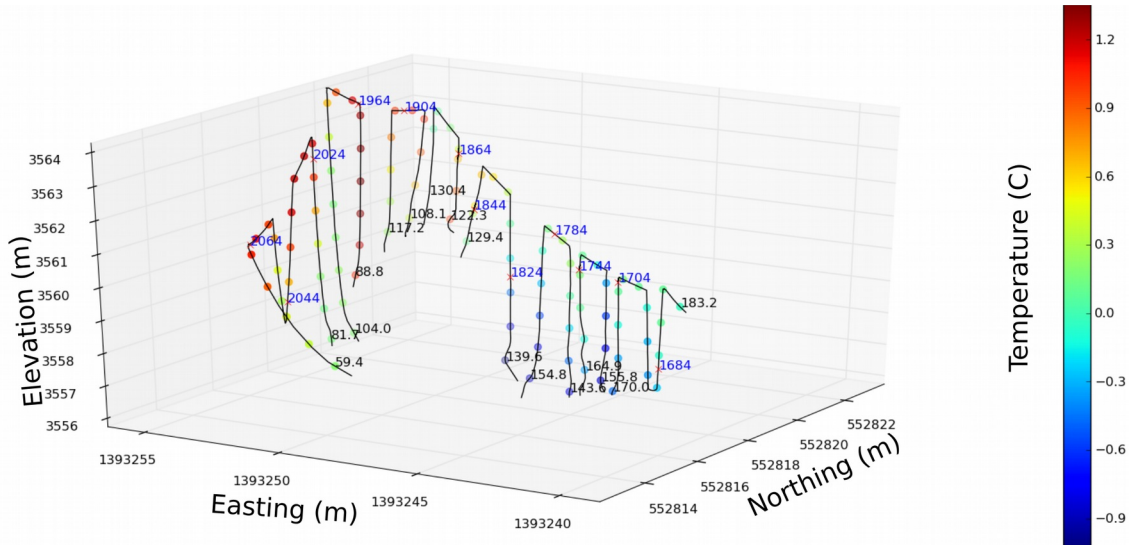


**Figure 3.4:** Estimated locations of fiber shown as black lines) and time-averaged temperature observations as colored circles. Fiber distances for the start and end of each fiber section (in meters) are displayed in black text. Cable distance reference locations are labeled with the cable jacket markings (in ft) and displayed as blue numbers.

The dominant spatial temperature pattern in Cinemax appears to be vertical stratification. After averaging the temperatures over time, least squares ordinary linear regression (OLS) reveals that air temperature increases  $0.265^{\circ}\text{C}$  with each meter of elevation inside the chamber (Figure 3.5).

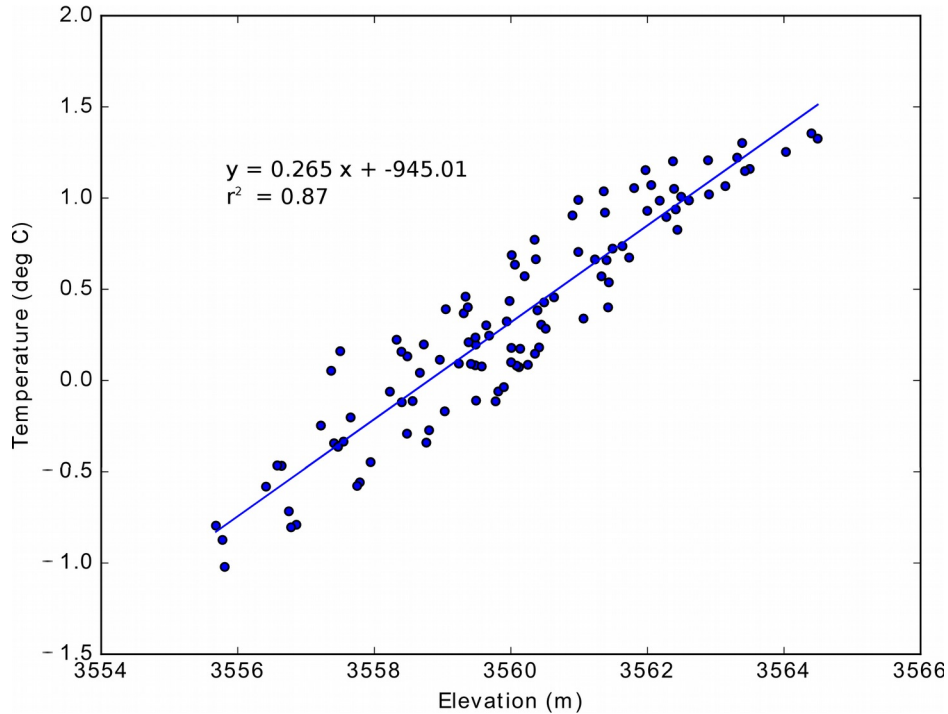


**Figure 3.5:** Linear relationship between time-averaged temperature and elevation inside Cinemax

Calculating a linear regression between elevation and temperature for each time step, we can see that the strength and coherence of the temperature stratification varies over time (Figure 3.6). The steepest and tightest relationships occur between 19:00 on 12 December and 07:00 on 15 December. Destabilization of the temperature gradient appears to occur on 11 December and around noon on 15 December. On 11 December, the temperature gradient weakens to a minimum of  $0.03^{\circ}\text{C m}^{-1}$  and the r-squared value drops to 0.44. These periods of weak vertical stratification coincide with warm periods. During the 11 December collapse of the vertical temperature gradient, the spatially averaged temperatures in the chamber reached  $-0.5^{\circ}\text{C}$ , the maximum recorded during the measurement period. These periods of elevated temperature and associated vertical temperature gradient collapse are also visible in Figure 3.3 as discontinuities in the warm “streaks”.

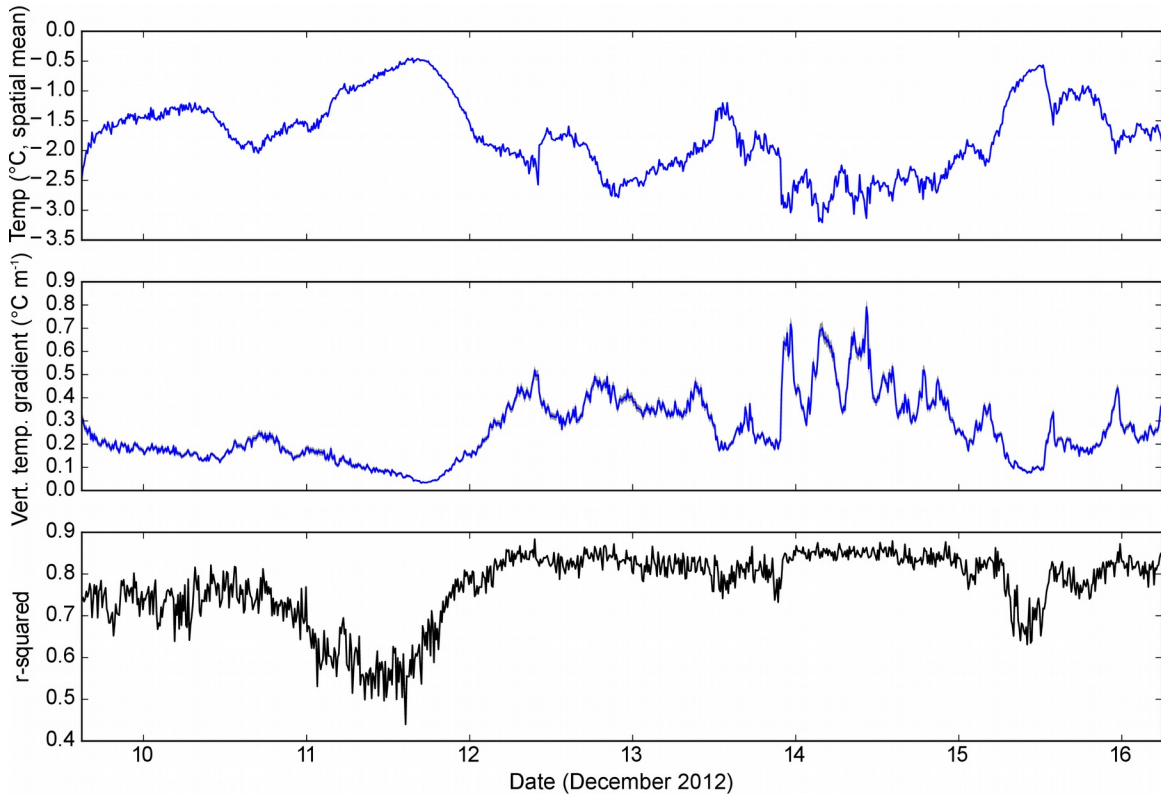


**Figure 3.6.** Changes in Cinemax vertical temperature gradient over time. Ticks represent midnight at the beginning of the labeled date.

In addition to this time-varying vertical trend, structure can be observed in the temperature field in the northing and easting directions. Figure 3.7 shows the results of universal kriging in 3D for the temperature field. Viewed from above and side-on (3.7b and 3.7c), it is clear that the northern part of the chamber is warmer than the southern by about 1°C. On the east-west axis, temperature is relatively uniform.

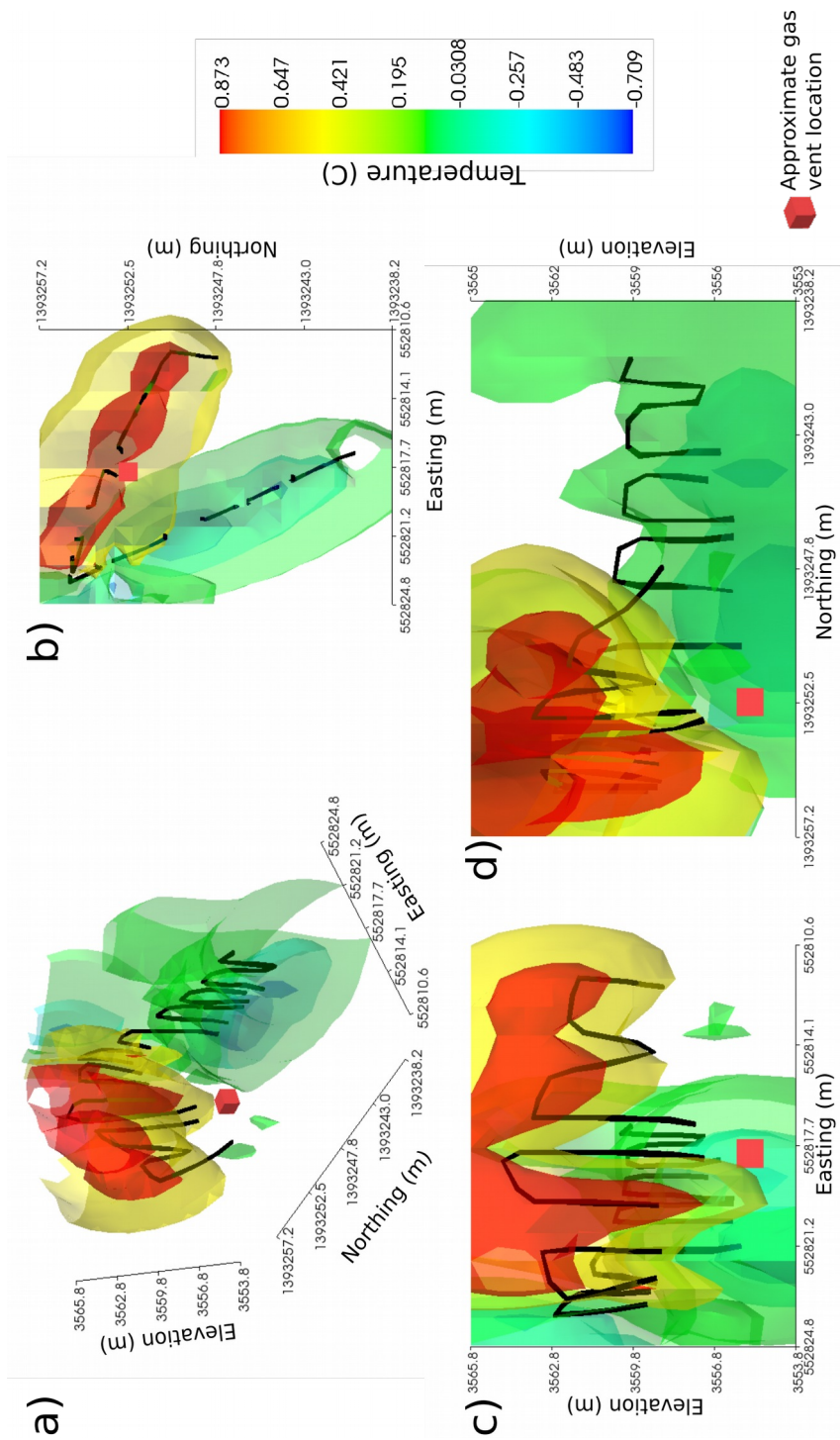


**Figure 3.7:** Isosurfaces of volume-interpolated temperature field based on the FODTS data. Gas vent location shown as red cube. **a)** Perspective view. **b)** Orthometric view, looking up from below. **c)** Orthometric view, looking south. **d)** Orthometric view, looking east.

## 3.6 Discussion

Influence of the Cinemax gas vent on the chamber dominates the temperature isosurfaces (Figure 3.7). A spatially extensive positive anomaly of up to  $1.6^{\circ}\text{C}$  occurs above the vent. The anomaly has a maximum vertical extent within several meters of the vent location (in the Easting-Northing plane). The anomaly is positive northwestwards and upwards. The northwest trend of the gradient corresponds to “uphill” for the chamber floor.

The fact that the vertical temperature trend is positive implies that advective heat transfer overwhelms conductive transfer – the warmest temperatures are observed farthest from the vent and closest to the  $\sim 0^{\circ}\text{C}$  ice roof. Positive vertical temperature stratification is rare in caves and a trend this strong (mean  $0.265^{\circ}\text{C m}^{-1}$  and peak  $0.884^{\circ}\text{C m}^{-1}$  during the period of observation) has not previously been reported in any cave, to the best of our knowledge. In Aven D'Orgnac, Bourges *et al.* [2006] reported temperature gradients ranging from  $-0.02^{\circ}\text{C m}^{-1}$  to  $-0.01^{\circ}\text{C m}^{-1}$ , noting that warmest temperatures were often in the middle of the column rather than near the floor or ceiling. Dwivedi [2010, figure 4.9] simulated temperature stratification for a range of geothermally heated cave scenarios, and predicted negative gradients with a slope closer to zero than  $-0.1^{\circ}\text{C m}^{-1}$ . It is certainly the heat source that distinguishes our data from that observed at limestone caves -- no temperature stratification measurements exist for fumarolic ice caves. Let us, then, explore the temperature regime that is expected to occur in a fumarole-dominated cave chamber, and how it relates to our results.

When gas is emitted from the Cinemax vent (GV2), should it be expected to rise? This depends on its buoyancy, which results from density contrast with the preexisting gas in the cave chamber. Relative density of the vent gas is affected by two competing effects: heat input and  $\text{CO}_2$  enrichment. For the moment, we will imagine initial conditions in which the vent gas flows into a gas mixture equivalent to Earth's troposphere. Around 2%  $\text{CO}_2$  has been observed in the emissions from this vent. Assuming simple dilution,  $\text{CO}_2$  enrichment causes an increase in the mean molar mass from the standard air value of 28.97 to 29.29  $\text{g mol}^{-1}$ , leading to a density increase of around  $0.01 \text{ g L}^{-1}$ , or the equivalent of about  $0.9^{\circ}\text{C}$  cooling (Figure 3.8). Because air leaving the vent is at least  $6^{\circ}\text{C}$  warmer than the coldest air observed in the chamber, the positive buoyancy effect of vent gas heat content overcomes the negative buoyancy effect of vent gas composition, and emissions from the vent rise relative to ambient atmospheric air.

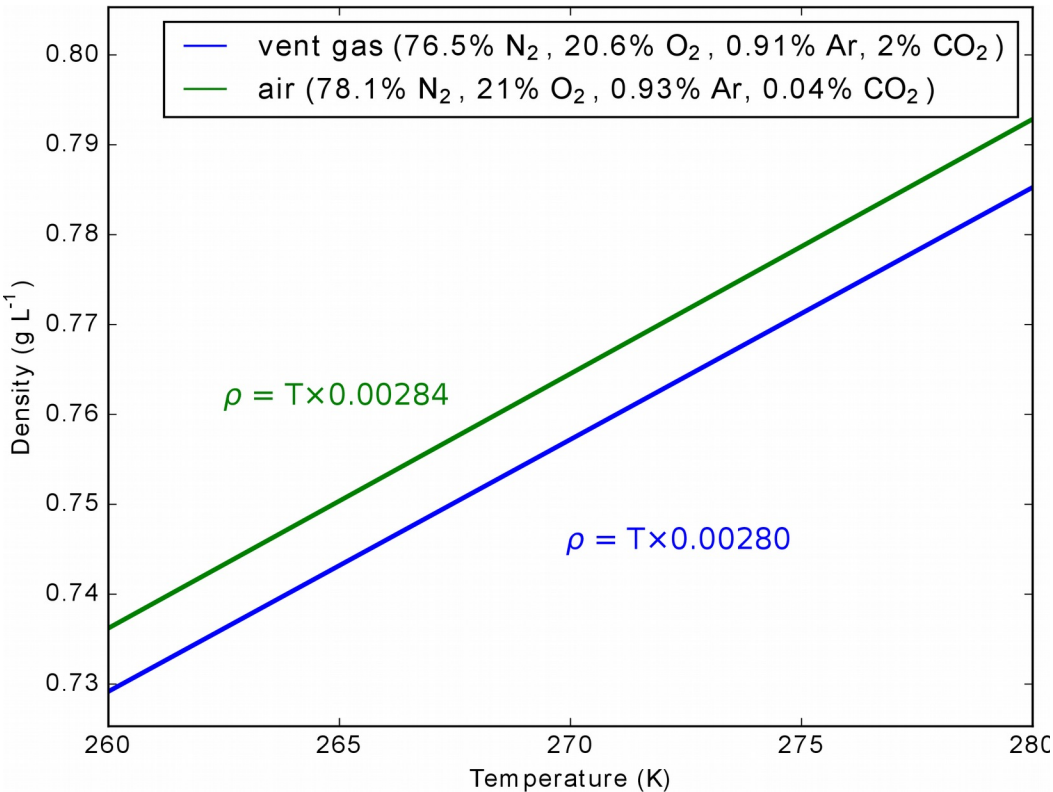


**Figure 3.8:** Expected variation in density of air with temperature and  $\text{CO}_2$  concentration

Consider what becomes of the air parcel once it rises to the ceiling. Diffusion of vent gas  $\text{CO}_2$  is negligible in comparison to buoyant advection of the whole air parcel [Badino, 2009]. Therefore,  $\text{CO}_2$  will not separate and descend from a rising air parcel. Fortunately for human researchers, this negates the possibility of a “ $\text{CO}_2$  trap” pooled near the vent. After rising to the ceiling, the air parcel may lose heat through conduction to the ice, increasing its density and causing it to sink buoyantly; natural convection occurs. This natural convection is opposed or resisted by the inertia of the air and thermal diffusion within it.

To determine the extent to which natural convection is expected in our system, and whether the regime is laminar or turbulent, we can consider the ratio of buoyancy forces to these stabilizing forces. This is known as the Rayleigh number ( $Ra$ ), expressed for buoyant flow by Cushman-Roisin and Beckers [2011] as:

$$Ra = \frac{g \beta \Delta T L^3}{\kappa v} \quad (3.1)$$

Parameters in the equation are:

Symbol	Description	Value (at 273K)
$g$	Acceleration due to gravity	9.81 m s <sup>-2</sup>
$\beta$	Thermal expansion coefficient	3.67x10 <sup>-3</sup> K <sup>-1</sup>
$\Delta T$	Input temperature difference	6 K
$L$	Characteristic length: the chamber height.	9 m
$\kappa$	Thermal diffusivity	1.5 x 10 <sup>-5</sup> m <sup>2</sup> S <sup>-1</sup>
$\nu$	Kinematic viscosity	2.2 x 10 <sup>-5</sup> m <sup>2</sup> S <sup>-1</sup>

**Table 3.1:** Parameters used in calculation of the Rayleigh number

While some of these parameters are a function of temperature, they do not vary significantly within the 6K temperature range of our situation.

The resulting  $Ra$  for Cinemax is large:  $4.767 \times 10^{11}$ . A value of only  $1.7 \times 10^3$  is required to initiate convection, and the transition from laminar to turbulent behavior typically occurs around  $10^4$  for air at this temperature [Shindo, 2005, p.36]. Our situation, then, is one of vigorous natural convection in a highly turbulent regime.

If natural convection is active, we might expect to observe convective cells in the volumetric temperature data. Multiple sheets or columns of cold air occurring in the temperature data would indicate downwelling and indicate convection cell boundaries. Such features are not definitively present when observing the temperature isosurfaces (Figure 3.7). The lack of observable convection cells is most likely a result of insufficient spatial resolution in the temperature observations. A large number of small convection cells (< 4m diameter) may be present. Alternately, the cells may be short-lived and not visible in our time-averaged isosurfaces, or the chamber may essentially be a single convecting torus.

The warm periods in which the vertical temperature gradient is reduced could be caused by weather systems outside the cave. A pulse of airflow through the cave might bring warm air from the downhill (southern) passage, warming and mixing the air column in Cinemax. Changes in the ambient weather above the cave, particularly in barometric pressure, could pump air through the cave, causing such a pulse.

The observed advective circulation of chamber gas is significant when considering fumarolic ice caves as microbial habitats, because it indicates that material from the vent can be transported to the ceiling of the cave. Trace gases from the vent are used in the metabolism of the native biota of these caves [Tebo *et al.*, 2015]. The availability of these gases near the cave ceiling is especially relevant in situations where light penetrates into the cave and photosynthetic microbes may be present at the air-ice interface of the ceiling. Volatile organics and particulate matter may also be transported in this manner, potentially creating trophic links between a cave floor community and a cave ceiling community.

## 3.7 Conclusions

The combination of DTS, TLS, automatic feature detection by dimensionality, and kriging is an effective technique to measure and visualize a volumetric temperature field. The spatial temperature resolution (average point spacing of several meters) achieved in this investigation may be inadequate for the detection of small convection cells. Future studies could obtain closer point spacing by increasing the density of vertical transects deployed and/or measuring temperature with a device such as the Silixa Ultima, which provides temperature data every 12.5cm along the cable in place of the 1.014m intervals with the Sensornet Oryx used here [Selker *et al.*, 2014]. Measurements would also benefit from data taken close to the cave wall and floor to observe the gradient at the boundary layer, which is the only precisely known location of convective cell edges [Perrier *et al.*, 2001].

Spatial temperature patterns in Cinemax chamber are markedly different from those reported in any limestone cave. The strong, persistent, positive vertical temperature gradient we observed is likely a hallmark of fumarolic ice caves. This provisional conclusion is pending replication of these findings in other Erebus caves as well as locations such as the fumarolic ice caves of Rainier [Zimbelman *et al.*, 2000] and St Helens [Anderson *et al.*, 1998]. Detection of a large warm anomaly above the temperature vent provides further evidence that the temperature regime of fumarolic ice caves is dominated by advection from discrete point sources of gas as proposed by *Curtis and Kyle* [2011] in contrast to previous conceptions of conductive transfer of heat to the air mass from warm rock [*Giggenbach*, 1976].

Advection of vent air implied by the observed temperature patterns is fortuitous for the biology of both resident microbes and visiting humans. The microbial ecology likely benefits from material transport from the cave floor to the cave ceiling. Humans researching fumarolic ice caves need not worry about “traps” of CO<sub>2</sub> pooled near vents. Due to advection, the gases will be well mixed, and in fact the CO<sub>2</sub> concentration is probably higher near the cave roof than the cave floor.

## 3.8 References

- Anderson, C. H., C. J. Behrens, G. A. Floyd, and M. R. Vining (1998), Crater Firn Caves of Mount St. Helens, Washington, *J. Cave Karst Stud.*, 60, 44–50.
- Badino, G. (2009), The legend of carbon dioxide heaviness, *J. Cave Karst Stud.*, 71(1), 100–107.
- Bourges, F., P. Genton, A. Mangin, and D. D'Hulst (2006), Microclimates of l'Aven d'Orgnac and other French limestone caves (Chauvet, Esparras, Marsoulas), *Int. J. Climatol.*, 26(12), 1651–1670.
- Brodu, N., and D. Lague (2012), 3D terrestrial lidar data classification of complex natural scenes using a multi-scale dimensionality criterion: Applications in geomorphology, *ISPRS J. Photogramm. Remote Sens.*, 68, 121–134.
- Connell, L., and H. Staudigel (2013), Fungal Diversity in a Dark Oligotrophic Volcanic Ecosystem (DOVE) on Mount Erebus, Antarctica, *Biology*, 2(2), 798–809, doi:10.3390/biology2020798.
- Cousins, C. R., and I. A. Crawford (2011), Volcano-Ice Interaction as a Microbial Habitat on Earth and Mars, *Astrobiology*, 11(7), 695–710, doi:10.1089/ast.2010.0550.
- Curtis, A. (2015), dtspy, doi:10.5281/zenodo.27383.
- Curtis, A., and P. Kyle (2011), Geothermal point sources identified in a fumarolic ice cave on Erebus volcano, Antarctica using fiber optic distributed temperature sensing, *Geophys. Res. Lett.*, 38(16), L16802.
- Cushman-Roisin, B., and J.-M. Beckers (2011), *Introduction to Geophysical Fluid Dynamics: Physical and Numerical Aspects*, Academic Press.
- Dwivedi, R. (2010), Modeling and field study of cave micrometeorology: Role of natural convection, Hydrology MS Thesis, New Mexico Institute of Mining and Technology.
- Fernandez-Cortes, A., J. M. Calaforra, and F. Sanchez-Martos (2006), Spatiotemporal analysis of air conditions as a tool for the environmental management of a show cave (Cueva del Agua, Spain), *Atmos. Environ.*, 40(38), 7378–7394, doi:10.1016/j.atmosenv.2006.06.045.
- Giggenbach, W. F. (1976), Geothermal ice caves on Mt Erebus, Ross Island, Antarctica, *N. Z. J. Geol. Geophys.*, 19(3), 365–72.

- Hausner, M. B., F. Suárez, K. E. Glander, N. van de Giesen, J. S. Selker, and S. W. Tyler (2011), Calibrating single-ended fiber-optic Raman spectra distributed temperature sensing data, *Sensors*, 11(11), 10859–10879, doi:10.3390/s111110859.
- Luetscher, M. (2005), Processes in ice caves and their significance for paleoenvironmental reconstructions, PhD Thesis, Swiss institute for speleology and karst studies (SISKA).
- Luetscher, M., B. Lismonde, and P. Y. Jeannin (2008), Heat exchanges in the heterothermic zone of a karst system: Monlesi cave, Swiss Jura Mountains, *J. Geophys. Res.*, 113(F2), doi:10.1029/2007JF000892.
- Palmer, A. N. (2007), *Cave geology*, Cave Books.
- Paulson, C., and G. Ragkousis (2015), pyKriging: A Python Kriging Toolkit, doi:10.5281/zenodo.21389.
- Perrier, F., P. Morat, and J.-L. Le Mouél (2001), Pressure induced temperature variations in an underground quarry, *Earth Planet. Sci. Lett.*, 191(1–2), 145–156, doi:10.1016/S0012-821X(01)00411-3.
- Selker, J. S., S. Tyler, and N. van de Giesen (2014), Comment on “Capabilities and limitations of tracing spatial temperature patterns by fiber-optic distributed temperature sensing” by Liliana Rose et al., *Water Resour. Res.*, 50(6), 5372–5374, doi:10.1002/2013WR014979.
- Shindo, S. (2005), Micrometeorological modeling of an idealized cave and application to Carlsbad Cavern, NM, Hydrology MS Thesis, New Mexico Institute of Mining and Technology.
- Silvestru, E. (1999), Perennial ice in caves in temperate climate and its significance, *Theor. Appl. Karstology*, 11(12), 83–93.
- Tebo, B. M., R. E. Davis, R. P. Anitori, L. B. Connell, P. Schiffman, and H. Staudigel (2015), Microbial communities in dark oligotrophic volcanic ice cave ecosystems of Mt. Erebus, Antarctica, *Front. Microbiol.*, 6, doi:10.3389/fmicb.2015.00179. PMID: 25814983PMCID: PMC4356161
- Zelinka, J. (2002), Microclimatic research in the Slovakian show caves, *Acta Carsologica*, 31(1), 151–163.

Zimbelman, D. R., R. O. Rye, and G. P. Landis (2000), Fumaroles in ice caves on the summit of Mount Rainier—preliminary stable isotope, gas, and geochemical studies, *J. Volcanol. Geotherm. Res.*, 97(1–4), 457–473, doi:10.1016/S0377-0273(99)00180-8.

# **CHAPTER 4. DETERMINING THE GLOBAL DISTRIBUTION OF VOLCANO-ICE INTERACTION**

*This chapter is a manuscript prepared for submission to The Cryosphere. It represents the original work of the author.*

## **4.1 Abstract**

I present three methods for mapping the location of potential Holocene and present volcano-ice interaction. All three involve intersecting buffer zones around known Holocene volcanic centers with existing datasets of snow, ice, and permafrost. Two locators, RGL and PZL, are simple spatial join operations (computed from the Randolph Glacier Inventory and the Permafrost Zonation Index, respectively). The third method, MDL, is an algorithm run on the entire MOD10A2 weekly snow cover product from the Terra MODIS satellite radiometer. Shortcomings and advantages of the three locators are discussed, including previously unreported blunders in the MOD10A2 dataset. Comparison of the results leads to an effective approach for integrating the three methods. I show that 19.8% of known Holocene volcanic centers are found to host glaciers or areas of permanent snow. A further 11.9% potentially interact with permafrost. I discuss the global distribution of Holocene volcanoes that could interact with snow, ice, and permafrost with reference to hazards, microbiological habitats, and changing climate.

## 4.2 Introduction

When volcanic systems interact with the cryosphere, a host of significant outcomes result. Human habitats become threatened by phreatomagmatic eruptions, lahars, and jökulhlaups. Uninhabitable environments become habitable for microbes. The processes leave a distinctive geological record, containing paleoclimate information. Thus, volcano-ice interaction provides a library of information, but also presents a danger. To access the former and mitigate the latter, we must learn its global distribution and extent on our planet.

Volcano-ice interaction, in the broad sense, includes any process whereby volcanic and geothermal systems contact four types of ice masses: snowfields, glaciers, ice sheets, and permafrost. Direct access to locations of volcano-ice interaction by humans is logistically difficult and hazardous, leading to the obscurity of certain important phenomena. Fumarolic ice caves (FICs), for example, have been treated as rare, isolated phenomena by workers exploring them on Erebus, Melbourne, Hood, Rainier, Wrangell, and Baker. FICs and other modes of volcano-ice interaction may be globally widespread, but largely undiscovered or unreported, leading to apparent rarity (Figure 4.1). The current work is driven by the concept that necessarily sparse, “boots on the ground” investigations of these often ephemeral phenomena should be complemented and targeted using worldwide assessments of volcano-ice interaction.



**Figure 4.1:** Photo taken by the author of a previously unreported fumarolic ice cave in the summit crater of Villarrica Volcano. Area of red salts on ground is a fumarole. This cave was most likely destroyed by eruption in March 2015.

NASA and others have recently created rich datasets regarding the distribution of these four ice types on Earth. The MODIS instrument aboard the Terra satellite provides a record of weekly (8-day) global snow cover at 500m spatial resolution extending back to 2000: the MOD10A2 product [Hall *et al.*, 2006]. A “globally complete” catalog of glaciers, the Randolph Glacier Inventory (RGI), was compiled by Pfeffer *et al.* [2014]. Global permafrost distribution is more readily modeled than observed. Gruber [2012] provides a global, high-resolution model called the Permafrost Zonation Index (PZI) which provides the best estimate for the extent of frozen ground worldwide.

Many decades of field investigation provide good constraints on the locations of Holocene volcanic centers. The best catalog is the Smithsonian Institution's Volcanoes of the World (VOTW) database, which contains entries for 1443 terrestrial volcanoes (and 113 seamounts). In this work, I join these four datasets (VOTW, MOD10A2, RGI, PZI) to determine the distribution and nature of global volcano-ice interaction. I develop three “locators” of potential Holocene volcano-ice interaction (MOD, RGL, and PZL) for evaluation and comparison.

## 4.3 Background

Previous work has focused primarily on what Chapman *et al.* [2000] call Type 2 volcano-ice interaction: eruptions occurring beneath ice sheets and ice streams, generally with 100m or more ice overburden. These produce the most recognizable deposits (tuyas, tindars, and associated lithofacies), pose the most serious threats, and are easiest to locate geographically and thus best represented in the literature. For example, a 2009 special issue of the Journal of Volcanology and Geothermal Research dedicated to volcano-ice interactions focused exclusively on Type 2 interactions [Edwards *et al.*, 2009]. In the “classic” formulations of this volcano-ice interaction model, an eruption begins beneath more than 500m of ice [Edwards *et al.*, 2015]. One paper from the special issue described the first discovery of an eruption deposit formed beneath “thin” ice, which was “only 35—55m thick” [Tuffen and Castro, 2009].

The most widespread type of volcano-ice interaction on Earth is what Chapman *et al.* [2000] referred to as Type 1. This category includes even thinner ice – the interaction of alpine volcanoes with the snow and ice on their summits and flanks. Alpine firn fields and glaciers respond not only to eruption of lava, but also undergo significant melting and deformation in response to fumarolic activity and flank degassing. Loss of alpine ice masses in response to increased degassing is often an early indicator of volcanic unrest [Kiver, 1978; Bleick *et al.*, 2013].

The remaining category of glaciovolcanic processes outlined by Chapman *et al.* [2000], Type 3, occurs when magma bodies and related hydrothermal and volcanic systems encounter permafrost. This may be the primary glaciovolcanic phenomenon in the geologic history of Mars [Head and Wilson, 2007]. Type 3 volcano-ice interaction also occurs on Earth and has been studied in Siberia [Abramov *et al.*, 2008].

In some arid environments, volcano-ice interaction is the only process capable of supplying water to biological communities and for aqueous mineral processes such as weathering. At Erebus volcano, Antarctica, fumarolic degassing not only produces liquid water, but also melts caves into the summit caldera ice mass. Native microbiological

ecosystems with unusual metabolic strategies and molecular machinery have recently been identified in the caves [*Connell and Staudigel*, 2013; *Tebo et al.*, 2015]. Ongoing work in Mount Rainier's crater firn caves is also likely to uncover microbiomes. These ecosystems depend on the water, thermally stable warm microclimate, and UV protection provided by the caves, which are themselves a manifestation of volcano-ice interaction.

It is becoming increasingly clear that interactions between the global cryosphere and magma bodies play a role in global climate. *Huybers and Langmuir* [2009] observed an increase in eruption rate during the last deglaciation and suggested depressurization of magma chambers by the removal of ice overburden as a causative factor. Recent work on submarine volcanism supports this type of process. Midocean ridge eruption frequency appears to increase in response to depressurization from falling sea levels [*Conrad*, 2015; *Tolstoy*, 2015]. Mapping the distribution of volcano-ice interaction is an important precursor to global models of the type of feedback between glaciation and subaerial volcanism.

## 4.4 Methods

I created three locators of potential volcano-ice interaction (Figure 4.2) by intersecting ellipsoid buffers of 10 km width (east-west) drawn around each VOTW volcano coordinate with a satellite snow cover product (MOD10A2), a global inventory of glaciers (RGI), and a global permafrost model (PZI). Most VOTW coordinates correspond to stratovolcano summit locations. VOTW coordinates representing volcanic fields, such as clusters of cinder cones, are generally located near the centroid of the cluster. The approximate minimum diameter required to capture the area where volcanic and fumarolic vents may be active for most VOTW locations is 10 km. Large caldera complexes are notable exceptions and volcano-ice interaction in those locations may be poorly represented in this study. This buffer zone also accounts for the up to 1 km error which VOTW states is inherent in their coordinates.

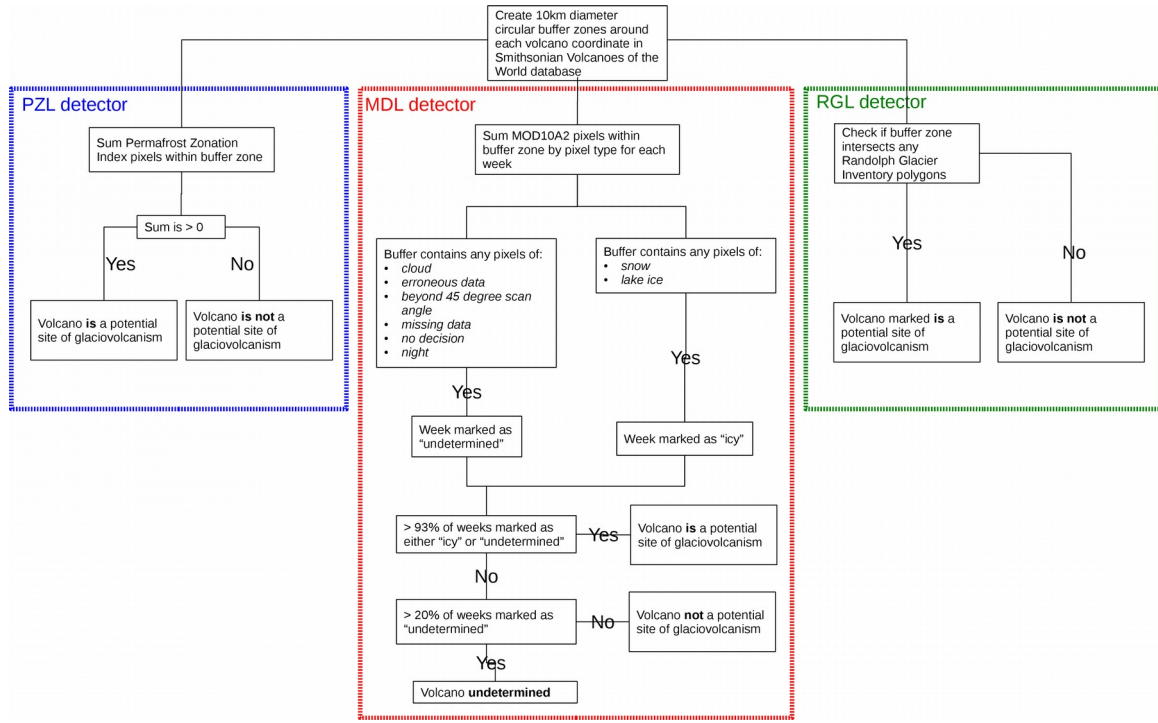


**Figure 4.2:** Algorithms used in this paper to detect locations of potential Holocene volcano-ice interaction.

I computed aggregate area statistics within each buffer zone. For the MOD10A2 data, I calculated pixel sums for each ground cover type within each volcano buffer zone for each week of data. A total of 711 weeks (from February 26, 2000 to August 13, 2015) were processed. MOD10A2 pixels represent roughly 500m squares on the earth surface. Unfortunately, this dataset lacks coverage of the polar regions during local winter, because MODIS is a passive radiometer, measuring reflected sunlight. Figure 4.4 shows the total pixel count for the most southerly and northerly volcanoes in VOTW.

The MOD10A2 product is computed using a “normalized difference snow index” based on the difference between MODIS bands 4 (0.55  $\mu\text{m}$ ) and 6 (1.6  $\mu\text{m}$ ) [Hall *et al.*, 1998]. Multiple values obtained during the 8-day period are combined, and if a pixel is detected to be snowy in any of the measurements, the reported value will be “snow” for that week. In this way, MOD10A2 minimizes the impact of obstructing factors – primarily clouds.

Hall and Riggs [2007] found MOD10A2 to be around 93% accurate when compared to ground truthing and other snow cover products. Known flaws include non-detection of thin snow and occasional misclassification between snow and clouds. I found blunders in the data that had not been reported in previous studies including the frequent detection of “lake ice” at the summits of stratovolcanoes, and one week in which large portions of Antarctica were reported to be ice-free ground (Figure 4.3).

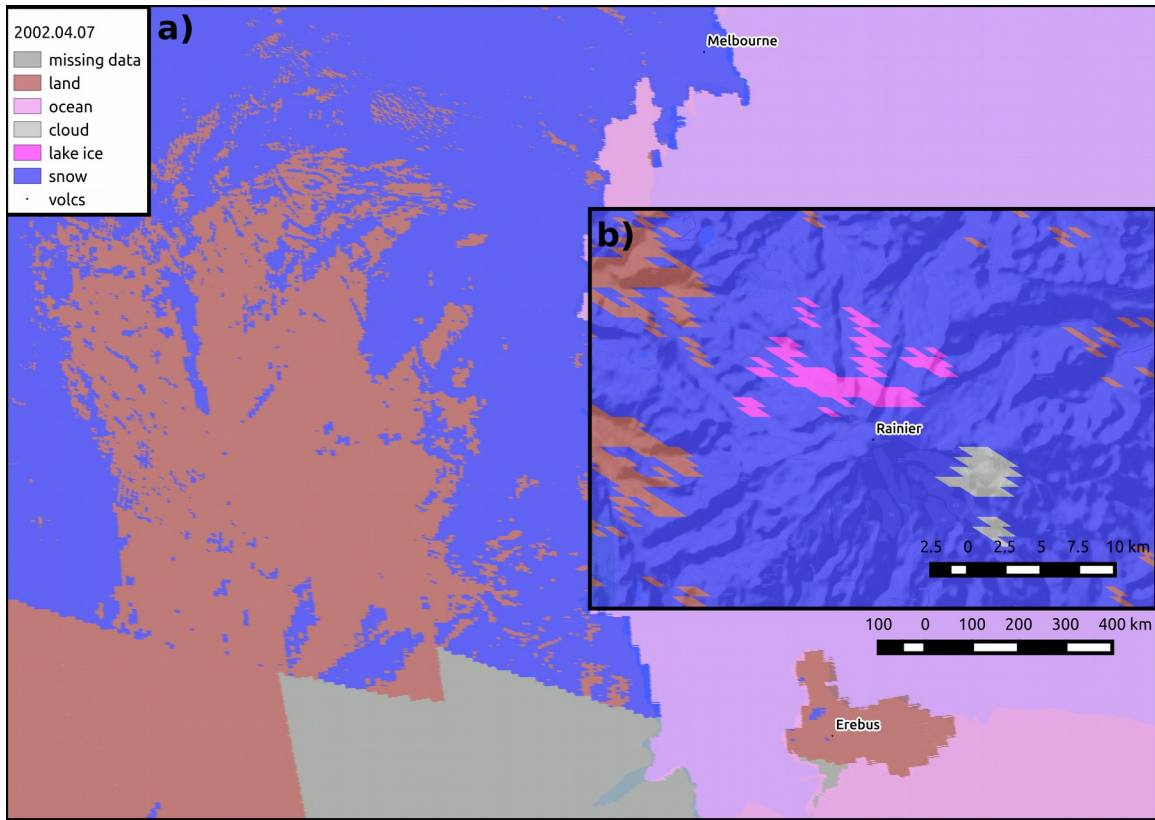


**Figure 4.3:** Previously unreported blunders in MOD10A2, shown for April 7, 2002. **a)** Bare ground covers much of Ross Island and Victoria land. **b)** Snow on certain volcanoes is often misclassified as “lake ice.” Although only one week of data is shown here, the problem persists at Mt. Rainier throughout the dataset.

Insufficient insolation likely accounts for the erroneous bare ground classification in Figure 4.3. A correct classification of these pixels is most likely “night”. Inside the polar circle, there is no direct insolation during the winter. This seasonal availability limits the usefulness of MODIS data at high latitudes (Figure 4.4). PZI and RGI are somewhat more useful for locating potential volcano-ice interaction in polar regions.

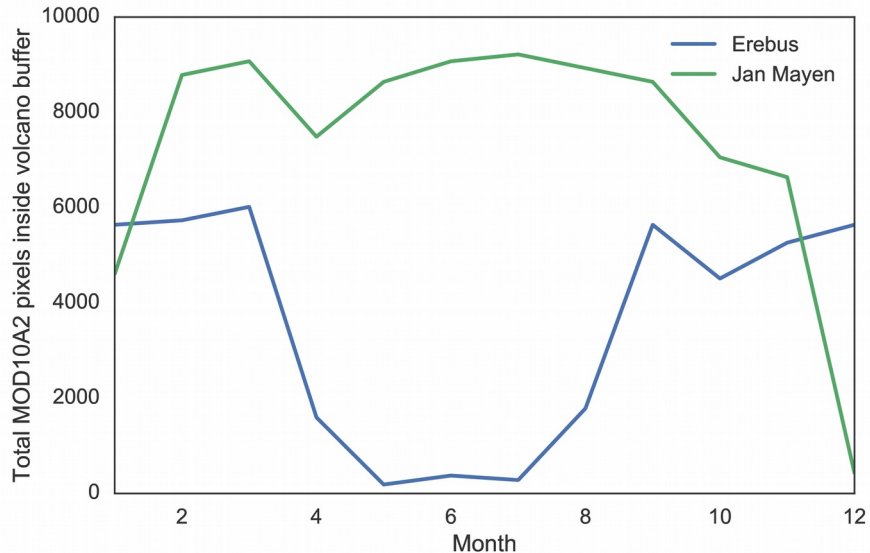


**Figure 4.4:** Availability of MOD10A2 data for the world's most northern and southern Holocene volcanoes is poor during local winter because of low insolation.

The permafrost zonation index (PZI) is also a raster dataset. It is calculated at 1km global resolution with input data from air temperature models (NCAR-NCEP and CRU TS 1.0) and global terrain elevation data. It extends to the North Pole, and to 60°S (beyond which the model would predict continuous permafrost). PZI values are given from 0 (no permafrost exists in this pixel) to 1 (continuous permafrost fills all environments in this pixel) with the recognition that ground temperatures are extremely heterogenous at the sub-pixel scale [Gruber, 2012].

Unlike PZI and MOD10A2, RGI is a vector dataset – it consists of polygons that represent the boundaries of known glaciers. I calculated polygon intersections between volcano buffer zones and the RGI polygons. The RGI locator considers any volcano whose buffer zone intersected an RGI polygon a potential location of volcano-ice interaction.

## 4.5 Results

A total of 471 terrestrial volcanoes (32.6%) were determined to be potential sites of volcano-ice interaction by at least one of the three locators (MDL, RGL, and PZL). Of those, 161 (11.1%) triggered all three locators. Most (170) locations by MDL (216 total) and RGL (240 total) triggered both of those locators. PZL located far more volcanoes than MDL or RGL, at 453. A full listing of locations is given in Appendix A (Section Error: Reference source not found), and totals are shown in Table 4.1.

	MDL	RGL	PZL
PZL	198	219	453
RGL	170	240	
MDL	216		

**Table 4.1:** Counts of located potential volcano-ice interaction centers active in the Holocene for MDL, RGL, and PZL. Where different locators are present in the table row and column, the corresponding cell represents the number of volcano-ice interaction centers located by both.

Geographically, the highest concentrations of PZL-only locations were in southern Kamchatka (Figure 4.5b) and in Japan. This is expected given local meteorological conditions, which are periglacial rather than glacial. The mean annual air temperature in the mountains at these locations is near zero, allowing for the formation of discontinuous permafrost but insufficient for the preservation of snow and ice above ground.

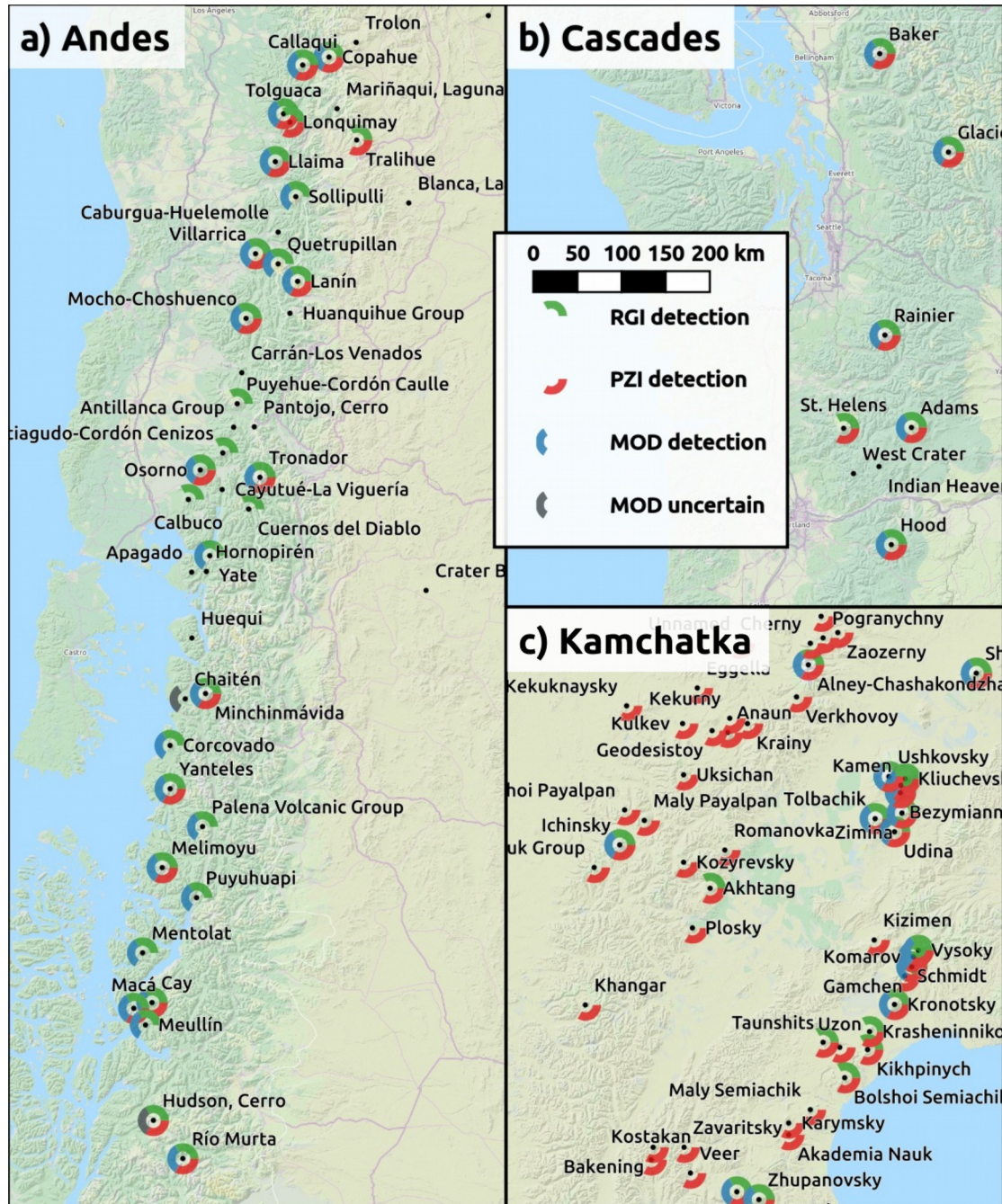


**Figure 4.5:** Locations of potential volcano-ice interaction using the three methods developed here in volcanically active regions.

The input to the RGL and PZL locators are datasets in which the dimension of time has already been integrated. MDL, however, calculates area statistics for all 771 weeks to look for volcanoes that always have an area of snow. Weekly area statistics provide an instructive intermediate data product (Figure 4.6). Erroneous “lake ice” pixels are a persistent pattern at many volcanoes, comprising several percent of the data (Table 4.2). Correcting these pixels is complicated by the fact that lake ice actually exists within the buffer zone of some of these volcanoes. However, the buffer zones for Rainier, Etna, Adams, Baker, and Fujisan contain no lakes, despite the fact that more than 1% of the data reports lake ice. To deal with this situation, lake ice pixels were treated as snow in the MDL locator algorithm (Figure 4.2).

Kurile Lake	20.1%	Eyjafjallajökull	3.9%	Ilyinsky	2.3%
Taryatu-Chulutu	16.2%	Crater Lake	3.7%	Krafla	2.2%
Craters of the Moon	9.8%	Atlin Volcanic Field	3.4%	Baker	2.2%
Askja	8.9%	Unnamed	2.6%	Ingakslugwat Hills	2.1%
Etna	7.1%	Newberry	2.5%	Akademia Nauk	1.8%
Rainier	6.4%	Sanford	2.5%	Fujisan	1.7%
Adams	5.3%	Yellowstone	2.5%	Tao-Rusyr Caldera	1.6%
Garibaldi Lake	4.9%	Mono Lake Volcanic Field	2.4%	Snaefellsjökull	1.6%

**Table 4.2:** Volcanoes with the most lake ice pixels reported in MOD10A2, shown as percentage of all data for 2000 through 2015.

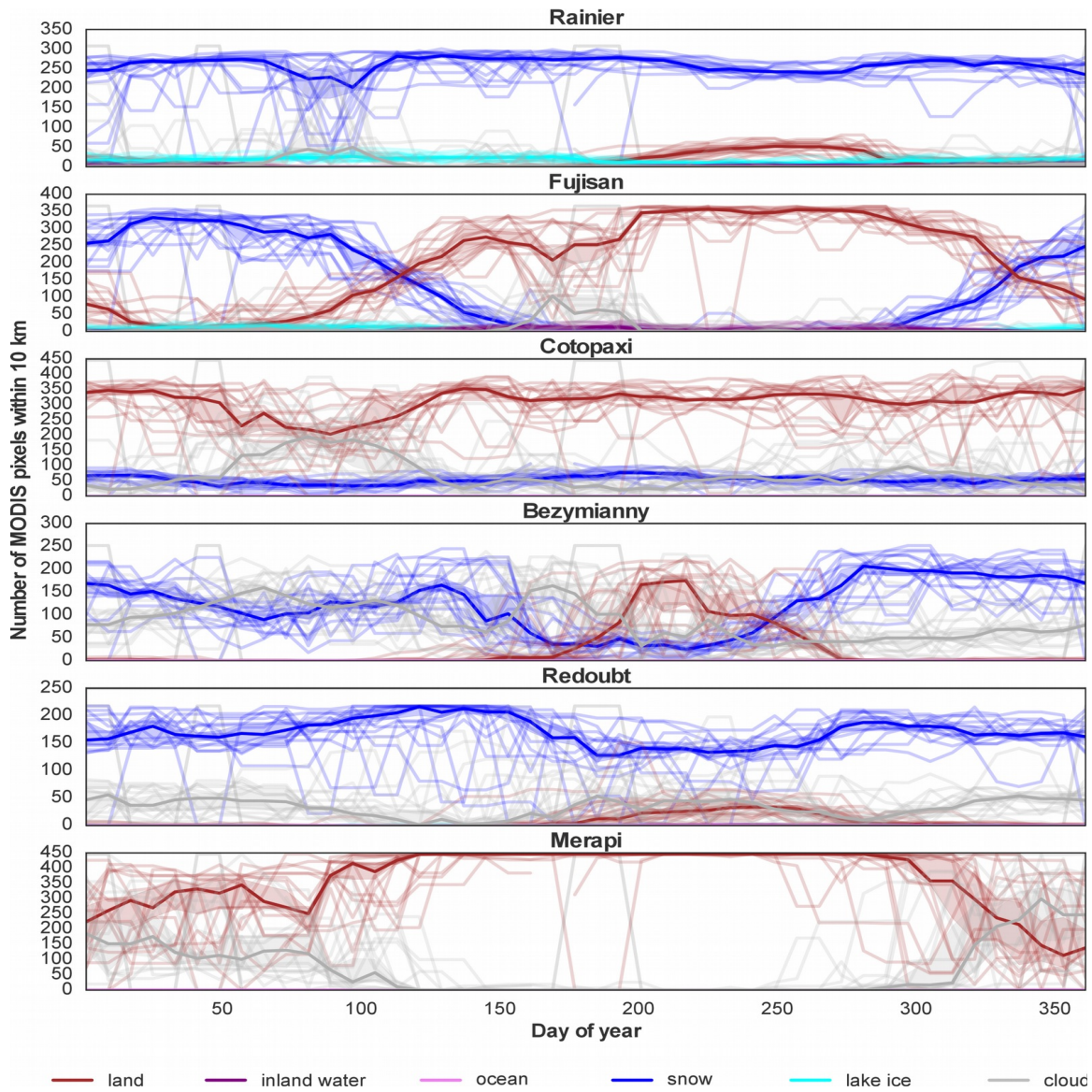


**Figure 4.6:** MOD10A2 pixel values within 10km buffer zones surrounding selected volcanoes. Data is shown for 2000 through 2015, with each year shown as one light-colored line on the plot. The median is shown as a darker line, and the 68% bootstrap confidence interval is shaded.

## 4.6 Discussion

The high level of agreement between these three locators of volcano-ice interaction, derived from independent datasets of global iciness, suggests that these methods are robust. In particular, the 77% agreement between MDL and RGL is encouraging. However, a McNemar's test (a chi-square test for use with paired samples) shows that in fact the three locators are not equivalent at  $p=0.05$  (Table 4.3). At a threshold of  $p=0.01$ , MDL and RGL might be considered equivalent, but it is clear that PZL is not equivalent to the other two locators.

	MDL	RGL
PZL	0.00	0.00
RGL	0.03	

**Table 4.3:** *p-values for McNemar's test with null hypothesis that the two locators are identical.*

Indeed, we would not expect PZL to be equivalent to MDL and RGL, because it is testing for interaction with frozen ground rather than above-ground ice. Permafrost and permanent snow cover are not globally congruent. Periglacial landscapes, in particular, are areas of permafrost which are not glaciated.

Lack of equivalence at  $p=0.05$  between MDL and RGL is primarily due to the fact that permanent snow may exist without forming a glacier. The majority of the 46 volcanoes identified as locations of potential volcano-ice interaction by MDL but not RGL are areas with small patches of permanent snow, such as Chikurachki volcano in the Kurile Islands and Mt. Edgecumbe in Alaska. These snowfields have not reached the thickness, about 30m, required to initiate the plastic flow required for them to be designated glaciers [Paterson, 1994]. In fact, the difference between MDL and RGL results could actually be considered a locator for volcano interaction with thin ice masses. In constructing a global map of volcano-ice interaction, it is most appropriate to combine MDL and RGL locations as indicating Type 1 and Type 2 volcano-ice interaction (*sensu* Chapman et al. 2000) but consider PZL-only locations as indicating Type 3 volcano-ice interaction. The global distribution of these two categories is shown in Figure 4.7.

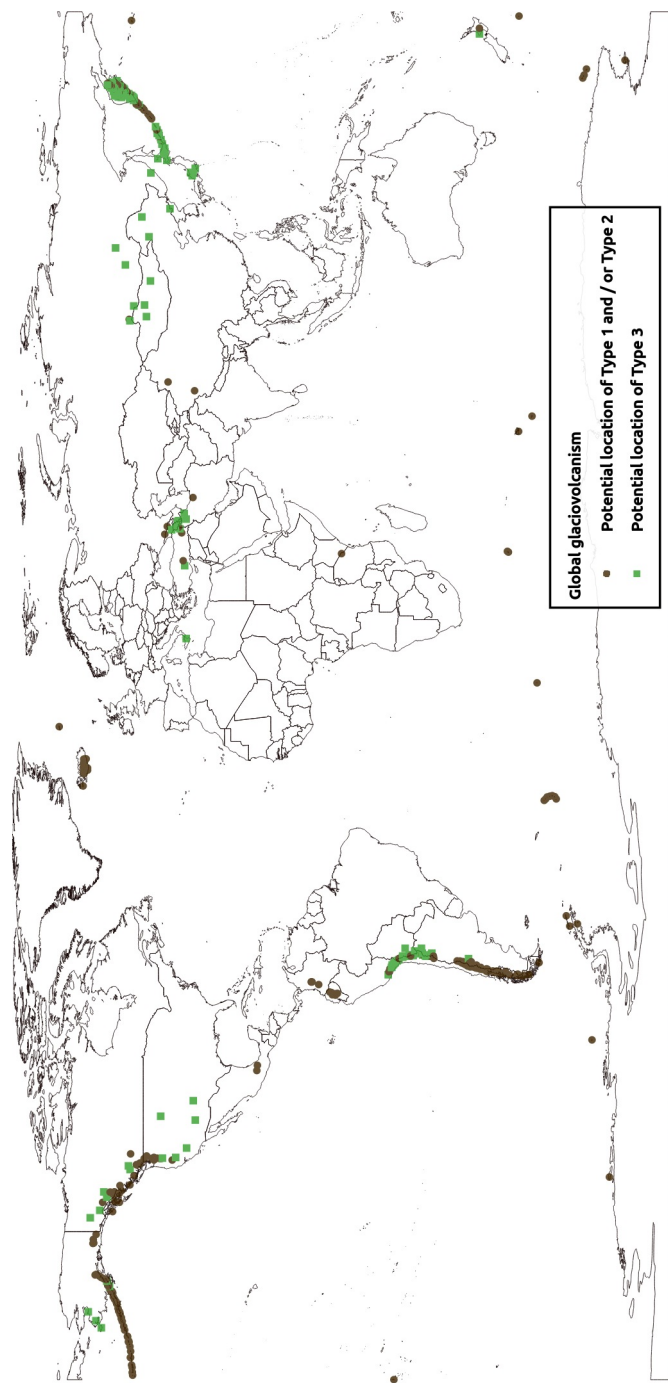


**Figure 4.7:** Global locations of Holocene and present potential volcano-ice interactions. Types follow Chapman et al. 2000; **Type 1:** Eruption beneath ice sheet or major glacier. **Type 2:** Volcanic activity beneath alpine snow. **Type 3:** Volcanic interaction with permafrost.

Some of the RGL non-locations are due to shortcomings in the expert-compiled RGI dataset. While RGI 5.0 claims to be globally complete, some Aleutian summit crater glaciers are missing. RGI contains no glacier polygons on Tanaga Island, Alaska, but the USGS hazard assessment states that one of the craters on the island's Takawangha summit is “covered partly by glacial ice” [Coombs *et al.*, 2007]. The same is true for nearby Gareloai [Coombs *et al.*, 2008]. In both cases, the hazard assessment states that lahars would likely result from volcano-ice interaction in case of eruption. Given this evidence, we can assume that other remote locations, for example, in the Kurile Islands, may also be missing in this database.

MDL's strength, as well as its greatest weakness, is that it is fully automated. In compiling RGI, experts take advantage of human fieldwork on glaciers which is free from the obstruction of clouds and not restricted by satellite orbital geometry. Clouds accounted for 45.8% of the MOD10A2 data within the volcano buffers, despite the fact that the algorithm combining daily data into MOD10A2 weekly data is designed to minimize cloudy pixels. On the other hand, weekly automatic observations allow for a richer dataset that can be analyzed for seasonal and interannual variation. For example, it is evident from Figure 4.6 that although both Cotopaxi and Bezymianny host snow year-round, Bezymianny has much higher seasonal variability in snow cover. This might suggest that volcano-ice interactions are significantly more of a concern at Bezymianny during the winter.

The PZL volcano-ice interaction locator is also fully automated, with the added benefit that it can be easily re-run for past or future scenarios. Because PZL is computed from mean annual air temperatures (MAAT) and topography, it could be run using output from a global circulation model. Provided that data is available for the location of volcanic centers, PZL could be used to create global volcano-ice interaction maps during previous glaciations and for the future, as global deglaciation continues.

## 4.7 Conclusions and implications

Volcano-ice interaction is pervasive on Earth, extending from the equator to beyond the polar circles. Of the 1443 known subaerial Holocene volcanic centers, 286 (19.8%) are glaciated or have permanent snowfields (Type 1 / Type 2 volcano-ice interaction). A further 171 (11.9%) are close enough to areas of permafrost to allow for Type 3 volcano-ice interaction. Type 1 and 2 are present in most plate-boundary and hotspot volcanic regions, with the notable exceptions of Southeast Asia and Central America. Volcanoes with exclusively Type 3 volcano-ice interaction are primarily clustered in five regions: Southwest Alaska, Western Canada, the Atacama Desert, a cluster in the Caucasus, and a band extending from Mongolia to Japan and including southern Kamchatka.

Each of the three locators presented here has unique capabilities and shortcomings. MDL can be used to investigate changes in the extent of snow and ice cover at volcanoes on a weekly timescale, but it is vulnerable to errors in edge cases, and ineffective in cloudy areas and the polar regions. RGL provides the most definitive determinations, but because it relies on a dataset compiled by humans it is vulnerable to omission of glaciers in remote areas and may be updated with insufficient frequency as global glacier area changes. Like MDL, PZL may be processed frequently and also can be run for

hypothetical climate regimes because of its minimal data requirements (global MAAT history and topography), but only locates volcano-permafrost interaction and so is not useful for evaluation of volcanic hazards. Combined, the three locators produce the most comprehensive view of global volcano-ice interaction possible with available data.

All three depend on availability of coordinates for volcanic centers – a dataset that is necessarily incomplete as many eruptions leave cryptic or nonexistent geological records due to erosion or burial. It is likely that many volcanic deposits, even those of Holocene age, are yet to be found and cataloged. Of particular concern are deep subglacial deposits such as the roughly 1000 anomalies located in aeromagnetic surveys beneath the West Antarctic Ice Sheet which *Behrendt* [2013] identifies as volcanic centers. Further investigation of these anomalies is strongly recommended. However, a greater focus on observations of Type 1 volcano-ice interaction – particularly interactions between stratovolcanoes and their alpine ice – could enable us to mitigate major volcano-ice interaction hazards. These thin ice masses are sensitive to increases in degassing which can indicate volcanic unrest [*Bleick et al.*, 2013].

## 4.8 References

- Abramov, A., S. Gruber, and D. Gilichinsky (2008), Mountain permafrost on active volcanoes: field data and statistical mapping, Klyuchevskaya volcano group, Kamchatka, Russia, *Permafro. Periglac. Process.*, 19(3), 261–277, doi:10.1002/ppp.622.
- Behrendt, J. C. (2013), The aeromagnetic method as a tool to identify Cenozoic magmatism in the West Antarctic Rift System beneath the West Antarctic Ice Sheet — A review; Thiel subglacial volcano as possible source of the ash layer in the WAISCORE, *Tectonophysics*, 585, 124–136, doi:10.1016/j.tecto.2012.06.035.
- Bleick, H. A., M. L. Coombs, P. F. Cervelli, K. F. Bull, and R. L. Wessels (2013), Volcano–ice interactions precursory to the 2009 eruption of Redoubt Volcano, Alaska, *J. Volcanol. Geotherm. Res.*, 259, 373–388, doi:10.1016/j.jvolgeores.2012.10.008.
- Chapman, M. G., C. C. Allen, M. T. Gudmundsson, V. C. Gulick, S. P. Jakobsson, B. K. Lucchitta, I. P. Skilling, and R. B. Waitt (2000), Volcanism and ice interactions on Earth and Mars, in *Environmental effects on volcanic eruptions*, pp. 39–73, Springer.
- Connell, L., and H. Staudigel (2013), Fungal Diversity in a Dark Oligotrophic Volcanic Ecosystem (DOVE) on Mount Erebus, Antarctica, *Biology*, 2(2), 798–809, doi:10.3390/biology2020798.
- Conrad, C. P. (2015), How climate influences sea-floor topography, *Science*, 347(6227), 1204–1205, doi:10.1126/science.aaa6813.
- Coombs, M. L., R. G. McGimsey, and B. L. Browne (2007), *Preliminary volcano-hazard assessment for the Tanaga volcanic cluster, Tanaga Island, Alaska*, US Geological Survey. <http://pubs.usgs.gov/sir/2007/5094/>
- Coombs, M. L., R. G. McGimsey, and B. L. Browne (2008), *Preliminary volcano-hazard assessment for Gareloi volcano, Gareloi Island, Alaska*, US Geological Survey. <http://pubs.usgs.gov/sir/2008/5159/>
- Edwards, B. R., H. Tuffen, I. P. Skilling, and L. Wilson (2009), Introduction to special issue on volcano–ice interactions on Earth and Mars: The state of the science, *J. Volcanol. Geotherm. Res.*, 185(4), 247–250, doi:10.1016/j.jvolgeores.2009.06.003.
- Edwards, B. R., Gudmundsson, M.T, and Russell, J.K. (2015), Glaciovolcanism, in *The encyclopedia of volcanoes*.

- Gruber, S. (2012), Derivation and analysis of a high-resolution estimate of global permafrost zonation, *The Cryosphere*, 6(1), 221, doi:10.5194/tc-6-221-2012.
- Hall, D. K., and G. A. Riggs (2007), Accuracy assessment of the MODIS snow products, *Hydrol. Process.*, 21(12), 1534–1547, doi:10.1002/hyp.6715.
- Hall, D. K., J. L. Foster, D. L. Verbyla, A. G. Klein, and C. S. Benson (1998), Assessment of snow-cover mapping accuracy in a variety of vegetation-cover densities in central Alaska, *Remote Sens. Environ.*, 66(2), 129–137, doi:10.1016/S0034-4257(98)00051-0.
- Hall, D. K., V. V. Salomonson, and G. A. Riggs (2006), *MODIS/Terra Snow Cover Daily L3 Global 500m Grid V0005*, National Snow and Ice Data Center, Boulder, CO USA. doi:10.5067/63NQASRDPDB0
- Head, J. W., and L. Wilson (2007), Heat transfer in volcano–ice interactions on Mars: synthesis of environments and implications for processes and landforms, *Ann. Glaciol.*, 45(1), 1–13, doi:10.3189/172756407782282570.
- Huybers, P., and C. Langmuir (2009), Feedback between deglaciation, volcanism, and atmospheric CO<sub>2</sub>, *Earth Planet. Sci. Lett.*, 286(3–4), 479–491, doi:10.1016/j.epsl.2009.07.014.
- Kiver, E. P. (1978), Mount Baker’s changing fumaroles, *Ore Bin*, 40, 133–145.
- Paterson, W. S. B. (1994), *The Physics of Glaciers*, Butterworth-Heinemann.
- Pfeffer, W. T., A. A. Arendt, A. Bliss, T. Bolch, J. G. Cogley, A. S. Gardner, J.-O. Hagen, R. Hock, G. Kaser, and C. Kienholz (2014), The Randolph Glacier Inventory: a globally complete inventory of glaciers, *J. Glaciol.*, 60(221), 537–552, doi:10.3189/2014JoG13J176.
- Tebo, B. M., R. E. Davis, R. P. Anitori, L. B. Connell, P. Schiffman, and H. Staudigel (2015), Microbial communities in dark oligotrophic volcanic ice cave ecosystems of Mt. Erebus, Antarctica, *Front. Microbiol.*, 6, doi:10.3389/fmicb.2015.00179. PMID: 25814983 PMCID: PMC4356161
- Tolstoy, M. (2015), Mid-ocean ridge eruptions as a climate valve, *Geophys. Res. Lett.*, 42(5), 1346–1351, doi:10.1002/2014GL063015.
- Tuffen, H., and J. M. Castro (2009), The emplacement of an obsidian dyke through thin ice: Hrafntinnuhryggur, Krafla Iceland, *J. Volcanol. Geotherm. Res.*, 185(4), 352–366, doi:10.1016/j.volgeores.2008.10.021.

## **4.9 Appendix A: Volcano-ice interaction determinations for Holocene-active volcanoes**

**Table 4.4: Volcano-ice interaction determinations for Holocene-active volcanoes**

Name	VOTW Number	MDL wks.	icy wks.	MDL undet.	PZL mean	Name	VOTW Number	MDL wks.	icy wks.	MDL undet.	PZL mean	MDL wks.	RGL	PZL
'Uwayrid, Harrat	231020	0.98%	2.39%	0.00		Autu		221270	0.42%	11.81%	0.00			
Abu	283001	46.27%	13.08%	0.00		Amak		311390	68.21%	31.79%	0.00			
Acamarachi	355096	56.12%	2.25%	0.09		Amasing		268072	11.53%	58.65%	0.00			
Acatenango	342080	2.95%	54.29%	0.00		Ambalatungan Group		273088	2.67%	40.08%	0.00			
Acıgöi-Nevşehir	213004	19.97%	8.02%	0.00		Ambang		266020	7.74%	61.18%	0.00			
Adagdak	311800	75.81%	24.19%	0.00		Ambite		254020	6.47%	91.00%	0.00			
Adams	321040	97.89%	2.11%	0.21		Ambire-Bobacmby		233011	5.20%	29.54%	0.00			
Adatarayama	283170	56.12%	20.82%	0.00		Ambrym		257040	2.67%	78.48%	0.00			
Adwa	221170	0.70%	10.55%	0.00		Amiata		211800	55.41%	6.61%	0.00			
Afderà	221110	0.28%	6.05%	0.00		Amorong		273085	0.28%	42.48%	0.00			
Agrigan	284160	4.08%	93.95%	0.00		Amsterdam Island		234001	30.10%	69.90%	0.00			
Agua	342100	3.09%	43.60%	0.00		Amukta		311190	80.17%	19.83%	0.01			
Agua de Pau	382090	41.77%	41.91%	0.00		Anatahan		284200	2.11%	95.08%	0.00			
Aguajito, El	341802	0.98%	48.10%	0.00		Anaun		300390	73.70%	10.27%	0.61			
Aguilera	358062	82.98%	17.02%	0.01		Andahuia-Orcopampa		354004	9.00%	6.19%	0.00			
Agung	264020	4.36%	56.68%	0.00		Andrus		390023	61.18%	38.68%	0.00			
Aira	282080	38.96%	59.49%	0.00		Aneityum		257110	10.69%	86.08%	0.00			
Akademia Nauk	300125	84.25%	6.89%	0.21		Aniakchak		312090	89.59%	9.99%	0.07			
Akagisan	283130	48.10%	17.30%	0.00		Ankaizina Field		233013	3.66%	13.64%	0.00			
Akan	285070	75.25%	9.56%	0.01		Ankaratra Field		233015	0.84%	16.60%	0.00			
Akandanayama	283069	68.07%	12.80%	0.00		Antillanca Group		357153	73.84%	11.67%	0.00			
Akhtang	300320	80.87%	9.28%	0.64		Antipodes Island		335010	80.31%	19.69%	1.00			
Akitá-Komagatake	283230	59.35%	20.11%	0.00		Antisana		352030	94.23%	5.77%	0.04			
Akitá-Yakeyama	283260	58.93%	18.28%	0.00		Antofagasta		355180	1.27%	2.39%	0.00			
Akuseki-jima	282022	4.78%	93.95%	0.00		Antuco		357080	88.33%	3.23%	0.01			
Akutan	311320	88.47%	11.53%	0.02		Aoba		257030	9.56%	66.24%	0.00			
Aiaid	290390	88.19%	9.14%	0.35		Aogashima		284060	11.39%	86.92%	0.00			
Alamagan	284180	1.13%	91.84%	0.00		Apagado		358024	72.43%	10.83%	0.00			
Alayta	221112	1.13%	4.36%	0.00		Apaneca Range		343010	3.38%	34.88%	0.00			
Alban Hills	211004	43.32%	5.49%	0.00		Apastepeque Field		343071	0.42%	20.11%	0.00			
Alcedo	353040	0.42%	58.65%	0.00		Apo		271030	5.34%	80.31%	0.00			
Ale Bagu	221090	0.00%	6.75%	0.00		Apoyeque		344091	0.70%	38.40%	0.00			
Alid	221040	0.28%	9.00%	0.00		Aracar		355160	45.99%	2.39%	0.24			
Aliso	352031	5.63%	88.33%	0.00		Aragats		214060	85.51%	3.52%	0.36			
Alligator Lake	320020	78.76%	9.85%	0.72		Aramuaca, Laguna		343101	0.14%	27.43%	0.00			
Almolonga	342040	2.39%	30.80%	0.00		Ararat		213040	97.47%	2.53%	0.46			
Alney-Chashakondzha	300450	97.19%	2.81%	0.94		Arayat		273084	1.41%	54.15%	0.00			
Aingey	300600	85.09%	11.25%	0.82		Ardoukôba		221126	0.14%	6.75%	0.00			
Alu	221060	0.00%	6.33%	0.00		Arenal		345033	1.97%	80.31%	0.00			

**Table 4.4 - Continued**

Name	VOTW Number	MDL wks.	icy wks.	MDL undet.	PZL mean	MDL RGL	RGL PZL	VOTW Number	MDL wks.	icy wks.	MDL undet.	PZL mean	MDL RGL	RGL PZL
Arenales	358059	94.09%	5.91%	0.33				Bal Haf, Harra of	231170	0.14%	26.58%	0.00		
Arhab, Harra of	231090	0.00%	2.81%	0.00				Balatukan	271072	4.22%	74.96%	0.00		
Ajuno-Welirang	263290	2.25%	61.74%	0.00				Balbi	255010	7.59%	79.18%	0.00		
Arshan	305011	52.74%	7.45%	0.27				Baluan	250020	3.38%	95.36%	0.00		
Asacha	300058	78.90%	9.70%	0.46				Baluran	263351	2.67%	45.43%	0.00		
Asamayama	283110	57.67%	18.99%	0.00				Balut	271010	6.61%	92.83%	0.00		
Asayo	221104	0.28%	4.22%	0.00				Bam	251010	0.98%	98.17%	0.00		
Ascension	385050	0.14%	98.87%	0.00				Bamus	252110	9.28%	74.12%	0.00		
Askja	373060	71.45%	25.04%	0.17				Banahaw	273050	3.94%	75.81%	0.00		
Asosan	282110	35.02%	17.58%	0.00				Banda Api	265090	3.66%	94.94%	0.00		
Assab Volcanic Field	221125	0.14%	3.66%	0.00				Bandasian	283160	54.43%	17.30%	0.00		
Asuncion	284150	0.98%	92.12%	0.00				Bárcena	341020	0.14%	88.33%	0.00		
Atacazo	352021	5.63%	67.79%	0.00				Bárdarbunga	373030	83.26%	16.74%	0.67		
Atakor Volcanic Field	225005	0.28%	2.39%	0.00				Barkhatnaya Sopka	300084	76.93%	7.74%	0.02		
Atitlán	342060	4.22%	51.48%	0.00				Baren Island	260010	0.56%	92.41%	0.00		
Atika	311160	89.59%	10.41%	0.05				Barrier, The	222030	0.28%	29.96%	0.00		
Atlin Volcanic Field	320030	86.08%	8.44%	0.36				Barú	346010	7.17%	63.71%	0.00		
Atlixcos, Los	341094	2.11%	20.11%	0.00				Barva	345050	9.85%	63.85%	0.00		
Atuel, Caldera del	357023	88.19%	2.25%	0.11				Bas Dong Nai	275050	0.98%	59.49%	0.00		
Aucanquilcha	355823	70.89%	2.39%	0.20				Batur	264010	4.36%	41.35%	0.00		
Auckland Field	241020	40.37%	19.55%	0.00				Bayo Gorbea, Cerro	355122	43.18%	2.25%	0.25		
Augustine	313010	80.17%	15.75%	0.07				Bayuda Volcanic Field	225060	0.00%	2.39%	0.00		
Auquihuato, Cerro	354001	21.66%	8.44%	0.00				Bazman	232030	13.50%	2.81%	0.00		
Avachinsky	300100	95.36%	3.94%	0.82				Behm Canal-Rudyerd Bay	315070	83.97%	15.47%	0.00		
Awu	267040	9.28%	72.43%	0.00				Belenkaya	300042	71.03%	9.99%	0.01		
Ayelu	221160	0.98%	10.55%	0.00				Belriang-Beriti	261200	4.64%	72.43%	0.00		
Azas Plateau	302070	83.54%	7.31%	0.95				Belknap	322060	72.01%	4.78%	0.00		
Azufíal	351090	2.25%	88.75%	0.00				Bely	300640	95.64%	4.36%	0.92		
Azufre, Cerro del	355061	38.12%	2.39%	0.12				Berlin	390022	60.62%	39.10%	0.00		
Azufres, Los	341824	14.91%	21.38%	0.00				Beru	221191	0.28%	4.08%	0.00		
Azul, Cerro	357060	77.92%	2.39%	0.03				Berutarubesan [Berutarube]	290040	77.22%	22.36%	0.01		
Azul, Cerro	353060	0.00%	65.96%	0.00				Besar	261250	3.52%	60.76%	0.00		
Azul, Volcán	344140	5.91%	64.70%	0.00				Bezymianny	300250	96.20%	3.80%	0.99		
Azumayama	283180	65.82%	18.85%	0.00				Bibinói	268073	15.05%	56.54%	0.00		
Babuyán Claro	274030	2.25%	97.33%	0.00				Bilate River Field	221291	0.84%	20.25%	0.00		
Bachelor	322090	78.62%	3.23%	0.03				Biliran	272080	4.22%	60.48%	0.00		
Bagana	255020	4.22%	88.75%	0.00				Billy Mitchell	255011	5.91%	81.86%	0.00		
Bakering	300123	80.87%	6.75%	0.56				Bir Borhut	231180	0.00%	2.53%	0.00		
Baker	321010	97.05%	2.95%	0.20				Birk, Harrat al	231072	0.56%	2.67%	0.00		

**Table 4.4 - Continued**

Name	vOTW Number	MDL wks.	icy wks.	MDL undet.	PZL mean	Name	vOTW Number	MDL wks.	icy wks.	MDL undet.	PZL mean	MDL RGL	RGL	PZL
Bishoftu Volcanic Field	221220	1.55%	18.00%	0.00		Bus-Obo	303030	33.33%	7.03%	0.01				
Biu Plateau	224050	1.13%	10.13%	0.00		Butajiri-Silti Field	221260	1.13%	22.93%	0.00				
Black Peak	312080	76.37%	19.13%	0.02		Buzzard Creek	315001	61.46%	23.21%	0.53				
Black Rock Desert	327050	23.63%	5.06%	0.00		Cabalian	272050	5.91%	81.86%	0.00				
Bianca, Laguna	357102	15.19%	4.22%	0.00		Caburgua-Huelemolle	273090	3.09%	54.71%	0.00				
Blancas, Lomas	357064	54.15%	3.94%	0.00		Caiinchique	357112	61.04%	5.63%	0.00				
Blanco, Cerro	355210	14.06%	2.39%	0.03		Calabozos	357104	46.41%	2.25%	0.00				
Bliznets	300490	79.04%	8.72%	0.48		Calatrava Volcanic Field	210040	8.02%	7.03%	0.00				
Bliznetsy	300552	66.95%	9.14%	0.02		Calbuco	358020	80.73%	12.24%	0.00				
Blue Lake Crater	322030	66.39%	2.95%	0.00		Callaqui	357091	97.19%	2.81%	0.06				
Blup Blup	251001	2.53%	96.91%	0.00		Cameroon	224010	2.11%	78.62%	0.00				
Bobrof	311100	59.63%	40.37%	0.00		Camiguin	271080	4.64%	93.25%	0.00				
Bogoria	2222803	0.56%	4.50%	0.00		Camiguin de Babuyanes	274010	2.39%	93.67%	0.00				
Boisa	251011	0.28%	95.92%	0.00		Campi Flegrei	211010	19.69%	60.62%	0.00				
Bola	252050	5.63%	92.12%	0.00		Campi Flegrei Mar Sicilia	211070	0.00%	2.25%	0.00				
Boishe-Bannaya	300087	75.39%	10.83%	0.14		Candilemas Island	390100	52.60%	47.40%	1.00				
Boishoi Payalpan	300300	76.09%	10.55%	0.84		Carlisle	311230	88.05%	11.95%	0.05				
Boishoi Semiacich	300150	83.83%	8.02%	0.29		Carrán-Los Venados	357140	61.74%	10.69%	0.00				
Boishoi-Kekukhnaysky	300360	78.20%	9.14%	0.48		Caririzo	327110	6.05%	2.81%	0.00				
Bombalai	269010	7.74%	72.71%	0.00		Casirri, Nevados	354060	69.76%	2.81%	0.07				
Bora-Bericcio	221240	0.14%	15.33%	0.00		Cay	358055	93.39%	6.33%	0.01				
Borale Ale	221071	0.00%	7.88%	0.00		Cayambe	352006	95.08%	4.92%	0.07				
Borawli	221121	0.42%	6.05%	0.00		Cayley Volcanic Field	320811	96.34%	3.66%	0.10				
Borawli	221107	0.28%	6.61%	0.00		Cayutitú-La Viguera	358012	78.90%	6.05%	0.00				
Boset-Bericha	221210	1.55%	9.56%	0.00		Ceboruco	341030	1.27%	9.42%	0.00				
Bouillante Chain	360811	7.88%	85.94%	0.00		Cendres, Ile des	275060	0.00%	2.53%	0.00				
Bouvet	386020	49.23%	50.77%	0.15		Central Island	222010	1.97%	16.03%	0.00				
Bratan	264001	4.78%	45.99%	0.00		Cereme	263170	4.64%	67.37%	0.00				
Brava	384020	0.14%	91.28%	0.00		Chuga-ryong	306020	23.07%	11.81%	0.00				
Brennisteinsföll	351012	2.67%	89.31%	0.00		Chacana	352022	4.50%	77.92%	0.00				
Bridge River Cones	371040	55.84%	28.13%	0.00		Chachadake [Tiatia]	290030	76.65%	11.67%	0.10				
Bristol Island	390080	56.40%	43.60%	1.00		Chachani, Nevado	354007	71.03%	3.94%	0.17				
Buckle Island	390010	73.42%	26.44%	0.00		Chachimbiro	352002	1.41%	84.53%	0.00				
Bufumbira	223070	13.92%	30.94%	0.00		Chagualak	311200	72.01%	27.99%	0.00				
Buldır	311010	61.18%	38.68%	0.00		Chaîne des Puys	210020	53.45%	10.97%	0.00				
Bulusan	273010	5.77%	72.57%	0.00		Challén	358041	62.03%	22.50%	0.00				
Bunyaruguru	223004	1.55%	21.10%	0.00		Changbaishan	305060	73.70%	12.38%	0.60				
Burney, Monte	358070	71.17%	28.83%	0.04		Chemy	300460	79.32%	10.69%	0.76				

**Table 4.4 - Continued**

Name	VOTW Number	MDL wks.	icy MDL undet.	PZL mean	VOTW Number	MDL wks.	icy MDL undet.	PZL mean	MDL RGL	RGL	PZL
Cherpuk Group	300273	81.01%	10.41%	0.83	Cordón de Puntas Negras	355101	59.63%	2.39%	0.16		
Chichinautzín	341080	2.95%	27.43%	0.00	Cordón del Azufre	355121	46.98%	2.25%	0.26		
Chichón, El	341120	0.84%	29.82%	0.00	Coronado	341005	0.84%	67.23%	0.00		
Chiginagak	312110	97.19%	2.81%	0.27	Coropuna	354003	97.75%	2.25%	0.41		
Chikurachki	290360	87.06%	12.80%	0.23	Corvo	382002	21.80%	78.20%	0.00		
Chiliques	355098	52.46%	2.39%	0.09	Cosigüina	344010	2.53%	24.33%	0.00		
Chillán, Nevados de	357070	90.58%	3.23%	0.03	Coso Volcanic Field	323180	3.80%	2.67%	0.00		
Chimborazo	352071	96.62%	3.38%	0.08	Cotopaxi	352050	95.08%	4.92%	0.06		
Chinameca	343090	0.56%	26.16%	0.00	Crater Basalt Volcanic Field	358025	5.63%	6.33%	0.00		
Chingo	342170	1.69%	27.29%	0.00	Crater Lake	322160	77.07%	3.38%	0.00		
Chiquimula Volcanic Field	342200	0.28%	43.88%	0.00	Crater Mountain	253001	10.41%	66.39%	0.00		
Chiracha	221300	0.14%	8.72%	0.00	Craters of the Moon	324020	41.91%	2.67%	0.00		
Chirinkotan	290260	56.40%	43.46%	0.01	Crow Lagoon	320110	90.01%	7.17%	0.00		
Chirippusán [Chirip]	290090	76.09%	13.64%	0.07	Cù-Lao Ré Group	275020	0.14%	98.17%	0.00		
Chirpoi	290150	76.51%	23.49%	0.01	Cuernos de Negros	272010	5.77%	77.50%	0.00		
Chokaisan	283220	66.10%	22.50%	0.01	Cuernos del Diablo	358021	78.62%	7.45%	0.00		
Churchill	315030	97.75%	2.25%	1.00	Cuicocha	352003	4.92%	63.71%	0.00		
Chyulu Hills	222130	4.08%	15.89%	0.00	Cuilapa-Barbatena	342111	1.55%	19.27%	0.00		
Ciguatepe, Cerro el	344132	0.70%	30.94%	0.00	Cumbal	351100	3.94%	87.20%	0.00		
Cinnamon Butte	322150	75.39%	2.53%	0.00	Cumbres, Las	341098	5.34%	28.69%	0.00		
Cinotepeque, Cerro	343051	0.28%	17.16%	0.00	Dabbahu	221113	1.27%	4.36%	0.00		
Clear Lake	323100	44.02%	3.66%	0.00	Dabbayra	221114	0.98%	3.94%	0.00		
Cleveland	311240	88.05%	11.81%	0.06	Dacht-i-Navar Group	232060	40.37%	2.81%	0.00		
Coatepeque Caldera	343041	4.36%	23.07%	0.00	Dakataua	252040	6.89%	51.76%	0.00		
Cochiquito Volcanic Group	357071	9.56%	2.81%	0.00	Dalaffilla	221070	0.14%	6.75%	0.00		
Cochons, Ile aux	234050	79.75%	20.25%	0.00	Dallo	221041	0.00%	6.19%	0.00		
Cofré de Perote	341096	8.58%	30.94%	0.00	Dama Ali	221141	0.84%	3.66%	0.00		
Colachi	355095	46.27%	2.25%	0.05	Damavand	232010	88.75%	2.81%	0.34		
Colima	341040	16.17%	39.52%	0.00	Dana	312050	76.37%	21.66%	0.04		
Colo [Una Una]	266010	14.91%	84.95%	0.00	Dar-Alages	214080	30.52%	8.02%	0.00		
Comondú-La Purísima	341012	0.56%	2.11%	0.00	Dariganga Volcanic Field	303040	39.38%	3.94%	0.00		
Concepción	344120	1.27%	64.98%	0.00	Darwin	353030	0.00%	75.53%	0.00		
Conchagua	343110	2.25%	49.09%	0.00	Dauh, Bukit	261210	5.49%	70.18%	0.00		
Conchagüita	343120	1.13%	76.79%	0.00	Davidof	311040	49.93%	50.07%	0.00		
Cónedor, El	355190	83.54%	2.25%	0.72	Davis Lake	322100	69.48%	2.53%	0.00		
Copahue	357090	95.78%	3.09%	0.01	Dawson Strait Group	253060	5.49%	91.56%	0.00		
Copiapó	355140	76.09%	2.25%	0.42	Deception Island	390030	0.00%	2.25%	0.00		
Corbetti Caldera	221290	1.13%	13.78%	0.00	Dempo	261230	3.66%	73.70%	0.00		
Corcovado	355050	81.01%	16.74%	0.00	Denison	312210	97.89%	2.11%	0.55		

**Table 4.4 - Continued**

Name	VOTW Number	MDL wks.	icy	MDL undet.	PZL mean	MDL RGL	PZL	Name	VOTW Number	MDL wks.	icy	MDL undet.	PZL mean	MDL RGL	PZL
Descabezado Grande	357050	89.31%	2.81%	0.07				Erciyes Dagı	213010	72.71%	3.66%	0.14			
Devils Garden	322120	37.69%	5.34%	0.00				Erebos	390020	58.93%	40.93%	0.00			
Dhamar, Harras of	231120	0.14%	2.81%	0.00				Ertा Ale	221080	0.42%	7.17%	0.00			
Diables, Morne aux	360080	8.44%	87.20%	0.00				Es Sata	230050	0.98%	2.67%	0.00			
Diablotins, Morne	360090	9.85%	53.16%	0.00				Esan	285011	60.06%	39.38%	0.00			
Diamond Craters	322170	18.42%	10.41%	0.00				Escorial	355112	39.94%	2.25%	0.18			
Didicas	274020	0.00%	2.53%	0.00				Esiúfjöll	374020	81.58%	18.42%	0.36			
Dieng Volcanic Complex	263200	0.70%	62.59%	0.00				Est. Ille de l'	234030	63.99%	36.01%	0.00			
Diky Greben	300022	81.15%	8.30%	0.03				Estelí	344131	1.13%	38.12%	0.00			
Dofen	221180	1.13%	4.64%	0.00				Enna	211060	64.70%	6.33%	0.02			
Doma Peaks	253000	15.33%	57.95%	0.00				Etorofú-Atotsanupuri [Atotsanupuri]	290050	80.31%	19.69%	0.01			
Domuyo	357067	97.61%	2.39%	0.34				Etorofú-Yakeyama [Grozny Gružnij]	290070	72.01%	12.80%	0.01			
Doña Juana	351070	15.05%	79.04%	0.00				Eyafallajökull	372020	84.53%	15.47%	0.20			
Dotsero	329010	45.43%	3.23%	0.00				Falso Azufre	355124	74.68%	2.25%	0.55			
Douglas	312270	97.47%	2.53%	0.46				Farallon de Pajaros	284140	0.14%	82.70%	0.00			
Druze, Jabal ad	230060	1.27%	3.52%	0.00				Faval	382010	48.10%	48.66%	0.00			
Dubbi	221100	0.56%	4.78%	0.00				Fedotych	300510	75.67%	7.59%	0.40			
Dukono	268010	10.41%	65.82%	0.00				Fentale	221190	0.42%	4.92%	0.00			
Duncan Canal	315050	86.50%	13.22%	0.00				Fernandina	353010	0.00%	71.87%	0.00			
Durango Volcanic Field	341022	0.84%	5.77%	0.00				Fisher	311350	74.54%	21.80%	0.00			
Dutton	312011	89.03%	10.97%	0.07				Flores	382001	48.38%	44.87%	0.00			
Dzenzursky	300110	89.87%	7.03%	0.59				Flores	342140	0.56%	24.33%	0.00			
East Zway	221252	1.27%	9.42%	0.00				Fogo	384010	0.28%	27.43%	0.00			
Easter Island	356011	0.00%	100.00%	0.00				Fonualei	243100	0.84%	89.87%	0.00			
Ebeko	290380	77.07%	17.02%	0.09				Fort Portal	223001	3.38%	28.69%	0.00			
Ebulobo	264110	2.95%	40.65%	0.00				Fort Selkirk	320010	72.86%	14.77%	0.55			
Eburru, Oi Doinyo	222080	2.25%	21.80%	0.00				Fournaise, Piton de la	233020	13.50%	36.71%	0.00			
Ecuador	353011	0.14%	96.20%	0.00				Fourpeaked	312260	97.05%	2.95%	0.52			
Edgecumbe	315040	81.72%	14.77%	0.01				Fremínamar	373070	58.65%	33.19%	0.01			
Edziza	320060	97.89%	2.11%	0.90				Frosty	312010	93.95%	6.05%	0.09			
Eggella	300420	74.40%	9.99%	0.51				Fuego	342090	2.53%	55.13%	0.00			
Egon	264160	4.50%	45.15%	0.00				Fueguino	358090	84.81%	15.19%	0.00			
Ekarma	290270	79.32%	20.68%	0.05				Fuerteventura	383050	1.41%	5.49%	0.00			
Elbrus	214010	97.61%	2.39%	0.99				Fujisan	283030	73.14%	14.06%	0.14			
Elmenteita Badlands	222071	0.14%	4.36%	0.00				Fukue	282091	27.43%	70.04%	0.00			
Elovsky	300590	80.31%	10.97%	0.67				Furnas	382100	45.57%	37.69%	0.00			
Emmons Lake	312020	91.70%	8.30%	0.03				Fuss Peak	290340	88.61%	11.39%	0.15			
Emuruangogolak	222051	0.84%	5.63%	0.00				Gabilmea	221150	0.28%	3.38%	0.00			
Epi	257060	1.13%	95.36%	0.00				Gada Ale	221050	0.00%	22.22%	0.00			

**Table 4.4 - Continued**

Name	vOTW Number	MDL wks.	icy wks.	MDL undet.	PZL mean	vOTW Number	MDL wks.	icy wks.	MDL undet.	PZL mean	MDL RGL	RGL	PZL
Galeras	351080	5.06%	88.47%	0.00		Grimsnes	371060	51.76%	24.61%	0.00			
Gallego	255062	4.92%	58.93%	0.00		Grimsvötn	373010	82.84%	17.16%	0.29			
Galunggung	263140	2.53%	62.03%	0.00		Groppo	221116	0.14%	3.94%	0.00			
Gamalama	268060	5.20%	92.41%	0.00		Guadalupe	341006	2.39%	60.90%	0.00			
Gamchen	300210	86.22%	9.14%	0.84		Guagua Pichinchana	352020	6.89%	61.60%	0.00			
Gamkonora	268040	7.17%	86.78%	0.00		Guallatiri	355020	92.26%	2.11%	0.09			
Garbuna Group	252070	9.28%	54.15%	0.00		Guayaques	355093	32.35%	2.39%	0.05			
Gareloi	311070	90.88%	9.14%	0.10		Guazapa	343052	0.28%	25.04%	0.00			
Garibaldi	320200	94.80%	5.20%	0.06		Gufa	221124	0.28%	3.80%	0.00			
Garibaldi Lake	320190	91.42%	5.49%	0.02		Guguan	284190	0.56%	83.40%	0.00			
Garove	252030	5.77%	91.98%	0.00		Guntur	263130	1.69%	54.43%	0.00			
Garua Harbour	252060	4.58%	93.53%	0.00		Gunungapi Wetar	265030	0.42%	82.84%	0.00			
Gaua	257020	7.17%	59.92%	0.00		Hachijojima	284050	34.88%	64.98%	0.00			
Gedamsa	221230	0.42%	12.38%	0.00		Hachimantai	283250	69.20%	15.19%	0.00			
Gede	263060	3.23%	73.00%	0.00		Hainan Dao	275001	1.13%	47.40%	0.00			
Genovesa	352081	0.14%	96.20%	0.00		Hakkodasan	283280	62.17%	19.55%	0.00			
Geodesistoy	300380	72.15%	10.55%	0.53		Hakoneyama	283020	52.46%	18.57%	0.00			
Geureudong	261809	4.92%	72.15%	0.00		Hakusan	283050	68.92%	13.08%	0.01			
Geysir	371803	59.21%	23.77%	0.00		Haleakala	332060	1.97%	29.96%	0.00			
Ghegam Ridge	214070	43.74%	7.59%	0.00		Halla	306040	42.62%	17.58%	0.00			
Girekol Tepe	213022	53.45%	4.08%	0.00		Hanish	221022	0.56%	65.96%	0.00			
Glacier Peak	321020	96.48%	3.52%	0.15		Hargy	252100	5.91%	69.34%	0.00			
Gloria, La	341097	2.25%	20.39%	0.00		Harrah, AL	231001	0.28%	2.25%	0.00			
Golan Heights	230030	9.14%	3.23%	0.00		Haruj	225007	0.28%	2.39%	0.00			
Golaya	300057	71.73%	9.42%	0.04		Harunasan	283122	44.44%	16.46%	0.00			
Golden Trout Creek	323170	58.93%	2.53%	0.00		Hasan Dagi	213002	57.24%	5.06%	0.01			
Göllü Dag	213003	35.44%	8.02%	0.00		Haut Dong Nai	275040	0.70%	43.32%	0.00			
Goodenough	253041	3.66%	94.80%	0.00		Hayes	313050	96.48%	3.52%	0.99			
Gordon	315021	92.12%	7.88%	0.98		Hayan, Jabal	231110	0.00%	2.39%	0.00			
Gorely	300070	83.97%	9.56%	0.52		Hayli Gubbi	221091	0.28%	7.31%	0.00			
Goriaschatai Sopka	290170	80.31%	19.41%	0.12		Heard	234010	25.74%	74.26%	0.65			
Gorny Institute	300550	88.19%	9.42%	0.93		Heart Peaks	320040	80.03%	10.13%	0.59			
Graciosa	382040	31.08%	67.51%	0.00		Hekla	372070	70.18%	27.85%	0.08			
Gran Canaria	383040	7.17%	11.95%	0.00		Heligrindur	370020	62.87%	30.66%	0.01			
Granada	344101	1.83%	58.93%	0.00		Hell's Half Acre	324040	29.68%	5.34%	0.00			
Great Sitkin	311120	94.23%	5.77%	0.13		Hengill	371050	59.77%	27.00%	0.01			
Grensdalur	371801	52.04%	25.60%	0.00		Herbert	311220	89.45%	10.55%	0.01			
Griggs	312190	93.95%	6.05%	0.50		Hertali	221171	0.42%	2.95%	0.00			
Grille, La	233001	8.86%	30.24%	0.00		Hierro	383020	13.78%	79.47%	0.00			

**Table 4.4 - Continued**

Name	VOTW Number	MDL wks.	icy	MDL undet.	PZL mean	Name	VOTW Number	MDL wks.	icy	MDL undet.	PZL mean	MDL	RGL	PZL
Hijiori	283191	58.51%	18.42%	0.00		Ilmuida	264170	2.53%	36.15%	0.00				
Hiri	268052	2.81%	93.67%	0.00		Illerung	264250	1.69%	76.79%	0.00				
Hiuchigatake	283131	71.31%	10.97%	0.00		Illiniza	352041	26.58%	63.01%	0.01				
Hobicha Caldera	221293	0.42%	32.49%	0.00		Illopango	343060	4.50%	25.18%	0.00				
Hodson	390110	80.45%	19.55%	1.00		Ilyinsky	300030	81.43%	7.88%	0.08				
Höfsjökull	371090	80.31%	19.69%	0.39		Imbabura	352004	3.38%	81.29%	0.00				
Hokkaido-Komagatake	285020	55.84%	13.36%	0.00		Imun	261101	4.36%	55.27%	0.00				
Homa Mountain	222070	1.27%	10.13%	0.00		Imuruk Lake	314060	54.71%	23.91%	0.54				
Honggeertu	305010	19.97%	11.67%	0.00		In Ezzane Volcanic Field	225003	0.14%	2.39%	0.00				
Hood	322010	97.47%	2.53%	0.14		Incahuasi, Nevado de	355125	84.25%	2.25%	0.57				
Hoodoo Mountain	320080	94.23%	5.77%	0.08		Indian Heaven	321070	76.09%	5.49%	0.00				
Hornopirén	358023	80.45%	8.72%	0.00		Infierillo	357041	44.16%	2.95%	0.00				
Hrómundartindur	371051	56.54%	24.89%	0.00		Ingaksligwat Hills	314030	73.42%	11.53%	0.09				
Hualalai	332040	0.70%	61.74%	0.00		Inielika	264090	2.11%	36.01%	0.00				
Huambo	354005	1.13%	6.61%	0.00		Inierie	264080	2.39%	39.80%	0.00				
Huangquique Group	357123	71.73%	8.58%	0.00		Inyo Craters	323130	69.48%	2.25%	0.00				
Huaynaputina	354030	6.75%	7.03%	0.01		Io-Torishima	282020	1.27%	94.37%	0.00				
Hudson Mountains	390028	61.74%	37.83%	0.00		Io	284120	1.13%	95.92%	0.00				
Hudson, Cerro	358057	24.47%	75.53%	0.01		Ipala	342190	0.42%	25.18%	0.00				
Huequi	358030	73.28%	14.35%	0.00		Iraya	274060	1.41%	98.17%	0.00				
Huilla, Nevada del	351050	77.64%	22.08%	0.01		Irazú	345060	7.31%	69.90%	0.00				
Hulubelu	2611280	2.81%	55.98%	0.00		Iriga	273041	5.06%	57.24%	0.00				
Humeros, Los	341093	0.70%	17.58%	0.00		Iruputuncu	355040	9.56%	3.09%	0.01				
Hunter Island	258020	0.00%	2.39%	0.00		Isabel, Isla	341023	0.70%	67.37%	0.00				
Hutapanjang	261172	6.19%	65.12%	0.00		Isanotski	311370	96.77%	3.23%	0.19				
Hveravellir	371080	82.70%	17.30%	0.19		Isatog	273042	4.92%	70.18%	0.00				
Hydrographers Range	253011	5.63%	83.26%	0.00		Ischia	211030	33.90%	51.48%	0.00				
Jamalele	253050	3.94%	94.37%	0.00		Iskut-Unuk River Cones	320090	91.00%	7.31%	0.02				
Ibu	268030	7.03%	62.31%	0.00		Istuga	355030	44.73%	3.09%	0.04				
Ibusuki Volcanic Field	282070	42.90%	28.13%	0.00		Itasy Volcanic Field	233014	0.98%	5.06%	0.00				
Ichinsky	300280	97.05%	2.95%	1.00		Itthnayn, Harrat	231050	0.28%	2.53%	0.00				
Iettunup	300710	82.42%	14.35%	0.74		Ivao Group	290111	76.93%	13.22%	0.06				
Igwisi Hills	222161	1.69%	11.95%	0.00		Wakisan	283270	62.73%	15.33%	0.00				
Ijen	263350	4.22%	48.95%	0.00		Watesan	283240	69.20%	16.74%	0.00				
Iktunup	300670	95.92%	4.08%	0.95		Ixtepeque	342180	0.70%	18.28%	0.00				
Ilamna	313020	96.91%	3.09%	0.78		Iya	264110	0.28%	89.31%	0.00				
Ilboleng	264220	3.66%	41.77%	0.00		Iyang-Aigapura	263330	2.11%	51.20%	0.00				
Ilkedeka	266800	3.38%	63.43%	0.00		Izalco	343030	1.55%	35.16%	0.00				
Ililabalekan	264240	3.09%	74.82%	0.00		Iztaccíhuatl	341082	55.70%	21.38%	0.01				

**Table 4.4 - Continued**

Name	VOTW Number	MDL wks.	icy MDL undet.	PZL mean	Name	VOTW Number	MDL wks.	icy MDL undet.	PZL mean	MDL RGL	RGL	PZL
IZU-Oshima	284010	43.04%	55.56%	0.00	Kalla	372030	84.53%	15.47%	0.09			
IZU-Tobu	283010	46.84%	37.69%	0.00	Katmai	312170	95.36%	4.64%	0.47			
IZU-Torishima	284090	1.69%	95.64%	0.00	Katunga	223005	4.36%	33.05%	0.00			
IZumbwe-Mpoli	222165	5.06%	12.66%	0.00	Kaiwe-Kikorongo	223003	0.70%	41.21%	0.00			
Jailolo	268051	4.22%	91.28%	0.00	Kawi-Butak	263281	2.95%	50.49%	0.00			
Jalua	221030	0.14%	74.40%	0.00	Kazbek	214020	97.47%	2.53%	0.89			
Jan Mayen	376010	70.89%	29.11%	0.80	Kebeney	300500	77.64%	10.97%	0.78			
Jaragua Volcanic Field	341004	1.55%	2.95%	0.00	Kelurny	300410	71.03%	11.81%	0.62			
Jayu Khotia, Laguna	355035	1.41%	4.92%	0.00	Kelimutu	264140	3.38%	37.69%	0.00			
Jefferson	322020	95.78%	2.95%	0.09	Kell	300041	77.78%	9.99%	0.02			
Jingbo	305040	40.79%	7.03%	0.00	Kelu Group	305020	45.15%	5.77%	0.01			
Jocotitlán	341062	9.28%	18.71%	0.00	Kelut	263280	1.83%	49.65%	0.00			
Jolo	270010	7.59%	69.76%	0.00	Kembar	261810	9.99%	49.37%	0.00			
Jordan Craters	322190	26.86%	5.77%	0.00	Kendang	263110	2.11%	52.74%	0.00			
Jumaytepeque	342121	1.55%	24.33%	0.00	Kerguelen Islands	234020	22.64%	77.36%	0.09			
Kaba	261220	5.49%	68.64%	0.00	Kerinci	261170	7.59%	83.26%	0.00			
Kadovar	251002	0.42%	91.56%	0.00	Ketoi	290200	90.44%	9.56%	0.04			
Kagamil	311260	73.00%	26.86%	0.00	Khangar	300272	77.07%	10.55%	0.75			
Kaguyak	312250	80.87%	8.86%	0.01	Khanuy Gol	303020	41.35%	4.36%	0.12			
Kaikohe-Bay of Islands	241010	35.02%	15.47%	0.00	Kharimkotan	290300	85.37%	14.63%	0.06			
Kaileney	300620	87.06%	10.97%	0.83	Khaybar, Harrat	231060	0.28%	2.25%	0.00			
Kalatungan	271061	6.47%	74.82%	0.00	Khodutka	300053	77.36%	9.70%	0.22			
Kambalny	300010	88.47%	7.45%	0.29	Kalagvik	312120	95.08%	4.92%	0.15			
Kamen	300251	97.47%	2.53%	1.00	Kkai	282060	12.66%	85.94%	0.00			
Kamjjang, Kawah	263805	2.11%	51.62%	0.00	Kikhpinych	300180	80.87%	9.70%	0.26			
Kanaga	311110	76.37%	23.63%	0.01	Klauea	332010	1.69%	22.50%	0.00			
Kanlaon	272020	4.92%	73.14%	0.00	Klimanjarao	222150	95.78%	2.81%	0.22			
Kao	243061	4.64%	94.37%	0.00	Kinenin	300551	73.70%	9.70%	0.27			
Karaca Dag	213011	36.15%	4.36%	0.00	Kirishimayama	282090	45.01%	19.41%	0.00			
Karang	263020	3.94%	61.04%	0.00	Kisho, Harrat	231071	0.00%	2.39%	0.00			
Karangetang [Api Siau]	267020	7.59%	90.44%	0.00	Kiska	311020	80.73%	19.13%	0.04			
Karapinar Field	213001	11.95%	5.63%	0.00	Kita-loto	284110	1.41%	95.92%	0.00			
Karisimbi	223040	15.89%	71.03%	0.00	Kizinen	300230	79.18%	12.10%	0.67			
Karkar	251030	11.53%	75.81%	0.00	Klabat	266120	8.16%	59.92%	0.00			
Karpinsky Group	290350	79.04%	12.38%	0.10	Kliuchevskoi	300260	97.47%	2.53%	1.00			
Kars Plateau	213050	36.01%	6.61%	0.00	Kogaja-Jima	282041	0.70%	94.80%	0.00			
Karthala	233010	10.13%	32.21%	0.00	Kolokol Group	290120	74.68%	24.33%	0.05			
Karymsky	300130	76.09%	10.83%	0.27	Komarov	300220	86.92%	9.42%	0.87			
Kasatochi	311130	42.62%	57.38%	0.00	Kone	221200	0.42%	13.78%	0.00			

**Table 4.4 - Continued**

Name	VOTW Number	MDL wks.	icy	MDL undet.	PZL mean	Name	VOTW Number	MDL wks.	icy	MDL undet.	PZL mean	MDL RGL	RGL	PZL
Koniujii	311140	30.80%	69.20%	0.00		Kuwae	257070	1.83%	97.19%	0.00				
Kookooligit Mountains	314050	63.99%	26.16%	0.71		Kverkfjöll	373050	81.86%	18.14%	0.47				
Koranga	253003	4.22%	48.95%	0.00		Kyatwa	223002	2.39%	25.32%	0.00				
Korath Range	221320	0.84%	12.66%	0.00		Kyejo	222170	5.91%	37.27%	0.00				
Koro	245020	6.33%	92.12%	0.00		La Palma	383010	12.80%	30.52%	0.00				
Korosí	222054	0.84%	4.64%	0.00		Labo	273804	6.05%	72.86%	0.00				
Korovin	311161	88.75%	11.25%	0.08		Laguna Caldera	273080	2.53%	31.36%	0.00				
Koryaksky	300090	96.91%	3.09%	0.91		Lasas, Las	344133	1.55%	47.96%	0.00				
Kos	212805	31.93%	31.79%	0.00		Lamington	253010	9.70%	71.45%	0.00				
Koshelev	300020	88.47%	8.02%	0.23		Lamongan	263320	0.84%	42.19%	0.00				
Kostakan	300122	75.25%	8.72%	0.23		Langjila	252010	7.59%	76.23%	0.00				
Koussi, Emi	225021	0.28%	2.67%	0.00		Langn	357122	94.37%	5.63%	0.17				
Kozushima	284030	34.88%	64.28%	0.00		Lanzarote	383060	2.25%	3.52%	0.00				
Kozyrevsky	300330	76.65%	11.53%	0.86		Larderello	211001	37.41%	6.33%	0.00				
Krafra	373080	55.13%	32.07%	0.01		Lásscar	355100	50.07%	2.25%	0.12				
Krainy	300400	74.26%	10.41%	0.72		Lassen Volcanic Center	323080	75.39%	2.11%	0.01				
Krakatau	262000	2.25%	95.50%	0.00		Lastaria	355120	52.46%	2.25%	0.21				
Krasheninnikov	300190	81.58%	8.16%	0.51		Late	243090	3.80%	93.39%	0.00				
Krísvík	371030	52.32%	27.29%	0.00		Latukan	271050	6.61%	67.51%	0.00				
Kronotsky	300200	97.05%	2.95%	0.82		Lautaio	358060	89.59%	10.41%	0.20				
Ksudach	300050	82.84%	9.42%	0.07		Lavic Lake	323190	0.98%	3.09%	0.00				
Kuchinoerabujima	282050	27.99%	71.03%	0.00		Lawu	263260	3.94%	63.99%	0.00				
Kuchinoshima	282043	11.95%	87.48%	0.00		Leizhou Banda	275010	1.55%	54.01%	0.00				
Kueishantao	281031	0.14%	94.80%	0.00		Lengai, Ol Doinyo	222120	0.98%	12.52%	0.00				
Kujusan	282120	34.18%	19.13%	0.00		Leonard Range	271031	4.08%	61.32%	0.00				
Kukak	312230	97.05%	2.95%	0.42		Leroboleng	264200	2.95%	36.01%	0.00				
Kula	213000	11.81%	5.63%	0.00		Leskov Island	390120	28.13%	71.87%	0.00				
Kulkev	300370	73.28%	8.72%	0.29		Leutongey	300530	73.56%	11.81%	0.59				
Kunlun Volcanic Group	304030	96.62%	3.38%	0.99		Level Mountain	320050	78.62%	10.41%	0.51				
Kumtomintar	290808	82.28%	17.72%	0.02		Lewotobi	264180	2.81%	47.40%	0.00				
Kunyit	261171	4.92%	68.92%	0.00		Lewotolo	264230	2.39%	78.48%	0.00				
Kupreanof	312060	96.20%	3.80%	0.23		Liaod Hayk	221172	0.98%	3.80%	0.00				
Kurikomayama	283210	57.67%	23.35%	0.00		Liamuiga	360030	4.92%	66.67%	0.00				
Kurile Lake	300023	89.73%	5.49%	0.00		Licancabur	355092	61.32%	2.25%	0.16				
Kurub	221120	0.28%	6.05%	0.00		Lictio	352081	5.34%	55.56%	0.00				
Kusatsu-Shiranesan	283120	60.34%	16.88%	0.00		Lihir	254010	4.92%	93.53%	0.00				
Kussharo	285080	60.06%	10.55%	0.00		Lipari	211042	34.04%	53.45%	0.00				
Kuttara	285034	64.28%	13.36%	0.00		Little Sitkin	311050	74.54%	25.46%	0.02				
Kutum Volcanic Field	225040	0.00%	2.95%	0.00		Ljósufjöll	370030	54.01%	26.44%	0.00				

**Table 4.4 - Continued**

Name	VOTW Number	MDL wks.	icy	MDL undet.	PZL mean	Name	VOTW Number	MDL wks.	icy	MDL undet.	PZL mean	MDL	RGL	PZL
Llaima	357110	90.58%	7.31%	0.06		Mallahé	221102	1.97%	3.52%	0.00				
Llullaillaco	355110	89.59%	2.25%	0.55		Mal y Payalpan	300290	76.93%	9.85%	0.75				
Lokon-Empung	266100	8.58%	61.04%	0.00		Mal y Semiacik	300140	77.92%	9.14%	0.25				
Lolo	252071	4.92%	91.28%	0.00		Mammoth Mountain	323150	69.62%	2.11%	0.01				
Lolobau	252130	5.34%	92.97%	0.00		Managliase Plateau	253021	5.20%	56.40%	0.00				
Lotoru	255030	9.42%	73.98%	0.00		Manam	251020	7.31%	91.00%	0.00				
Long Island	251050	5.63%	66.10%	0.00		Manda Gorgori	221127	0.28%	5.91%	0.00				
Long Valley	323822	44.59%	2.53%	0.00		Manda Hararo	221115	0.56%	4.92%	0.00				
Longaví, Nevado de	357063	83.54%	3.23%	0.01		Manda-Inakir	221122	0.14%	3.66%	0.00				
Longgang Group	305050	57.38%	9.56%	0.00		Mandalagan	272203	4.50%	78.06%	0.00				
Longonot	222100	0.14%	10.27%	0.00		Manengouba	224020	5.20%	60.48%	0.00				
Longquimay	357100	75.39%	5.34%	0.01		Manuk	265080	0.00%	2.53%	0.00				
Lopevi	257050	2.95%	96.91%	0.00		Manzaz Volcanic Field	225006	0.14%	2.11%	0.00				
Lower Chindwin	275090	0.14%	49.09%	0.00		Marapí	261140	6.47%	82.42%	0.00				
Lubukraya	261111	4.50%	74.54%	0.00		Marchena	353080	0.28%	97.33%	0.00				
Lumut Balai, Bukit	261240	6.75%	59.63%	0.00		Mare	268062	1.13%	95.08%	0.00				
Lunayir, Harrat	231040	0.56%	2.25%	0.00		Marha, Jabal el-	231100	0.28%	2.67%	0.00				
Lurus	263321	0.56%	73.00%	0.00		Marináqui, Laguna	357092	64.56%	2.95%	0.00				
Ma Alalta	221111	1.13%	3.66%	0.00		Marion Island	234070	35.86%	63.15%	0.01				
Macá	358056	87.62%	12.38%	0.07		Mariveles	273081	2.11%	54.57%	0.00				
Macauley Island	242021	0.00%	100.00%	0.00		Markagunt Plateau	327040	59.35%	3.66%	0.00				
Machin	351040	7.74%	84.25%	0.00		Maroa	241061	61.04%	7.74%	0.00				
Madeira	382120	36.57%	25.18%	0.00		Marra, Jebel	225030	0.98%	11.25%	0.00				
Maderas	344130	2.67%	68.78%	0.00		Marsabit	222021	1.55%	18.42%	0.00				
Madilogo	253004	3.94%	37.55%	0.00		Martin	312140	96.77%	3.23%	0.39				
Mageik	312150	97.19%	2.81%	0.47		Maruyama	285061	73.84%	11.39%	0.04				
Mahagnao	272070	5.34%	71.45%	0.00		Masaraga	273031	7.17%	63.15%	0.00				
Mahawu	266110	5.91%	63.71%	0.00		Masaya	344100	0.70%	58.23%	0.00				
Maipo	357021	97.61%	2.25%	0.28		Mascota Volcanic Field	341031	3.09%	11.67%	0.00				
Makaturing	271040	6.19%	75.67%	0.00		Mashkovtsev	30001	70.60%	29.25%	0.00				
Makian	268070	10.13%	86.22%	0.00		Mashu	285081	75.39%	9.28%	0.00				
Makushin	311310	96.91%	3.09%	0.18		Mat Alia	221105	0.00%	8.30%	0.00				
Malabar	263081	1.69%	53.87%	0.00		Matthew Island	258010	0.00%	2.39%	0.00				
Malang Plain	263292	0.98%	51.90%	0.00		Matutum	271020	5.34%	70.89%	0.00				
Malinao	273801	6.33%	67.93%	0.00		Maug Islands	284143	0.14%	83.12%	0.00				
Malinche, La	341091	18.42%	31.50%	0.00		Maule, Laguna del	357061	68.64%	2.25%	0.00				
Malindang	271071	4.50%	77.64%	0.00		Mauna Kea	332030	18.57%	4.36%	0.00				
Malindig	273044	2.53%	91.98%	0.00		Mauna Loa	332020	19.41%	3.38%	0.00				
Malintang	261121	9.14%	65.68%	0.00		Mayon	273030	7.03%	73.14%	0.00				

**Table 4.4 - Continued**

Name	VOTW Number	MDL wks.	icy	MDL wks.	undet.	PZL mean	Name	VOTW Number	MDL wks.	icy	MDL wks.	undet.	PZL mean	MDL RGL	RGL	PZL
Mayor Island	241021	43.74%	53.16%	0.00			Mono Craters	323120	44.73%	3.09%	0.00					
Mayotte Island	233005	7.03%	59.92%	0.00			Mono Lake Volcanic Field	323110	35.58%	2.95%	0.00					
McDonald Islands	234011	0.00%	2.39%	0.00			Montagu Island	390081	50.91%	49.09%	1.00					
Meager	320180	96.91%	3.09%	0.13			Morning, Mount	390017	57.10%	42.90%	0.00					
Medicine Lake	323020	73.00%	2.39%	0.00			Moti	268063	3.66%	92.97%	0.00					
Mega Basalt Field	221330	0.56%	6.75%	0.00			Mottav	257001	6.61%	92.55%	0.00					
Megata	283262	58.51%	41.21%	0.00			Mousa Ali	221123	0.42%	3.66%	0.00					
Mehetia	333040	0.70%	81.43%	0.00			Moutohora Island	241815	13.78%	71.59%	0.00					
Meidob Volcanic Field	225050	0.42%	2.95%	0.00			Moyorodake [Medvezhia]	290100	82.98%	9.99%	0.01					
Melbourne	390015	62.73%	37.27%	0.00			Moyuta	342130	1.69%	28.41%	0.00					
Melimoyu	358052	89.45%	10.55%	0.06			Muhavura	223060	10.27%	68.92%	0.00					
Menengai	222060	0.14%	5.49%	0.00			Mundua	252021	0.84%	98.17%	0.00					
Mentolat	358054	77.78%	19.97%	0.00			Muria	263251	2.81%	52.18%	0.00					
Merapi	263250	1.83%	57.67%	0.00			Musuan	271070	0.84%	56.68%	0.00					
Merbabu	263240	2.53%	60.62%	0.00			Mutnovsky	3000060	90.44%	6.75%	0.53					
Mere Lava	257021	2.81%	97.05%	0.00			Mutsu-Hiuchi-dake	283892	72.43%	19.41%	0.00					
Meru	222160	7.88%	60.62%	0.00			Myokosan	283100	67.09%	19.41%	0.00					
Methana	212020	27.43%	48.24%	0.00			Nabro	221101	2.67%	3.80%	0.00					
Meulín	358064	84.25%	12.94%	0.00			Nabukelevu	245030	4.92%	92.55%	0.00					
Mezhdusopochny	300570	79.18%	12.24%	0.78			Nakanoshima	282040	21.66%	77.07%	0.00					
Michael	390090	64.84%	35.16%	1.00			Namarunu	222040	0.56%	10.97%	0.00					
Michoacán-Guanajuato	341060	1.55%	9.99%	0.00			Nantai	283141	65.12%	18.28%	0.00					
Midagahara	283080	74.54%	9.99%	0.01			Nablinco Volcanic Field	341095	1.97%	28.27%	0.00					
Middle Gobi	303050	17.02%	10.83%	0.00			Narage	252801	0.00%	95.64%	0.00					
Mikurajima	284041	40.08%	59.35%	0.00			Narcondum	260001	1.27%	84.25%	0.00					
Milbanke Sound Group	320120	81.86%	15.75%	0.00			Naruko	283200	55.98%	16.17%	0.00					
Milne	290161	85.23%	14.63%	0.10			Nasudake	283150	52.46%	25.18%	0.00					
Milos	212030	12.10%	53.59%	0.00			Natib	273082	3.94%	45.43%	0.00					
Minchinmávida	358040	82.14%	17.86%	0.06			Nazko	320140	80.45%	4.64%	0.01					
Miriñiques	355102	53.59%	2.25%	0.16			Negrilla, Sierra	353050	0.14%	85.65%	0.00					
Miravalles	345030	4.36%	77.07%	0.00			Negrillar, El	355106	3.09%	2.25%	0.00					
Misti, El	354010	29.40%	7.59%	0.15			Negrillar, La	355108	9.56%	2.25%	0.00					
Miyakejima	284040	33.78%	65.12%	0.00			Negro de Mayasquer, Cerro	351110	5.63%	75.67%	0.00					
Mocho-Choshuenco	357130	86.78%	12.38%	0.01			Negro, Cerro	344070	0.70%	42.48%	0.00					
Moekeshiwan [Lvinaya Past]	290041	79.18%	20.82%	0.00			Nejapa-Miraflores	344092	0.84%	64.28%	0.00					
Moffett	311111	82.42%	17.58%	0.01			Nemo Peak	290320	81.29%	18.71%	0.02					
Mojanda	352005	2.95%	80.03%	0.00			Nemrut Dagi	213020	59.63%	2.81%	0.00					
Mombacho	344110	2.67%	48.95%	0.00			Nevada, Sierra	355123	91.42%	2.25%	0.70					
Momotombo	344090	1.69%	31.36%	0.00			Nevis Peak	360040	3.80%	26.72%	0.00					

**Table 4.4 - Continued**

Name	VOTW Number	MDL wks.	icy	MDL undet.	PZL mean	Name	VOTW Number	MDL wks.	icy	MDL undet.	PZL mean	MDL	RGL	PZL
Newberry	322110	75.53%	3.38%	0.00		Olkokwe	222055	3.23%	6.61%	0.00				
Newer Volcanics Province	259010	21.94%	7.74%	0.00		Olcá-Paruma	355050	24.05%	2.39%	0.06				
Ngaoundere Plateau	224040	1.55%	25.60%	0.00		Olkaria	222090	0.56%	9.99%	0.00				
Ngozi	222164	9.14%	25.18%	0.00		Olkoviy Volcanic Group	300052	69.62%	10.83%	0.01				
Nichoison, Cerro	354008	0.14%	2.81%	0.00		Ollagüe	355060	42.90%	2.53%	0.12				
Nightingale Island	386011	30.38%	69.06%	0.00		Olot Volcanic Field	210030	42.19%	5.06%	0.00				
Nigorikawa	285805	63.43%	12.38%	0.00		Omanago Group	283142	64.98%	21.10%	0.00				
Niigata-Yakeyama	283090	65.96%	18.00%	0.00		Onikobe	283879	56.82%	16.88%	0.00				
Nijima	284020	35.16%	64.28%	0.00		Ontakesan	283040	69.62%	16.32%	0.03				
Nikko-Shiranesan	283140	67.65%	13.78%	0.00		Opala	300080	82.56%	10.41%	0.35				
Nilia	265060	1.41%	93.53%	0.00		Öraefajökull	374010	83.97%	16.03%	0.62				
Niseko	285031	63.43%	16.46%	0.00		Orizaba, Pico de Orosí	341100	84.25%	11.67%	0.06				
Nishihitokapuyama [Bogatyr]	1290060	72.57%	12.94%	0.07		Orosí	345010	3.52%	75.39%	0.00				
Nishinoshima	284096	0.00%	2.53%	0.00		Oshima-Oshima	285010	31.22%	68.50%	0.00				
Nisyros	212050	18.71%	47.68%	0.00		Osorezan	283290	68.07%	12.52%	0.00				
Niuafou'ou	243110	7.03%	90.15%	0.00		Osorno	358010	93.11%	6.75%	0.08				
Niuafo'ou	243140	0.00%	1.83%	0.00		Ostanets	300055	70.04%	12.52%	0.01				
Nonda	255803	9.56%	74.40%	0.00		Ostry	300680	95.92%	4.08%	0.99				
Norikuradake	283060	73.28%	12.10%	0.01		Otdelniy	300056	69.90%	12.66%	0.01				
North Island	222001	3.09%	9.56%	0.00		Overo, Cerro	355097	47.26%	2.39%	0.01				
North Vate	257081	4.22%	92.12%	0.00		Ozernoy	300051	70.46%	11.25%	0.01				
Nosy-Be	233012	1.83%	71.17%	0.00		Pacaya	342110	1.13%	41.91%	0.00				
Novarupta	312180	83.97%	15.19%	0.16		Paco	271090	4.78%	56.40%	0.00				
Nuevo Mundo	355036	57.95%	3.23%	0.02		Pagan	284170	2.39%	93.81%	0.00				
Numazawa	283151	56.40%	11.67%	0.00		Paka	222053	0.70%	5.63%	0.00				
Nunivak Island	314020	72.01%	16.88%	0.10		Palena Volcanic Group	358051	85.79%	14.21%	0.00				
Nyambeni Hills	222056	4.78%	23.49%	0.00		Pali-Aike Volcanic Field	358080	18.85%	17.44%	0.00				
Nyamuragira	223020	12.10%	67.09%	0.00		Palomo	357022	96.91%	3.09%	0.28				
Nyiragongo	223030	16.88%	71.59%	0.00		Paluweh	264150	1.41%	77.78%	0.00				
Nylgimelkin	300650	95.64%	4.36%	0.88		Pampa Luxsar	355042	2.67%	3.52%	0.01				
O'a Caldera	221280	0.56%	8.44%	0.00		Panarea	211041	9.85%	67.79%	0.00				
Odamoisan [Tebenkov]	290072	73.14%	12.52%	0.01		Panay	273806	0.84%	96.20%	0.00				
Otu-Olosega	244010	3.80%	94.09%	0.00		Pantelleria	211071	24.05%	44.30%	0.00				
Ojos del Salado, Nevados	355130	96.20%	2.39%	0.92		Pantigio, Cerro	357152	63.15%	15.33%	0.00				
Oka Plateau	302060	83.97%	5.77%	0.96		Papandayan	263100	1.69%	53.16%	0.00				
Okataina	241050	59.49%	8.02%	0.00		Papayo	341081	10.83%	24.61%	0.00				
Oki-Dogo	283003	50.35%	47.40%	0.00		Parinacota	355012	95.92%	2.39%	0.12				
Okmok	311290	73.84%	25.32%	0.00		Parker	271011	7.88%	70.75%	0.00				
Oku Volcanic Field	224030	4.22%	41.63%	0.00		Patah	261231	6.89%	66.81%	0.00				

**Table 4.4 - Continued**

Name	VOTW Number	MDL wks.	icy	MDL undet.	PZL mean	Name	VOTW Number	MDL wks.	icy	MDL undet.	PZL mean	MDL RGL	RGL	PZL
Patoc	273087	2.11%	25.04%	0.00		Prieto, Cerro	341000	5.34%	5.34%	0.00				
Patuha	263070	2.81%	52.18%	0.00		Primavera, Sierra la	341820	0.84%	17.58%	0.00				
Paulet	390041	10.27%	22.36%	0.00		Prince Edward Island	234060	83.26%	16.74%	0.00				
Pavlof	312030	96.91%	3.09%	0.30		Puesto Cortaderas	357073	7.03%	4.92%	0.00				
Pavlof Sister	312040	96.34%	3.52%	0.20		Pular	355107	72.43%	2.25%	0.33				
Payún Matru	357066	62.45%	2.81%	0.02		Pulau Weh	261800	4.78%	94.51%	0.00				
Peinado	355200	32.21%	2.25%	0.10		Pulosari	263010	2.25%	54.29%	0.00				
Pelée	360120	10.13%	54.99%	0.00		Pulito, Punta	341804	0.70%	57.52%	0.00				
Penanggungan	263291	0.84%	51.90%	0.00		Pululagua	352011	2.25%	19.83%	0.00				
Pendan	261191	9.28%	46.98%	0.00		Puntiagudo-Cordón Cenizos	357160	81.01%	11.25%	0.00				
Pengchiahsu	281805	0.84%	92.69%	0.00		Puracé	351060	8.30%	78.90%	0.00				
Penguin Island	390031	82.14%	17.30%	0.00		Puríco Complex	355094	43.74%	2.25%	0.04				
Perbaiki-Gagak	263040	2.67%	59.49%	0.00		Putana	355090	60.06%	2.39%	0.15				
Peracás	351062	10.13%	83.12%	0.00		Puyehue-Cordón Caulle	357150	74.68%	15.19%	0.00				
Peter I Island	390029	0.00%	100.00%	0.00		Puyuhuapi	358053	84.53%	12.24%	0.00				
Peuet Sague	261030	7.45%	65.26%	0.00		Qaleh Hasan Ali	232020	7.88%	2.39%	0.00				
Pico	382020	48.52%	38.68%	0.00		Qualibou	360140	6.33%	86.64%	0.00				
Picos Volcanic System	382081	24.33%	52.60%	0.00		Quetrupillan	357121	89.03%	9.00%	0.00				
Pilas, Las	344080	0.70%	42.48%	0.00		Quetzaltepeque	342210	0.84%	28.69%	0.00				
Pinacate	341001	2.25%	2.11%	0.00		Quill, The	360020	1.55%	91.56%	0.00				
Pinatubo	273083	2.25%	50.07%	0.00		Quillotao	352060	1.55%	50.63%	0.00				
Pinta	353070	0.14%	97.75%	0.00		Quimsachata	354000	2.53%	15.89%	0.00				
Piratkovsky	300054	75.81%	10.41%	0.10		Rabaul	252140	4.08%	95.78%	0.00				
Planchón-Peteroa	357040	97.47%	2.53%	0.07		Ragang	271060	9.56%	61.88%	0.00				
Plat Pays, Morne	360110	8.30%	86.08%	0.00		Rahah, Harrat ar	231010	0.84%	2.53%	0.00				
Platanar	345034	2.53%	78.76%	0.00		Rahat, Harrat	231070	0.70%	2.25%	0.00				
Pleiades, The	390013	65.40%	34.32%	0.00		Raikeke	290250	57.24%	42.76%	0.01				
Plosky	300310	78.90%	7.17%	0.22		Rainier	321030	97.75%	2.25%	0.47				
Plosky	300630	76.37%	11.39%	0.56		Raiabasa	261290	5.91%	87.90%	0.00				
Poás	345040	6.05%	73.70%	0.00		Rakkibetsudake [Demon]	290110	87.06%	8.58%	0.02				
Pocdol Mountains	273020	6.75%	69.34%	0.00		Ranakah	264071	0.84%	39.24%	0.00				
Poco Leok	264070	2.25%	45.85%	0.00		Ranau	261251	5.49%	50.21%	0.00				
Pogranichny	300470	77.22%	11.25%	0.72		Raoul Island	242030	33.90%	65.54%	0.00				
Popa	275080	1.83%	45.85%	0.00		Rasshua	290220	85.37%	14.63%	0.00				
Popocatepetl	341090	49.23%	30.94%	0.02		Raung	263340	3.94%	53.45%	0.00				
Porak	214090	72.29%	4.50%	0.01		Rausudake	285082	73.00%	10.83%	0.05				
Possession, Ile de la	234040	63.71%	36.01%	0.00		Raususan [Mendeleev]	290020	75.11%	10.13%	0.00				
Prestahnukur	371070	82.84%	17.16%	0.11		Recheschnoi	311280	96.06%	3.94%	0.10				
Prevo Peak	290190	89.03%	10.97%	0.09		Reclus	358063	72.57%	27.43%	0.17				

**Table 4.4 - Continued**

Name	VOTW Number	MDL wks.	icy	MDL undet.	PZL mean	Name	VOTW Number	MDL wks.	icy	MDL undet.	PZL mean	MDL	RGL	PZL
Redoubt	313030	96.77%	3.23%	0.70		San Félix	356010	0.00%	1.97%	0.00	0.00			
Reporoa	241060	27.71%	12.24%	0.00		San Francisco Volcanic Field	329020	76.51%	5.06%	0.02	0.02			
Resago	357065	61.04%	2.81%	0.00		San Joaquín	224003	4.36%	89.59%	0.00	0.00			
Reventador	352010	5.34%	93.67%	0.00		San Jorge	382030	47.40%	50.35%	0.00	0.00			
Reykjanes	371020	47.12%	24.05%	0.00		San José	357020	97.47%	2.53%	0.76	0.76			
Rincón de la Vieja	345020	2.39%	84.67%	0.00		San Luis, Isla	341003	0.84%	60.76%	0.00	0.00			
Rinjani	264030	1.83%	53.87%	0.00		San Martín	341110	3.66%	48.52%	0.00	0.00			
Río Murta	358058	92.97%	7.03%	0.01		San Miguel	343100	1.27%	31.36%	0.00	0.00			
Risco Plateado	357024	97.33%	2.11%	0.26		San Pablo Volcanic Field	273060	3.09%	69.20%	0.00	0.00			
Rishirizan	285041	74.26%	13.78%	0.04		San Pedro	355070	56.26%	2.25%	0.24	0.24			
Ritter Island	251070	0.00%	2.39%	0.00		San Pedro-Pellado	357062	87.20%	2.39%	0.03	0.03			
Rittmann, Mount	390812	65.40%	34.32%	0.00		San Quintín Volcanic Field	341002	1.83%	86.50%	0.00	0.00			
Robinson Crusoe	356020	27.71%	72.15%	0.00		San Salvador	343050	1.27%	28.83%	0.00	0.00			
Romanovka	300340	76.65%	9.14%	0.56		San Vicente	343070	0.98%	31.36%	0.00	0.00			
Romeral	351011	2.81%	86.78%	0.00		Sanbesan	283002	46.13%	13.22%	0.00	0.00			
Rota	344060	0.28%	41.63%	0.00		Sand Mountain Field	322040	69.90%	3.66%	0.00	0.00			
Rotorua	241816	52.32%	7.03%	0.00		Sanford	315010	91.70%	8.30%	1.00	1.00			
Roundtop	311380	96.77%	3.23%	0.13		Sangangüey	341024	3.38%	13.22%	0.00	0.00			
Royal Society Range	390021	56.96%	43.04%	0.00		Sangay	352090	58.51%	40.79%	0.01	0.01			
Ruang	267010	3.66%	94.09%	0.00		Sangeang Api	264050	4.50%	51.76%	0.00	0.00			
Ruapehu	241100	95.36%	2.81%	0.01		Sano, Wai	264060	3.38%	36.15%	0.00	0.00			
Rucharuyama [Golets-Torriy]	C290091	70.60%	29.40%	0.00		Santa Ana	343020	1.41%	37.97%	0.00	0.00			
Rudakov	290112	73.98%	25.88%	0.00		Santa Cruz	353091	0.42%	80.73%	0.00	0.00			
Ruiz, Nevado del	351020	90.01%	9.99%	0.04		Santa Fe	353804	0.28%	98.31%	0.00	0.00			
Rungwe	222166	12.80%	40.37%	0.00		Santa Isabel	351021	42.48%	50.63%	0.01	0.01			
Ruruidake [Smirnov]	290021	78.34%	19.97%	0.02		Santa Isabel	224004	7.59%	86.22%	0.00	0.00			
Saba	360010	0.14%	92.69%	0.00		Santa María	342030	2.81%	52.88%	0.00	0.00			
Sabalán	232002	66.95%	4.78%	0.11		Santiago	353090	0.42%	83.54%	0.00	0.00			
Sabancaya	354006	93.39%	2.53%	0.25		Santiago, Cerro	342150	0.42%	21.52%	0.00	0.00			
Sahand	232001	63.85%	3.09%	0.01		Santo Tomás	273086	1.83%	47.68%	0.00	0.00			
Sairecabur	355091	53.02%	2.25%	0.20		Santo Tomás	342800	5.63%	59.21%	0.00	0.00			
Sakar	251080	2.81%	96.62%	0.00		Santorini	212040	4.64%	65.68%	0.00	0.00			
Salak	263050	1.83%	65.12%	0.00		Sao Tome	224001	2.95%	91.84%	0.00	0.00			
Salton Buttes	323200	8.58%	4.50%	0.00		Sao Vicente	384030	0.00%	61.74%	0.00	0.00			
San Borja Volcanic Field	341007	0.98%	2.25%	0.00		Sara Sara	354002	68.07%	5.63%	0.06	0.06			
San Carlos	224002	2.53%	91.98%	0.00		Satigan	284192	0.56%	83.83%	0.00	0.00			
San Cristóbal	344020	0.84%	30.66%	0.00		Satik-Gajah	261131	4.08%	57.67%	0.00	0.00			
San Cristóbal	353120	0.84%	82.98%	0.00		Satychev Peak	290240	75.95%	23.91%	0.09	0.09			
San Diego	343001	1.13%	15.05%	0.00		Sashiusudake [Baransky]	290080	73.98%	10.69%	0.01	0.01			

**Table 4.4 - Continued**

Name	VOTW Number	MDL wks.	icy	MDL undet.	PZL mean	Name	VOTW Number	MDL wks.	icy	MDL undet.	PZL mean	MDL RGL	RGL	PZL
Satah Mountain	320130	78.06%	6.47%	0.03		Silverthrone	320160	95.64%	4.36%	0.07				
Savai'i	244040	14.49%	33.19%	0.00		Simbo	255050	1.97%	97.05%	0.00				
Savo	255070	3.38%	93.95%	0.00		Snabung	261080	3.52%	70.46%	0.00				
Sawâd, Harrâ es-	231160	0.28%	2.81%	0.00		Sinarka	290290	88.33%	11.67%	0.03				
Schmidt	300201	83.40%	7.88%	0.69		Singu Plateau	275100	0.00%	41.91%	0.00				
Seal Nunataks Group	390050	0.00%	12.52%	0.00		Singüil, Cerro	343002	0.56%	24.75%	0.00				
Sedankinsky	300520	73.84%	11.67%	0.73		Sirung	390025	64.70%	34.88%	0.00				
Segererua Plateau	222050	9.98%	10.27%	0.00		Slamet	263180	2.95%	70.60%	0.00				
Seguan	311180	82.42%	17.02%	0.01		Snaefellsjökull	370010	81.29%	18.71%	0.10				
Segula	311030	76.23%	23.77%	0.01		Snegovoy	300690	96.91%	3.09%	0.95				
Sekincau Belirang	261260	2.39%	57.67%	0.00		Snezhnyi	300660	96.48%	3.52%	0.94				
Semeru	263300	2.95%	71.59%	0.00		Snowy Mountain	312200	97.61%	2.39%	0.48				
Semisopochnoi	311060	65.26%	34.32%	0.01		Socche	352001	4.22%	90.44%	0.00				
Sempu	266040	6.19%	75.53%	0.00		Socompa	355109	50.91%	2.25%	0.25				
Serdán-Oriental	341092	1.27%	12.80%	0.00		Socorro	341021	2.81%	71.87%	0.00				
Sergief	311150	62.17%	37.83%	0.00		Soda Lakes	326010	7.45%	5.06%	0.00				
Serua	265070	0.56%	94.80%	0.00		Sodore	221222	0.70%	7.88%	0.00				
Sessagara	253031	3.09%	32.77%	0.00		Sofugan	284091	0.00%	2.53%	0.00				
Seite Cidades	382080	43.18%	52.74%	0.00		Sollipulli	357111	91.42%	8.02%	0.00				
Seulawah Agam	261020	5.63%	73.70%	0.00		Solo, El	355131	73.14%	4.22%	0.67				
Severny	300700	89.59%	8.86%	0.92		Soputan	266030	6.05%	74.40%	0.00				
Sharat Kovakab	230010	2.11%	7.74%	0.00		Sorikmarapi	261120	4.78%	69.76%	0.00				
Shasta	323010	97.75%	2.11%	0.24		Sork Ale	221103	0.70%	4.64%	0.00				
Shiga	283121	61.32%	15.75%	0.00		Sorárá	351061	9.14%	84.25%	0.00				
Shikaribetsu Group	285062	76.79%	10.69%	0.01		Soufrière Guadeloupe	360060	8.02%	68.50%	0.00				
Shikotsu	285040	64.84%	13.78%	0.00		Soufrière Hills	360050	2.11%	87.20%	0.00				
Shiretoko-Iozan	285090	77.64%	20.68%	0.05		Soufrière St. Vincent	360150	8.44%	88.47%	0.00				
Shirinki	290331	66.81%	33.19%	0.02		South Island	222020	0.70%	29.68%	0.00				
Shishaldin	311360	98.03%	1.97%	0.36		Spectrum Range	320070	96.91%	3.09%	0.63				
Shisheika	300511	66.81%	8.86%	0.06		Spokointy	300671	95.36%	4.64%	0.96				
Shishel	300580	95.36%	4.64%	0.96		Spurr	313040	97.75%	2.25%	0.99				
Shiveluch	300270	95.92%	4.08%	0.93		St. Andrew Strait	250010	5.20%	94.09%	0.00				
Shoshone Lava Field	324010	30.24%	3.52%	0.00		St. Catherine	360170	7.45%	59.63%	0.00				
Sibayak	261070	3.09%	79.89%	0.00		St. Helens	321050	78.76%	4.78%	0.04				
Sibualbuali	261110	4.50%	74.12%	0.00		St. Michael	314040	59.49%	19.55%	0.26				
Sikhote-Alin	302010	70.18%	6.75%	0.08		St. Paul	234002	14.77%	84.81%	0.00				
Sili	222052	0.56%	5.06%	0.00		St. Paul Island	314010	69.62%	29.82%	0.00				
Silay	272040	4.22%	80.45%	0.00		Steamboat Springs	326801	37.69%	3.38%	0.00				
Silver Lake	323050	61.88%	2.95%	0.00										

**Table 4.4 - Continued**

Name	vOTW Number	MDL wks.	icy MDL undet.	PZL mean	Name	vOTW Number	MDL wks.	icy MDL undet.	PZL mean	MDL RGL	RGL	PZL
Steller	312220	97.47%	2.53%	0.52	Tambo Quemado	355021	0.84%	5.06%	0.00			
Stepovak Bay 2	312051	93.11%	6.89%	0.10	Tambora	264040	0.56%	45.15%	0.00			
Stepovak Bay 3	312052	95.50%	4.50%	0.14	Tampomas	263131	2.39%	48.66%	0.00			
Stepovak Bay 4	312053	96.77%	3.23%	0.15	Tana	311241	82.98%	17.02%	0.01			
Stromboli	211040	24.05%	63.43%	0.00	Tanaga	311080	92.97%	7.03%	0.15			
Sturge Island	390012	73.14%	26.30%	0.00	Tandikat	261150	5.63%	75.39%	0.00			
Suchitán	342160	0.28%	27.57%	0.00	Tanga	254801	2.95%	96.77%	0.00			
Sukaria Caldera	264120	2.11%	37.69%	0.00	Tangkubanparahu	263090	2.67%	64.28%	0.00			
Sulu Range	252090	3.80%	87.76%	0.00	Tao-Rusyr Caldera	290310	88.05%	10.69%	0.04			
Sumaco	352040	11.53%	87.20%	0.00	Tara, Batu	264260	0.14%	87.34%	0.00			
Sumbing	261180	8.72%	69.90%	0.00	Tarakan	268001	7.17%	83.83%	0.00			
Sumbing	263220	1.68%	61.46%	0.00	Taranaki [Egmont]	241030	84.53%	7.88%	0.01			
Sundoro	263210	1.41%	61.04%	0.00	Taryatu-Chulutu	303010	65.96%	4.64%	0.52			
Suoh	261170	2.95%	42.33%	0.00	Tat Ali	221106	0.42%	6.05%	0.00			
Súphan Dagi	213021	75.25%	2.67%	0.20	Tata, Sabaya	355032	7.59%	5.20%	0.01			
Suretamatai	257010	8.72%	67.93%	0.00	Tatun Group	281032	6.19%	55.13%	0.00			
Suswa	222110	0.14%	13.92%	0.00	Taunshits	300160	84.39%	7.74%	0.69			
Swanoseijima	282030	12.10%	87.62%	0.00	Taupo	241070	45.99%	5.63%	0.00			
SW Usanggu Basin	222163	0.56%	9.00%	0.00	Taveuni	245010	96.34%	3.66%	0.01			
Ta'u	244001	7.03%	89.17%	0.00	Tavui	252150	0.70%	94.37%	0.00			
Taal	273070	3.23%	45.15%	0.00	Tecapa	343080	1.69%	33.47%	0.00			
Taapaca	355011	56.96%	3.80%	0.08	Tecuamburro	342120	1.97%	29.54%	0.00			
Taburete	343072	1.97%	36.57%	0.00	Felicia	344040	0.98%	32.07%	0.00			
Tacaná	341130	10.69%	52.74%	0.00	Telomoyo	263231	1.41%	51.62%	0.00			
Tacora	355010	66.53%	3.38%	0.08	Tei Long, Bur ni	261050	2.95%	66.81%	0.00			
Tafahi	243101	1.69%	91.28%	0.00	Tenchozan	285083	71.73%	11.25%	0.04			
Taftan	232050	25.60%	2.67%	0.00	Tendüreke Dagi	213030	70.04%	4.22%	0.05			
Tahalra Volcanic Field	225004	0.00%	2.11%	0.00	Tenerife	383030	30.80%	3.80%	0.00			
Tahual	342141	0.98%	31.79%	0.00	Tengchong	275110	23.35%	36.71%	0.00			
Tair, Jepel at	221010	0.28%	67.65%	0.00	Tengger Caldera	263310	1.13%	50.91%	0.00			
Taisetsuzan	285060	74.12%	16.17%	0.22	Tenorio	345031	3.80%	80.87%	0.00			
Tajumulco	342020	3.38%	48.95%	0.00	Teon	265050	1.13%	89.17%	0.00			
Takaharatayama	283143	51.34%	21.38%	0.00	Tepi	221292	24.47%	47.26%	0.00			
Takahe	390027	61.04%	38.96%	0.00	Terceira	382050	42.33%	35.16%	0.00			
Takawangha	311090	95.78%	4.22%	0.13	Terpuuk	300512	71.17%	9.14%	0.26			
Takuan Group	255021	10.27%	73.00%	0.00	Theistareykjartbunga	373090	54.43%	30.24%	0.01			
Talagabodas	263150	2.53%	60.48%	0.00	Three Sisters	322070	86.92%	2.53%	0.06			
Talakmau	261130	6.47%	78.90%	0.00	Thule Islands	390070	69.62%	30.38%	1.00			
Talang	261160	5.77%	74.96%	0.00	Tianshan Volcanic Group	304020	96.06%	3.52%	0.39			

**Table 4.4 - Continued**

Name	VOTW Number	MDL wks.	icy	MDL undet.	PZL mean	Name	VOTW Number	MDL wks.	icy	MDL undet.	PZL mean	MDL RGL	RGL	PZL
Ticsani	354031	32.77%	3.94%	0.02		Toussidé, Tarso	225010	0.14%	2.67%	0.00				
Tidore	268061	4.78%	93.11%	0.00		Towada	283271	67.37%	13.92%	0.00				
Tigalalu	268071	7.17%	90.15%	0.00		Toya	285030	61.60%	11.81%	0.00				
Tigre, El	343082	1.41%	30.52%	0.00		Traitor's Head	257090	8.02%	91.00%	0.00				
Tigre, Isla el	343130	0.98%	77.36%	0.00		Tralihue	357101	65.40%	5.49%	0.01				
Tilocalar	355105	1.13%	2.25%	0.00		Tres Virgenes	341010	3.23%	2.95%	0.00				
Tin Zaouatene Volcanic Field	225002	0.00%	2.39%	0.00		Tri Sestry	290113	70.04%	27.99%	0.01				
Tinkakula	256010	2.11%	96.77%	0.00		Trident	312160	87.48%	12.52%	0.29				
Tindfjallajökull	372040	81.43%	18.57%	0.05		Trindade	385051	0.84%	93.67%	0.00				
Tinguiririca	357030	97.47%	2.53%	0.24		Tristan da Cunha	386010	64.98%	34.88%	0.00				
Tipas	355220	94.51%	2.39%	0.95		Trois Pitons, Morne Trois Pitons	360100	12.10%	65.26%	0.00				
Titia	300560	74.12%	12.80%	0.76		Troton	357081	53.16%	6.47%	0.00				
Tlevak Strait-Suemez Is.	315060	84.11%	14.63%	0.00		Tromen	357072	88.61%	3.52%	0.13				
Toba	261090	4.78%	66.39%	0.00		Tronador	358011	95.50%	4.50%	0.16				
Tobaru	268020	9.56%	47.82%	0.00		Tseax River Cone	320100	89.45%	6.75%	0.02				
Todoko-Ranu	268050	9.42%	68.21%	0.00		Tshibinda	223080	10.83%	43.32%	0.00				
Todra Volcanic Field	225001	0.14%	2.39%	0.00		Tskhouk-Karckar	214100	69.90%	4.36%	0.03				
Tofua	243060	8.30%	90.86%	0.00		Tujile, Cerro	355103	4.22%	2.39%	0.00				
Tōh, Tarso	225009	0.14%	2.53%	0.00		Tullu Moje	221250	0.70%	24.05%	0.00				
Tokachidake	285050	73.28%	15.19%	0.10		Tungnafellsjökull	373040	82.42%	17.58%	0.18				
Tolbachik	300240	97.19%	2.81%	0.99		Tungurahua	352080	18.28%	74.40%	0.01				
Tolguaca	357093	91.84%	5.06%	0.01		Tunkin Depression	302050	84.25%	6.33%	0.74				
Tollima, Nevado del	351030	52.32%	45.15%	0.01		Tupungatito	357010	97.19%	2.81%	0.86				
Tollmán	342070	5.34%	44.30%	0.00		Turfan	304010	2.81%	10.27%	0.00				
Tolmachev Dol	300082	78.34%	9.42%	0.12		Turrialba	345070	7.31%	81.86%	0.00				
Toluca, Nevado de	341070	12.66%	42.62%	0.00		Tutuila	244020	10.27%	88.33%	0.00				
Tomariyama [Golovnin]	290010	66.95%	18.71%	0.00		Tutupaca	354040	70.75%	3.80%	0.05				
Tombel Graben	224011	2.39%	74.82%	0.00		Tuya Volcanic Field	320031	86.08%	6.75%	0.47				
Tondano Caldera	266070	6.61%	48.95%	0.00		Tuzgle	355150	15.61%	2.81%	0.06				
Toney Mountain	390026	60.90%	38.82%	0.00		Tuzovsky	300540	74.96%	11.11%	0.77				
Tongariro	241080	58.51%	11.53%	0.00		Ubehebe Craters	323160	0.42%	2.39%	0.00				
Tongkoko	266130	9.99%	82.00%	0.00		Ubinales	354020	37.55%	5.34%	0.05				
Tor Zawar	232080	16.32%	2.95%	0.00		Udina	300241	90.30%	6.75%	0.87				
Tore	255000	3.66%	77.22%	0.00		Udkan Plateau	302030	77.50%	9.00%	0.99				
Torfajökull	372050	72.15%	27.43%	0.01		Ugashlik-Peulik	312130	86.64%	9.99%	0.10				
Toroeng Prong	275030	4.08%	43.04%	0.00		Unkarlet Field	329010	36.99%	3.94%	0.00				
Tortuga, Isla	341011	0.56%	69.90%	0.00		Uka	300610	84.39%	10.83%	0.75				
Tosa Sucha	221310	4.22%	15.61%	0.00		Ukinrek Maars	312131	78.20%	11.81%	0.00				
Toshima	284011	22.50%	74.96%	0.00		Uksichan	300350	73.56%	11.67%	0.78				

**Table 4.4 - Continued**

Name	VOTW Number	MDL wks.	icy	MDL undet.	PZL	MDL RGL PZL	Name	VOTW Number	MDL wks.	icy	MDL undet.	PZL	MDL RGL PZL
Ujawun	252120	10.13%	72.15%	0.00			Veer	300121	73.28%	7.74%	0.10		
Uliaga	311250	63.29%	36.71%	0.00			Veniaminof	312070	96.34%	3.66%	0.69		
Ulreung	306030	60.76%	37.13%	0.00			Verkhovoy	300440	73.98%	11.67%	0.70		
Umboi	251060	8.02%	66.95%	0.00			Vernadskii Ridge	290370	77.07%	16.46%	0.11		
Umm Arafeb, Jebel	225070	0.00%	2.67%	0.00			Vestmannayjar	372010	64.56%	35.44%	0.00		
Ungaran	263230	2.11%	47.68%	0.00			Vesuvius	211020	43.18%	5.63%	0.00		
Unnamed	300085	78.06%	21.24%	0.00			Victory	253030	7.74%	74.68%	0.00		
Unnamed	300420	76.65%	8.86%	0.45			Viedma	358061	8.30%	91.70%	0.01		
Unnamed	300086	74.12%	6.75%	0.01			Villarica	357120	84.25%	15.75%	0.05		
Unnamed	300232	71.73%	8.02%	0.03			Vilyuchik	300083	87.20%	7.03%	0.24		
Unnamed	300081	71.45%	12.52%	0.06			Visoke	223050	10.41%	72.71%	0.00		
Unnamed	312132	65.54%	17.44%	0.01			Visokiy	300059	74.68%	9.42%	0.10		
Unnamed	390014	64.98%	34.60%	0.00			Vitim Plateau	302040	59.21%	6.47%	0.62		
Unnamed	214050	52.74%	5.91%	0.01			Volcano W	242001	0.00%	100.00%	0.00		
Unnamed	355161	20.68%	2.25%	0.03			Voon, Tarso	225020	0.14%	2.39%	0.00		
Unnamed	232000	19.41%	7.17%	0.00			Voyarnopolsky	300720	75.81%	10.69%	0.72		
Unnamed	230020	5.06%	6.33%	0.00			Vsevidof	311270	96.48%	3.52%	0.15		
Unnamed	230040	2.81%	3.66%	0.00			Vulcano	211050	30.10%	54.01%	0.00		
Unnamed	257080	1.83%	96.62%	0.00			Vulsini	211003	25.32%	5.49%	0.00		
Unnamed	221311	1.69%	30.80%	0.00			Wysoky	300221	84.11%	10.69%	0.80		
Unnamed	222162	1.27%	12.66%	0.00			Waesche	390024	58.93%	40.51%	0.00		
Unnamed	221221	1.27%	20.39%	0.00			Waiowa	253040	2.95%	80.03%	0.00		
Unnamed	221201	0.98%	9.56%	0.00			Wallis Islands	244050	8.86%	83.97%	0.00		
Unnamed	232040	0.84%	2.39%	0.00			Wapi Lava Field	324030	31.08%	3.38%	0.00		
Unnamed	221251	0.70%	7.45%	0.00			Washiba-Kumonotaira	283071	75.53%	7.74%	0.01		
Unnamed	285061	0.00%	2.11%	0.00			Watt, Morne	360101	7.88%	72.71%	0.00		
Unnamed	252001	0.00%	2.39%	0.00			Wau-en-Namus	225008	0.00%	2.39%	0.00		
Unzendake	282100	47.68%	17.02%	0.00			Wayang-Windu	263080	1.69%	45.01%	0.00		
Upolu	244030	11.25%	52.32%	0.00			Wells Gray-Clearwater	320150	87.90%	6.33%	0.10		
Urataman	290191	89.17%	10.83%	0.01			West Crater	321060	71.31%	7.59%	0.00		
Ushishur	290210	59.63%	40.23%	0.00			West Eifel Volcanic Field	210010	48.24%	17.44%	0.00		
Ushkovsky	300261	97.19%	2.81%	1.00			Westdahl	311340	95.64%	4.36%	0.17		
Usulután	343081	1.83%	34.74%	0.00			Whangarei	241011	41.77%	20.11%	0.00		
Utila Island	343160	2.67%	91.84%	0.00			White Island	241040	1.69%	87.90%	0.00		
Uturuncu	355838	56.26%	2.39%	0.07			Willis	263270	2.39%	59.35%	0.00		
Uzon	300170	78.34%	6.33%	0.25			Witori	252080	7.59%	56.26%	0.00		
Vakak Group	232070	38.40%	2.67%	0.00			Wolf	353020	0.28%	63.71%	0.00		
Valle, El	346030	4.36%	57.81%	0.00			Wrangell	315020	92.69%	7.31%	1.00		
Valles Caldera	327817	70.18%	4.92%	0.01			Wudalianchi	305030	48.66%	7.88%	0.00		

**Table 4.4 - Continued**

Name	VOTV Number	MDL wks.	icy	MDL undet.	PZL	MDL mean	RGL	PZL
Wuriali	265040	4.50%	88.89%	0.00				
Xianjindao	306010	47.54%	7.03%	0.00				
Yakedake	283070	66.67%	10.97%	0.00				
Yali	212051	3.66%	59.35%	0.00				
Yangudi	221151	0.28%	3.52%	0.00				
Yantarni	312100	88.33%	11.67%	0.07				
Yanteles	358049	84.53%	15.47%	0.01				
Yar, Jada!	231080	0.28%	9.28%	0.00				
Yasur	257100	5.63%	70.60%	0.00				
Yate	358022	89.87%	10.13%	0.00				
Yavinsky	300021	72.71%	13.50%	0.01				
Yeguadada, La	346801	1.83%	60.76%	0.00				
Yelia	253002	15.33%	49.37%	0.00				
Yellowstone	3225010	75.81%	3.38%	0.01				
Yohoia, Lake	343150	0.98%	21.52%	0.00				
Yokoate-iima	282021	0.98%	96.06%	0.00				
Yokodake	283031	60.06%	11.53%	0.00				
Yomba	251041	0.00%	2.39%	0.00				
Yonemaru-Sumiyoshiike	282081	39.24%	15.61%	0.00				
Yoteizan	285032	71.31%	12.80%	0.05				
Young Island	390011	74.54%	25.18%	0.00				
Yucamane	354050	27.00%	4.36%	0.04				
Yufu-Tsurumi	282130	39.38%	20.53%	0.00				
Yunaska	311210	70.75%	27.57%	0.00				
Zacate Grande, Isla	343140	0.98%	77.50%	0.00				
Zaozan	283190	59.07%	19.13%	0.00				
Zaozerny	300480	73.98%	11.53%	0.54				
Zapatera	344111	2.39%	19.97%	0.00				
Zavaritsky	300124	79.89%	7.88%	0.39				
Zavaritzki Caldera	290180	63.99%	35.86%	0.01				
Zayodovski	390130	55.13%	44.87%	1.00				
Zealandia Bank	284191	0.00%	2.53%	0.00				
Zhellovsky	300040	82.14%	9.56%	0.22				
Zhupanovsky	300120	95.78%	4.08%	0.70				
Zimina	300242	96.06%	3.94%	0.96				
Zitácuaro-Valle de Bravo	341061	20.68%	30.94%	0.00				
Zubair Group	221020	0.14%	79.32%	0.00				
Zukur	221021	0.28%	61.60%	0.00				
Zuni-Bandera	327120	18.99%	3.38%	0.00				

# **CHAPTER 5. TOPOGRAPHIC SIGNATURES OF SUBNIVEAN DEGASSING RESULTING FROM GROWTH OF FUMAROLIC ICE CAVES OBSERVED AT EREBUS VOLCANO, ANTARCTICA**

## **5.1 Abstract**

We mapped Warren Cave, an extensive fumarolic ice cave, annually between 2009 and 2014. The geometry of the cave changed significantly from year to year. Four of the maps were derived from high-resolution laser scans and were co-registered for detailed comparison. The domed chamber above gas vent 6 (GV6) enlarged about  $100\text{m}^3$  each year. In 2011, 2012, and 2013, we obtained laser scans of the ground surface above the cave and observed a pattern of subsidence of 0.5 to 0.7 m  $\text{yr}^{-1}$ , with the highest rates of subsidence directly above GV6 chamber.

We also obtained measurements to constrain heat transfer and deformation processes in the cave wall ice. A temperature transect measured into the cave wall revealed a linear temperature drop of  $0.06\text{ C m}^{-1}$ , and density measurements showed that the ice is between 0.78 and 0.9  $\text{0g cm}^{-3}$ . We estimated heat flux from gas vents similar to GV6 and incorporated relevant data into a computational fluid dynamics “toy model” of one GV6 chamber melting scenario consistent with the observations.

## **5.2 Introduction**

Fumarolic ice caves (FICs) are diagnostic of degassing at subnivean volcanoes. At these volcanoes, basal melting of ice overburden provides an early indicator of volcanic unrest. Loss of ice from above Redoubt volcano preceding the 2009 eruption was apparent before any other eruption precursors [Bleick *et al.*, 2013]. At Redoubt, ice loss was reported in the form of subsidence cauldrons, newly exposed rock, “holes in the snow” emitting steam, and a jökulaup. Bleick considered the role of water-filled cavities in the ice mass, but did not discuss the air-filled cavities (FICs) which must also have existed. I posit that FICs are an important thermal and mechanical component of these systems.

When human entry to an FIC can be obtained, observations of passage size and morphology may provide information about the magnitude of and trends in the volcanic heat flux. *Kiver* [1978] estimated an increase of 20% in the passage cross-sectional area in response to a period of unrest at Mt. Baker during 1975. Subsidence cauldrons similar to those reported at Redoubt formed above the FIC at Baker. These cauldrons provide a topographic signature that can be observed using terrestrial, airborne or satellite-borne altimetry techniques and represents the underlying FIC and ultimately the underlying heat flux.

Kiver's FIC morphology observations did not include a description of methods used, and have yet to be replicated. We set out to do so over a longer time period using state-of-the art methods on Erebus, the world's southernmost active volcano. Erebus provides an exceptional variety of geothermal features. The Erebus Cave and Fumarole Database lists over 100 caves, distributed throughout the summit caldera [*Curtis*, 2010].

Initial work on one of the Erebus caves (Upper Hut Cave) suggested that caves were formed by heat conduction from areas of warm rock [*Giggenbach*, 1976]. However, the majority of Erebus caves appear to be composed mainly of large domed rooms, with an obvious fumarolic vent in the floor, roughly beneath the apex of the dome. *Curtis and Kyle* [2011] demonstrated that along with cold vents in the cave roof which carry ambient air into the cave, these fumarolic warm gas vents, as opposed to conduction from warm rock, dominate the cave thermal regime in one Erebus FIC (Warren Cave).

We obtained 6 years of morphological data, along with physical and thermal data necessary to build models, from Warren Cave, a FIC on Erebus Volcano. Modern terrestrial laser scanning (TLS) techniques enabled 3D imaging of the FIC system, and the overlying subsidence cauldron, with centimeter-scale precision and accuracy. Additionally, computational fluid dynamics (CFD) techniques and a simple ice creep model based on Glen's flow law [*Glen*, 1958] allow simulation of the processes by which fumarolic warm gas vent emissions cause FIC growth, and, in turn, cauldron subsidence.

### 5.3 Habitability properties and microbial communities

While the present paper investigates the Erebus FICs from a volcano-ice interaction standpoint and a goal of eruption prediction, our findings also have implications that relate to the microbiology and geochemistry of the caves. Recent work identified fungal and bacterial extremophile communities in the Erebus FICs. The FICs provide an extremely oligotrophic habitat; sediment in Warren Cave was measured at 126 µg/g total organic carbon, roughly 10 times less nutrient-rich than the sand of the Atacama [*Tebo et al.*, 2015]. Metabolic processes of the microbes in this environment are of great interest for the study of life on Earth and elsewhere in the universe [*Cousins and Crawford*, 2011]. Photoautotrophy and chemoautotrophy have been observed, with some of the autotrophs fixing carbon using a unique variant of the RubisCO protein [*Tebo et al.*, 2015]. Although the bacterial genetic sequences observed appear to represent pristine native flora, analysis of fungal sequences with recombinant elements of cereals indicate human contamination in at least one cave [*Connell and Staudigel*, 2013]. The thermal and physical measurements and analysis reported here address questions which provide

important contexts for understanding the FIC habitats and inhabitants. In particular, we address questions regarding the stability and longevity of cave passages, and the FIC air and ice temperature regimes.

## 5.4 Observations

### 5.4.1 Cave morphology and growth

#### Methods

We recorded the shape and size of Warren Cave in great detail each Austral Winter from 2009 to 2014 (Table 5.1). In 2009, we produced a cave map using techniques that qualify as a UISv1 grade 5-4 survey [Häuselmann, 2011]. We used a DistoX combined rangefinder / compass / clinometer [Redovniković *et al.*, 2014] but discarded the compass data because backsights showed that the measurements were unreliable, most likely due to ferromagnetic mineral content in the cave rock. Instead, we used a surveyor's transit to record horizontal angle data.

From 2010 to 2013, to obtain dense three-dimensional cave data, we conducted terrestrial laser scan (TLS) surveys of Warren Cave. TLS has recently become a well-established geodetic technique for volcanology on Erebus [Jones *et al.*, 2015]. The scanner and survey control methods varied from one year to the next and are detailed in Table 5.1. The dataset from each year consists of between 10 and 50 individual scans. For the years in which we collected data with Riegl scanners, initial alignments were completed in RiScan Pro and improved using the iterative closest points (ICP) algorithm in InnovMetrics IMAAlign [Besl and McKay, 1992; InnovMetric, inc., 2010]. Results are shown in Figure 5.1.

	<b>Instrument</b>	<b>Survey Control</b>	<b>Cauldron data</b>	<b>Primary personnel</b>	<b>Scans</b>
2009	DistoX, Transit	Cave rock only	No	AC, NP	N/A
2010	VZ-400	DGPS x4	No	AC, MO	22
2011	VZ-400	DGPS x4	Yes	MO, DK	27
2012	Leica Scanstation C60	DGPS x4	Yes	JF, DK	36
2013	VZ-400	DGPS x4	Yes	AC, BH	18
2014	Sony A6000 digital camera	Cave rock only	No	AC, NP	N/A

**Table 5.1:** Summary of cave morphology data. AC: Aaron Curtis, NP: Nial Peters, MO: Marianne Okal, DK: Drea Killingsworth, JF: Jed Frechette, BH: Brendan Hodge

Four differential GPS positions were obtained above the cave as part of the cauldron geometry observations to provide georeferencing of the cave 3D model. The cave entrance is georeferenced with centimeter-scale accuracy, but errors accumulate towards the end of the cave. Because of our focus on interannual change, we elected to georeference the 2012 survey using GPS, and register the other annual scans by identifying reliably immobile areas of cave floor lava rock and completing manually assisted “cloud to cloud” registration using the object\_alignment python plugin for the open-source 3D modeling package Blender [Moore and Curtis, 2015].

TLS proved effective, but some shortcomings were apparent. Thin films of liquid water on the cave walls and floor resulted in weak laser returns from some surfaces, leading to gaps in the point cloud. Due to frequent meanders in the passage, the line of sight distances achievable were very short, necessitating a scan from a new position roughly every 15m. Warren Cave has low passages and constrictions which barely admit a human, especially near the South end of the cave. The scanner's bulk precluded data collection in many of these areas. In others, it made scanning extremely labor intensive.

In 2014 we pioneered the application of Structure from Motion (SfM) photogrammetry as a replacement for TLS data collection in Warren Cave. SfM replaces the laser scanner with a commodity digital camera, decreasing the monetary value of equipment involved by a factor of about 100. SfM allows modeling smaller spaces with more difficult access, such as the fumarolic vents themselves. Unlike TLS, however, SfM requires illumination of surfaces with visible light, and requires that an image can be taken in sharp focus. SfM relies on feature matching between images taken [Lowe, 2004] from a range of angles to provide parallax data. We were able to produce a 3D model of Warren Cave with density and coverage similar to our TLS models (2014; shown in Figure 5.1c).

SfM did pose a new set of challenges and advantages compared to TLS. Specular reflections from ice crystals caused spurious feature matches and disruption of potential matches in many areas of Warren Cave, leading to gaps in the point cloud and subsequent mesh. As a windfall benefit of SfM, color data could be mapped onto the cave walls from the data collection images. In the resulting dataset, ice is easily distinguishable from rock, and details such as accumulations of tephra on ice surfaces are visible. TLS does not provide this information.

To enable further analysis, we calculated triangular irregular network meshes from the TLS and SfM data, representing the cave walls and floor. We used the Screened Poisson Surface Reconstruction method, as implemented in PoissonRecon [Kazhdan and Hoppe, 2013], to construct the meshes. Poisson Surface Reconstruction output triangle size is a function of input point cloud density. To ignore areas of low point density and extrapolated triangles that do not represent reality, we removed all mesh triangles above a threshold size for each mesh.

## Results

Only the 2009 survey is a complete representation of all human-accessible areas of Warren Cave. Each SfM and TLS dataset omits sections of the cave in which data collection was prohibitively difficult. Change in the extent of the geometry datasets (Figure 5.1) cannot be interpreted as reflecting change in the overall extent of Warren Cave. Instead, the data allows analysis of morphological change in individual passages and chambers.

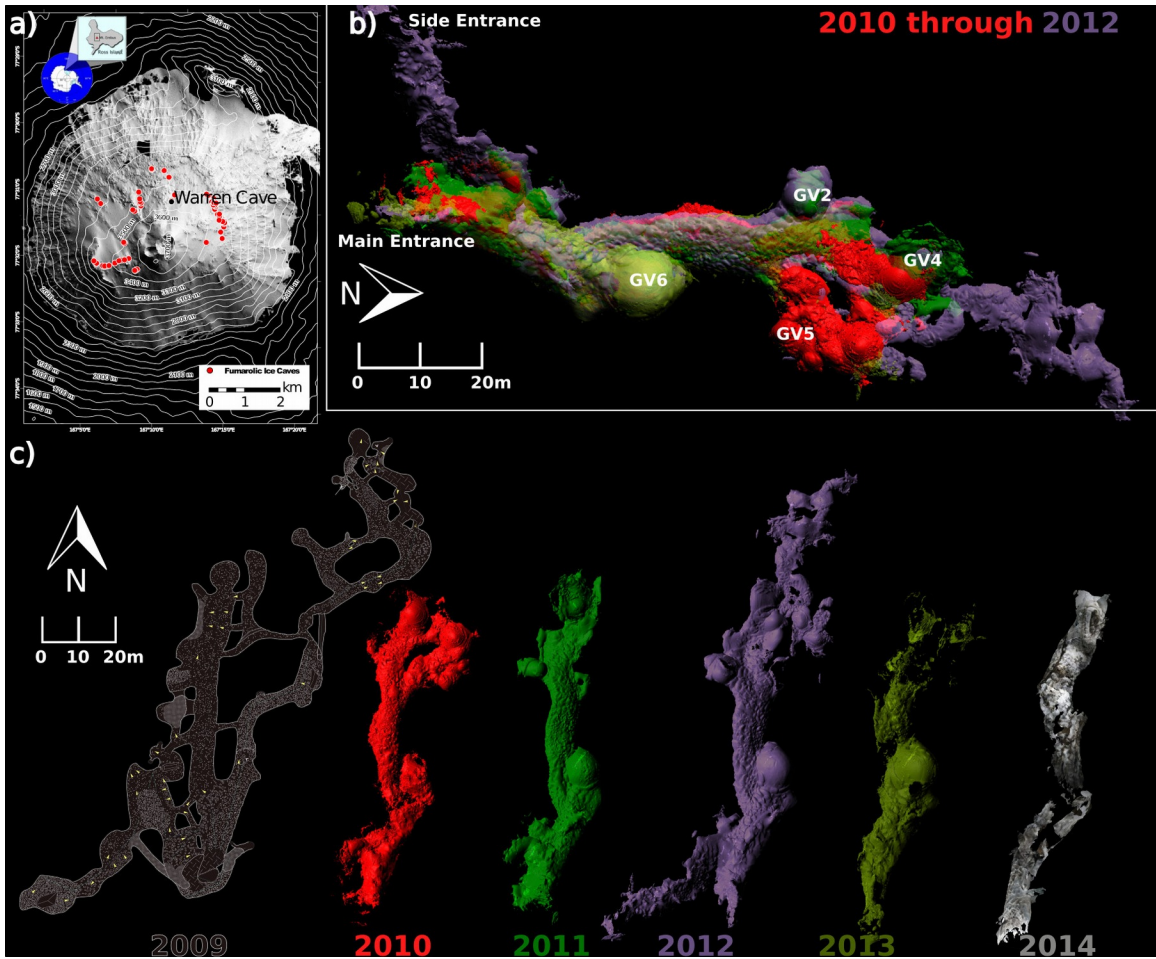


**Figure 5.1:** Warren Cave shown in plan view from above. **a)** Locator map with Erebus summit caldera topography from airborne lidar. **b)** Georeferenced TLS datasets rendered partially transparent. **c)** All geometric data for Warren Cave. Datasets are offset in the E-W direction, but anchored relative to one another in N-S, with the exception of the 2014 SFM data, which is not georeferenced or drawn to scale. Surfaces displayed for 2010-2014 data are reconstructed triangle mesh data representing the cave walls.

The cave area above the fumarole known as GV6 is fully represented in the 2009 through 2013 geometric datasets, and partially represented in the 2014 dataset. We focus on this chamber because of the abundant data and dramatic morphological change there. In the 2009 survey, GV6 was noted as a minor fumarole just north of an icy ledge, which could be climbed over. At some point during 2009, the ledge grew into a wall that closed off the passage north of GV6, forming GV6 chamber.

From 2010 through 2013, GV6 grew into a large dome. Ceiling height increased on the order of  $1\text{m yr}^{-1}$  (Figure 5.2). The dome grew outwards as well as upwards, with a total ice mass loss of around  $100\text{m}^3 \text{yr}^{-1}$  (Table 5.2). In 2014, poor imagery of the dome ceiling precluded computation of geometric data for the GV6 dome.

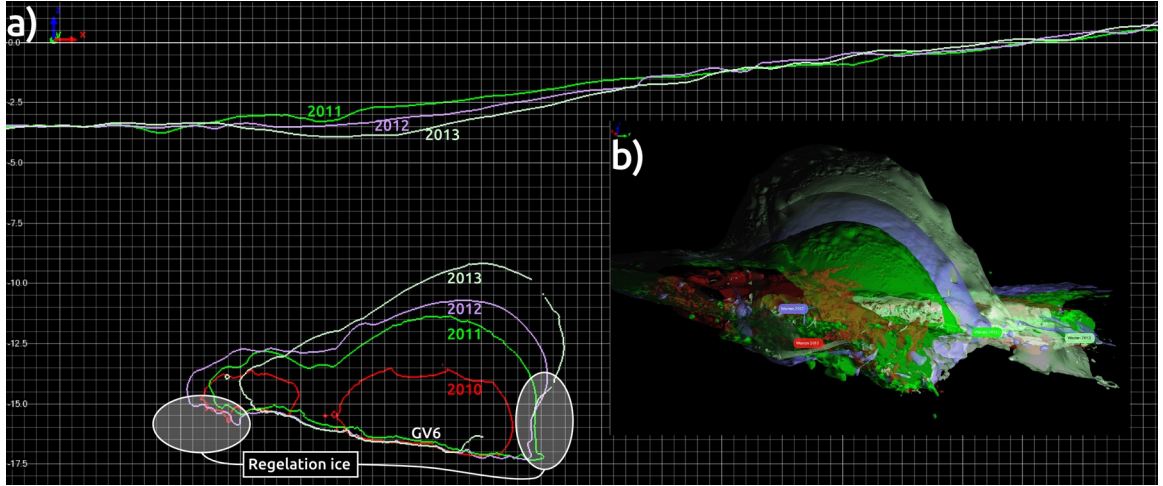


**Figure 5.2:** Subsidence in relation to growth of GV6 chamber. **a)** Cross-section through GV6 Chamber, looking south. **b)** Detail of GV6 chamber triangle meshes, 2010 through 2013, rendered partially transparent with lighting from back right.

2010	136 m <sup>3</sup>
2011	99 m <sup>3</sup>
2012	124 m <sup>3</sup>

**Table 5.2:** Annual volume of GV6 chamber growth

#### 5.4.2 Cauldron morphology and subsidence

##### Methods

In 2010, 2011, and 2012, in addition to conducting TLS inside Warren Cave, we scanned the snow surface above the cave. During these campaigns we also collected DGPS data to provide georeferencing of the entire Warren TLS data suite. Four permanent DGPS sites were established by driving iron rods (rapiforms) into lava flow outcrops which protrude through the snow surrounding the Warren collapse cauldron. We leveled tripods a known distance directly above the end of each rod. Then we occupied each tripod with a DGPS for at least 30 minutes, replaced the antenna with a TLS reflector, and conducted the TLS scans. We aligned the cauldrons and produced triangle meshes following an essentially identical procedure to the cave scans (Section 5.4.1). In InnovMetric IMSurvey, I computed the deviations in the vertical direction of successive pairs of cauldron scan triangle meshes to obtain an image of snow lost or gained each year. I employed the same technique to compare the 2013 triangle mesh to the 2001 airborne lidar survey [Csatho *et al.*, 2008].

In that survey, Csatho *et al.* [2008] delineated four “Small Collapse Features” and one “Large Collapse Feature” on the airborne lidar data obtained in 2001. All five of these features are ice subsidence cauldrons. Although the cauldron above Warren Cave

was not one of the features identified by Csatho et. al (2008), it is clearly present in the raw airborne lidar data provided to us by the authors, and we were able to compare it to TLS scans of the cauldron.

Further topographical data of the Warren Cave cauldron was obtained from stereophotogrammetry computed using Quickbird imagery. However, the data was unusable for cross-annual comparisons due to artifacts probably caused by steam from the cave entrance. Unfortunately, the prevailing southerly wind carries the cave steam over the entire cauldron. Stereophotogrammetry may be an appropriate method for FIC cauldron observation at caves elsewhere, but it was not useful at Warren Cave.

## Results

The resulting images reveal cauldron subsidence of between 0.2 and 0.7m yr<sup>-1</sup> above Warren Cave during 2011 and 2012 (Figure 5.3). Subsidence magnitude is highest above GV6 Chamber, where the snow surface dropped 1.6m (Figure 5.4). During 2010, there was a noticeable loss of snow of around 0.3m yr<sup>-1</sup> in the area outside the subsidence cauldron, with localized deep pits several meters across dropping down as much as 2m. This snow loss likely represents ablation through wind scour or sublimation.

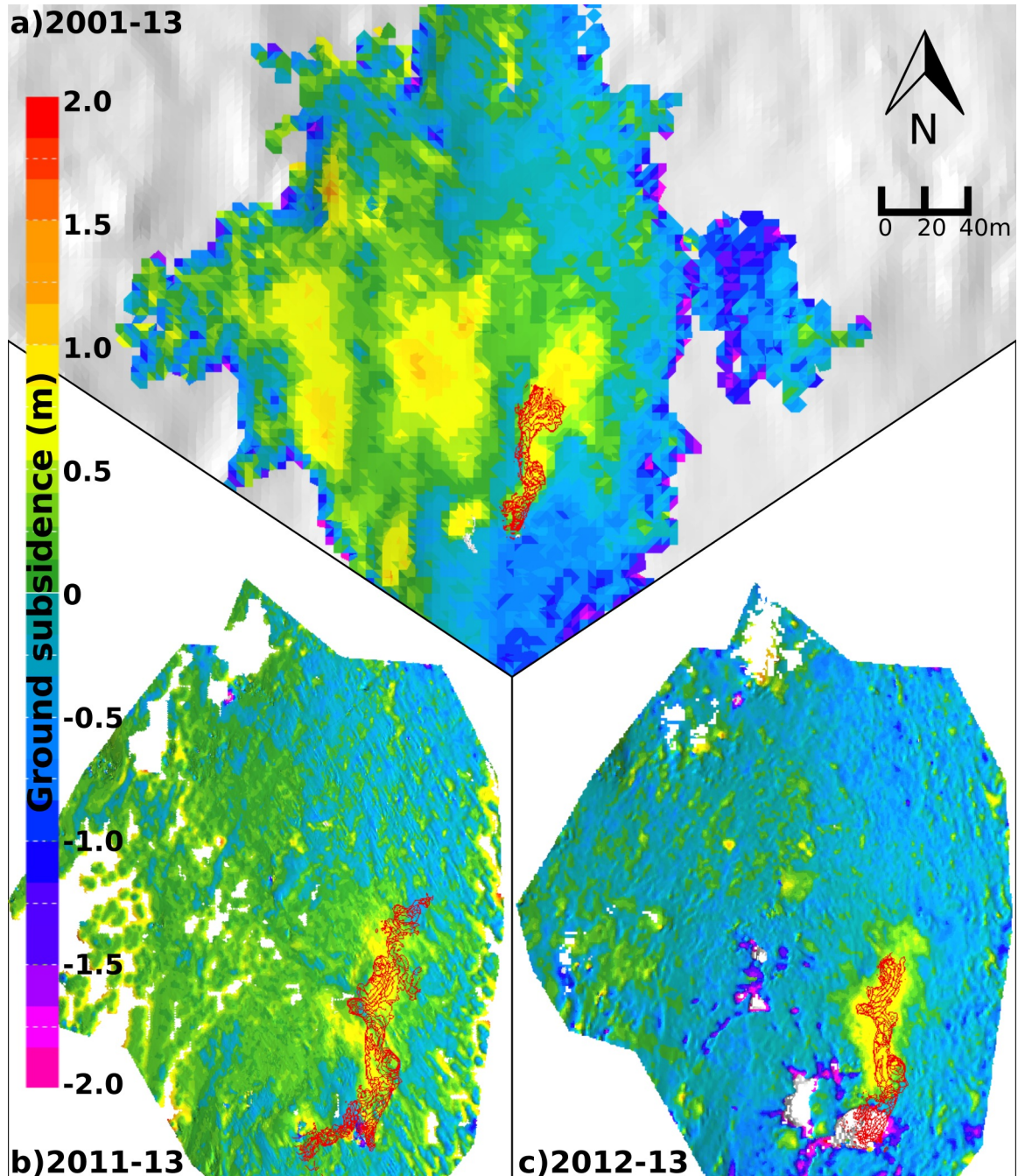


**Figure 5.3:** Various views of ground subsidence above Warren cave computed from TLS (2010-2013) and ALS (2001) scans. **a)** 2013 ground surface mesh colored by elevation difference with 2001 ALS. Contours of 2010 cave data are shown in red. **b)** 2011 ground surface mesh colored by elevation difference with 2013. Contours of 2011 cave data are shown in red. **c)** 2012 ground surface mesh colored by elevation difference with 2013. Contours of cave data are shown in red.

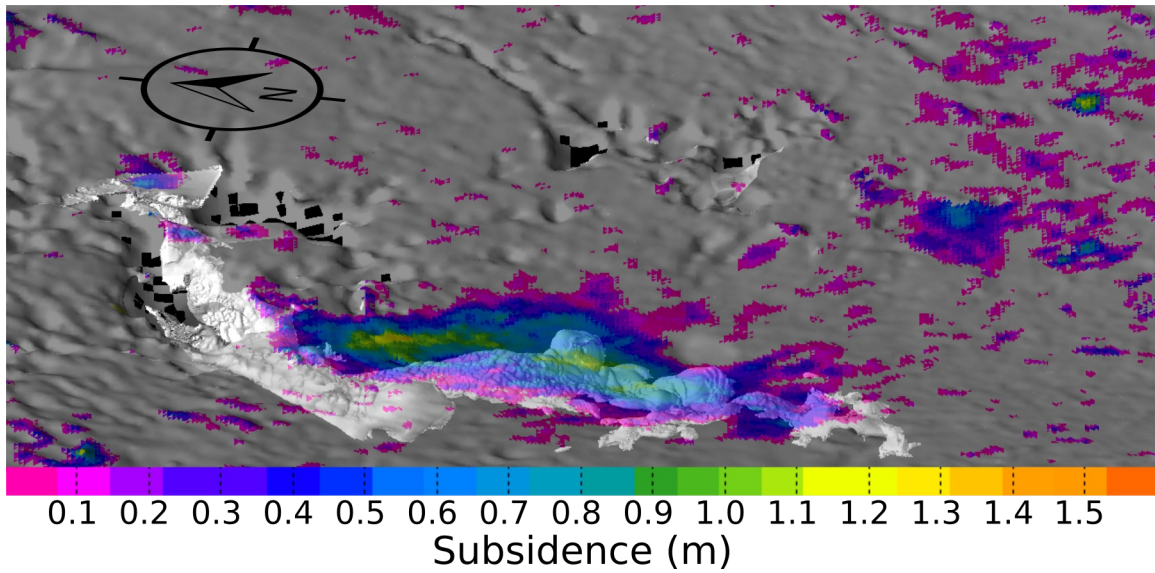


**Figure 5.4:** Oblique view, showing 2011 ground surface mesh colored by elevation difference with 2013. Areas of upward ground change (snow accumulation) are rendered with no hue. The ground is partially transparent and the 2012 cave mesh is visible beneath.

Subsidence in the Warren Cave cauldron is also apparent at the decadal timescale, with a magnitude of up to 1.5m (Figure 5.3b). When comparing the 2001 surface to 2013, at least two more areas of subsidence, elongated parallel to the Warren Cave cauldron, are also evident to the east of Warren Cave. The subsidence feature adjacent to the Warren Cave cauldron appears to be above a known (but unmapped) cave named Chair Cave. There are no known cave entrances near the feature which is the furthest one to the east.

### 5.4.3 Heat flow

#### Methods

We opportunistically made measurements of mass and heat flux from gas vents. Selected observations are shown in Table 5.3. Temperatures and flow rates were measured with a Kestrel 4000 wind meter, and CO<sub>2</sub> concentration with an RAE Systems MultiRAE Lite.

		Temp (C)	Flow (m s <sup>-1</sup> )	Area (m <sup>2</sup> )	Heat flux (kW)	CO <sub>2</sub> (ppm)
Warren V1	8 Dec 2013	1.6	1.02	0.5	0.67	6200
Warren V6	9 Dec 2013	10.6	1.85	1	16.04	15000
Warren V4	12 Dec 2013	17.7	0.87	0.2	2.52	19900
Crevasse Cave	13 Dec 2013	4	10.7	0.1	3.50	1000

**Table 5.3:** Properties of typical Erebus cave fumarole vent emissions and resulting melt.

To investigate heat flux into the cave wall ice, we measured a temperature profile into the wall. The wall temperature also provides important information on thermal dynamics, and determines rheological properties of the ice including viscosity, thus providing boundary conditions for modeling [Stoffel, 2006]. From inside Warren cave, we inserted a rigid thermocouple probe (chromel-alumel, Omega Scentific Type K) into the ice of the cave wall 5cm at a time, waiting for the temperature to equilibrate and recording the measurements at each stop. Ideally we would like to have data far enough into the ice that the temperature reaches the average annual temperature of around -32°C, but the thermocouple used was only 60cm long.

## Results

The resulting temperature profile, shown in Figure 5.5, is linear, as expected for a conduction-dominated volume in a steady state with constant temperature or heat flux boundary conditions. Using Fourier's law, which relates heat flux density  $Q$  to the gradient of the temperature,

$$Q = k \frac{dT}{dx} , \quad (5.1)$$

we can estimate the heat flux into the cave wall. The observed gradient  $dT/dx$  is 0.06°C m<sup>-1</sup> d, and the thermal conductivity of pure ice between 0°C and -3°C is 2.2 W m<sup>-1</sup> K<sup>-1</sup>. Heat flux through this volume is then 12.12 W m<sup>-2</sup>. If this gradient were to remain constant throughout the ice mass, it would reach the average annual temperature of -32°C at 516m distance from the cave wall surface.

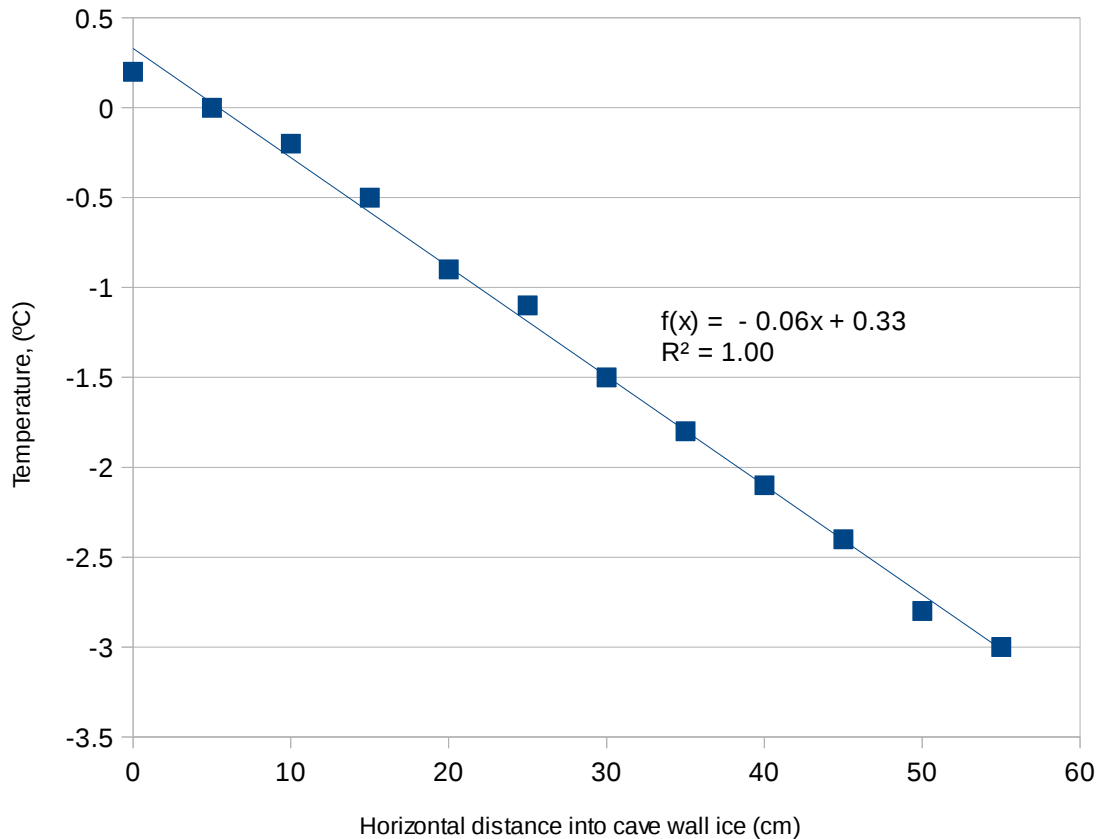


**Figure 5.5:** Warren Cave wall ice temperature profile, measured on January 1<sup>st</sup>, 2012.

#### 5.4.4 Snow Density

##### Methods

The mechanical behavior of ice depends “tremendously” on density [Meussen *et al.*, 1999], as does the thermal behavior. Thus, it is an important initial parameter for our FIC melting model. Ice density is a function of the pressure - temperature history and age of the ice and might provide a proxy for those values. Studying FICs in the summit crater of Mt. St. Helens, Anderson *et al.* [1998] observed progressive snow densification in cave wall ice between 1986 and 1998, with observed densities ranging from 0.55 to 0.85 g cm<sup>-3</sup>. During the May 1980 eruption, all ice in the St. Helens crater was destroyed. Subsequently, firn accumulated in the crater, eventually densifying to form a glacier and circumferential network of FICs. On Erebus, the age of the FICs and the ice that hosts them is unknown, but comparing ice density to St. Helens caves, as well as data from Antarctica in general [Ligtenberg *et al.*, 2011], may provide first-order information regarding the age of the ice.

To measure snow density, we collected samples of cave wall ice with a known volume and then determined their mass. To obtain samples, we inserted 22cm Black Diamond Express ice screws, normal to the ice surface, and collected the cuttings in a 500mL Nalgene bottle. We collected subsamples from nearby (within a 2m radius) until the Nalgene was full. We filled 6 Nalgene bottles, at various locations in Warren Cave selected to encompass the variability of wall ice types. Between 4 and 6 subsamples filled one Nalgene.

I allowed the samples to melt, and then weighed them on a digital balance to obtain net mass  $m_{net}$ . Each sample was then discarded and its Nalgene dried fully and weighed to obtain bottle mass  $m_b$ . I calculated density as

$$d = \frac{m_{net} - m_b}{n * v_s} \quad (5.2)$$

where  $n$  is the number of subsamples collected into the Nalgene  $v_s$  is the subsample volume collected by one ice screw insertion. We assume that all snow displaced by the screw is collected, although we recognize that a small portion of that volume (less than the volume of the thread on the screw) may be accounted for by compression in-place of the ice surrounding the screw. The volume of the working region of the screw, including the hollow area inside, is 46.5cm<sup>3</sup> (Black Diamond, email comm) Two values, DS1 and DS3, were discarded due to a note-taking error leading to uncertainty regarding the volume collected.

## Results

Density results (Table 5.4) indicate that samples are all near or well above the pore close-off density of 0.83 g cm<sup>-3</sup> [van den Broeke, 2008], with the surprising implication that the material surrounding the FIC is not firn, but glacial ice. Glacial ice forms from firn when ice density surpasses the pore close-off depth of 0.83 g cm<sup>-3</sup>. All but one of the measurements in Table 5.4 exceed this threshold, and the lowest density is only 0.04 g cm<sup>-3</sup> short of pore close-off.

	$M_{net}$ (g)	$M_b$ (g)	$d$ (g / cm <sup>3</sup> )	Sample description
DS2	239.9	57.4	0.78	LHW a little past W. Elephant.
DS4	267.4	57.4	0.90	LH wall of entrance slope, above visible contrast line
DS5	263.7	57.2	0.89	Ostrich Hall RH wall
DS6	249.6	56.3	0.83	LH wall of entrance slope, below visible contrast line

**Table 5.4:** Density measurements collected in Warren Cave

### 5.4.5 Melting simulation

Symbol	Description	Units
$\rho$	Density	$\text{kg m}^{-3}$
$C_p$	Heat capacity at constant pressure	$\text{J g}^{-1} \text{K}^{-1}$
$T$	Temperature	K
$t$	Time	s
$\mathbf{Q}$	Conductive heat flux matrix	$\text{W m}^{-2}$
$k$	Thermal conductivity	$\text{W m}^{-1} \text{K}^{-1}$
$\mu$	Dynamic viscosity	$\text{m}^2 \text{s}^{-1}$
$\mathbf{u}$	Fluid velocity matrix	$\text{m s}^{-1}$
$p$	Fluid pressure	Pa
$g$	Acceleration due to gravity	$\text{m s}^{-2}$
$\alpha$	Thermal expansion coefficient	$\text{K}^{-1}$
R	Ideal gas constant	$\text{m}^3 \text{Pa K}^{-1} \text{mol}^{-1}$
$H_{fus}^o$	Specific heat of phase change (liquid / solid)	$\text{J kg}^{-1}$
$T_{lm}$	Lagrange multiplier of temperature field	Dimensionless
$\mathbf{I}$	Identity matrix	None
$T$	Transpose operator	None

**Table 5.5:** Symbols used in melting simulation

### Methods

I created a 2D finite element model that predicts cave ceiling and wall melt rates and geometries for a given thermal input using Comsol Multiphysics 5.0. The model (Figure 5.6) has only two domains: one representing ice and one representing air. Material properties for the ice were primarily literature values, except for density, which I set at the average of the data in Table 5.4. I selected the air material available in the Comsol material library without modification.

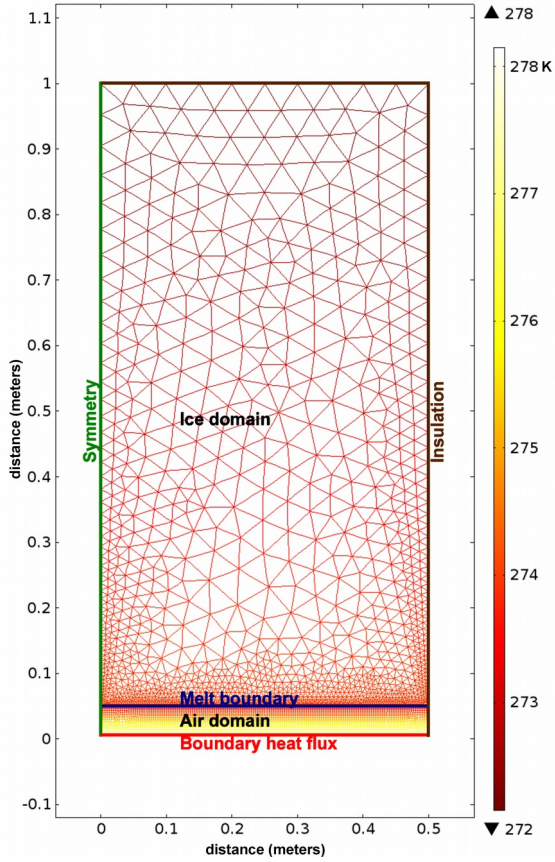


**Figure 5.6:** Initial conditions and mesh for 2D finite element model melting simulation.

To avoid sharp changes in boundary conditions, the boundary heat flux representing the gas vent was smoothed using the following function:

$$50 \times \sin \frac{(x+0.25)\pi}{0.5} + 25 [W\ m^{-1}] \quad (5.3)$$

which integrates to 12W. Equation 5.3 is slightly negative on the right hand side of the domain, which is realistic as the cave floor would be expected to absorb some of the heat from the vent.

I implemented heat transfer within and between the two domains, and airflow within the air domain using the conjugate heat transfer multiphysics interface. The temperature field is constrained to satisfy

$$\rho C_p \frac{\partial T}{\partial t} + \nabla \cdot (-k \nabla T) = Q \quad (5.4)$$

in the solid domain. The fluid domain is modeled as non-isothermal, laminar flow using Comsol's Conjugate Heat Transfer physics interface. The heat transfer equation is coupled to the Navier-Stokes equation in the Boussinesq approximation (allowing natural convection but neglecting the effect of thermal expansion on inertia), expressed as:

$$\rho \frac{\partial \mathbf{u}}{\partial t} + \rho(\mathbf{u} \cdot \nabla) \mathbf{u} = \nabla \cdot [-p \mathbf{I} + \mu(\nabla \mathbf{u})^T - \frac{2}{3}\mu(\nabla \cdot \mathbf{u})\mathbf{I}] + \mathbf{F} \quad (5.5)$$

$$\partial \frac{\rho}{\partial t} t + \nabla \cdot (\rho \mathbf{u}) = 0 \quad (5.6)$$

$$\rho C_p \frac{\partial T}{\partial t} + \rho C_p \mathbf{u} \cdot \nabla T + \nabla \cdot (-k \nabla T) = \mathbf{Q} \quad (5.7)$$

$\mathbf{F}$  is the volume force, expressed as:

$$\mathbf{F} = \rho g \quad (5.8)$$

but  $\rho$  depends on temperature through the thermal expansion coefficient, so (5.8) becomes:

$$\frac{p \alpha}{R} g \quad (5.9)$$

Phase change occurs at the interface between the two domains. We simulate phase change using a moving mesh, where the boundary is prescribed to move based on the lagrange multiplier  $T_{lm}$  of the temperature field divided by the latent heat of phase change.

$$\frac{dx}{dt} = -\frac{T_{lm}}{\rho \Delta H_{fus}} \quad (5.10)$$

Deforming the mesh changes the size and aspect ratio of individual mesh elements, which becomes problematic. To address this issue, I enabled the automatic remeshing feature and set it to recreate the mesh when the element quality parameter of any element drops below 0.3. Localized irregularities ("kinks" in the melting interface) were a problem in initial testing of the simulation, but selecting hyperelastic smoothing for computation of the mesh deformation solved this issue.

The remaining boundary conditions for the model are symmetry (thermal and flow) on the left hand side, and insulating walls on the top and right hand side. I attempted to run the model with range of mesh types and the fastest convergence and best model stability was attained using a dense quadrangular mesh in the air domain and an upwards-sparsening triangular mesh in the ice domain. The simulation is computationally intensive; it runs on the order of real-time (i.e. one real day is required to compute one simulated day) when running a 0.5m by 1m domain (on a quadcore Xeon E5430 CPU).

## Results

I was able to simulate 14.24 days of melting. Around that time, solver progress slows dramatically. Over the simulated period, the increase in melted cross-sectional area is perfectly linear with time (Figure 5.7). The area melt rate is constant at  $5 \cdot 10^{-8} \text{ m}^2 \text{ s}^{-1}$ , ( $1.6 \text{ m}^2 \text{ yr}^{-1}$ ). As in real life, the resulting ceiling geometry is the cross-section of a dome.

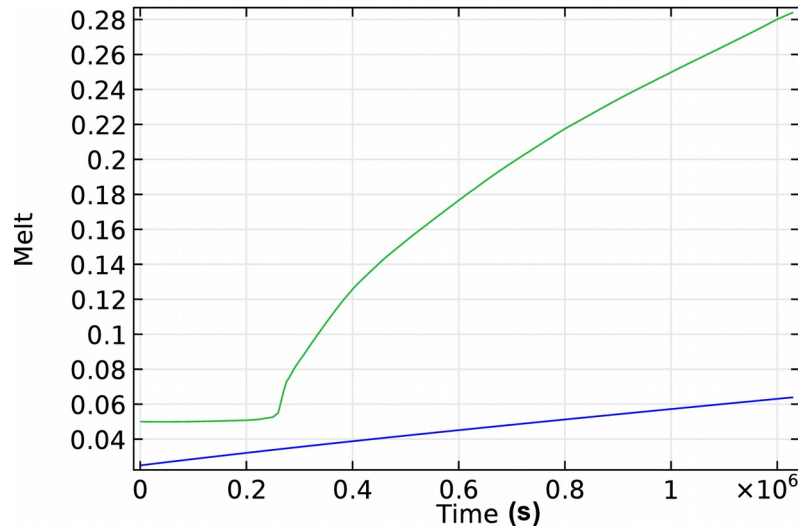


**Figure 5.7:** Melting simulation. Blue line: total melt area ( $\text{m}^2$ ). Green line: melt dome apex height (m)

Heat transfer within the air domain is dominated by natural convection (Figure 5.8). Metastable convection cells are established and collapse during the first three days of the model, and these temporary cells have a lasting impact on the geometry of the roof. The initial convection cell drives air counterclockwise, melting a dome apex about 0.18 m from the right hand side of the model. The initial cell grows towards the left into the stably stratified air column. Between 1.7 and 2.3 days, the initial cell is replaced by two counter-rotating convection cells on either side of a plume of hot gas. The plume moves leftwards until it encounters the symmetry boundary of the model, destroying the counterclockwise cell at 3.0 days. The resulting convection cell rotates clockwise with air velocities of around  $0.6 \text{ m s}^{-1}$  for the remainder of the studied period.

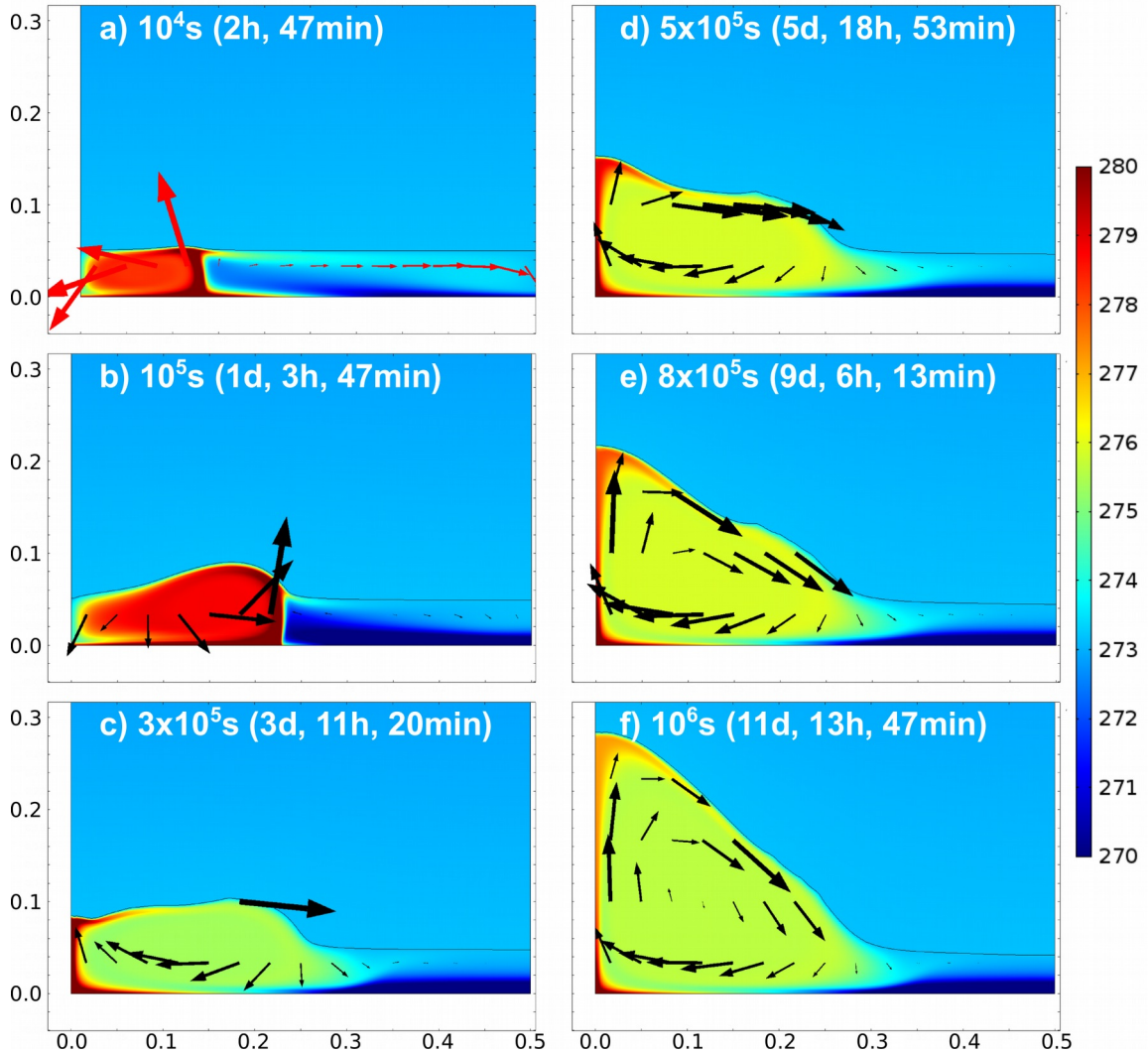


**Figure 5.8:** 2D fumarolic ice cave melting model. Colors represent temperature. Arrows represent airflow direction and magnitude.

## 5.5 Discussion

Previous work established the presence of gas vents in Warren Cave and their thermal impact on the cave atmosphere [Curtis and Kyle, 2011]. Observations herein allow us to go two steps further: we discuss the impact of the vents on the cave walls, and then on the topography above the cave.

### 5.5.1 Melt and densification

The finite element simulation matches reality in that it produces a realistic geometry, airflow velocities, temperature magnitudes, and gradients. There is a linear relationship between time, or equivalently, heat applied to the system, and area of the roof melted

(Figure 5.7). In the simulation, a total of 12W of heating was applied, and resulted in a melt rate of about  $1.6\text{m}^2 \text{yr}^{-1}$ , and a melt efficiency of about  $2.4 \times 10^8 \text{ J m}^{-2}$ . Warren Cave GV6 emits about 16kW, with about  $10\text{m}^2 \text{yr}^{-1}$  of resulting cross-sectional area ice loss, an efficiency of about  $5.0 \times 10^{10} \text{ J m}^{-2}$ . In this sense, the simulated melting process appears roughly 100 times more efficient than the observed melting process in Warren Cave.

However, the cave domain in the simulation is only 0.5m in width, and results are not directly comparable to our melt observations due to scaling issues. Flow within the air domain becomes turbulent at larger cavity sizes, and I have not yet modeled a turbulent flow scenario with melting. The model is most relevant for a small, “protocave,” i.e. a void that might occur during the initiation of FIC formation.

Oversimplification of the phase transition boundary physics provides another possible culprit for the apparent discrepancy in melt efficiency. In the simulation I use the latent heat of phase transition  $\Delta H_{fus}^\circ$  published for melting ice to water, and assume that all liquid water has been instantly removed from the system. In a more realistic model, liquid may exist on the surface of the ice as a thin film, may be drawn into capillaries in the ice, or may drip. Besides melting, two other phase transitions may be involved: evaporation and sublimation, each with its own  $\Delta H^\circ$ . In the nearly vapor-saturated cave atmosphere, evaporation may be diffusion-limited, further slowing the melt process [de Freitas and Schmekal, 2003]. Mechanical deformation of the ice mass is another factor that would reduce the observed melt rate in GV6 chamber, and was not accounted for in the finite element simulation. It is further discussed in section 5.5.2.

Further complicating the situation, the expansion of GV6 is a transient process which began when the south side of the chamber sealed off between the 2009 map survey and the first TLS scan in 2010. The mechanism for sealing appears to have been accumulation of regelation ice. Dripping and flowing liquid water formed ice stalagmites that eventually grew into a solid wall across the cave passage. Continued accretion of regelation ice is notable in Figure 5.2.

Elsewhere in the caves long-term stability is apparent, implying a dynamic equilibrium where melting is balanced by inward ice creep, in a similar manner to a subglacial Röthlisberger channel [Walder, 2010]. Peripheral sections of the cave are particularly vulnerable to growth and collapse, while the central passage is present in all six datasets (albeit with varying passage diameter). This is of interest for studying microbiological succession in the caves, because it implies that areas of previously ice-covered lava rock are constantly becoming newly exposed to the cave environment, providing fresh habitat for chemolithoautotrophic communities to colonize.

Beyond the question of cave passage stability, what can we learn about the cave-hosting ice mass? To begin with, is it a glacier? In Figure 5.2 we see that ice above Warren Cave is between 5m and 10m thick. An ice mass must undergo flow to be considered a glacier, which typically constrains its depth to more than 30m. In a compilation of data from 15 polar sites [Cuffey and Paterson, 2010, p.18], the shallowest firn-ice transition observed was 38m. In the glacier thickness database GlaThiDa [Gärtner-Roer et al., 2014], I find that 7382 (5.5%) of entries are thinner than 10m, and

490 (0.0037%) are thinner than 5m. The majority of the thin glacier entries in the database (132 of which are thinner than 1m) appear to be in error – they are referenced to [Cogley, 2008], an unavailable conference abstract.

Accumulation in the region is extremely low [Arthern *et al.*, 2006] and significant flow of ice is not observed within the Erebus summit caldera. Even at the caldera margin, in the beginning of the accumulation zone for the Fang Glacier, rocks left on the ice by the expedition of Raymond Priestley in 1912 were observed to be unmoved 100 years later [C. Oppenheimer, Pers. Comm, 2014].

Despite the small ice overburden and lack of glacial flow, we observed ice of glacial density in the walls of Warren Cave (Table 3). Fresh snow density inland of the Ross Sea is modeled to be around  $0.39 \text{ g cm}^{-3}$  [Ligtenberg *et al.*, 2011], and it is reasonable to expect the snowfall on Erebus to have a similar initial density. The most relevant densification rates available are those observed for other low-accumulation sites in Antarctica, all of which are below  $0.01 \text{ g cm}^{-3} \text{ yr}^{-1}$  [Spencer *et al.*, 2001], and the rates decline further to a typical  $0.001 \text{ g cm}^{-3} \text{ yr}^{-1}$  as density increases above  $0.7 \text{ g cm}^{-3}$ . At these rates, snow falling above Warren Cave would need between 50 and 500 years to reach the observed density.

Densification is also temperature dependent, and FIC are significant heat sources. The temperature dependence  $k(T)$  of densification rate is expressed using the Arrhenius relation:

$$k(T) = e^{\frac{-Q}{RT}} \quad (5.11)$$

where  $T$  is temperature,  $Q$  is an activation energy, and  $R$  is the universal gas constant [Cuffey and Paterson, 2010, p.23]. The temperature dependence is incorporated as:

$$\frac{1}{\rho} \frac{d\rho}{dt} = k(T) f(\rho, P) \quad (5.12)$$

where  $f(\rho, P)$  represents the dependence on density and load stress or overburden pressure. Using a typical activation energy  $Q$  for firn densification of  $40 \text{ kJ mol}^{-1}$ ,  $k(T)$  at Erebus' mean annual air temperature of  $-32.9^\circ\text{C}$  is  $1.998 \times 10^{-9}$ , and at the mean temperature of the ice in which we measured density ( $-0.4^\circ\text{C}$ ), it is  $2.172 \times 10^{-8}$ . Therefore, the presence of Warren Cave is expected to cause a tenfold increase in the densification rate of the surrounding ice. In addition to enhanced densification due to temperature, it is likely that the presence of the cave adds liquid water to the ice, which is expected to further hasten densification.

### 5.5.2 Ice deformation by creep

On many occasions, even on the first entry to an Erebus FIC, we have found incongruous items from the surface, such as blades from wind turbines or bamboo flags used to mark snowmobile routes, inside the cave. It is clear that these items have fallen from the cave roof into the cave; they were buried by snow on the surface and traveled downwards with creeping ice flow. This anecdotal evidence of ice creep corroborates the TLS observations of subsidence above Warren Cave (Section 5.4.1). Downward ice flow

presumably would slowly collapse the caves, except that it is opposed by melting. The net result is a “conveyor belt” carrying items and snow from the surface down into the caves.

The following is an attempt to predict the downward flow rate from physical principles, for comparison with the observed  $\sim 0.7\text{ m yr}^{-1}$  subsidence. Viscous strain is by far the largest component of ice deformation in a cold polycrystalline regime such as ours [Stoffel, 2006]. To the best of my knowledge, an analytical solution for viscous closure rate of a hemispherical dome such as GV6 has not been formulated. However, Nye [1953], in Weertman [1983] published an equation for the collapse of round tunnels based on a version of Glen's flow law in which stress is applied from multiple directions. Modified from Weertman's version to contain the ideal gas constant rather than Boltzmann's constant, and without the PV term, which is close enough to 1 to be neglected, the equation is

$$s = \frac{Be^{\frac{-Q}{nRT}} P^3 r}{6}, \quad (5.13)$$

where  $s$  is the radial wall velocity,  $P$  is the overburden pressure,  $R$  is the ideal gas constant,  $n$  is Avogadro's number,  $Q$  is the activation energy, and  $B$  is a well-studied empirical constant reflecting the grain fabric, density, and temperature of the ice. Nye's cylindrical formulation is applicable to the discussion of Warren GV6 chamber. Our finite element model (Section 5.4.5) melts an arch into a 2D cross-section in the X-Y plane, which can be imagined as repeating in the Z plane and therefore already describes a half-cylinder.

We can estimate the overburden pressure  $P$  from knowledge that the fresh snow value is  $0.39\text{ g cm}^{-3}$  (Section 5.5.1) and the average observed cave wall density of  $0.85\text{ g cm}^{-3}$ . Schytt [1958], in Cuffey and Patterson [2010], calculated an empirical depth – density curve

$$\rho(z) = \rho_i - (\rho_i - \rho_s) e^{\frac{-z}{z_p}}, \quad (5.14)$$

where  $z$  is depth,  $\rho_i$  is the density of pure ice ( $0.917\text{ g cm}^{-3}$ ),  $\rho_s$  is the density of fresh snow ( $0.39\text{ g cm}^{-3}$ ),  $z_p$  is a site-specific constant which approximates to 0.52 times the pore close-off depth. To determine  $P$  for 8m of overburden, assuming that the firn – ice transition occurs at 4m depth, the function becomes

$$\rho(z) = 0.917 - 0.572 e^{\frac{-z}{2.1}}, \quad (5.15)$$

which integrated between 0 and 8m, provides an overburden mass estimate of  $732\text{ g cm}^{-2}$ , or  $71.8\text{ kPa}$  using Earth's gravitational constant.

We adopt a commonly used laboratory B value of  $3.5 \times 10^{-25}\text{ s}^{-1}\text{ Pa}^{-3}$ , which lies within range of empirical values determined by MacAyeal *et al.* [1996] for flow of the Ross Ice Shelf. For ice creep activation energy, we use  $60\text{ kJ mol}^{-1}$ , and for activation volume  $-1.4 \times 10^{-5}\text{ m}^3\text{ mol}^{-1}$ , both values from Cuffey and Patterson [2010]. We approximate the passage radius at 5m. Equation 5.13 now becomes

$$s[m\ s^{-1}] = \frac{3.5 \cdot 10^{-25} [s^{-1}\ Pa^{-3}] e^{\frac{-60[\text{kJ mol}^{-1}]}{nR[J\ K^{-1}\ mol^{-1}]\cdot 273[K]}} (71.8[\text{kPa}])^3 5[m]}{6} \quad (5.16)$$

and produces an expected inward wall movement rate of  $s = 3.4\ \text{mm yr}^{-1}$  for a cylindrical Warren Cave. This theoretical value is about a factor of 100 smaller than the observed subsidence.

### 5.5.3 Global applicability of findings

We know that 19.8% of the volcanoes which have known activity in the holocene are perennially subnivean (Chapter 4.). Degassing at any of these volcanoes is likely to melt ice, and will form FICs unless the ice overburden is sufficiently thick to cause a creep rate that exceeds the melt rate. The 500 to 700m ice cap above the Gjálp eruption in Iceland is one such example. *Gudmundsson et al.* [2003] estimated 3.6 MPa of overburden pressure at the eruption site, which according to Equation 11 would lead to a tunnel closure rate of  $429\ \text{m yr}^{-1}$ . The inconceivable melt rate required to maintain a basal FIC at Gjálp would remove the entire thickness of the ice sheet in a matter of years.

The majority of subnivean volcanoes are not like Gjálp – their ice mantle has under 100m thickness, providing conditions suitable for FIC formation. In the Cascades, FICs have been reported on Mt. Hood, Mt. Baker, Mt. Rainier [*Kiver and Steele*, 1975], and Mt. St. Helens, but are rarely a target of scientific inquiry. Unexplored FIC undoubtedly exist at many degassing subnivean volcanoes.

The work of *Bleick et al.* [2013] strongly suggests that FICs were present precursory to the 2009 Redoubt eruption. When calculating ice mass loss and equivalent heatflow, the paper assumes that ice loss mass is fully represented by subsidence and meltwater outflow. Despite describing “tunnels in the ice” and “holes in the ice,” Bleick et al. neglect the possibility of FIC formation, in which cauldron subsidence volume is less than melt volume. As a result, they may have underestimated the pre-eruptive heat flow during early stages of melt. For example, if FICs existed beneath the two major ice subsidence cauldrons they observed ( $21,000\text{m}^2$  and  $680,000\text{m}^2$ ), with an average ceiling height of 3m, and formed between the first pre-eruptive observations of ice loss in Quickbird imagery (July 31, 2008) and when the first cauldron was observed (Jan 31, 2009), this would represent 54 MW of heat transfer melting ice. This would more than double Bleick et al.’s estimated heat transfer rate during that period.

## 5.6 Conclusions and outlook

We observed conclusive evidence of a continuing multi-year subsidence trend with a magnitude of between  $0.2$  and  $0.7\text{m yr}^{-1}$  above Warren Cave in response to melt from below. In recent years, subsidence is strongest above GV6, where a passage closure in 2009 led to growth of a domed chamber, with a ceiling height increase of between  $0.3$  and  $1.2\text{m yr}^{-1}$ . Subsidence results from downward ice creep. Ceiling height is determined by the balance between ice creep and melt, with the net result that ice and objects carried in the ice are cycled down from the snow surface, down through the roof and into the FIC.

I conducted a melting simulation using CFD, and considered ice creep using a formulation of Glen's flow law for closure of a cylindrical tunnel in ice. In the current state, these models should be considered "toy models" as they represent only a subset of the physics involved and do not reproduce the observed melt or deformation rates. The melting simulation is more applicable to cave initiation, in which air inside a small cavity undergoes laminar flow, than it is to a mature cave situation such as Warren GV6 chamber. It predicts a melt efficiency of  $2.37 \times 10^8 \text{ J m}^{-2}$  in terms of cross-sectional area, and a value of approximately  $3.78 \times 10^{10} \text{ J m}^{-2}$  was observed in GV6 chamber. The creep model predicts  $3.4 \text{ mm yr}^{-1}$  of inward wall movement, but between 200mm and 700mm  $\text{yr}^{-1}$  of subsidence was observed.

Warren Cave is hosted in ice of glacial density, but not in a glacier. I calculate that warmth from the cave accelerates densification of nearby ice by a factor of around 10. An interesting test of this theory would be to collect ice cores and construct depth-density profiles. Density should increase with proximity to cave passages or collapsed cave passages.

I caution against inferring changes in volcanic activity from passage growth in the manner of Kiver [1978]. Six years of morphologic observations at Warren Cave revealed that these systems are extremely dynamic, and major fluctuations in passage size occur without any change in the magmatic system. Rapid expansion of GV6 chamber was in response to the close-off of a nearby wall, rather than a change in volcanic activity.

However, the formation of *new* FIC, such as those that I infer formed at Redoubt before the 2009 eruption, is a useful indicator of increasing unrest at subnivean volcanoes. The subsidence cauldron that is actively forming above Warren Cave is detectable by airborne lidar and other altimetry techniques. I recommend the development of automated systems that can monitor for the topographic signature of newly developing FICs. Further underground work is required to characterize these systems in a broader range of climatic regimes and should target the many unexplored FICs that are certain to exist, particularly in the Andes and in Alaska.

## 5.7 References

- Anderson, C. H., C. J. Behrens, G. A. Floyd, and M. R. Vining (1998), Crater Firn Caves of Mount St. Helens, Washington, *J. Cave Karst Stud.*, 60, 44–50.
- Arthern, R. J., D. P. Winebrenner, and D. G. Vaughan (2006), Antarctic snow accumulation mapped using polarization of 4.3-cm wavelength microwave emission, *J. Geophys. Res. Atmospheres*, 111(D6), D06107, doi:10.1029/2004JD005667.
- Besl, P. J., and N. D. McKay (1992), Method for registration of 3-D shapes, *IEEE Trans. Pattern Anal. Mach. Intell.*, 14(2), 239–256, doi:10.1109/34.121791.
- Bleick, H. A., M. L. Coombs, P. F. Cervelli, K. F. Bull, and R. L. Wessels (2013), Volcano–ice interactions precursory to the 2009 eruption of Redoubt Volcano, Alaska, *J. Volcanol. Geotherm. Res.*, 259, 373–388, doi:10.1016/j.volgeores.2012.10.008.
- van den Broeke, M. (2008), Depth and Density of the Antarctic Firn Layer, *Arct. Antarct. Alp. Res.*, 40(2), 432–438, doi:10.1657/1523-0430(07-021)[BROEKE]2.0.CO;2.
- Cogley, J. G. (2008), Measured rates of glacier shrinkage, *EGU General Assembly*, in *Geophysical Research Abstracts*, vol. 10, Vienna, Austria.
- Connell, L., and H. Staudigel (2013), Fungal Diversity in a Dark Oligotrophic Volcanic Ecosystem (DOVE) on Mount Erebus, Antarctica, *Biology*, 2(2), 798–809, doi:10.3390/biology2020798.
- Cousins, C. R., and I. A. Crawford (2011), Volcano-Ice Interaction as a Microbial Habitat on Earth and Mars, *Astrobiology*, 11(7), 695–710, doi:10.1089/ast.2010.0550.
- Csatho, B., T. Schenk, P. Kyle, T. Wilson, and W. B. Krabill (2008), Airborne laser swath mapping of the summit of Erebus volcano, Antarctica: applications to geological mapping of a volcano, *J. Volcanol. Geotherm. Res.*, 177(3), 531–548, doi:10.1016/j.volgeores.2008.08.016.
- Cuffey, K. M., and W. S. B. Paterson (2010), *The Physics of Glaciers*, Academic Press.
- Curtis, A. (2010), Erebus Cave and Fumarole Database, Available from: <http://erebuscaves.nmt.edu/>

- Curtis, A., and P. Kyle (2011), Geothermal point sources identified in a fumarolic ice cave on Erebus volcano, Antarctica using fiber optic distributed temperature sensing, *Geophys. Res. Lett.*, 38(16), L16802, doi:10.1029/2011GL048272.
- de Freitas, C. R., and A. Schmekal (2003), Condensation as a microclimate process: measurement, numerical simulation and prediction in the Glowworm Cave, New Zealand, *Int. J. Climatol.*, 23(5), 557–575.
- Gärtner-Roer, I., K. Naegeli, M. Huss, T. Knecht, H. Machguth, and M. Zemp (2014), A database of worldwide glacier thickness observations, *Glob. Planet. Change*, 122, 330–344, doi:10.1016/j.gloplacha.2014.09.003.
- Giggenbach, W. F. (1976), Geothermal ice caves on Mt Erebus, Ross Island, Antarctica, *N. Z. J. Geol. Geophys.*, 19(3), 365–72.
- Glen, J. W. (1958), The flow law of ice: A discussion of the assumptions made in glacier theory, their experimental foundations and consequences, *IASH Publ.*, 47, 171–183.
- Gudmundsson, M. T., F. Sigmundsson, H. Björnsson, and T. Högnadóttir (2003), The 1996 eruption at Gjálp, Vatnajökull ice cap, Iceland: efficiency of heat transfer, ice deformation and subglacial water pressure, *Bull. Volcanol.*, 66(1), 46–65, doi:10.1007/s00445-003-0295-9.
- Häuselmann, P. (2011), UIS Mapping Grades, *Int. J. Speleol.*, 40(2), 15.
- InnovMetric, inc. (2010), *Polyworks v11*.
- Jones, L. K., P. R. Kyle, C. Oppenheimer, J. D. Frechette, and M. H. Okal (2015), Terrestrial laser scanning observations of geomorphic changes and varying lava lake levels at Erebus volcano, Antarctica, *J. Volcanol. Geotherm. Res.*, 295, 43–54, doi:10.1016/j.jvolgeores.2015.02.011.
- Kazhdan, M., and H. Hoppe (2013), Screened poisson surface reconstruction, *ACM Trans. Graph. TOG*, 32(3), 29, doi:10.1145/2487228.2487237.
- Kiver, E. P. (1978), Mount Baker's changing fumaroles, *Ore Bin*, 40, 133–145.
- Kiver, E. P., and W. K. Steele (1975), Firn caves in the volcanic craters of Mount Rainier, Washington, *NSS Bull.*, 37, 45–55.
- Ligtenberg, S. R. M., M. M. Helsen, and M. R. van den Broeke (2011), An improved semi-empirical model for the densification of Antarctic firn, *The Cryosphere*, 5(4), 809–819, doi:10.5194/tc-5-809-2011.

- Lowe, D. G. (2004), Distinctive image features from scale-invariant keypoints, *Int. J. Comput. Vis.*, 60(2), 91–110, doi:10.1023/B:VISI.0000029664.99615.94.
- MacAyeal, D. R., V. Rommelaere, P. Huybrechts, C. L. Hulbe, J. Determann, and C. Ritz (1996), An ice-shelf model test based on the Ross Ice Shelf, *Ann. Glaciol.*, 23, 46–51.
- Meussen, B., O. Mahrenholz, and H. Oerter (1999), Creep of polar firn, *Cold Reg. Sci. Technol.*, 29(3), 177–200, doi:10.1016/S0165-232X(99)00018-X.
- Moore, P., and A. Curtis (2015), object\_alignment plugin for Blender: Release Preview 2, doi:10.5281/zenodo.31462.
- Nye, J. F. (1953), The flow law of ice from measurements in glacier tunnels, laboratory experiments and the Jungfraufirn borehole experiment, *Proc. R. Soc. Lond. Ser. Math. Phys. Sci.*, 219(1139), 477–489.
- Redovniković, L., M. Ivković, V. Cetl, and I. Sambunjak (2014), Testing DistoX Device for Measuring in the Unfavourable Conditions, in *Proceedings of the 6th International Conference on Engineering Surveying*.
- Schytt, V. (1958), Snow and ice studies in Antarctica, PhD Thesis, Stockholm College.
- Spencer, M. K., R. B. Alley, and T. T. Creyts (2001), Preliminary firn-densification model with 38-site dataset, *J. Glaciol.*, 47(159), 671–676, doi:10.3189/172756501781831765.
- Stoffel, M. (2006), *Numerical Modelling of Snow Using Finite Elements*, vdf Hochschulverlag AG, Zurich, Switzerland.
- Tebo, B. M., R. E. Davis, R. P. Anitori, L. B. Connell, P. Schiffman, and H. Staudigel (2015), Microbial communities in dark oligotrophic volcanic ice cave ecosystems of Mt. Erebus, Antarctica, *Front. Microbiol.*, 6, doi:10.3389/fmicb.2015.00179. PMID: 25814983 PMCID: PMC4356161
- Walder, J. S. (2010), Röthlisberger channel theory: its origins and consequences, *J. Glaciol.*, 56(200), 1079–1086, doi:10.3189/002214311796406031.
- Weertman, J. (1983), Creep deformation of ice, *Annu. Rev. Earth Planet. Sci.*, 11, 215.

# **CHAPTER 6. OXYGEN AND HYDROGEN ISOTOPIC EVIDENCE FOR A PLUME-DERIVED MAGMATIC COMPONENT IN THE SNOW AND FUMAROLIC ICE TOWERS AT EREBUS VOLCANO, ANTARCTICA**

*This chapter is a paper which was submitted to Geophysical Research Letters, and is under revision to be re-submitted. The manuscript is presented in GRL format.*

*It is a collaborative effort. My role was to collect and analyze the fumarolic ice tower samples, and complete most of the text and figures. Non-tower snow samples were collected by Jamie Margolin and Melissa Kammerer.*

**Oxygen and hydrogen isotopic evidence for a plume–derived magmatic component in the snow and fumarolic ice towers at Erebus volcano, Antarctica**

Aaron Curtis<sup>1</sup>, Philip Kyle<sup>1</sup>, Laura Jones<sup>1</sup>, Melissa Kammerer<sup>1</sup>, Andrew R. Campbell<sup>1</sup>

<sup>1</sup>Department of Earth and Environmental Science, New Mexico Institute of Mining and Technology, Socorro, NM 87801 USA

For Submission to: Geophysical Research Letters

Corresponding author: Aaron Curtis, aarongc@nmt.edu

## 6.1 Abstract

Oxygen and hydrogen isotope analysis of 210 snow, firn and ice samples collected on Erebus volcano have a  $\delta^2\text{H}$  /  $\delta^{18}\text{O}$  relationship inconsistent with a purely meteoric source. The samples were collected from fumarolic ice towers, areas of steaming warm ground, and surface snow. 66% of the Erebus samples are enriched in  $^{18}\text{O}$  relative to the Antarctic Meteoric Water Line (AMWL) [Masson-Delmotte *et al.*, 2008]. We propose that magmatic water emitted in the persistent gas plume from the permanent phonolite lava lake is the source of the magmatic water. The shift from the AMWL is consistent with the presence of up to 41% magmatic water in some of the samples. Fumarolic ice towers have O and H isotopes in the range of the snow from the summit area of the volcano, and are similarly shifted to the right of the AMWL. Chemical analysis of the snow samples demonstrated a lack of geographic correspondence between volcanic plume-derived F, Cl and S concentrations and isotopic signatures, suggesting at least two separate modes of transport for plume material. “Dry” aerosol transport is decoupled from that of ice particles, and may also undergo different diagenetic processes. Isotopic enrichment was observed further from the plume source than chemical enrichment and therefore has important potential as a proxy for volcanic activity.

## 6.2 Introduction

Water and CO<sub>2</sub> are the most abundant volatiles emitted in volcanic gas plumes [Delmelle and Stix, 2000]. In volcanic gases and fluids at depth in a magmatic system, the isotopic composition of O and H in water has a limited range of isotopic composition centered on  $\delta^{18}\text{O} = 7\text{--}8\text{\textperthousand}$  and  $\delta^2\text{H} = -65\text{\textperthousand}$  [Giggenbach, 1992; Sharp, 2007]. This “magmatic water box” contrasts strongly with the isotopic compositions of meteoric waters. The Meteoric Water Line (MWL) exhibits a strong correlation between  $\delta^{18}\text{O}$  and  $\delta^2\text{H}$  [Craig, 1961] and ranges from seawater to  $\delta^{18}\text{O} = -60$  and  $\delta^2\text{H} = -450$  in the most depleted fresh Antarctic snow samples [Jouzel and Merlivat, 1984]. There is no overlap between the magmatic water box and the MWL. Thus it is possible to distinguish between meteoric and magmatic-derived water, particularly in regions where the two signatures are furthest removed. In the Polar Regions, isotopic compositions of precipitation are strongly depleted in the heavy isotopes of oxygen and hydrogen and are isotopically the lightest in the world and thus the furthest removed from the magmatic water box. Taking advantage of this phenomenon, we examine the  $\delta^{18}\text{O}$  and  $\delta^2\text{H}$  of snow samples and ice cores from fumarolic ice towers near the summit crater of the active Erebus volcano and demonstrate a magmatic signature in the snow.

Degassing from the flanks of volcanoes is increasingly recognized as an important component of volcanic gas emission [Giannanco *et al.*, 1997; Hernández and Salazar, 2002; Mörner and Etiope, 2002; Notsu *et al.*, 2005; D’Alessandro, 2006] and thus snow and ice composition may be affected by flank degassing in addition to crater emissions. The composition of water vapor released by fumaroles reflects processes occurring inside the volcanic edifice. Panichi and la Ruffa [2001] reviewed isotopic studies of fumarole

condensate water at seven volcanoes, finding that this was an effective tool for identifying hydrothermal systems, near-surface magma chambers, and determining the contribution of each in mixing situations.

### 6.3 Erebus volcano

Erebus volcano is an active 3794-meter high stratovolcano located on Ross Island in the southern Ross Sea area of Antarctica (Figure 6.1a). It is characterized by a degassing convecting anorthoclase phonolite lava lake with irregular Strombolian eruptions. The main gas composition of the plume is H<sub>2</sub>O (57.88 mol %), CO<sub>2</sub> (36.41 mol %), and SO<sub>2</sub> (1.40 mol %) [Oppenheimer and Kyle, 2008]. The plume is typically dispersed by the prevailing winds to the NE and by the strongest winds to the W and NW. At the peak elevation and average temperature of -32.9°C, the δ<sup>2</sup>H values of snow in the summit of Erebus volcano would be expected to range from around -350‰ to -450‰, bounded by the Antarctic Meteoric Water Field (AMWF). Fumarolic ice towers (FIT) form on the summit plateau of Erebus when steam released from fumaroles in areas of relatively thin snowpack de-sublimates upon contact with the ambient air, and presenting a unique measurement opportunity. FITs grow into sub-conical chimneys which can reach 15m in height with several meters of wall thickness. Fumarolic ice caves (FICs) are found beneath many FIT.

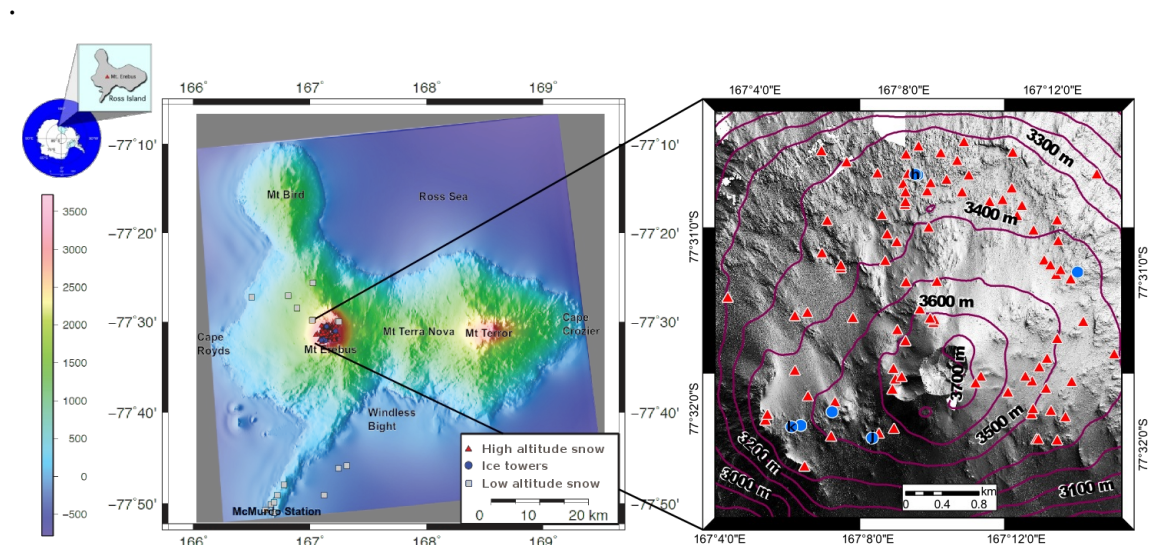


**Figure 6.1:** Lefthand map: Ross Island showing the location of snow and ice samples. Righthand inset: map of the summit of Erebus volcano and sample sites with Hut Cave is marked as h, Kachina Cave as k, and Jack-in-the-Pulpit as j.

Gas released by the Erebus fumaroles contains between 5,000 and 15,000 ppm H<sub>2</sub>O content and 380 to 20,000 ppm CO<sub>2</sub> [Curtis and Kyle, 2011]. δ<sup>13</sup>C of fumarole gas samples range from -2.1 to -4.7 ‰, indicating a magmatic source [Wardell et al, 2003]. No other volcanic gases have been detected in measurable quantity, despite testing for

CO, NO<sub>2</sub>, SO<sub>2</sub>, H<sub>2</sub>S, and alkanes using a Draeger Multiwarn II handheld gas monitor. N<sub>2</sub> is by far the dominant species and therefore although CO<sub>2</sub> demonstrates a magmatic component, the gas most likely undergoes significant mixing with air before reaching the fumarole.

Aerosol particles in the plume from the Erebus lava lake contain: Na<sup>+</sup>, K<sup>+</sup>, Al<sup>3+</sup>, Pb<sup>2+</sup>, F<sup>-</sup>, Cl<sup>-</sup>, Br<sup>-</sup>, NO<sup>3-</sup>, SO<sub>4</sub><sup>2-</sup> [Ilyinskaya *et al.*, 2010]. Dry deposition of aerosol provides components necessary for the formation of widespread volcanogenic salt deposits. Chemical analysis of those deposits revealed volcanogenic alunite, khademite, mirabilite, ralstonite, and thenardite along with marine salts [Zreda-Gostynska 1995]. X-ray diffraction analysis by Kammerer [2011] confirmed those findings and identified several more volcanogenic phases, including millosevichite, rancieite, sodiumalum, and elemental sulfur. Erebus aerosols can also be dispersed hundreds of miles, and appear to affect the trace element composition measured in snow throughout Antarctica [Zreda-Gostynska *et al.*, 1997].

## 6.4 Antarctic Snow

Oxygen and Hydrogen isotope analyses of Antarctic snow samples from over 1000 locations were compiled by *Masson-Delmotte et al.* [2008] and show an extremely well-defined relationship between  $\delta^{18}\text{O}$  and  $\delta^2\text{H}$ . It is unlikely the samples are affected by volcanic sources as none were collected closer than 240 km to any historically active volcano. For the 789 samples with both  $\delta^{18}\text{O}$  and  $\delta^2\text{H}$  analyses,  $\delta^2\text{H} = \delta^{18}\text{O} \cdot 7.75 - 4.93$ , with an  $R^2 = 0.998$ . As with most local meteoric water lines, the slope is slightly decreased in comparison to the global meteoric water line (GMWL) of  $\delta^2\text{H} = \delta^{18}\text{O} \cdot 8 + 10$  [Craig, 1961]. Treating the *Masson-Delmotte et al.* [2008] data as a suite of control samples for normal Antarctic snow, we define an Antarctic Meteoric Water Field (AMWF) with boundaries parallel to the regression (Figure 6.2a), encompassing all 789 data points (see Appendix C for details). This AMWF covers the range of isotopic variations in Antarctic snow associated with all geographical and environmental conditions including temperature, elevation, and distance from moisture source.

## 6.5 Methods

A total of 210 snow and ice samples were collected during the 2004 and 2009 Austral Summer, consisting of 190 samples from Erebus summit, 10 samples on the flanks, 6 samples on Hut Point Peninsula, and 4 samples in Windless Bight (Figure 6.1). The snow samples were collected from: short profiles, fresh snow, loose surface snow, compacted older snow, and firn layers. All samples were collected in plastic Ziploc bags, melted, and then transferred into Nalgene bottles and sealed for shipment.

Seven ice cores were collected during the 2009 Austral Summer from FIT using a 4" diameter SIPRE auger. The cores were drilled from the outside walls of towers towards their interior, angled downwards between 25 and 35 degrees. Core lengths ranged between 0.5m (Puny Tower) and 4.0m (Jack in the Pulpit) and penetrated the entire thickness of the tower wall in three cases (Puny Tower, Jack in the Pulpit, and Kachina Cave). Cores were packaged in polyethylene lay-flat tubing and maintained at -20°C

during transport to New Mexico Tech. The ice cores were sampled in a -20°C cold facility using a drill press with a 1" hole saw. A uniform sample spacing was not possible due to fractures in the cores, but samples were collected every 15cm where possible. 66 samples were melted and yielded between 2 and 8 mL of water each.

Snow samples collected in 2004 were measured at the New Mexico Institute of Mining and Technology mass spectrometry lab on a Thermo Finnigan Delta Plus XP mass spectrometer. The  $\delta^2\text{H}$  values were measured using an H-device in a chromium reactor, with a reaction temperature of 850°C. This technique employs a water-metal reaction where the water reacts with the chromium to produce chromium oxide and hydrogen gas. The hydrogen gas was introduced into the mass spectrometer via a dual inlet for analysis with Oxtech gas standards. The reproducibility of the  $\delta^2\text{H}$  values was +/- 0.4%. The  $\delta^{18}\text{O}$  values were measured using the  $\text{CO}_2$ — $\text{H}_2\text{O}$  equilibration technique and introduced into the mass spectrometer after equilibrating for 24 hours under continuous flow with the Thermo Finnigan Gas Bench. The reproducibility of the  $\delta^{18}\text{O}$  values was +/- 0.1%. Both  $\delta^2\text{H}$  and  $\delta^{18}\text{O}$  values were corrected with in-house lab standards calibrated to SMOW.

Samples from the 2009 season were measured using a Picarro Cavity Ring Down Spectrometer (CRDS). The CRDS allows for simultaneous measurement of  $\delta^2\text{H}$  and  $\delta^{18}\text{O}$  from a 1mL sample. Each sample was run four times, the first point was discarded, and the remaining three were averaged to eliminate any memory effects between samples. Both  $\delta^2\text{H}$  and  $\delta^{18}\text{O}$  values were corrected with in-house lab standards calibrated to SMOW.

Since the samples from 2004 and 2009 were analyzed on two different instruments the samples were normalized to current lab standards. This was done by re-running twenty samples from each year on the CRDS and comparing them to the values originally measured. A small correction factor was applied so that all  $\delta^2\text{H}$  and  $\delta^{18}\text{O}$  values could be compared between the two analytical techniques.

General water chemistry was measured for snow samples excluding the ice tower samples. Samples were analyzed for  $\text{F}^-$ ,  $\text{Cl}^-$ , and  $\text{SO}_4^{2-}$  by Ion Chromatography (IC) at the New Mexico Bureau of Geology Water Chemistry Lab.

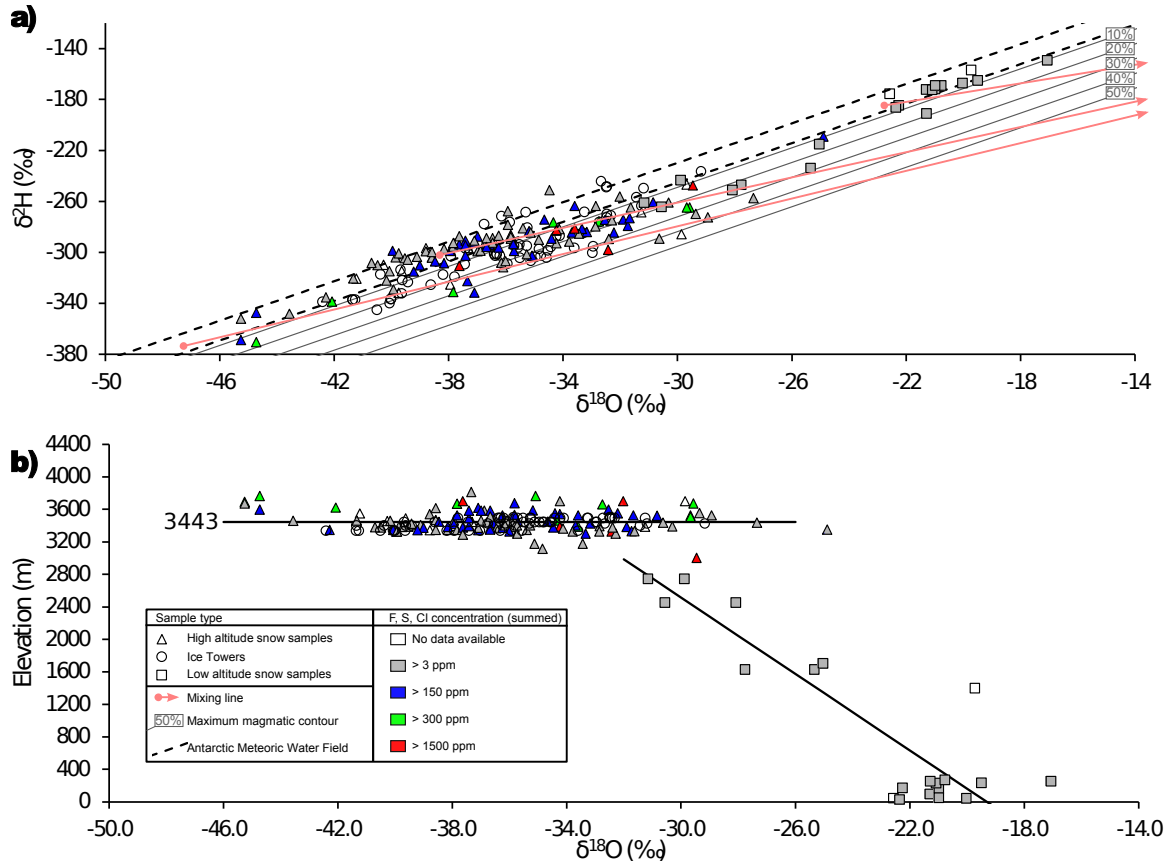


**Figure 6.2:** **a)** Relationship between  $\delta^{2\text{H}}$  and  $\delta^{18\text{O}}$  for all Erebus samples. Included in the plot is the AMWL as discussed in the text. All 789 samples reported by Masson-Delmotte et al. [2008] fit between the dotted lines. Red arrows indicate the mixing path for three example hypothetical meteoric waters, when magmatic water ( $\delta^{2\text{H}} = -62.5$  ‰,  $\delta^{18\text{O}} = 7.75$  ‰) is added. **b)** Relationship between elevation and  $\delta^{18\text{O}}$ . For the samples below 3000m, the black line represents the best linear fit ( $y = -235.31x - 4544.5$ ,  $R^2 = 0.7973$ ) and for the samples above 3000m, the black line represents the average (3443m)

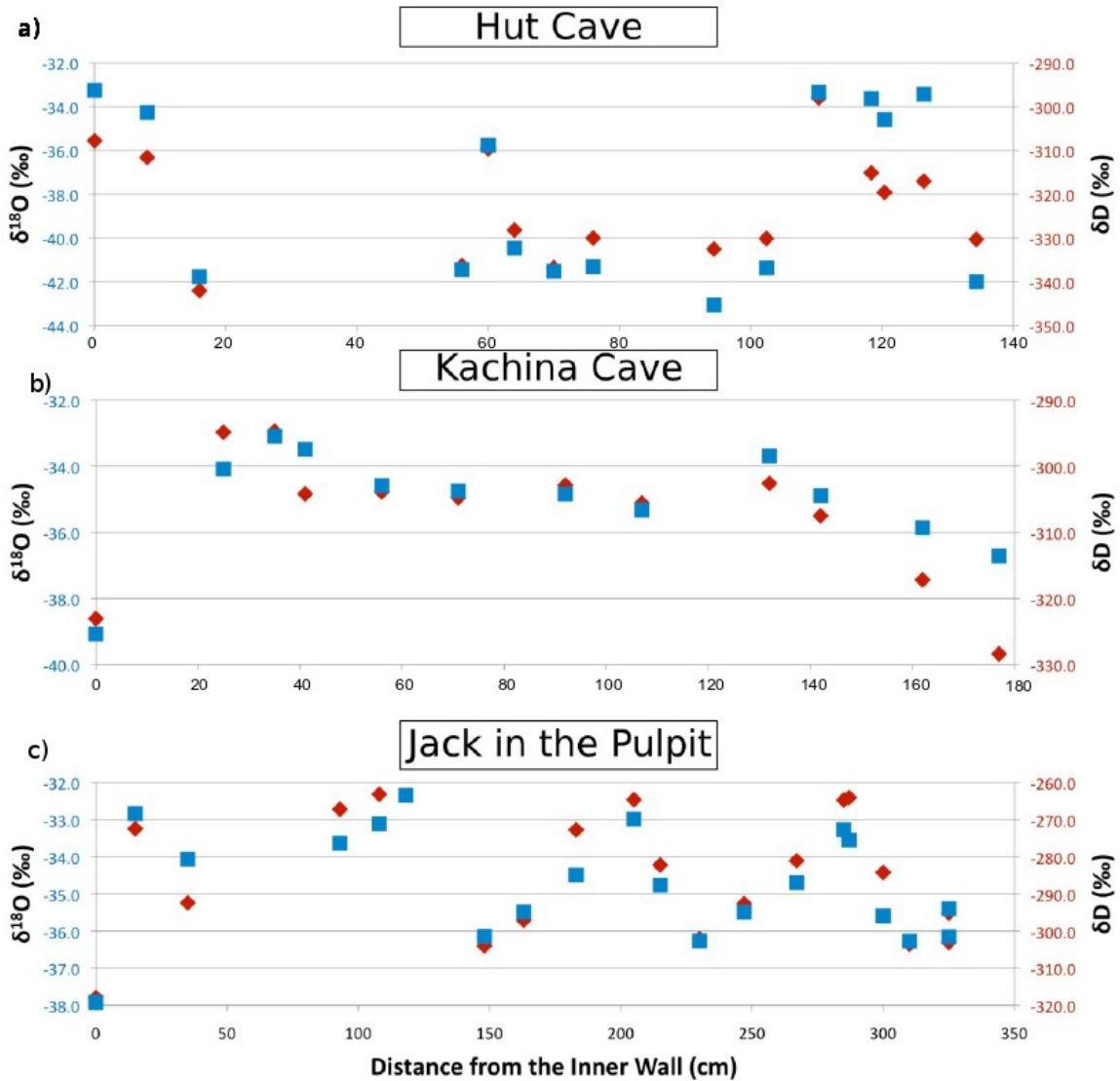


**Figure 6.3:**  $\delta^2\text{H}$  and  $\delta^{18}\text{O}$  of the Erebus FIT cores plotted against the sample's distance from the inner tower wall. The  $\delta^2\text{H}$  values are plotted as blue squares and the  $\delta^{18}\text{O}$  values are plotted as red diamonds.

## 6.6 Results

A complete listing of the isotope analyses, and the S, F, and Cl concentrations where available, are given in Appendix A. The snow and ice samples display a wide range of  $\delta^{18}\text{O}$  and  $\delta^2\text{H}$  (Figure 6.2). The  $\delta^2\text{H}$  ranges from -370.5‰ to -149.5‰ with a mean of -286.9‰, and  $\delta^{18}\text{O}$  ranges from -45.3‰ to -17.1‰ with a mean of -34.9‰. The summit caldera snow samples and FIT ice cores had comparable slopes and ranges of  $\delta^{18}\text{O}/\delta^2\text{H}$  (Figure 6.2a). All samples below an altitude of 3000m (roughly the altitude of the summit caldera rim) demonstrate a linear relationship between elevation and isotope ratio

( $r^2=0.797$ ), where  $\delta^{18}\text{O}$  decreases with altitude at a rate of  $0.00425\text{\textperthousand m}^{-1}$  (Figure 6.2b). A marked break in slope occurs at 3000m, above which  $\delta^{18}\text{O}$  exhibits a wider range of values which is independent of elevation. In  $\delta^{18}\text{O}/\delta^2\text{H}$  space, 61% of the data fall to the right of the AMWF, 5% fall to the left, and only 33% are within the AMWF. The  $\delta^2\text{H}$  and  $\delta^{18}\text{O}$  of FIT ice samples from individual ice towers tend to cluster along the trendline exhibited by all the samples. FIT samples deviated from the AMWF slightly more frequently than the snow samples. Only 11% were within the AMWF whereas 73% fell to the right, and 4% fell to the left. The  $\delta^2\text{H}$  and  $\delta^{18}\text{O}$  values of the FIT cores varied significantly with distance into the tower walls (Figure 6.3). The type and strength of this relationship varies significantly between the cores. Hut and Kachina caves do not seem to display a systematic relationship. Kachina Cave displays heavier values towards the center of the tower with the notable exception of the subsample closest to the inner wall, which is dramatically lighter. Jack in the Pulpit appears to have a cyclic pattern, with four sections where the  $\delta^{18}\text{O}$  values decrease towards the tower's center. Pirate's Tower, Heroine Tower, Harry's Dream, and Puny Tower all have too few subsamples to determine any distance relationships.

Anionic concentrations of the five samples with a combined F, Cl and S concentration above  $1500 \text{ mg L}^{-1}$  all fall to the right of the AMWL in  $\delta^2\text{H} / \delta^{18}\text{O}$  space, as do 63% of the 300 to  $1500 \text{ mg L}^{-1}$  samples. However, no clear relationship was observed between the isotopic variance and chemical composition, either in geographical space or in  $\delta^2\text{H} / \delta^{18}\text{O}$  space (Figure 6.2). Despite a lack of strong correlation between isotopic ratios and chemistry, the highest anionic concentrations are associated with isotopic values shifted to the right from the AMWL.

## 6.7 Discussion

For snow samples collected below 3000m the correlations of decreasing  $\delta^2\text{H}$  and  $\delta^{18}\text{O}$  with increased altitude (Figure 6.2b) are examples of the well-established "altitude effect", where depletion of the heavier isotopes of  $^{18}\text{O}$  and  $^2\text{H}$  increases with elevation [Ambach *et al.*, 1968; Siegenthaler and Oeschger, 1980; Niewodniczanski *et al.*, 1981]. The altitude effect results from a combination of adiabatic temperature drop with altitude, and a decrease in the fraction of remaining moisture (known as the F-value if modeled as a Rayleigh distillation process). The altitude effect generally ranges from 0.002 to  $0.006\text{\textperthousand } \delta^{18}\text{O } \text{m}^{-1}$ , [Gonfiantini *et al.*, 2001] consistent with our observed value of  $0.00425\text{\textperthousand } \delta^{18}\text{O } \text{m}^{-1}$ . Above the summit caldera rim at 3000m, there is no correlation between  $\delta^{18}\text{O}$  and elevation (Figure 6.2b) and the altitude effect is overwhelmed by another source of isotopic variation.

This anomalous behavior of  $\delta^2\text{H}$  and  $\delta^{18}\text{O}$  in the summit snow and ice samples is evidenced by the fact that 66% of the samples do not fall within the AMWF. Some data points fall outside of three standard deviations from the isotopic compositions of all non-Erebus Antarctic snow samples. FIT subsamples show an even stronger isotopic discrepancy from the AMWF with the majority (73%) of the FIT subsamples falling to the right of the AMWF. This begs the question: what conditions on Erebus differ from those on Antarctica as a whole?

One explanation is that a primary magmatic water component has been introduced to the snow through interaction with the plume degassing from the crater lava lake. The large flux of CO<sub>2</sub> (15.4 kg/s) and H<sub>2</sub>O (10.0 kg/s) from Erebus [Oppenheimer and Kyle, 2008] seems a sufficient explanation for this isotopic enrichment; mixing between an initial meteoric component and a magmatic source would account for our data. We can estimate the percent of primary igneous water in each subsample (Appendix B). In the case of the FIT samples, this estimation results in between 7 and 22% magmatic water.

The lack of geographic trends and correlation between isotopic values and chemistry indicates either a decoupling between the dry deposition of aerosol particles (mainly HF and HCl) and ice particles, or differential diagenesis of the two signals. Airborne particulates are expected to have different masses and cross-sectional areas from ice particles, causing different dispersal patterns in the same wind conditions. Alternatively, or in combination with this effect, diffusion, melting, and sublimation may modify the ionic but not isotopic enrichment signal, or vice versa.

In addition to the plume component, several secondary factors may contribute to the isotopic signature of snow and FIT ice at Erebus. Many volcanoes exhibit subsurface circulation of hydrothermal fluids which affect the isotopic signature of fumarolic vapor. Hydrothermal circulation, in which meteoric water is altered by high temperature interaction with the volcanic edifice, results in <sup>18</sup>O enrichment without a shift in <sup>2</sup>H. This is a result of the high O concentration in rocks relative to H. If hydrothermally altered water is a component of the FIT vapor, this could account for some of our  $\delta^{18}\text{O}$  shift but not the  $\delta^2\text{H}$ . Transport of coastal moisture from the Ross Sea would result in the relative depletion of heavy isotopes. Evaporation, sublimation, and recondensation processes likely occur in the summit region. In the case of evaporation and sublimation light isotopes are removed from the snowpack while recondensation of vapor will deposit heavy isotopes. However, the *Masson-Delmotte et al.* [2008] dataset does contain samples from high altitudes and coastal regions where these post-depositional processes occur, so they do not explain the majority of our isotopic shift from the AMWL.

## 6.8 Conclusions

Our analysis reveals a shift in isotopic ratios of the Erebus snow and ice samples towards magmatic water. This strongly suggests that water condensing out of the volcanic plume mixes with snow and is deposited in the summit caldera. Although the samples in the highest category of anionic content corresponded to large isotopic shifts, there is a poor overall correspondence between chemical and isotopic proxies for magmatic influence. This implies a decoupled system of deposition in which dry aerosol particulates containing S, F, and Cl undergo a dispersal pathway separate from that of magmatically-derived water vapor.

The volcanic component in FIT ice could provide a time-averaged indicator which can complement condensate sampling at discrete points in time. Many glaciated volcanoes in temperate regions do have ice in close proximity to fumaroles, and such an indicator could be applied to Mt. Rainier, for example, where *Zimbelman et al.* [2000] collected condensate from inside of firn caves, but not from the surrounding ice.

However, isotopic ratios of FIT samples were only slightly more shifted than the snow samples overall, indicating FIT-forming steam is primarily sourced by local melting of plume-influenced snow.

The lack of a detectable plume component outside of the Erebus summit caldera indicates that persistent volcanic degassing is unlikely to influence isotopic records from ice core records, unless cores are collected in close proximity (< 10km) to a major volcanic source.

**Acknowledgments** Funding for this project was provided by the NSF Office of Polar Programs through Grant ANT- 1142083. Jamie Margolin collected many of the snow samples. Assistance in the field was provided by the entire G-081 team, especially Harry Keys, Nial Peters Bill McIntosh, and Nelia Dunbar. Field work was supported by Raytheon Polar Services Company, PHI and Helicopters New Zealand.

## 6.9 References

- Ambach, W., W. Dansgaard, H. Eisner, and J. Møller (1968), The altitude effect on the isotopic composition of precipitation and glacier ice in the Alps, *Tellus*, 20(4), 595–600.
- Craig, H. (1961), Isotopic Variations in Meteoric Waters, *Science*, 133(3465), 1702 – 1703, doi:10.1126/science.133.3465.1702.
- Curtis, A., and P. Kyle (2011), Geothermal point sources identified in a fumarolic ice cave on Erebus volcano, Antarctica using fiber optic distributed temperature sensing, *Geophysical Research Letters*, 38(16), L16802.
- D'Alessandro, W. (2006), Gas hazard: an often neglected natural risk in volcanic areas, vol. 1, pp. 369–378, WIT Press. [online] Available from: <http://library.witpress.com/pages/PaperInfo.asp?PaperID=16242> (Accessed 25 July 2012)
- Giammanco, S., S. Gurrieri, and M. Valenza (1997), Soil CO<sub>2</sub> degassing along tectonic structures of Mount Etna (Sicily): the Pernicana fault, *Applied Geochemistry*, 12(4), 429–436, doi:10.1016/S0883-2927(97)00011-5.
- Giggenbach, W. F. (1992), Isotopic shifts in waters from geothermal and volcanic systems along convergent plate boundaries and their origin, *Earth and Planetary Science Letters*, 113(4), 495–510, doi:10.1012/821X(92)90127-H.
- Gonfiantini, R., M. A. Roche, J. C. Olivry, J. C. Fontes, and G. M. Zuppi (2001), The altitude effect on the isotopic composition of tropical rains, *Chemical Geology*, 181(1-4), 147–167.
- Hernández, P., and J. M. Salazar (2002), Continuous Monitoring of Diffuse CO<sub>2</sub> and H<sub>2</sub>S Degassing Rates at Masaya Volcano, Nicaragua, Central America, in *AGU Fall Meeting Abstracts*, p. 1205.
- Ilyinskaya, E., C. Oppenheimer, T. A. Mather, R. S. Martin, and P. R. Kyle (2010), Size-resolved chemical composition of aerosol emitted by Erebus volcano, Antarctica, *Geochem. Geophys. Geosyst.*, 11, 14 PP., doi:2010 10.1029/2009GC002855.
- Jouzel, J., and L. Merlivat (1984), Deuterium and Oxygen 18 in Precipitation: Modeling of the Isotopic Effects During Snow Formation, *J. Geophys. Res.*, 89(D7), 11749–11,757, doi:10.1029/JD089iD07p11749.

Kammerer, M. (2011), Nature and Origin of Salt Deposits Around the Crater of Erebus Volcano, Antarctica, Masters Thesis, New Mexico Institute of Mining and Technology, Socorro, NM, October. [online] Available from: [http://www.ees.nmt.edu/outside/alumni/papers/2011t\\_kammerer\\_mm.pdf](http://www.ees.nmt.edu/outside/alumni/papers/2011t_kammerer_mm.pdf)

Masson-Delmotte, V., S. Hou, A. Ekaykin, J. Jouzel, A. Aristarain, R. T. Bernardo, D. Bromwich, O. Cattani, M. Delmotte, and S. Falourd (2008), A review of Antarctic surface snow isotopic composition: observations, atmospheric circulation, and isotopic modeling, *Journal of Climate*, 21(13), 3359–3387.

Mörner, N.-A., and G. Etiope (2002), Carbon degassing from the lithosphere, *Global and Planetary Change*, 33(1-2), 185–203, doi:10.1016/S0921-8181(02)00070-X.

Niewodniczanski, J., J. Grabczak, L. Baranski, and J. Rzepka (1981), The altitude effect on the isotopic composition of snow in high mountains, *Journal of Glaciology*, 27, 99–111.

Notsu, K., K. Sugiyama, M. Hosoe, A. Uemura, Y. Shimoike, F. Tsunomori, H. Sumino, J. Yamamoto, T. Mori, and P. A. Hernandez (2005), Diffuse CO<sub>2</sub> efflux from Iwojima volcano, Izu-Ogasawara arc, Japan, *Journal of Volcanology and Geothermal Research*, 139(3-4), 147–161, doi:doi: DOI: 10.1016/j.jvolgeores.2004.08.003.

Oppenheimer, C., and P. R. Kyle (2008), Probing the magma plumbing of Erebus volcano, Antarctica, by open-path FTIR spectroscopy of gas emissions, *Journal of Volcanology and Geothermal Research*, 177(3), 743–754, doi:10.1016/j.jvolgeores.2007.08.022.

Panichi, C., and G. La Ruffa (2001), Stable isotope geochemistry of fumaroles: an insight into volcanic surveillance, *Journal of Geodynamics*, 32(4-5), 519–542, doi:10.1016/S0264-3707(01)00046-1.

Sharp, Z. (2007), *Principles of stable isotope geochemistry*, Pearson/Prentice Hall.

Siegenthaler, U., and H. Oeschger (1980), Correlation of <sup>18</sup>O in precipitation with temperature and altitude, *Nature*, 285(5763), 314–317, doi:10.1038/285314a0.

Wardell, L. J., P. R. Kyle, and A. R. Campbell (2003), Carbon dioxide emissions from fumarolic ice towers, Mount Erebus volcano, Antarctica, *Geological Society, London, Special Publications*, 213(1), 231–246.

Zimbelman, D. R., R. O. Rye, and G. P. Landis (2000), Fumaroles in ice caves on the summit of Mount Rainier—preliminary stable isotope, gas, and geochemical studies, *Journal of Volcanology and Geothermal Research*, 97(1-4), 457–473.

Zreda-Gostynska, G., P. R. Kyle, D. Finnegan, and K. M. Prestbo (1997), Volcanic gas emissions from Mount Erebus and their impact on the Antarctic environment, *J. Geophys. Res.*, 102(B7), 15039–15,055, doi:10.1029/97JB00155.

Zreda-Gostynska, G. A. (1995), Characterization of gas and aerosol emissions from Mount Erebus Volcano, Antarctica, PhD Dissertation, New Mexico Institute of Mining and Technology.

**6.10 Appendix A: Ross island snow and ice samples  
with stable isotope data, chemistry data, and  
percent magmatic water estimates.**

**Table 6.1: Ross island snow and ice samples with stable isotope data, chemistry data, and percent magmatic water estimates**

S	Snow	JM	Jayne Margolin
I	Ice	MK	Melissa Kammerer
F	Firm	AC	Aaron Curtis
I	Ice Core		
SP	Snow Profile		

Collected by Sample #	Date	Lat	Lon	Elev (m)	Depth (m)	$\delta^2\text{H}$	Type $\delta^{18}\text{O}$	S (ppm)	
								Comments	Cl (ppm)
1	JM Dec 1, 04	-77.5104	167.1471	3389	0	-261.1	-30.3	S Snowing through the plume (mm-size flakes)	18% 4.3 19.6 4.9
2	JM Dec 2, 04	-77.5104	167.1471	3389	0	-268.5	-31.3	S Snowing through plume (wet and heavy)	18% 0.8
3	JM Dec 3, 04	-77.5177	167.2150	3466	0	-304	-38.6	S 25 m from the skidoo track	0% 3.8
4	JM Dec 4, 04	-77.5174	167.2082	3458	0.02	-299	-35.7	S Small rocks under the snow surface	15% 11.6 11.8
5	JM Dec 5, 04	-77.5161	167.2024	3460	0.01	-298.7	-37.9	S 10 m from the skidoo track	2.3 7.8
6	JM Dec 6, 04	-77.5141	167.2077	3440	0.01	-294.5	-36.8	S Outcrops nearby (dirty snow)	4% 4.4 8.4
7	JM Dec 7, 04	-77.5133	167.1963	3417	0	-299.1	-37.9	S Fresh snow falling	0% 10.1 10
8	JM Dec 8, 04	-77.5120	167.1884	3406	0.01	-303.6	-39.1	S No refreezing seen in the snow	3 6.1
9	JM Dec 9, 04	-77.5094	167.1850	3374	0.02	-310.2	-40.5	S 2 cm of fresh snow accumulation	1.6 12.5
10	JM Dec 10, 04	-77.5107	167.1755	3379	0.02	-308.4	-40.7	S In wind drifts and rocks nearby	1.8 5.4 1.3
11	JM Dec 11, 04	-77.5109	167.1754	3384	0.03	-304.7	-39.5	I Clear, blue-tinted ice under snow	1.4
12	JM Dec 12, 04	-77.5102	167.1628	3395	0.02	-304	-39.8	S Some freezing - Snow hard to collect	3.6 6.8
13	JM Dec 13, 04	-77.5340	167.0834	3447	0	-296.8	-37.3	S Small snow crystals (< 1 mm)	2% 7%
14	JM Dec 14, 04	-77.5289	167.0948	3459	0.01	-299.3	-37	S Lots of snow drifts	1.1
15	JM Dec 15, 04	-77.5232	167.0981	3393	0.04	-263.7	-32.9	S Very clean snow and temperature dropping	4% 3.4 6.2 1.1
16	JM Dec 16, 04	-77.5173	167.1024	3346	0.02	-295.6	-37.8	S 5 m South of skidoo track	1.5 5.2
17	JM Dec 17, 04	-77.5141	167.1034	3345	0.03	-296.8	-38.8	S Fresh snow, but sticky	2 6.5

**Table 6.1 – continued**

Sample #	Collected by	Date	Lat	Lon	Elev (m)	Depth (m)	Type $\delta^{18}\text{O}$	$\delta^2\text{H}$	S (ppm)	Cl (ppm)	F (ppm)	Est. mag. $\text{H}_2\text{O}$	Comments
18	JM	Dec 18, 04	-77.5131	167.1276	3374	0.03	-293.8	-37.6	S	Wet and heavy snow	50.2	24.8	
19	JM	Dec 19, 04	-77.5119	167.1376	3393	0.03	-291	-37.4	S	Re-melt texture	32.2	7.9	
20	JM	Dec 20, 04	-77.5105	167.1474	3398	0	-331.8	-39.7	S	In a large cavern with needle-like snow crystals	16%	0.2	
21	JM	Dec 21, 04	-77.5231	167.1551	3671	0	-264.7	-29.6	S	Near outcrops with salt encrustations	27%		
22	JM	Dec 22, 04	-77.5228	167.1554	3666	0.03	-331.2	-37.8	S	Directly on rock that may be shielding the plume	29%		
23	JM	Dec 23, 04	-77.5227	167.1535	3659	0	-275.7	-32.7	S	Icy snow	15%	177	169.2
24	JM	Dec 24, 04	-77.5219	167.1485	3620	0.1	-338.7	-42.1	S	On outcrops with yellow salt encrustations	7%		517.9
25	JM	Dec 25, 04	-77.5191	167.1550	3539	0.01	-299.3	-38.8	S	Rock and ash in snow	7.3		46.4
26	JM	Dec 26, 04	-77.5139	167.1493	3422	0.02	-305.9	-39.4	S	Large wind drifts and sampled from 7 cm down			16.8
27	JM	Dec 27, 04	-77.5091	167.1241	3371	0.07	-310.4	-39	S	Medium to small crystals (1 mm and less)	3%	29.9	31.7
28	JM	Dec 28, 04	-77.5083	167.1098	3323	0.02	-298.8	-40	S	Clean snow, but surrounded by columnar jointing			
29	JM	Dec 29, 04	-77.5074	167.0981	3287	0.03	-287.5	-37.6	S	Dry snow, but it keeps a shape			
30	JM	Dec 30, 04	-77.5061	167.1414	3382	0.02	-300.8	-39.7	S	Clean snow and at the end of the transect from the summit			
31	JM	Dec 31, 04	-77.5104	167.1471	3345	0	-287.1	-35.8	SP	Snow that is melted for drinking	4%	11.3	11.9
32	JM	Dec 1, 04	-77.5104	167.1471	3345	0.36	-281.1	-35.4	SP	Near an ash layer	2%	2.1	5.7
33	JM	Dec 2, 04	-77.5104	167.1471	3345	0.58	-297.3	-38.2	SP	Ash present in snow		7.6	9
34	JM	Dec 3, 04	-77.5104	167.1471	3345	0.76	-335.3	-42.3	SP	Small, clumpy crystals (< 1 mm)	2%	10.2	11.2
35	JM	Dec 4, 04	-77.5089	167.1377	3388	0.02	-291.3	-36.5	I	Yellow ice about 50 m from Hut Caves	3%		600.1
36	JM	Dec 5, 04	-77.5099	167.1359	3386	0	-281.4	-33.6	I	Milky yellow ice around outcrops	14%	263.2	1089.3
37	JM	Dec 6, 04	-77.5333	167.0842	3459	0.3	-320.5	-41.3	S	Thermal area - wet snow from 30 cm down		1.7	5.2
38	JM	Dec 7, 04	-77.5334	167.0842	3458	0	-309.8	-40.3	SP	At a vent with steam coming out		0.4	1.1
39	JM	Dec 8, 04	-77.5334	167.0842	3458	0.23	-322.2	-40.2	SP	Wet and heavy snow	5%	0.6	1.5
40	JM	Dec 9, 04	-77.5334	167.0842	3458	0.38	-348.3	-43.6	SP	Course and crystalline textured snow	5%	1.3	3.3
41	JM	Dec 10, 04	-77.5251	167.1432	3594	0	-274.6	-32.5	S	Clean and frozen snow	15%	75.6	54.2
42	JM	Dec 11, 04	-77.5251	167.1432	3594	0.22	-347.6	-44.7	F	Clean and frozen snow from 22 cm down		48.5	61.2

**Table 6.1 – continued**

Sample #	Collected by	Date	Lat	Lon	Elev (m)	Depth (m)	Type $\delta^{18}\text{O}$	$\delta^2\text{H}$	S (ppm)	Cl (ppm)	F (ppm)	Est. mag. $\text{H}_2\text{O}$	Comments
43	JM	Dec 12, 04	-77.5106	167.1470	3425	0	-284.1	-33.2	S	Numerous small outcrops	19%	29.5	36.6
44	JM	Dec 13, 04	-77.5311	167.2029	3523	0.25	-292.7	-37.8	F	Frozen snow from 23 cm down		10.2	11.8
45	JM	Dec 14, 04	-77.5306	167.2113	3489	0	-294.6	-37.4	S	Frozen surface snow		12.5	21.2
46	JM	Dec 15, 04	-77.5276	167.2195	3488	0.28	-278.3	-35.9	S	From a wind drift and 28 cm down		0.8	6.6
47	JM	Dec 16, 04	-77.5217	167.2223	3460	0	-289.3	-35.8	S	Clean snow		6%	5.5
48	JM	Dec 17, 04	-77.5165	167.2054	3451	0.3	-274.3	-34.7	S	Dirty snow, against outcrops		1%	24.7
49	JM	Dec 18, 04	-77.5165	167.2054	3451	0.01	-288.9	-36.5	S	From 1 cm of old snow accumulation		1%	5.2
50	JM	Dec 19, 04	-77.5059	167.1839	3343	0	-267.9	-35.9	SP	Powdery, re-melt snow		1.7	7.8
51	JM	Dec 20, 04	-77.5059	167.1839	3343	0.18	-315.2	-39.2	SP	Dirty snow and near yellow encrustations		5%	19.3
52	JM	Dec 21, 04	-77.5059	167.1839	3343	0.71	-292.2	-37.1	SP	Cloudy, white colored ice		19.6	17.2
53	JM	Dec 22, 04	-77.5343	167.1349	3551	0.48	-320.6	-41.2	F	Clean snow from 48 cm down		0.2	1.7
54	JM	Dec 23, 04	-77.5337	167.1415	3612	0.02	-304.3	-38.6	S	Sticky snow		0%	3.2
55	JM	Dec 24, 04	-77.5316	167.1141	3554	0	-269.8	-29.4	S	Frozen surface snow		32%	1.8
56	JM	Dec 25, 04	-77.5313	167.1016	3532	0.28	-288	-35.8	S	Recrystallized texture		5%	11.8
57	JM	Dec 26, 04	-77.5116	167.1377	3459	0.01	-276.7	-34.3	I	Yellow ice surrounded by large outcrops		5%	271.3
58	JM	Dec 27, 04	-77.5311	167.2180	3489	0.03	-314.7	-39.6	S	Heavy plume almost directly overhead		2%	1
59	JM	Dec 28, 04	-77.5334	167.2154	3447	0.28	-307.2	-38.5	I	Grey/Brown ice about 28 cm down		4%	21.3
60	JM	Dec 29, 04	-77.5285	167.2082	3519	0	-260.9	-30.8	S	Low plume directly overhead		15%	10.9
61	JM	Dec 30, 04	-77.5279	167.2017	3586	0	-283.4	-35.2	S	Ash present in snow		5%	80
62	JM	Dec 31, 04	-77.5275	167.1985	3540	0	-283.3	-34.2	S	Heavy plume directly overhead		11%	45.2
63	JM	Dec 1, 04	-77.5256	167.2076	3429	0.24	-294.2	-36.6	S	25 cm down near encrusted outcrops		5%	64.7
64	JM	Dec 2, 04	-77.5236	167.2113	3508	0.01	-264.7	-29.7	S	Recrystallized texture		26%	9.6
65	JM	Dec 3, 04	-77.5110	167.1901	3387	0.26	-286.4	-35.8	S	25 m West of the skidoo track		3%	6.1
66	JM	Dec 4, 04	-77.5106	167.1812	3385	0	-282.6	-34.2	S	Recrystallized yellow snow		11%	1006.5
67	JM	Dec 5, 04	-77.5085	167.1652	3383	0.03	-308.7	-38.2	S	Frozen snow near encrusted outcrops		7%	35.8
68	JM	Dec 6, 04	-77.5085	167.1652	3383	0	-274.3	-31.9	S	Wind blown and powdery snow		19%	18
69	JM	Dec 7, 04	-77.5105	167.1474	3398	0.05	-325.3	-37.9	S	Cavern roof is now open with a thick accumulation		23%	0.2
													1.4

**Table 6.1 – continued**

Sample #	Collected by	Date	Lat	Lon	Elev (m)	Depth (m)	Type $d^{18}\text{O}$	$d^2\text{H}$	S (ppm)	Cl (ppm)	F (ppm)	Est. mag. $\text{H}_2\text{O}$	Comments
70	JM	Dec 8, 04	-77.5091	167.1554	3437	0	-289.3	-30.6	S	Pencil-like crystals off of a rock surface	41%	1232.2	79.1
71	JM	Dec 9, 04	n/a	n/a	3761	0.01	-302.7	-35.1	S	Sticky, yellow-brown snow crystals	22%	122	121.5
72	JM	Dec 10, 04	n/a	n/a	3761	0.03	-370.5	-44.7	S	In the plume	16%	142.4	157.1
73	JM	Dec 11, 04	-77.5279	167.1786	3675	0.04	-288	-35.8	S	Dirty snow with elongated crystals	5%	2083.7	338.4
74	JM	Dec 12, 04	-77.5286	167.1765	3615	0	-331.7	-37.1	S/I	Yellow snow and ice	34%	10.1	21.8
75	JM	Dec 13, 04	-77.5292	167.1914	3580	0	-298.9	-36.9	SP	Refrozen, wind blown snow	7%	9.8	12
76	JM	Dec 14, 04	-77.5292	167.1914	3580	0.18	-287.7	-37	SP	Clean, granular crystals	24.6	27.9	5.9
77	JM	Dec 15, 04	-77.5292	167.1914	3580	0.41	-294.6	-36.7	SP	Dirty snow (frozen and clumpy)	5%	52.5	17.9
78	JM	Dec 16, 04	-77.5292	167.1914	3580	0.66	-302.6	-37.4	SP	Dirty snow, near base rock	7%	59.6	18.6
79	JM	Dec 17, 04	-77.5175	167.1310	3435	0.01	-257.5	-27.3	I	Yellow ice from a thermal region	35%	6.6	6.6
80	JM	Dec 18, 04	-77.5169	167.2101	3510	0	-292.3	-36.7	S	Clean, frozen snow	3%	11.2	1.8
81	JM	Dec 19, 04	-77.5121	167.2066	3362	0.05	-281.9	-34.1	S	Frozen snow that breaks easily	11%	0.9	3.9
82	JM	Dec 20, 04	-77.5012	167.2432	2743	0.05	-243.6	-29.9	S	Frozen snow with wet crystals	6%	9.3	5.7
83	JM	Dec 21, 04	-77.5011	167.2406	2743	0	-261.3	-31.2	S	Hard, frozen surface snow	13%	10.5	15.5
84	JM	Dec 22, 04	-77.5073	167.2224	3000	0	-247.7	-29.5	S	Sticky, frozen surface surrounded by outcrops	12%	1899.9	1890.5
85	JM	Dec 23, 04	-77.5107	167.1374	3364	0	-292.6	-36.5	S	Yellow snow with brown and white colors	4%	5	15.7
86	JM	Dec 24, 04	-77.5149	167.1308	3373	0.06	-287.1	-36.2	S	Clean, smooth snow	1%	584.5	707
87	JM	Dec 25, 04	-77.5156	167.1355	3373	0	-290.9	-37.1	I	Yellow, cloudy ice	8.9	15.7	2.5
88	JM	Dec 26, 04	-77.5194	167.1412	3373	0.43	-288.9	-36.7	F	Clean sample from 43 cm down	5.4	13.1	1.5
89	JM	Dec 27, 04	-77.5306	167.2033	3525	0	-246.8	-29.7	S	Clean, frozen snow with thick plume	10%		
90	JM	Dec 28, 04	-77.5335	167.2060	3525	0.01	-296.3	-36.2	S	Final transect point from the Eastern summit	9%	34.2	30.5
91	JM	Dec 29, 04	-77.5335	167.2068	3525	0.55	-263.8	-33.6	S	Clean, frozen snow	47.1	19.6	4.5
92	JM	Dec 30, 04	-77.5299	167.1393	3690	0.02	-368.9	-45.3	S	Within the side crater (only small snow patches)	11%	105	41.8
93	JM	Dec 31, 04	-77.5289	167.1402	3700	0.17	-310.6	-37.6	S	Dirty snow from 20 cm down on the rocks	12%	630.4	158.5
94	JM	Dec 1, 04	-77.5286	167.1430	3700	0.02	-293	-34.2	S	Pores and air pockets in brown-green snow	20%	4.9	13.1

**Table 6.1 – continued**

Sample #	Collected by	Date	Lat	Lon	Elev (m)	Depth (m)	Type $\delta^{18}\text{O}$	$\delta^2\text{H}$	S (ppm)	Cl (ppm)	F (ppm)	Est. mag. $\text{H}_2\text{O}$	Comments
95	JM	Dec 2, 04	-77.5279	167.1390	3670	0.13	-352.2	-45.3	S	10 cm down and surrounded by Erebus crystals	1.8	2.7	
96	JM	Dec 3, 04	-77.5104	167.1471	3345	0.04	-314.9	-40.1	S	Showng hard with no visibility	11.2	6.2	1.9
97	JM	Dec 4, 04	-77.5104	167.1471	3345	0.06	-299.7	-38.6	S	From 7 cm down in fresh snow	1.1	12.4	1.8
98	JM	Dec 5, 04	-77.8463	166.6189	91	0.18	-172.3	-21.3	S	Wet snow near the sea	2%	13.8	5.7
99	JM	Dec 6, 04	-77.8369	166.6650	159	0.12	-171.9	-21	S	Clean, wet and heavy snow	4%	1.8	0.9
100	JM	Dec 7, 04	-77.8520	166.6943	228	0.05	-172.5	-21.1	S	Heavy snow on the rocks	4%		1
101	JM	Dec 8, 04	-77.8013	166.7750	230	0.19	-165.3	-19.5	S	Frozen surface but powdery under 2 cm depth	8%	1.1	
102	JM	Dec 9, 04	-77.8203	166.7205	267	0.12	-169.1	-20.8	S	25 m East of a scoria cone	3%		1
103	JM	Dec 10, 04	-77.8329	166.6909	167	0.07	-184.8	-22.2	S/I	Clean snow with a thin dirty yellow ice layer around 5 cm	6%	3.7	
104	JM	Dec 11, 04	-77.7660	167.3152	46	0	-169.1	-21	S	Lightweight snow (not wet snow)	1%		1
105	JM	Dec 12, 04	-77.7660	167.3152	46	0.3	-175.7	-22.6	S	Very clean snow			
106	JM	Dec 13, 04	-77.7711	167.2468	39	0	-167.3	-20	S	Sticky snow	6%	0.6	1.8
107	JM	Dec 16, 04	-77.8201	167.1218	26	0.03	-186.5	-22.4	S	In wind drifts	7%	0.2	2.1
108	MK	Dec 13, 09	-77.5096	167.1483	3350	-	-209.3	-24.9	S	Old snow	10%	8.2	2
109	MK	Dec 13, 09	-77.5096	167.1483	3350	-	-295.8	-36.7	I		6%	16.4	20
110	MK	Dec 13, 09	-77.5072	167.1596	3300	-	-281.7	-33.3	S		16%	13.5	4
111	MK	Dec 13, 09	-77.5072	167.1593	3325	-	-298.1	-32.4	I		36%	889.3	192
112	MK	Dec 13, 09	-77.5053	167.1617	3300	-	-275	-32.3	S	Old snow	17%	7	14
113	MK	Dec 13, 09	-77.5053	167.1617	3300	0	-292.8	-35.7	S	New Snow	9%	1.2	1
114	MK	Dec 13, 09	-77.5066	167.1517	3330	-	-279.3	-31.7	S	Old snow	25%	22.1	3
115	MK	Dec 13, 09	-77.5070	167.1362	3330	-	-264.8	-31.6	S	Old snow	13%	4.2	13
116	MK	Dec 14, 09	-77.5219	167.1485	3550	-	-289.3	-34.4	S	Old snow	15%	51.3	46
117	MK	Dec 14, 09	-77.5219	167.1485	3550	0	-284.6	-32.2	S	New Snow	26%	20.9	17
118	MK	Dec 14, 09	-77.5241	167.1391	3525	-	-273.2	-31.7	S	Old snow	20%	31.1	43
119	MK	Dec 14, 09	-77.5241	167.1391	3525	0	-272.6	-28.9	S	New Snow	38%	7.3	15
120	MK	Dec 14, 09	-77.5233	167.1187	3400	-	-284.7	-33.7	S	Old snow	16%	15.3	21

**Table 6.1 – continued**

Sample #	Collected by	Date	Lat	Lon	Elev (m)	Depth (m)	$d^2H$	Type $d^{18}O$	S (ppm)	Cl (ppm)	F (ppm)	Est. mag. $H_2O$	Comments
121	MK	Dec 14, 09	-77.5233	167.1187	3400	0	-293.6	-35.7	S	New Snow	10%	6.3	24
122	MK	Dec 14, 09	-77.5236	167.0927	3325	-	-329.1	-39.9	S	Old snow	13%	2.8	11
123	MK	Dec 14, 09	-77.5236	167.0927	3325	-	-279.8	-32.9		-	17%	4.7	9
124	MK	Dec 14, 09	-77.5224	167.0618	3175	-	-285.4	-33.4	S	Old snow	18%	1.5	5
125	MK	Dec 14, 09	-77.5224	167.0618	3175	0	-284.5	-35.1	S	New snow	6%	0.2	4
126	MK	Dec 14, 09	-77.5244	167.0483	3110	-	-290.1	-34.8	S	Old snow	13%	2.9	6
127	MK	Dec 14, 09	-77.5350	167.1136	3460	-	-311.7	-36.1	S	Old snow	23%	1.4	3
128	MK	Dec 14, 09	-77.5381	167.1028	3400	-	-308.2	-36.2	S	Old snow	20%	2.2	3
129	MK	Dec 14, 09	-77.5381	167.1028	3400	0	-301.5	-35.3	S	New snow	20%	0.2	3
130	MK	Dec 17, 09	-77.4292	167.0248	1625	-	-247.2	-27.8	S	Old snow	23%	0.4	3
131	MK	Dec 17, 09	-77.4292	167.0248	1625	0	-234.1	-25.3	S	New snow	28%	0.3	2
132	MK	Dec 17, 09	-77.4560	166.4978	250	-	-191.3	-21.3	S	Old snow	19%	0.1	6
133	MK	Dec 17, 09	-77.4560	166.4978	250	-	-149.5	-17.1		-	11%	0.2	7
134	MK	Dec 17, 09	-77.4530	166.8146	1400	-	-157	-19.7	S	Old snow	0.1	1	1
135	MK	Dec 17, 09	-77.4768	166.8902	1700	-	-215.2	-25	S	Old snow	14%	0.2	2
136	MK	Dec 17, 09	-77.4980	167.0220	2450	-	-264.4	-30.6	S	Old snow	20%	1.2	3
137	MK	Dec 17, 09	-77.4980	167.0220	2450	0	-251.3	-28.1	S	New snow	25%	2.6	4
138	MK	Dec 17, 09	-77.5246	167.2374	3375	-	-289.5	-34.5	S	Old snow	15%	26.8	13
139	MK	Dec 17, 09	-77.5246	167.2374	3375	0	-285.8	-32.4	S	New snow	26%	1.2	4
140	MK	Dec 17, 09	-77.5265	167.2044	3700	-	-256.3	-29.9	S	Old snow	17%	13.6	20
141	MK	-	-	-	3700	-	-291.6	-32	S	-	33%	35558.1	403
142	MK	Dec 16, 09	-77.5186	167.1114	3325	-	-307	-33.8	S	-	35%	8	13
143	MK	Dec 16, 09	-77.5186	167.1114	3325	-	-322.6	-36		-	33%	28.5	43
144	MK	Dec 16, 09	-77.5183	167.1113	3811	-	-321.8	-37.3	S	-	24%	6.3	16
145	AC	Dec 19, 09	-77.5090	167.1422	3339	0.8	-328.6	-38.3	IC	C1A10	23%		
146	AC	Dec 19, 09	-77.5090	167.1422	3339	0.45	-322.5	-36.8	IC	C1A45	28%		
147	AC	Dec 19, 09	-77.5090	167.1422	3339	0.85	-338.6	-41.3	IC	C1A5	12%		
148	AC	Dec 19, 09	-77.5090	167.1422	3339	0.35	-330.2	-39.9	IC	C1A55	14%		

**Table 6.1 – continued**

Sample #	Collected by	Date	Lat	Lon	Elev (m)	Depth (m)	$d^2H$	Type $d^{18}O$	S (ppm)	Cl (ppm)	F (ppm)	Est. mag. $H_2O$	Comments
149	AC	Dec 19, 09	-77.5090	167.1422	3339	0	-317.5	-38.2	C	C1A90		14%	
150	AC	Dec 21, 09	-77.5089	167.1411	3337	1.86	-308.9	-35.9	C	C2A15		22%	
151	AC	Dec 21, 09	-77.5089	167.1411	3337	1.76	-332.4	-39.6	C	C2A25		17%	
152	AC	Dec 21, 09	-77.5089	167.1411	3337	1.61	-337.6	-41.4	C	C2A40		10%	
153	AC	Dec 21, 09	-77.5089	167.1411	3337	1.96	-337.2	-41.3	C	C2A5		11%	
154	AC	Dec 21, 09	-77.5089	167.1411	3337	1.46	-336.6	-40	C	C2A55		19%	
155	AC	Dec 21, 09	-77.5089	167.1411	3337	3.16	-301.3	-36.3	C	C2B25		13%	
156	AC	Dec 21, 09	-77.5089	167.1411	3337	2.96	-338.9	-42.4	C	C2B45		5%	
157	AC	Dec 21, 09	-77.5089	167.1411	3337	3.36	-296.3	-35.6	C	C2B5		14%	
158	AC	Dec 21, 09	-77.5089	167.1411	3337	0.8	-336.9	-40	C	C2C25		19%	
159	AC	Dec 21, 09	-77.5089	167.1411	3337	0.6	-296.8	-33.6	C	C2C45		27%	
160	AC	Dec 21, 09	-77.5089	167.1411	3337	1	-345.3	-40.5	C	C2C5		23%	
161	AC	Dec 21, 09	-77.5089	167.1411	3337	0.4	-298.1	-37	C	C2D0		5%	
162	AC	Dec 21, 09	-77.5089	167.1411	3337	0.2	-297.1	-37.4	C	C2D20		2%	
163	AC	Dec 21, 09	-77.5089	167.1411	3337	0	-340	-40.1	C	C2D40		21%	
164	AC	Dec 21, 09	-77.5089	167.1411	3337	0.35	-303	-37.9	C	C2D5		4%	
165	AC	Dec 24, 09	-77.5342	167.0995	3445	1.52	-300.4	-33	C	C3A30		35%	
166	AC	Dec 24, 09	-77.5342	167.0995	3445	1.42	-295.4	-32.9	C	C3A40		30%	
167	AC	Dec 24, 09	-77.5342	167.0995	3445	1.77	-325.4	-38.6	C	C3A5		18%	
168	AC	Dec 24, 09	-77.5342	167.0995	3445	1.21	-302.9	-34.8	C	C3B20		25%	
169	AC	Dec 24, 09	-77.5342	167.0995	3445	1.06	-303.7	-35	C	C3B35		24%	
170	AC	Dec 24, 09	-77.5342	167.0995	3445	1.36	-297.5	-34.8	C	C3B5		19%	
171	AC	Dec 24, 09	-77.5342	167.0995	3445	0.85	-304.2	-34.6	C	C3C10		27%	
172	AC	Dec 24, 09	-77.5342	167.0995	3445	0.7	-306.6	-35.1	C	C3C25		26%	
173	AC	Dec 24, 09	-77.5342	167.0995	3445	0.45	-298.4	-34.5	C	C3C50		22%	
174	AC	Dec 24, 09	-77.5342	167.0995	3445	0.15	-309.3	-37.4	C	C3D25		12%	
175	AC	Dec 24, 09	-77.5342	167.0995	3445	0	-313.6	-39.7	C	C3D40		1%	
176	AC	Dec 24, 09	-77.5342	167.0995	3445	0.35	-304.5	-35.5	C	C3D5		21%	

**Table 6.1 – continued**

Sample #	Collected by	Date	Lat	Lon	Elev (m)	Depth (m)	$d^2H$	Type $d^{18}O$	S (ppm)	Cl (ppm)	F (ppm)	Est. mag. $H_2O$	Comments
177	AC	Dec 24, 09	-77.5348	167.1321	3494	3.1	-268.4	-33.2	C	C4A20		5%	
178	AC	Dec 24, 09	-77.5348	167.1321	3494	2.9	-280.7	-35.2	C	C4A40		2%	
179	AC	Dec 24, 09	-77.5348	167.1321	3494	3.25	-319.2	-37.8	C	C4A5		18%	
180	AC	Dec 24, 09	-77.5348	167.1321	3494	0.25	-295.9	-34.4	C	C4B20		21%	
181	AC	Dec 24, 09	-77.5348	167.1321	3494	0	-301.6	-36.3	C	C4B45		13%	
182	AC	Dec 24, 09	-77.5348	167.1321	3494	0.4	-272.8	-32.5	C	C4B5		14%	
183	AC	Dec 24, 09	-77.5348	167.1321	3494	2.17	-271.1	-32.3	C	C4C20		14%	
184	AC	Dec 24, 09	-77.5348	167.1321	3494	2.07	-263.5	-31.3	C	C4C30		14%	
185	AC	Dec 24, 09	-77.5348	167.1321	3494	2.32	-276.4	-32.7	C	C4C5		15%	
186	AC	Dec 24, 09	-77.5348	167.1321	3494	1.62	-294.9	-35.7	C	C4D20		11%	
187	AC	Dec 24, 09	-77.5348	167.1321	3494	1.42	-285	-33.3	C	C4D40		19%	
188	AC	Dec 24, 09	-77.5348	167.1321	3494	1.77	-301.5	-36.4	C	C4D5		12%	
189	AC	Dec 24, 09	-77.5348	167.1321	3494	1.1	-287.6	-34.2	C	C4E15		15%	
190	AC	Dec 24, 09	-77.5348	167.1321	3494	0.95	-302.7	-36.2	C	C4E30		15%	
191	AC	Dec 24, 09	-77.5348	167.1321	3494	1.2	-269.9	-32.5	C	C4E5		12%	
192	AC	Dec 24, 09	-77.5348	167.1321	3494	0.58	-287	-34.1	C	C4F25		15%	
193	AC	Dec 24, 09	-77.5348	167.1321	3494	0.38	-275.6	-32.4	C	C4F45		17%	
194	AC	Dec 24, 09	-77.5348	167.1321	3494	0.78	-294.9	-35.3	C	C4F5		14%	
195	AC	Dec 24, 09	-77.5348	167.1321	3494	0.15	-302.7	-36.4	C	C4G15		14%	
196	AC	Dec 24, 09	-77.5348	167.1321	3494	0	-294	-35.5	C	C4G30		12%	
197	AC	Dec 26, 09	-77.5170	167.2177	3402	0.35	-256.8	-31.4	C	C5A10		7%	
198	AC	Dec 26, 09	-77.5170	167.2177	3402	0.25	-321.9	-39.6	C	C5A20		9%	
199	AC	Dec 26, 09	-77.5170	167.2177	3402	0.15	-323.4	-39.4	C	C5A30		11%	
200	AC	Dec 27, 09	-77.5170	167.2177	3402	0	-337.2	-41.3	C	C5A45		10%	
201	AC	Dec 26, 09	-77.5170	167.2177	3402	0.4	-317.4	-40.4	C	C5A5			
202	AC	Dec 27, 09	-77.5326	167.1131	3503	0.1	-248.9	-32.5	C	C6A20			
203	AC	Dec 27, 09	-77.5326	167.1131	3503	0	-276.2	-35.9	C	C6A30			
204	AC	Dec 27, 09	-77.5344	167.0955	3503	0.25	-248.5	-32.5	C	C6A5			

**Table 6.1 – continued**

			S (ppm)		
			Cl (ppm)		
			F (ppm)		
			Est. mag. $\text{H}_2\text{O}$		
			Comments		
	Type				
	$\delta^{18}\text{O}$				
	$\delta^2\text{H}$				
	Depth (m)				
	Elev (m)				
	Lon				
	Lat				
	Date				
Collected by					
Sample #					

205 AC Dec 28, 09 -77.5344 167.0955 3425 1.23 -236.6 -29.2 |C C7A5 5%

206 AC Dec 28, 09 -77.5344 167.0955 3425 1.03 -244.3 -32.7 |C C7A15

207 AC Dec 28, 09 -77.5344 167.0955 3425 1.33 -268.5 -35.3 |C C7A35

208 AC Dec 28, 09 -77.5344 167.0955 3425 0.74 -277.9 -36.8 |C C7C10

209 AC Dec 28, 09 -77.5344 167.0955 3425 0.49 -271.8 -36.2 |C C7C35

210 AC Dec 28, 09 -77.5344 167.0955 3425 0 -249.8 -31.2 |C C7D30 3%

## 6.11 Appendix B: Estimation of percent magmatic water

We employed a simple model assuming that sample concentrations ( $\delta^2 H_{\text{samp}}, \delta^{18} O_{\text{samp}}$ ) result from linear mixing between an initial meteoric value ( $\delta^2 H_{\text{met}}, \delta^{18} O_{\text{met}}$ ) and a magmatic water value ( $\delta^2 H_{\text{mag}}, \delta^{18} O_{\text{mag}}$ ). The model allows estimation of the maximum magmatic component contributing to each sample analyzed. All snow and ice samples begin as precipitation with isotopic compositions on the Antarctic Meteoric Water Line (AMWL), expressed as

$$\delta^2 H_{\text{AMWL}} = m_{\text{AMWL}} \delta^{18} O + b_{\text{AMWL}} . \quad (6.1)$$

The mixing line is

$$\delta^2 H_{\text{AMWL}} = m_{\text{mix}} \delta^{18} O + b_{\text{mix}} \quad (6.2)$$

with slope

$$m_{\text{mix}} = \frac{\delta^2 H_{\text{met}} - \delta^2 H_{\text{samp}}}{\delta^{18} O_{\text{met}} - \delta^{18} O_{\text{samp}}} \quad (6.3)$$

and  $\delta^2 H$  - intercept

$$b_{\text{mix}} = \delta^2 H_{\text{samp}} - m_{\text{mix}} \delta^{18} O_{\text{samp}} . \quad (6.4)$$

Substituting (6.3) and (6.4) into (6.2), the mixing line becomes

$$\delta^2 H_{\text{mix}} = \delta^{18} O \frac{\delta^2 H_{\text{mag}} - \delta^2 H_{\text{samp}}}{\delta^{18} O_{\text{mag}} - \delta^{18} O_{\text{samp}}} - \delta^{18} O_{\text{samp}} \frac{\delta^2 H_{\text{mag}} - \delta^2 H_{\text{samp}}}{\delta^{18} O_{\text{mag}} - \delta^{18} O_{\text{samp}}} + \delta^2 H_{\text{samp}} . \quad (6.5)$$

At the initial meteoric value ( $\delta^2 H_{\text{met}}, \delta^{18} O_{\text{met}}$ ),

$$\delta^2 H_{\text{AMWL}} = \delta^2 H_{\text{mix}} . \quad (6.6)$$

(6.6) can be solved to find  $\delta^{18} O_{\text{met}}$

$$\delta^{18} O_{\text{met}} = \frac{-b_{\text{AMWL}} \delta^{18} O_{\text{mag}} + b_{\text{AMWL}} \delta^{18} O_{\text{samp}} - \delta^{18} O_{\text{samp}} \delta^2 H_{\text{mag}} + \delta^{18} O_{\text{mag}} \delta^2 H_{\text{samp}}}{m_{\text{AMWL}} \delta^{18} O_{\text{mag}} - m_{\text{AMWL}} \delta^{18} O_{\text{samp}} - \delta^2 H_{\text{mag}} + \delta^2 H_{\text{samp}}} \quad (6.7)$$

at this point,  $\delta^{18} O_{\text{met}}$  could be plugged in to the AMWL equation to obtain  $\delta^2 H_{\text{met}}$  but this step is unnecessary for our ultimate goal, calculation of  $p_{\text{mag}}$ , the (estimated maximum) percent magmatic water in the sample.

$p_{\text{mag}}$  is calculated as the distance between the initial meteoric point and the sample point over the distance between the meteoric point and the estimated magmatic source value. Calculation of actual euclidean distance is unnecessary because  $\delta^{18} O$  distance,  $\delta^2 H$  distance, and euclidean distance are proportional to each other and therefore the ratio will be equal for these three methods. We use  $\delta^{18} O$  :

$$p_{\text{mag}} = \frac{\delta^{18}\text{O}_{\text{met}} - \delta^{18}\text{O}_{\text{samp}}}{\delta^{18}\text{O}_{\text{met}} - \delta^{18}\text{O}_{\text{mag}}} \quad (6.8)$$

substituting leads to

$$p_{\text{mag}} = \frac{b_{\text{AMWL}} + m_{\text{AMWL}} \delta^{18}\text{O}_{\text{samp}} - \delta^2\text{H}_{\text{samp}}}{b_{\text{AMWL}} + m_{\text{AMWL}} \delta^{18}\text{O}_{\text{mag}} - \delta^2\text{H}_{\text{mag}}} \quad (6.9)$$

To draw lines of equal magmatic percentage, we can solve equation (6.9) for  $\delta^2\text{H}_{\text{samp}}$  :

$$\delta^2\text{H}_{\text{samp}} = b_{\text{AMWL}} - p_{\text{mag}} b_{\text{AMWL}} - p_{\text{mag}} m_{\text{AMWL}} \delta^{18}\text{O}_{\text{mag}} + m_{\text{AMWL}} \delta^{18}\text{O}_{\text{samp}} + p_{\text{mag}} \delta^2\text{H}_i \quad (6.10)$$

Introducing the parameters of the AMWL and the literature values for magmatic water

$\delta^{18}\text{O}_{\text{mag}}$	7.5‰
$\delta^2\text{H}_{\text{mag}}$	-62.5‰
$m_{\text{AMWL}}$	7.75
$b_{\text{AMWL}}$	-4.93‰

**Table 6.2:** Literature values of isotopic parameters used for estimation of magmatic water component

further simplifies equation (6.10) :

$$\delta^2\text{H}_{\text{samp}} = -4.93 - 120.7 p_{\text{mag}} + 7.75 \delta^{18}\text{O}_{\text{samp}} . \quad (6.11)$$

## 6.12 Appendix C. Calculation of AMWF

For comparison of Erebus data with data from the rest of the continent, we constructed an expected “Antarctic Meteoric Water Field” based on the data presented by *Masson-Delmotte et al.*, [2008]. The field was determined simply by determining the linear regression of the *Masson-Delmotte et al.*, [2008] dataset, and adding upper and lower bound and lower boundary lines by adding to and subtracting from the  $\delta^2\text{H}$ -intercept of the regression so that the boundary lines ran through the data points the  $\delta^{18}\text{O}$  values furthest removed from the regression line. We created an AMWF using all available data, and then a second AMWF using only the 236 non-averaged data points (that where each data point represented one physical sample) to determine whether averaging had affected the overall range and variability of the dataset. As shown in Figure 6.4, eliminating the averaged data points shrunk the AMWF. Comparing Erebus data with the larger of the two fields reduced the chance of incorrectly declaring non-congruence of the two datasets, so we chose to include the averaged data in the AMWF construction. This larger AMWF increases the significance of our determination that Erebus data is distinct from data obtained on the rest of the continent.

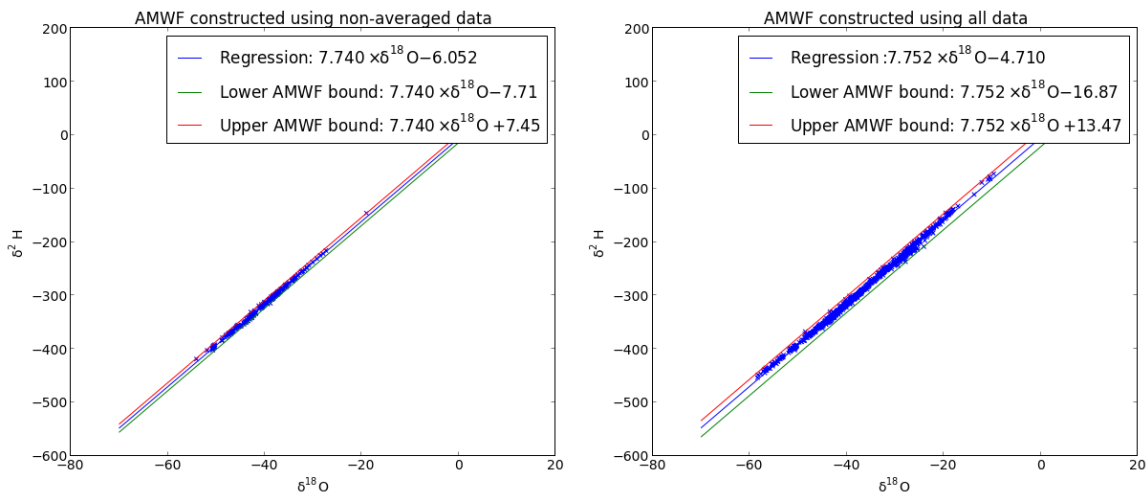


**Figure 6.4:** Antarctic Meteoric Water Field (AMWF) construction. We used the field that encompassed all data from *Masson-Delmotte et al.*, [2008]. This field is shown in black dotted lines on Figure 6.2.

## CHAPTER 7. SUMMARY AND OUTLOOK

FICs are characteristic of volcanic degassing beneath a moderate thickness (2m to 50m) of snow and / or ice. This process is common on Earth, where around 286 active volcanic centers are glaciated or host permanent snowfields (Chapter 4). On Erebus, FIC speleogenesis is driven by melting in response to advective heat flux from discrete gas vents (Chapter 2). The gas vents represent deep degassing, probably modified by shallow hydrothermal circulation and focused by permeability features of the near-surface geology. Although FICs persist for decades or longer, their geometry is extremely dynamic on an annual scale (Chapter 5). The complex set of physical processes operating in the caves makes it difficult or impossible to use changes in FIC passage geometry as an indicator of volcanic unrest, but the initiation of new FIC speleogenesis is a sign of increased heat flow (Chapter 4). FIC formation results in densification of the surrounding ice and causes subsidence cauldrons to appear in the overlying ice topography (Chapter 5).

A recent awakening among cave scientists is leading to the recognition of a growing diversity of speleogenetic mechanisms and settings. As we become acquainted with the processes that create geologically stranger and less human-accessible caves, we broaden our expectations of potential cave conditions on Earth and beyond. A series of recent developments in planetary science suggests that these conditions are present elsewhere in our solar system. New Horizons found geologically active N<sub>2</sub> and H<sub>2</sub>O ice on Pluto, with the tentative identification of cryovolcanoes. Cassini gave us a taste of geysers erupting from a global ocean through the icy crust of Enceladus. Much as Erebus represents the prime nexus of volcanism and cold on earth, Io (one of Jupiter's Galilean moons) does so for the solar system. Intense silicate and sulfur volcanism abounds on this moon of Jupiter where surface temperatures average -160°C. The H<sub>2</sub>O ice at the south pole of Enceladus, the SO<sub>2</sub> frosts and local H<sub>2</sub>O ice patches of Io, the ice of Pluto (H<sub>2</sub>O, N<sub>2</sub>, CH<sub>4</sub>) could all host FICs.

Whether on Earth or elsewhere, phase change caves grow as a function of their microclimate. Findings presented here illuminate some of the thermal processes at work and shows that microclimatic frameworks developed for limestone cave systems on Earth will need heavy modification to predict conditions in FICs. Due to the presence of point sources of advective heat, and the lack of typical temperate zone diurnal and annual insolation variations, concepts such as the heterothermic/homothermic zone division and the seasonal chimney effect do not apply in the Erebus FICs. These concepts are similarly unlikely to apply on FICs of dwarf planets or icy moons. Chapters 2 and 3 present

microclimatic observation of a system whose temperatures are buffered near the freezing point of ice by phase change processes, are affected by barometric pumping of gas from within the volcano edifice, and exhibit strong upward-positive thermal gradients.

The stable thermal stratification observed in a chamber in Cathedral cave makes the cave ceiling of particular interest for further investigation. Microbiological investigations, which have thus far focused on the gas vents in the floor of the chambers, should consider targeting the ceiling. At the spatial scale of our volumetric FODTS investigation, the ceiling was by far the warmest part of the cave chamber. It is the locus of melting and thus the place where tephra in the ice is first delivered into the cave chamber, providing an energy source for chemolithoautotrophs. Additionally, the ceiling is inaccessible to humans and likely less impacted by microbiological contamination in frequently visited caves.

FIC formation can be the first indicator of unrest before an eruption, as it was when Mt. Redoubt, Alaska, erupted in 2009. From a hazards perspective, it is imperative that we monitor the ice masses above the volcanic centers which host ice. Fortunately, ice subsidence cauldrons associated with FIC formation can be observed from airborne or spaceborne platforms. Chapter 5 provides a view of the FIC formation subsidence process from both above and below the ice mass. It should be instructive for the interpretation of any sudden ice mass loss that may be observed above an awakening volcano in the future.

It is likely that only a small number of Earth's fumarolic ice caves have been studied, and the continuation of this work requires a search for the remainder, which are bound to exist in the Andes, Aleutians, and elsewhere. In future FIC work, human expeditions are required to reach the target area, but methods for "unmanned caving" should be developed. Robotic exploration may be necessary when the cave configuration precludes human access, or involves risks such as prohibitively high levels of volcanic gas. Potential robotic platforms include small unmanned aircraft, cryobots, and wall-climbing robots. From a cave protection standpoint, a sanitized robot can conduct exploration in a far more sterile manner than the most cautious human.

Future study should consider FICs in the broader context of snow porosity and macroporosity. The "cold vents" (AKA cold tubes or negative fumaroles) which channel fresh air into the caves through holes in cave walls appear to lack a corresponding hole on the surface; instead they branch into the ice like bronchioles in lungs. The extent, formation processes, and nature of their connectivity with the external atmosphere are mysteries worthy of investigation. There is also evidence, including the subsidence cauldrons to the east of Warren (Figure 5.3a), that FIC-like features exist on Erebus which lack entrances. A cryobot, similar to that developed by the IceMole project, could tunnel from Warren Cave into these suspected "entranceless caves". These unexplored spaces are sure to hold further physical, microbiological, and volcanological secrets.